Summer 2014

Maximum crosstalk estimation and modeling of electromagnetic radiation from PCB/high-density connector interfaces

Matthew Scott Halligan

Department: Electrical and Computer Engineering

Recommended Citation

Halligan, Matthew Scott, "Maximum crosstalk estimation and modeling of electromagnetic radiation from PCB/high-density connector interfaces" (2014). *Doctoral Dissertations*. 2324.
https://scholarsmine.mst.edu/doctoral_dissertations/2324

MAXIMUM CROSSTALK ESTIMATION AND MODELING OF ELECTROMAGNETIC RADIATION FROM PCB/HIGH-DENSITY CONNECTOR INTERFACES

by

MATTHEW SCOTT HALLIGAN

A DISSERTATION

Presented to the Faculty of the Graduate School of the

MISSOURI UNIVERSITY OF SCIENCE AND TECHNOLOGY

In Partial Fulfillment of the Requirements for the Degree

DOCTOR OF PHILOSOPHY

in

ELECTRICAL ENGINEERING

2014

Approved
Daryl G. Beetner, Advisor
Jun Fan
David J. Pommerenke
James L. Drewniak
Lorena Basilio

PUBLICATION DISSERTATION OPTION

This dissertation has been prepared in the form of five papers for publication. The presented papers in this dissertation are extended versions of the papers and are prepared in the style utilized by the Institute of Electrical and Electronics Engineers (IEEE). IEEE holds the copyright for the condensed versions of the journal papers contained in this dissertation. These papers are used in with permission from the respective authors. Pages 3-38 are from the publication, “Maximum crosstalk estimation in weakly coupled transmission lines,” *IEEE Transactions on Electromagnetic Compatibility*, vol. 56, no. 3, pp. 736-744, June 2014. Pages 39-64 are from the future publication, “Maximum crosstalk estimation in lossless and homogeneous transmission lines,” to be published in the journal, *IEEE Transactions on Microwave Theory and Techniques*. This article has been accepted for publication. Pages 65-95 are from the publication, “Electromagnetic radiation resulting from PCB/high-density connector interfaces,” *IEEE Transactions on Electromagnetic Compatibility*, vol. 55, no. 4, pp. 624-638, Aug. 2013. Pages 96-124 are to be submitted for publication in the journal, *IEEE Transactions on Electromagnetic Compatibility*. Pages 125-152 are to be submitted for publication in the journal, *IEEE Transactions on Electromagnetic Compatibility*.

ABSTRACT

This dissertation explores two topics pertinent to electromagnetic compatibility research: maximum crosstalk estimation in weakly coupled transmission lines and modeling of electromagnetic radiation resulting from printed circuit board/high-density connector interfaces. Despite an ample supply of literature devoted to the study of crosstalk, little research has been performed to formulate maximum crosstalk estimates when signal lines are electrically long. Paper one illustrates a new maximum crosstalk estimate that is based on a mathematically rigorous, integral formulation, where the transmission lines can be lossy and in an inhomogeneous media. Paper two provides a thorough comparison and analysis of the newly derived maximum crosstalk estimates with an estimate derived by another author. In paper two the newly derived estimates in paper one are shown to be more robust because they can estimate the maximum crosstalk with fewer and less restrictive assumptions.

One current industry challenge is the lack of robust printed circuit board connector models and methods to quantify radiation from these connectors. To address this challenge, a method is presented in paper three to quantify electromagnetic radiation using network parameters and power conservation, assuming the only losses at a printed circuit board/connector interface are due to radiation. Some of the radiating structures are identified and the radiation physics explored for the studied connector in paper three. Paper four expands upon the radiation modeling concepts in paper three by extending radiation characterization when material losses and multiple signals may be present at the printed circuit board/connector interface. The resulting radiated power characterization method enables robust deterministic and statistical analyses of the radiated power from printed circuit board connectors. Paper five shows the development of a statistical radiated power estimate based on the radiation characterization method presented in paper four. Maximum radiated power estimates are shown using the Markov and Chebyshev inequalities to predict a radiated power limit. A few maximum radiated power limits are proposed that depend on the amount of known information about the radiation characteristics of a printed circuit board connector.

ACKNOWLEDGMENTS

I would like to thank my advisor, Dr. Daryl Beetner, for supporting me throughout my graduate studies in the EMC lab. I am grateful for my exposure to a wide array of projects as I know this will help me with my career development in the future. I would also like to thank the other members of my committee, Dr. Jun Fan, Dr. David Pommerenke, Dr. James Drewniak, and Dr. Lorena Basilio, for their additional insights as I have progressed on my research. A special thanks to Sandia National Laboratories for providing support for the computational resources needed for much of this research. Lastly, I would like to thank my parents for their support during my academic studies.

TABLE OF CONTENTS

Page

PUBLICATION DISSERTATION OPTION iii

ABSTRACT iv

ACKNOWLEDGMENTS v

LIST OF ILLUSTRATIONS ix

LIST OF TABLES xiii

SECTION

1. INTRODUCTION 1

PAPER

I. Maximum Crosstalk Estimation in Weakly Coupled Transmission Lines 3

Abstract 3

I. INTRODUCTION 3

II. MAXIMUM CROSSTALK FORMULATION 6

A. Transmission Line Circuit and Transmission Line Equations 6

B. General Solution to the Transmission Line Equations for a Distributed Voltage Source 10

C. General Solution to the Transmission Line Equations for a Distributed Current Source 13

D. Total Solution to the Transmission Line Equations for an Electrically Small Coupling Region 16

E. Total Solution to the Transmission Line Equations for an Electrically Large Coupling Region 19

F. Maximum Crosstalk Estimation 21

III. ANALYTIC VALIDATION 24

IV. SIMULATIONS AND MEASUREMENTS 27

V. CONCLUSION 35

REFERENCES 36

II. Maximum Crosstalk Estimation in Lossless and Homogeneous Transmission Lines 39

Abstract 39

I. INTRODUCTION 40

II. MAXIMUM CROSSTALK ESTIMATES FROM AN INTEGRAL FORMULATION......... 42

III. MAXIMUM CROSSTALK ESTIMATES FROM INFINITELY LONG TRANSMISSION LINES 46

A. Introduction 46

B. Mathematical Derivations 48

IV. MAXIMUM CROSSTALK ESTIMATE COMPARISON AND VALIDATION 52

V. CONCLUSION 62

REFERENCES 63

III. Electromagnetic Radiation Resulting From PCB/High-Density Connector Interfaces 65

Abstract 65

I. INTRODUCTION 65

II. TRANSMISSION LINE AND ANTENNA CURRENTS AT PCB/CONNECTOR INTERFACES 71

III. SCATTERING AT THE PCB/CONNECTOR INTERFACE IN DIFFERENTIAL-MODE SIGNALING 73

IV. PCB/CONNECTOR GEOMETRY 75

V. RADIATED POWER CALCULATIONS USING NETWORK PARAMETERS 78

VI. RADIATION FROM THE PCB/CONNECTOR ASSEMBLY 82

VII. RADIATION CALCULATIONS WITH A DIGITAL SIGNAL 89

VIII. CONCLUSION 92

REFERENCES 93

IV. Quantifying High-Density Connector Radiation in a Lossy Multi-Signal Environment 96

Abstract 96

I. INTRODUCTION 96

II. POWER LOSS CALCULATIONS FROM NETWORK PARAMETERS 98

A. Power Loss as a Function of Loss Constant Matrices 99

B. Properties of the Power Loss Calculation and Port Excitation Solutions for the Power Loss Constants 102

C. Power Loss Relationships for Total Power Loss, Radiated Power Loss, and Material Power Loss 108

D. A Multi-signal Power Loss Quantification Example 109

        - E. Radiated Power Characterization with Reverberation Chamber Measurements 112
    - III. PRACTICAL ISSUES ARISING FROM SOLVING FOR THE POWER LOSS CONSTANT MATRICES 113
        - A. Computational Considerations in Solving for the Material and Radiated Power Losses 113
        - B. Computational Reduction Methods with Known Input Signaling and Worst Case Analysis 114
    - IV. CONCLUSION 120
    - REFERENCES 121
- V. Statistical Estimates of Maximum Radiated Power from High-Density Connectors 125
    - Abstract 125
    - I. INTRODUCTION 125
    - II. POWER LOSS CALCULATIONS 126
    - III. DERIVATIONS ON A STATISTICAL RADIATED POWER ESTIMATE 128
    - IV. VALIDATION 133
        - A. Simulation with Impulse Excitations 135
        - B. Simulation with Pseudo-Random Bit Sequences 140
        - C. Measurement with Pseudo-Random Bit Sequences 146
    - V. CONCLUSION 149
    - REFERENCES 150

SECTION

    - 2. CONCLUSION 153

APPENDICES

    - A. FINITE DIFFERENCE SIMULATION FORMULATION 157
    - B. FINITE DIFFERENCE CODES 190

VITA 237

LIST OF ILLUSTRATIONS

Page

PAPER I

Fig. 1. Coupled three-conductor transmission line system used to formulate an estimate of maximum crosstalk. 7

Fig. 2. Victim circuit with distributed voltage and current sources due to coupling from the aggressor circuit under the weak coupling assumption. 9

Fig. 3. Circuit representing the Green’s function problem for a distributed voltage source in the victim circuit. 11

Fig. 4. Circuit representing the Green’s function problem for a distributed current source in the victim circuit. 14

Fig. 5. Coupled microstrip PCB used to validate the maximum crosstalk equations. 29

Fig. 6. Crosstalk example for the Case 1 configuration without SMA connector parasitics. 31

Fig. 7. Crosstalk example for the modified Case 1 configuration without SMA connector parasitics. 31

Fig. 8. Crosstalk example for the Case 1 configuration with SMA connector parasitics. 32

Fig. 9. Crosstalk example for the Case 1 configuration with SMA connector parasitics. 32

Fig. 10. Crosstalk example for the Case 1 configuration with SMA connector parasitics. 33

Fig. 11. Crosstalk example for the Case 4 configuration with SMA connector parasitics. 34

Fig. 12. Crosstalk example for the Case 4 configuration with SMA connector parasitics. 34

Fig. 13. Crosstalk example for the Case 4 configuration with SMA connector parasitics. 35

PAPER II

Fig. 1. Coupled three conductor transmission line system used to formulate an estimate of maximum crosstalk [10]. 42

Fig. 2. Equivalent circuit model of weak inductive coupling to the victim circuit at a single location [8]. 47

Fig. 3. Cable bundle crosstalk example for the Case 1 and Case 2 loading conditions in Table I. 55

Fig. 4. Cable bundle crosstalk example for the Case 3 and Case 4 loading conditions... 56

Fig. 5. Cable bundle crosstalk example for the Case 5 loading conditions in Table I..... 56

Fig. 6. Cable bundle crosstalk example for the Case 6 loading conditions. 57

Fig. 7. Cable bundle crosstalk example for the Case 6 loading conditions in Table I..... 57

Fig. 8. Coupled stripline measurement setup used to validate the maximum crosstalk equations. 58

Fig. 9. Coupled stripline crosstalk example for the Case 1 loading conditions in Table II.. 60

Fig. 10. Coupled stripline crosstalk example for the Case 2 loading conditions in Table II. 60

Fig. 11. Coupled stripline crosstalk example for the Case 3 loading conditions in Table II. 61

Fig. 12. Coupled stripline crosstalk example for the Case 4 loading conditions in Table II. 61

PAPER III

Fig. 1. Original sketch from [6] identifying the physics associated with illumination and EMI from cables as a result of nonzero impedance (inductance) in a signal return conductor. 68

Fig. 2. Geometry used in [10] for numerical and experimental demonstration of the decomposition of a signal path with extended reference structures into symmetric and asymmetric components and quantifying and comparing the EMI associated with each. 70

Fig. 3. (a) Odd-mode or differential-mode currents in a coupled, microstrip printed circuit board. (b) Even-mode or common-mode currents in a coupled, microstrip printed circuit board. 72

Fig. 4. (a) Left PCB/connector structure is the simulated “connector only” case. The right PCB/connector structure is the simulated “large PCB plane” case. These simulations were formulated without conductor and dielectric losses. The connector consisted of two differential signaling pairs. (b) Wafer cross-sectional layout for the connector of (a). The connector in (a) consisted of two wafer layers. (c) Front connector wafer signal blades layout for the connector in (a). 76

Fig. 5. Single-ended and mixed-mode port assignments for a single signal pair in a connector.. 80

Fig. 6. Radiated power when the outermost signal pair, Pair 1, was fed and all other ports were matched for the PCB/connector structures of Fig. 4(a)...................... 83

Fig. 7. Radiated power when the innermost signal pair, Pair 2, was fed and all other ports were matched for the PCB/connector structures of Fig. 4(a)...................... 84

Fig. 8. Surface current density plot at 0.49 GHz when Pair 1 was fed with a TL CM excitation and all other ports were matched. 85

Fig. 9. Surface current density plot at 1.14 GHz when Pair 1 was fed with a TL CM excitation and all other ports were matched. 85

Fig. 10. Connector TL common-mode radiated power response for varying return plane width when Pair 2 was fed. 87

Fig. 11. Connector CM antenna currents at 3.30, 3.89, and 7.17 GHz resonances when Pair 1 was fed with a TL common-mode excitation. 88

Fig. 12. Time-domain incident port voltages in the single-ended and modal domains applied to Port 1 and Port 3 of the right PCB/connector structure in Fig. 4(a). . 90

Fig. 13. (a) Connector frequency-domain modal radiated power. The solid trace represents the radiated power due to the DM incident voltages. The dashed trace represents the radiated power due to the CM incident voltages. The dashed-dotted trace represents the radiated power due to the CM and DM incident voltage product. (b) Connector radiated electric field comparison with FCC Class B Limit at three meters. 91

PAPER IV

Fig. 1. Full-wave connector model used to formulate methods to quantify PCB/connector interface radiation. 100

Fig. 2. A radiated power calculation example illustrating the non-linear property of the power loss calculations for the connector in Fig. 1. 104

Fig. 3. Comparison of the total power loss, material power loss, and the radiated power loss for the random excitation in (30). 111

Fig. 4. Comparison of the material power loss calculations for the random excitation in (30). 111

Fig. 5. Comparison of a measured and calculated radiated power loss for a continuous wave common-mode excitation with unequal cable lengths. 113

PAPER V

Fig. 1. Full-wave connector model used to validate statistical estimates for maximum radiated power. 134

Fig. 2. Comparison of the total power loss, material power loss, and the radiated power loss for the random excitation in (24). 135

Fig. 3. Comparison of the radiated power mean, standard deviation, and worst case standard deviation for an impulse excitation and a single-ended signaling port connectivity matrix. 137

Fig. 4. Comparison of the maximum radiated power limit curves for an impulse excitation and single-ended signaling port connectivity matrix. 137

Fig. 5. Comparison of the maximum radiated power limit curves for an impulse excitation and a differential-mode signaling port connectivity matrix. 139

Fig. 6. Comparison of the spliced Markov and worst case Chebyshev limit curves using a single-ended signaling port connectivity matrix and a differential-mode signaling port connectivity matrix for impulse excitations.... 139

Fig. 7. Total power loss and radiated power loss limit curve comparison for differential-mode and single-ended signaling port connectivity matrices for an impulse excitation. 140

Fig. 8. Comparison of the radiated power mean, standard deviation, and worst case standard deviation for a PRBS7 excitation and a single-ended signaling port connectivity matrix. 142

Fig. 9. Comparison of the maximum radiated power limit curves for a PRBS7 excitation and single-ended signaling port connectivity matrix. 142

Fig. 10. Comparison of the maximum radiated power limit curves for a PRBS7 excitation and a differential-mode signaling port connectivity matrix. 144

Fig. 11. Comparison of the spliced Markov and worst case Chebyshev limit curves using a single-ended signaling port connectivity matrix and a differential-mode signaling port connectivity matrix for PRBS7 excitations. . 145

Fig. 12. Total power loss and radiated power loss limit curve comparison for differential-mode and single-ended signaling port connectivity matrices for a PRBS7 excitation. 145

Fig. 13. PCB/connector pair used to measure radiated power. 147

Fig. 14. Calculated radiated power envelope and measured radiated power for a differential pair fed with a differential PRBS7 signal. 148

Fig. 15. Comparison of the singled-ended signaling radiated power limit curves with the deterministically calculated envelope for a differential PRBS7 signal. 148

LIST OF TABLES

Page

PAPER I

TABLE I. MEASUREMENT SETUP DIMENSIONS (MILS) 29
TABLE II. WEAK COUPLING RATIOS FOR TWO CASE 1 SIMULATIONS AT 3 GHZ 31

PAPER II

TABLE I. CABLE BUNDLE SIMULATION LOADING CONDITIONS 54
TABLE II. PCB MEASUREMENT LOADING CONDITIONS 58

1. INTRODUCTION

Crosstalk is an increasing problem in electronic designs due to circuit miniaturization and increasing design density. This problem is often studied using numerical simulations, however, the resulting information from these studies often do not provide the necessary insight into the exact causes or solution strategies to mitigate crosstalk. Analytical formulations can provide much needed insight to solve crosstalk problems and are often used for this purpose. Crosstalk is well-studied in the literature and has been analyzed from many different viewpoints. Most literature has focused on exact crosstalk formulations that capture every peak and valley in the crosstalk over frequency. While these exact formulations are necessary, design decisions are often better formulated from a maximum, worst case crosstalk envelope rather than an exact response because the transmission line parameters are never fully known. Little information in literature is available to formulate maximum crosstalk estimates when signal lines are electrically long.

Paper one and paper two in this dissertation are designed to supplement existing crosstalk literature with newly derived maximum crosstalk estimates. Paper one introduces maximum crosstalk estimates in the frequency domain where signal lines are weakly coupled and the characteristic impedances are assumed to be approximately the same inside and outside a designated coupling region. The maximum crosstalk estimates in paper one are shown to be a significant improvement from the estimates derived by another author since the new formulation is not limited to lossless and homogeneous media. Measurements and simulations are presented that illustrate the maximum crosstalk estimates can predict the maximum crosstalk envelope within a few decibels. A thorough analysis and comparison of the newly derived maximum crosstalk estimates with the previously derived estimates by another author are presented in paper two. The purpose of this analysis is to validate the mathematical basis for the previously derived estimate and to show limitations of the previous estimate that were not apparent in the original paper. The analysis in paper two provides additional validation to the previously published maximum crosstalk estimate and the estimates presented in paper one.

Design methods for creating intentional electromagnetic radiators, namely antennas, are widely available in literature. Despite the abundance of engineering knowledge to create intentional antenna structures, the knowledge of radiation physics in general is still lacking. In the area of unintentional radiators there is even less understanding of how these structures radiate, and there is a strong need to understand the radiation physics of these structures. Such knowledge could be used to make unintentional antennas less effective as radiators and prevent electromagnetic interference problems. Unintentional radiators of commercial interest include board-to-board and cable-to-enclosure interfaces. The focus of the research in this dissertation is on board-to-board interfaces with high-density printed circuit board connectors.

To better understand the radiation physics in high-density printed circuit board connectors, a method is presented in paper three and paper four to quantify the radiation in these structures. In paper three, the radiation physics for a simplified connector model is analyzed and characterized using network parameters. The material losses are neglected and the basic radiating antenna structures are identified in paper three. Paper four expands upon the radiation modeling concepts in paper three by extending radiation characterization when material losses and multiple signals may be present at the printed circuit board/connector interface. The presented radiated power loss characterization methodology in paper four allows deterministic and stochastic analysis on the electromagnetic interference properties of connectors that were not previously available in the literature. Measurements and simulations are shown in paper four that validate the radiated power loss characterization method and illustrate the analysis can apply to both measurements and simulations. Paper five expands upon the theory presented in paper four with the development of statistical radiated power estimates. Challenges related to predicting a maximum radiated power are addressed in paper five with incomplete radiation characteristics knowledge of a printed circuit board connector with the statistical estimates. Maximum radiated power estimates are proposed that depend on the amount of known information about the radiation characteristics of a printed circuit board connector. Simulations and measurements are also shown with impulse and pseudo-random bit sequences to validate the statistical, maximum radiated power estimates.

PAPER

I. Maximum Crosstalk Estimation in Weakly Coupled Transmission Lines

Matthew S. Halligan and Daryl G. Beetner, *Senior Member*, IEEE

Abstract—Eliminating crosstalk problems in a complex system requires methods that quickly predict where problems may occur and that give intuitive feedback on how best to solve these problems. Solutions for the maximum crosstalk are often used for this purpose. Limit lines for maximum crosstalk in the frequency domain are available in the literature when signal lines are electrically small and weak coupling is assumed; however, little research has been performed for the case where signal lines are electrically large. This paper provides derivations for maximum crosstalk in the frequency domain when signal lines are electrically large and weak coupling applies. The coupling mechanisms are represented by distributed voltage and current sources. These sources result from aggressor circuit voltages and currents as well as mutual terms in the transmission line per-unit-length parameters. The maximum crosstalk expressions for the victim loads are represented by piecewise expressions dependent on the total electrical length of the aggressor circuit and the electrical length of the coupling region. Measurements and simulations are presented which show the maximum crosstalk estimates can predict the maximum envelope of crosstalk within a few decibels.

Index Terms—Analytical models, coupling circuits, crosstalk, electromagnetic coupling, estimation, prediction algorithms, transmission lines.

I. INTRODUCTION

One of the biggest challenges facing electronics designers in high-density, high-data-rate systems is crosstalk. Fundamentally, crosstalk is undesirable because it can degrade system performance by worsening signal integrity and creating logic errors. Although one of the simplest methods to reduce crosstalk is to increase the spacing between signal lines, this solution may not always be possible due to system size requirements. In such cases, design engineers must resort to other methods such as modifying termination impedances and coupling lengths to reduce the impacts of crosstalk. Numerical electromagnetic tools are often used to better understand crosstalk issues. Although these tools can be used to quantify crosstalk for a given system, the results do not provide much insight into the major contributing factors for crosstalk. Analytical expressions can provide this much needed insight and are used for this purpose.

Crosstalk has been extensively studied in literature in both the time and frequency domains [1]-[26]. Early work developed models for inductive and capacitive coupling in electrically small systems and their impacts on near-end and far-end crosstalk waveforms [1], [2]. Paul [3] expanded on these initial concepts by solving for the near-end and far-end crosstalk analytically using matrix equations in the frequency domain. In subsequent work, Paul [4]-[6] and Olsen [7] were able to derive the crosstalk response for circuits at low frequencies as a summation of inductive, capacitive, and common impedance coupling mechanisms. Initially much of the crosstalk analysis was limited to two transmission line systems; however, Paul [8], [9] was also able to expand crosstalk analysis to systems containing more than two transmission lines. Some recent work expands upon initial formulations presented in [1]-[9] with crosstalk analysis in the time domain [10]-[14], in non-uniform transmission lines [15], [16], and in systems with signal lines that are not parallel [17], [18]. Statistical characterization of crosstalk in multiconductor transmission lines has also been explored [19]-[21]. While [10]-[21] represent some recent advances in crosstalk analysis in additional domains and in more generalized transmission line structures, these exact formulations do not provide insight into worst case crosstalk performance over frequency.

Although exact formulations for crosstalk are beneficial, the most useful tool for many designers is the maximum, worst case crosstalk over frequency [22]-[24]. Designers are often interested in a worst case performance limit because passing this limit obviates the need for further design analysis and modifications. This type of analysis is also preferred over exact crosstalk calculations in many cases because the system parameters are not perfectly known. Small shifts in resonant frequencies in this case can significantly change a crosstalk estimate. If the maximum crosstalk is found using a closed-form estimate, this technique may also give a better understanding of what causes crosstalk problems and how these problems might be solved.

A maximum crosstalk curve can be defined in two separate frequency regions dependent upon the electrical length of the signal lines. When the signal lines are electrically small, the maximum crosstalk can be found using the exact, analytical equations given in [4]-[6]. The exact equations also represent the maximum possible crosstalk because there are no resonances in the crosstalk response for most practical terminations. When the signal lines are electrically large, resonances in the crosstalk response occur due to the electrical length of the signal lines and, in many cases, due to load impedance resonances.

Presently, there is little information in the literature about predicting the maximum crosstalk when signal lines are electrically large. This is not to say that there are no exact formulations when transmission lines are electrically large as there is an ample supply of literature devoted to this subject [3], [6], [8], [9]; rather, little information is available in literature to estimate the maximum crosstalk. An effort was made in [24] to predict maximum crosstalk at “high frequencies”, where the signal lines were electrically large and weak coupling was assumed. Although the results in [24] were shown to predict the crosstalk well, the maximum crosstalk formulations lacked the inclusion of transmission line loss and mathematical rigor. One critical assumption in [24] was that the coupling mechanisms could be represented by a single, lumped source based on infinite transmission line voltages or currents. Although this assumption simplifies the crosstalk analysis, the resulting maximum crosstalk expression mixes boundary conditions between infinite and finite transmission lines which is not strictly mathematically correct. In addition, [24] defined crosstalk as a ratio of maximum voltages or currents in the victim and aggressor circuits. This definition of crosstalk can suffer from over-prediction and under-prediction problems at the near-end and far-end victim loads. The purpose of this paper is to develop a mathematically rigorous, worst-case, high-frequency crosstalk estimate that includes transmission line losses. Results are validated by demonstrating the newly derived crosstalk formulation reduces analytically to a well-known crosstalk formulation and by demonstrating performance through multiple simulations and measurements.

II. MAXIMUM CROSSTALK FORMULATION

The maximum crosstalk formulation is derived in the following sections. First, the transmission line circuit and the transmission line equations are presented. Next, the solutions to the transmission line wave equations are presented for a distributed voltage and a distributed current source. The total victim transmission line voltage solution is then shown as a superposition of the responses due to the distributed sources when the coupling region is electrically small and electrically large. Lastly, modifications to the exact, total victim transmission line voltage solutions are given that estimate the maximum crosstalk at the victim near-end and far-end loads.

A. Transmission Line Circuit and Transmission Line Equations

The three-conductor transmission line system in Fig. 1 was used as a reference to develop maximum crosstalk expressions at frequencies where the signal lines were electrically long. This system consists of an aggressor circuit and a victim circuit. The primary quantity of interest is the voltage at the near-end and far-end loads of the victim circuit. Coupling is assumed to occur within a region where the cross-sectional geometry and electrical characteristics are uniform along its length. Outside of the coupling region, the aggressor and victim circuits are assumed to have the same cross section (i.e., the signal and returns have the same size and orientation) as in the coupling region, but the circuits are now uncoupled. This transmission line system is loosely based on a typical modular system where connections among different modules are established using cable bundles, and coupling occurs when the aggressor and victim share the same harness. This crosstalk formulation allows for different aggressor and victim circuit lengths, independent of the coupling region size, which many other crosstalk formulations do not permit. Weak coupling is assumed, and the characteristic impedance is assumed to be approximately the same over the entire lengths of the aggressor and victim circuits. The weak coupling conditions are typically well satisfied in cable bundles where the conductor separation is at least three to five times the conductor height from a reference structure.

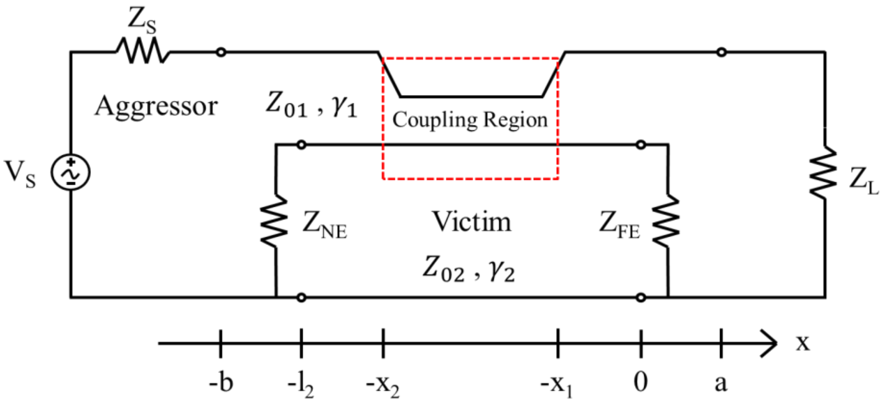

Fig. 1. Coupled three-conductor transmission line system used to formulate an estimate of maximum crosstalk.

The transmission line equations for the system in Fig. 1 are given by [9]

$$\frac{\partial}{\partial x}V_1(x) = -R_{11}I_1(x) - R_{12}I_2(x) - j\omega[L_{11}I_1(x) + L_{12}I_2(x)] \tag{1a}$$

$$\frac{\partial}{\partial x}V_2(x) = -R_{21}I_1(x) - R_{22}I_2(x) - j\omega[L_{21}I_1(x) + L_{22}I_2(x)] \tag{1b}$$

$$\frac{\partial}{\partial x}I_1(x) = -G_{11}V_1(x) - G_{12}V_2(x) - j\omega[C_{11}V_1(x) + C_{12}V_2(x)] \tag{1c}$$

$$\frac{\partial}{\partial x}I_2(x) = -G_{21}V_1(x) - G_{22}V_2(x) - j\omega[C_{21}V_1(x) + C_{22}V_2(x)] \tag{1d}$$

where the aggressor circuit is denoted as signal line one, and the victim circuit is denoted as signal line two, *V* and *I* are the voltage and current along each transmission line as a function of length, *x*, and *R*, *L*, *G*, and *C* are per-unit-length parameters for resistance, inductance, conductance, and capacitance. The per-unit-length parameters contained in (1) are defined as [9],

$$\mathbf{R} = \begin{bmatrix} r_1 + r_{11} & r_{12} \\ r_{21} & r_2 + r_{22} \end{bmatrix} = \begin{bmatrix} R_{11} & R_{12} \\ R_{21} & R_{22} \end{bmatrix}$$

$$\mathbf{L} = \begin{bmatrix} l_{11} & l_{12} \\ l_{21} & l_{22} \end{bmatrix} = \begin{bmatrix} L_{11} & L_{12} \\ L_{21} & L_{22} \end{bmatrix}$$

$$\mathbf{G} = \begin{bmatrix} g_{11}+g_{12} & -g_{12} \\ -g_{21} & g_{21}+g_{22} \end{bmatrix} = \begin{bmatrix} G_{11} & G_{12} \\ G_{21} & G_{22} \end{bmatrix}$$

$$\mathbf{C} = \begin{bmatrix} c_{11}+c_{12} & -c_{12} \\ -c_{21} & c_{21}+c_{22} \end{bmatrix} = \begin{bmatrix} C_{11} & C_{12} \\ C_{21} & C_{22} \end{bmatrix}. \tag{2}$$

The per-unit-length parameter matrices are symmetric for the system in Fig. 1 due to reciprocity. Under the weak coupling assumption, the transmission line equations become [6], [9],

$$\frac{\partial}{\partial x}V_1(x) = -R_{11}I_1(x) - j\omega L_{11}I_1(x) \tag{3a}$$

$$\frac{\partial}{\partial x}V_2(x) = -R_{21}I_1(x) - R_{22}I_2(x) - j\omega\left[L_{21}I_1(x) + L_{22}I_2(x)\right] \tag{3b}$$

$$\frac{\partial}{\partial x}I_1(x) = -G_{11}V_1(x) - j\omega C_{11}V_1(x) \tag{3c}$$

$$\frac{\partial}{\partial x}I_2(x) = -G_{21}V_1(x) - G_{22}V_2(x) - j\omega\left[C_{21}V_1(x) + C_{22}V_2(x)\right]. \tag{3d}$$

Two critical insights can be found from the weak coupling transmission line equations. The first insight is that the voltage and current of the culprit circuit can be solved using traditional methods for a single transmission line problem. This result implies that the voltage and current in the culprit circuit is not impacted by the voltage and current in the victim circuit, as expected for the weak coupling case. The second insight is that the coupling terms in the victim circuit can be represented by a distributed voltage and a distributed current source. The differential equations describing wave propagation in the victim circuit can be rewritten using distributed voltage and distributed current sources as

$$\frac{\partial}{\partial x}V_2(x) = -\left[R_{22} + j\omega L_{22}\right]I_2(x) + v(x) \tag{4a}$$

$$\frac{\partial}{\partial x}I_2(x) = -\left[G_{22} + j\omega C_{22}\right]V_2(x) + i(x) \tag{4b}$$

where the distributed voltage and distributed current sources are given by,

$$v(x) = \begin{cases} -[R_{21} + j\omega L_{21}]I_1(x) & -x_2 \le x \le -x_1 \\ 0 & else \end{cases} \tag{5a}$$

$$i(x) = \begin{cases} -[G_{21} + j\omega C_{21}]V_1(x) & -x_2 \le x \le -x_1 \\ 0 & else \end{cases} . \tag{5b}$$

Analytically, the transmission line system in Fig. 1 can then be reduced to a single transmission line system with distributed sources as in Fig. 2.

An integral formulation was used to solve for the voltage and current in the victim circuit in Fig. 2. Since the circuit was linear, superposition was used to find the total circuit response. The total response includes the response due to a distributed voltage source (related to inductive and common impedance coupling) and the response due to a distributed current source (related to capacitive and common impedance coupling). The responses from these sources were found separately. To minimize complexity, the propagation constant, γ, was assumed to be the same for both the aggressor and victim circuits.

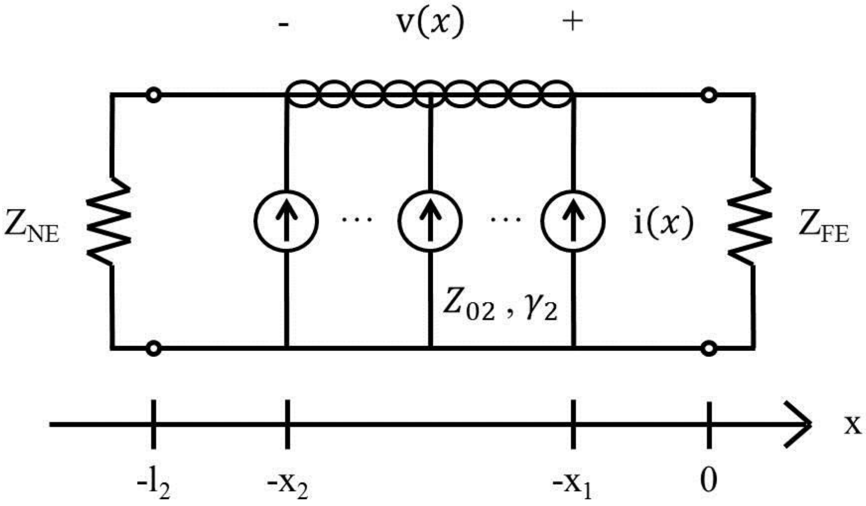

Fig. 2. Victim circuit with distributed voltage and current sources due to coupling from the aggressor circuit under the weak coupling assumption.

B. General Solution to the Transmission Line Equations for a Distributed Voltage Source

The differential equations representing the response due to the distributed voltage source can be found from (4), where the distributed current source is set equal to zero. A wave equation for the current on the victim transmission line and the near-end and far-end boundary conditions can then be written as,

$$\frac{\partial^2}{\partial x^2} I_{2,v}(x) - \gamma^2 I_{2,v}(x) = -yv(x) \tag{6a}$$

$$\frac{1}{y}\frac{\partial}{\partial x} I_{2,v}(-l_2) - I_{2,v}(-l_2) Z_{NE} = 0 \tag{6b}$$

$$\frac{1}{y}\frac{\partial}{\partial x} I_{2,v}(0) + I_{2,v}(0) Z_{FE} = 0 \tag{6c}$$

where

$$z = R_{22} + j\omega L_{22} \tag{7a}$$

$$y = G_{22} + j\omega C_{22} \tag{7b}$$

$$\gamma^2 = yz \tag{7c}$$

$$Z_{02} = \frac{\gamma}{y} = \sqrt{\frac{z}{y}}\,. \tag{7d}$$

The subscript v in the current terms in (6) denotes the functional response due to the distributed voltage source. An equivalent Green’s function problem can be formulated using the wave equation and boundary equations as written in (6). The Green’s function problem is graphically represented by the circuit in Fig. 3.

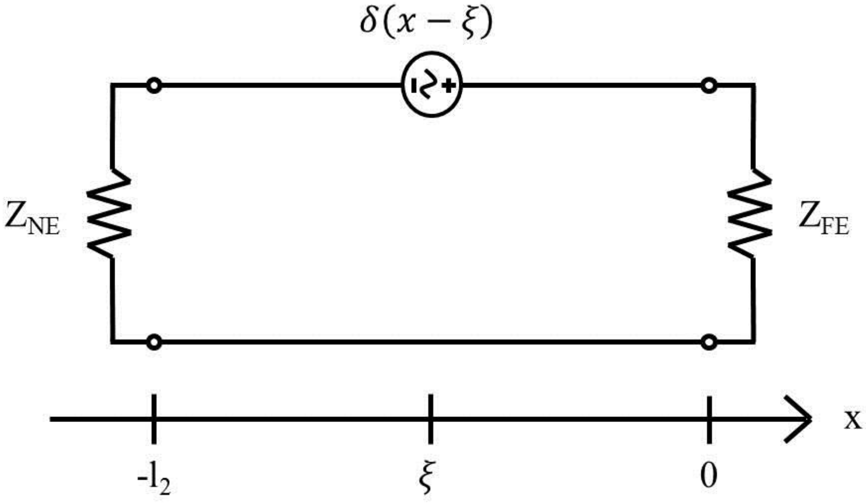

Fig. 3. Circuit representing the Green's function problem for a distributed voltage source in the victim circuit.

The wave equation for the Green's function problem and the near-end and far-end boundary conditions can then be written as,

$$\frac{\partial^2}{\partial x^2} g_{i,v}(x) - \gamma^2 g_{i,v}(x) = 0 \text{ for } (x \neq \xi) \tag{8a}$$

$$\frac{1}{y}\frac{\partial}{\partial x} g_{i,v}(-l_2) - g_{i,v}(-l_2) Z_{NE} = 0 \tag{8b}$$

$$\frac{1}{y}\frac{\partial}{\partial x} g_{i,v}(0) + g_{i,v}(0) Z_{FE} = 0. \tag{8c}$$

The general solution for the Green's function is given as,

$$g(x,\xi) = \begin{cases} g_<(x,\xi) \\ g_>(x,\xi) \end{cases} = \begin{cases} Ae^{-\gamma x} + Be^{\gamma x} & x < \xi \\ Ce^{-\gamma x} + De^{\gamma x} & x > \xi \end{cases} \tag{9}$$

where the unknown constants A, B, C, and D must be found through four independent equations. Two of these equations are given in the near-end and far-end boundary conditions of (8b) and (8c). Another two equations can be found by using the continuity condition and the jump condition at the voltage source as given in (10).

$$g\left(\xi^{-}\right) = g\left(\xi^{+}\right) \tag{10a}$$

$$\left.\frac{dg}{dx}\right|_{\xi^{+}} - \left.\frac{dg}{dx}\right|_{\xi^{-}} = -1 \tag{10b}$$

The Green's function for the victim circuit current response due to a distributed voltage source was found to be [25],

$$g_{i,v}(x,\xi) = \frac{1}{2\gamma}\frac{1}{1-\Gamma_{NE}\Gamma_{FE}e^{-2\gamma l_2}} \times \begin{cases} \left(\Gamma_{FE}e^{\gamma\xi} - e^{-\gamma\xi}\right)\left(\Gamma_{NE}e^{-\gamma(x+2l_2)} - e^{\gamma x}\right) & x < \xi \\ \left(\Gamma_{FE}e^{\gamma x} - e^{-\gamma x}\right)\left(\Gamma_{NE}e^{-\gamma(\xi+2l_2)} - e^{\gamma\xi}\right) & x > \xi \end{cases} \tag{11}$$

where

$$\Gamma_{NE} = \frac{Z_{NE} - Z_{02}}{Z_{NE} + Z_{02}} \tag{12a}$$

$$\Gamma_{FE} = \frac{Z_{FE} - Z_{02}}{Z_{FE} + Z_{02}}\,. \tag{12b}$$

The Green's function in (11) is symmetric as expected because the Green's function problem is self-adjoint. The general solution to the differential equation (6a) can be found from,

$$I_{2,v}(x) = \int yv(\xi)g_{i,v}(x,\xi)d\xi\,. \tag{13}$$

The particular solution for the current can be written in a piecewise manner as,

$$I_{2,v}(x) = \begin{cases} y\displaystyle\int_{-x_2}^{-x_1} g_{<i,v}(x,\xi)v(\xi)d\xi & x \le -x_2 \\ y\displaystyle\int_{-x_2}^{x} g_{>i,v}(x,\xi)v(\xi)d\xi + y\int_{x}^{-x_1} g_{<i,v}(x,\xi)v(\xi)d\xi & -x_2 < x < -x_1 \\ y\displaystyle\int_{-x_2}^{-x_1} g_{>i,v}(x,\xi)v(\xi)d\xi & x \ge -x_1 \end{cases}$$

$$I_{2,v}(x)=\frac{1}{2Z_{02}}\frac{1}{1-\Gamma_{NE}\Gamma_{FE}e^{-2\gamma l_2}}$$
$$\times\begin{cases}\displaystyle\int_{-x_2}^{-x_1}\left(\Gamma_{FE}e^{\gamma\xi}-e^{-\gamma\xi}\right)\left(\Gamma_{NE}e^{-\gamma(x+2l_2)}-e^{\gamma x}\right)v(\xi)d\xi & x\le -x_2\\ \displaystyle\int_{-x_2}^{x}\left(\Gamma_{FE}e^{\gamma x}-e^{-\gamma x}\right)\left(\Gamma_{NE}e^{-\gamma(\xi+2l_2)}-e^{\gamma\xi}\right)v(\xi)d\xi & \\ \displaystyle+\int_{x}^{-x_1}\left(\Gamma_{FE}e^{\gamma\xi}-e^{-\gamma\xi}\right)\left(\Gamma_{NE}e^{-\gamma(x+2l_2)}-e^{\gamma x}\right)v(\xi)d\xi & \text{-}\mathrm{x}_2<x<-x_1\\ \displaystyle\int_{-x_2}^{-x_1}\left(\Gamma_{FE}e^{\gamma x}-e^{-\gamma x}\right)\left(\Gamma_{NE}e^{-\gamma(\xi+2l_2)}-e^{\gamma\xi}\right)v(\xi)d\xi. & x\ge -x_1\end{cases}\tag{14}$$

Re-arranging (4b), the voltage on the transmission line can be found from (13)-(14) as,

$$V_{2,v}(x)=-\frac{1}{y}\frac{\partial}{\partial x}I_{2,v}(x)$$

$$V_{2,v}(x)=\frac{1}{2}\frac{1}{1-\Gamma_{NE}\Gamma_{FE}e^{-2\gamma l_2}}$$
$$\times\begin{cases}\displaystyle\int_{-x_2}^{-x_1}\left(\Gamma_{FE}e^{\gamma\xi}-e^{-\gamma\xi}\right)\left(\Gamma_{NE}e^{-\gamma(x+2l_2)}+e^{\gamma x}\right)v(\xi)d\xi & x\le -x_2\\ \displaystyle\int_{-x_2}^{x}-\left(\Gamma_{FE}e^{\gamma x}+e^{-\gamma x}\right)\left(\Gamma_{NE}e^{-\gamma(\xi+2l_2)}-e^{\gamma\xi}\right)v(\xi)d\xi & \\ \displaystyle+\int_{x}^{-x_1}\left(\Gamma_{FE}e^{\gamma\xi}-e^{-\gamma\xi}\right)\left(\Gamma_{NE}e^{-\gamma(x+2l_2)}+e^{\gamma x}\right)v(\xi)d\xi & \text{-}\mathrm{x}_2<x<-x_1\\ \displaystyle\int_{-x_2}^{-x_1}-\left(\Gamma_{FE}e^{\gamma x}+e^{-\gamma x}\right)\left(\Gamma_{NE}e^{-\gamma(\xi+2l_2)}-e^{\gamma\xi}\right)v(\xi)d\xi. & x\ge -x_1\end{cases}\tag{15}$$

C. General Solution to the Transmission Line Equations for a Distributed Current Source

The differential equations representing the response due to the distributed current source can be found from (4), where the distributed voltage source is set equal to zero. Using (7) in (4), the wave equation for the voltage on the victim transmission line and the near-end and far-end boundary conditions can then be written as,

$$\frac{\partial^2}{\partial x^2}V_{2,i}(x)-\gamma^2V_{2,i}(x)=-zi(x)\tag{16a}$$

$$\frac{1}{z}\frac{\partial}{\partial x}V_{2,i}(-l_2)Z_{NE} - V_{2,i}(-l_2) = 0 \tag{16b}$$

$$\frac{1}{z}\frac{\partial}{\partial x}V_{2,i}(0)Z_{FE} + V_{2,i}(0) = 0 \tag{16c}$$

where, the subscript i in the voltage terms denotes the functional response due to the distributed current source. An equivalent Green's function problem can be formulated using the wave equation and boundary equations as written in (16). The Green's function problem is graphically represented by the circuit in Fig. 4.

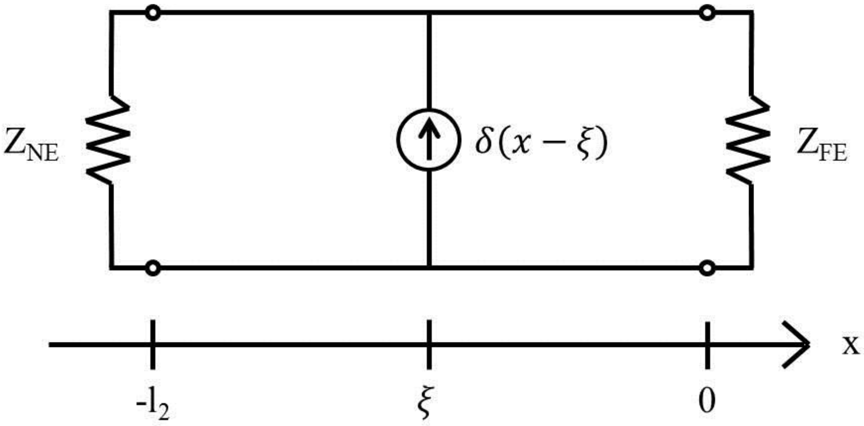

Fig. 4. Circuit representing the Green's function problem for a distributed current source in the victim circuit.

The wave equation for the Green's function problem is the same as (8a) and the near-end and far-end boundary conditions can then be written as,

$$\frac{1}{z}\frac{\partial}{\partial x}g_{v,i}(-l_2)Z_{NE} - g_{v,i}(-l_2) = 0 \tag{17a}$$

$$\frac{1}{z}\frac{\partial}{\partial x}g_{v,i}(0)Z_{FE} + g_{v,i}(0) = 0 \cdot \tag{17b}$$

The general solution for the Green's function is given in (9). The unknown constants may be found with the near-end and far-end boundary conditions as given in (17) and the continuity condition and jump condition at the current sources as given in (10). The

Green’s function for the victim circuit voltage response due to a distributed current source was found to be [25],

$$g_{v,i}(x,\xi)=\frac{1}{2\gamma}\frac{1}{1-\Gamma_{NE}\Gamma_{FE}e^{-2\gamma l_2}}\times\begin{cases}\left(\Gamma_{FE}e^{\gamma\xi}+e^{-\gamma\xi}\right)\left(\Gamma_{NE}e^{-\gamma(x+2l_2)}+e^{\gamma x}\right) & x<\xi\\ \left(\Gamma_{FE}e^{\gamma x}+e^{-\gamma x}\right)\left(\Gamma_{NE}e^{-\gamma(\xi+2l_2)}+e^{\gamma\xi}\right) & x>\xi.\end{cases} \tag{18}$$

The Green’s function in (18) is symmetric as expected because the Green’s function problem is self-adjoint. The general solution to the differential equation (16a) can then be found from,

$$V_{2,i}(x)=\int zi(\xi)g_{v,i}(x,\xi)d\xi\ . \tag{19}$$

The particular solution for the voltage can be written in a piecewise manner as,

$$V_{2,i}(x)=\begin{cases} z\displaystyle\int_{-x_2}^{-x_1} g_{<v,i}(x,\xi)i(\xi)d\xi & x\le -x_2\\ z\displaystyle\int_{-x_2}^{x} g_{>v,i}(x,\xi)i(\xi)d\xi + z\displaystyle\int_{x}^{-x_1} g_{<v,i}(x,\xi)i(\xi)d\xi & -x_2<x<-x_1\\ z\displaystyle\int_{-x_2}^{-x_1} g_{>v,i}(x,\xi)i(\xi)d\xi & x\ge -x_1\end{cases}$$

$$V_{2,i}(x)=\frac{Z_{02}}{2}\frac{1}{1-\Gamma_{NE}\Gamma_{FE}e^{-2\gamma l_2}}$$

$$\times\begin{cases}\displaystyle\int_{-x_2}^{-x_1}\left(\Gamma_{FE}e^{\gamma\xi}+e^{-\gamma\xi}\right)\left(\Gamma_{NE}e^{-\gamma(x+2l_2)}+e^{\gamma x}\right)i(\xi)d\xi & x\le -x_2\\ \displaystyle\int_{-x_2}^{x}\left(\Gamma_{FE}e^{\gamma x}+e^{-\gamma x}\right)\left(\Gamma_{NE}e^{-\gamma(\xi+2l_2)}+e^{\gamma\xi}\right)i(\xi)d\xi & \\ +\displaystyle\int_{x}^{-x_1}\left(\Gamma_{FE}e^{\gamma\xi}+e^{-\gamma\xi}\right)\left(\Gamma_{NE}e^{-\gamma(x+2l_2)}+e^{\gamma x}\right)i(\xi)d\xi & -x_2<x<-x_1\\ \displaystyle\int_{-x_2}^{-x_1}\left(\Gamma_{FE}e^{\gamma x}+e^{-\gamma x}\right)\left(\Gamma_{NE}e^{-\gamma(\xi+2l_2)}+e^{\gamma\xi}\right)i(\xi)d\xi & x\ge -x_1\end{cases} \tag{20}$$

Re-arranging (4a), the current on the transmission line can be found with,

$$I_{2,i}(x) = -\frac{1}{z}\frac{\partial}{\partial x}V_{2,i}(x)$$

$$I_{2,i}(x) = \frac{1}{2}\frac{1}{1-\Gamma_{NE}\Gamma_{FE}e^{-2\gamma l_2}} \times \begin{cases} \int_{-x_2}^{-x_1}\left(\Gamma_{FE}e^{\gamma\xi}+e^{-\gamma\xi}\right)\left(\Gamma_{NE}e^{-\gamma(x+2l_2)}-e^{\gamma x}\right)i(\xi)d\xi & x \le -x_2 \\ \int_{-x_2}^{x}\left(-\Gamma_{FE}e^{\gamma x}+e^{-\gamma x}\right)\left(\Gamma_{NE}e^{-\gamma(\xi+2l_2)}+e^{\gamma\xi}\right)i(\xi)d\xi & \\ +\int_{x}^{-x_1}\left(\Gamma_{FE}e^{\gamma\xi}+e^{-\gamma\xi}\right)\left(\Gamma_{NE}e^{-\gamma(x+2l_2)}-e^{\gamma x}\right)i(\xi)d\xi & -x_2 < x < -x_1 \\ \int_{-x_2}^{-x_1}\left(-\Gamma_{FE}e^{\gamma x}+e^{-\gamma x}\right)\left(\Gamma_{NE}e^{-\gamma(\xi+2l_2)}+e^{\gamma\xi}\right)i(\xi)d\xi & x \ge -x_1 \end{cases} \tag{21}$$

D. Total Solution to the Transmission Line Equations for an Electrically Small Coupling Region

By the superposition principle, the total solution for the victim voltage response is given by the sum of the responses from the distributed voltage and distributed current sources,

$$V_2(x) = V_{2,v}(x) + V_{2,i}(x). \tag{22}$$

The voltage response in the victim circuit is directly related to the voltages and currents in the aggressor circuit in addition to the mutual coupling parameters seen in (4) and (5). The aggressor circuit voltages and currents when the aggressor is electrically long are given by,

$$V_1(x) = V_S\frac{Z_{01}}{Z_{01}+Z_S}\frac{e^{-\gamma l_1}}{1-\Gamma_L\Gamma_S e^{-2\gamma l_1}}\left(e^{-\gamma(x-a)}+\Gamma_L e^{\gamma(x-a)}\right) \tag{23a}$$

$$I_1(x) = V_S\frac{1}{Z_{01}+Z_S}\frac{e^{-\gamma l_1}}{1-\Gamma_L\Gamma_S e^{-2\gamma l_1}}\left(e^{-\gamma(x-a)}-\Gamma_L e^{\gamma(x-a)}\right) \tag{23b}$$

where,

$$l_1 = a + b \tag{24a}$$

$$\Gamma_L = \frac{Z_L - Z_{01}}{Z_L + Z_{01}} \tag{24b}$$

$$\Gamma_S = \frac{Z_S - Z_{01}}{Z_S + Z_{01}}\,. \tag{24c}$$

When the coupling region is electrically small, the distributed voltage and current sources given in (5) can be approximately lumped into single lumped sources. In this case, (5) can be rewritten as,

$$v(x) = -[R_{12} + j\omega L_{12}]I_1(x)[x_2 - x_1]\delta(x + x_0) \tag{25a}$$

$$i(x) = -[G_{12} + j\omega C_{12}]V_1(x)[x_2 - x_1]\delta(x + x_0) \tag{25b}$$

where,

$$x_0 = \frac{x_1 + x_2}{2}\,. \tag{26}$$

The victim voltage due to the voltage source in (25a) can be found from (11), (13), and (15) as,

$$\begin{aligned} V_{2,v}(x) = {} & -(R_{12} + j\omega L_{12})(x_2 - x_1)V_S \frac{1}{Z_{01} + Z_S} \frac{e^{-\gamma l_1}}{1 - \Gamma_L \Gamma_S e^{-2\gamma l_1}} \frac{1}{2} \frac{\left(e^{\gamma(x_0 + a)} - \Gamma_L e^{-\gamma(x_0 + a)}\right)}{1 - \Gamma_{NE}\Gamma_{FE} e^{-2\gamma l_2}} \\ & \times \begin{cases} -\left(1 - \Gamma_{FE} e^{-2\gamma x_0}\right)\left(1 + \Gamma_{\mathrm{NE}} e^{-2\gamma(x + l_2)}\right) e^{\gamma(x + x_0)} & x < -x_0 \\ \left(1 + \Gamma_{FE} e^{2\gamma x}\right)\left(1 - \Gamma_{\mathrm{NE}} e^{-2\gamma(l_2 - x_0)}\right) e^{-\gamma(x + x_0)} & x > -x_0 \end{cases} \end{aligned} \tag{27}$$

The victim voltage due to the current source in (25b) can be found from (18)-(19) as,

$$V_{2,i}(x) = -(G_{12} + j\omega C_{12})(x_2 - x_1)V_S \frac{Z_{01}}{Z_{01} + Z_S} \frac{e^{-\gamma l_1}}{1 - \Gamma_L \Gamma_S e^{-2\gamma l_1}} \frac{Z_{02}}{2} \frac{\left(e^{\gamma(x_0+a)} + \Gamma_L e^{-\gamma(x_0+a)}\right)}{1 - \Gamma_{NE}\Gamma_{FE} e^{-2\gamma l_2}} \\ \times \begin{cases} \left(1 + \Gamma_{FE} e^{-2\gamma x_0}\right)\left(1 + \Gamma_{\mathrm{NE}} e^{-2\gamma(x+l_2)}\right) \mathrm{e}^{\gamma(\mathrm{x}+\mathrm{x}_0)} & x < -x_0 \\ \left(1 + \Gamma_{FE} e^{2\gamma x}\right)\left(1 + \Gamma_{\mathrm{NE}} e^{-2\gamma(l_2-x_0)}\right) \mathrm{e}^{-\gamma(\mathrm{x}+\mathrm{x}_0)} & x > -x_0 \end{cases} \tag{28}$$

The total victim voltage can then be written from (22) and (27)-(28) as,

$$V_2(x) = \frac{V_S}{2} \frac{1}{Z_{01} + Z_S} (x_2 - x_1) \frac{e^{-\gamma l_1}}{1 - \Gamma_L \Gamma_S e^{-2\gamma l_1}} \frac{e^{\gamma(x+x_0)}}{1 - \Gamma_{NE}\Gamma_{FE} e^{-2\gamma l_2}} \left(1 + \Gamma_{\mathrm{NE}} e^{-2\gamma(x+l_2)}\right) \\ \times \left\{(R_{12} + j\omega L_{12})\left(e^{\gamma(x_0+a)} - \Gamma_L e^{-\gamma(x_0+a)}\right)\left(1 - \Gamma_{FE} e^{-2\gamma x_0}\right) \right. \\ \left. - Z_{01} Z_{02} (G_{12} + j\omega C_{12})\left(e^{\gamma(x_0+a)} + \Gamma_L e^{-\gamma(x_0+a)}\right)\left(1 + \Gamma_{FE} e^{-2\gamma x_0}\right)\right\} \quad \mathrm{x} < \text{-}\mathrm{x}_0 \tag{29a}$$

$$V_2(x) = -\frac{V_S}{2} \frac{1}{Z_{01} + Z_S} (x_2 - x_1) \frac{e^{-\gamma l_1}}{1 - \Gamma_L \Gamma_S e^{-2\gamma l_1}} \frac{e^{-\gamma(x+x_0)}}{1 - \Gamma_{NE}\Gamma_{FE} e^{-2\gamma l_2}} \left(1 + \Gamma_{\mathrm{FE}} e^{2\gamma x}\right) \\ \times \left\{(R_{12} + j\omega L_{12})\left(e^{\gamma(x_0+a)} - \Gamma_L e^{-\gamma(x_0+a)}\right)\left(1 - \Gamma_{NE} e^{-2\gamma(l_2-x_0)}\right) \right. \\ \left. + Z_{01} Z_{02} (G_{12} + j\omega C_{12})\left(e^{\gamma(x_0+a)} + \Gamma_L e^{-\gamma(x_0+a)}\right)\left(1 + \Gamma_{NE} e^{-2\gamma(l_2-x_0)}\right)\right\} \quad \mathrm{x} > \text{-}\mathrm{x}_0 \tag{29b}$$

An alternative form to (27)-(29) may also be written when the coupling region is electrically small and the distributed voltage and current sources in (5) have a uniform distribution. The culprit and voltages and currents then only need to be evaluated at a point –x$_0$ in the coupling region. The victim voltage due to the distributed voltage source in (5a) can then be written as,

$$V_{2,v}(x) = -(R_{12} + j\omega L_{12})V_S \frac{1}{Z_{01} + Z_S} \frac{e^{-\gamma l_1}}{1 - \Gamma_L \Gamma_S e^{-2\gamma l_1}} \frac{1}{2\gamma} \frac{\left(e^{\gamma(x_0+a)} - \Gamma_L e^{-\gamma(x_0+a)}\right)}{1 - \Gamma_{NE}\Gamma_{FE} e^{-2\gamma l_2}} \\ \times \begin{cases} \left(1 + \Gamma_{\mathrm{NE}} e^{-2\gamma(x+l_2)}\right)\left[\left(1 + \Gamma_{FE} e^{-2\gamma x_1}\right) e^{\gamma x_1} - \left(1 + \Gamma_{FE} e^{-2\gamma x_2}\right) e^{\gamma x_2}\right] \mathrm{e}^{\gamma x} & x \le -x_2 \\ \left(1 + \Gamma_{\mathrm{NE}} e^{-2\gamma(x+l_2)}\right)\left(1 + \Gamma_{FE} e^{-2\gamma x_1}\right) e^{\gamma(x+x_1)} \\ - \left(1 + \Gamma_{FE} e^{2\gamma x}\right)\left(1 + \Gamma_{NE} e^{-2\gamma(l_2-x_2)}\right) e^{-\gamma(x+x_2)} & -x_2 < x < -x_1 \\ \left(1 + \Gamma_{FE} e^{2\gamma x}\right)\left[\left(1 + \Gamma_{NE} e^{-2\gamma(l_2-x_1)}\right) e^{-\gamma x_1} - \left(1 + \Gamma_{NE} e^{-2\gamma(l_2-x_2)}\right) e^{-\gamma x_2}\right] \mathrm{e}^{-\gamma x} & x \ge -x_1 \end{cases} \tag{30}$$

The victim voltage due to the distributed current source in (5b) can then be written as,

$$V_{2,i}(x) = -(G_{12} + j\omega C_{12})V_S \frac{Z_{01}}{Z_{01}+Z_S}\frac{e^{-\gamma l_1}}{1-\Gamma_L\Gamma_S e^{-2\gamma l_1}}\frac{Z_{02}}{2\gamma}\frac{\left(e^{\gamma(x_0+a)}+\Gamma_L e^{-\gamma(x_0+a)}\right)}{1-\Gamma_{NE}\Gamma_{FE}e^{-2\gamma l_2}}$$
$$\times\begin{cases}\left(1+\Gamma_{\mathrm{NE}}e^{-2\gamma(x+l_2)}\right)\left[-\left(1-\Gamma_{FE}e^{-2\gamma x_1}\right)e^{\gamma x_1}+\left(1-\Gamma_{FE}e^{-2\gamma x_2}\right)e^{\gamma x_2}\right]e^{\gamma x} & x \le -x_2 \\ -\left(1-\Gamma_{FE}e^{-2\gamma x_1}\right)\left(1+\Gamma_{\mathrm{NE}}e^{-2\gamma(x+l_2)}\right)e^{\gamma(x+x_1)}+2\left(1-\Gamma_{\mathrm{NE}}\Gamma_{FE}e^{-2\gamma l_2}\right) & \\ -\left(1-\Gamma_{NE}e^{-2\gamma(l_2-x_2)}\right)\left(1+\Gamma_{FE}e^{2\gamma x}\right)e^{-\gamma(x+x_2)} & -x_2 < x < -x_1 \\ \left(1+\Gamma_{FE}e^{2\gamma x}\right)\left[\left(1-\Gamma_{NE}e^{-2\gamma(l_2-x_1)}\right)e^{-\gamma x_1}-\left(1-\Gamma_{NE}e^{-2\gamma(l_2-x_2)}\right)e^{-\gamma x_2}\right]e^{-\gamma x} & x \ge -x_1\end{cases} \tag{31}$$

The total victim voltage outside the coupling region can then be written from (22) as,

$$\begin{aligned}V_2(x) = &-\frac{V_S}{2\gamma}\frac{1}{Z_{01}+Z_S}\frac{e^{-\gamma l_1}}{1-\Gamma_L\Gamma_S e^{-2\gamma l_1}}\frac{e^{\gamma x}}{1-\Gamma_{NE}\Gamma_{FE}e^{-2\gamma l_2}}\left(1+\Gamma_{\mathrm{NE}}e^{-2\gamma(x+l_2)}\right)\\ &\times\Big\{(R_{12}+j\omega L_{12})\left(e^{\gamma(x_0+a)}-\Gamma_L e^{-\gamma(x_0+a)}\right)\left[\left(1+\Gamma_{FE}e^{-2\gamma x_1}\right)e^{\gamma x_1}-\left(1+\Gamma_{FE}e^{-2\gamma x_2}\right)e^{\gamma x_2}\right]\\ &+Z_{01}Z_{02}(G_{12}+j\omega C_{12})\left(e^{\gamma(x_0+a)}+\Gamma_L e^{-\gamma(x_0+a)}\right)\\ &\times\left[-\left(1-\Gamma_{FE}e^{-2\gamma x_1}\right)e^{\gamma x_1}+\left(1-\Gamma_{FE}e^{-2\gamma x_2}\right)e^{\gamma x_2}\right]\Big\}\quad \mathrm{x} \le \text{-}\mathrm{x}_2\end{aligned} \tag{32a}$$

$$\begin{aligned}V_2(x) = &-\frac{V_S}{2\gamma}\frac{1}{Z_{01}+Z_S}\frac{e^{-\gamma l_1}}{1-\Gamma_L\Gamma_S e^{-2\gamma l_1}}\frac{e^{-\gamma x}}{1-\Gamma_{NE}\Gamma_{FE}e^{-2\gamma l_2}}\left(1+\Gamma_{\mathrm{FE}}e^{2\gamma x}\right)\\ &\times\Big\{(R_{12}+j\omega L_{12})\left(e^{\gamma(x_0+a)}-\Gamma_L e^{-\gamma(x_0+a)}\right)\\ &\times\left[\left(1+\Gamma_{NE}e^{-2\gamma(l_2-x_1)}\right)e^{-\gamma x_1}-\left(1+\Gamma_{NE}e^{-2\gamma(l_2-x_2)}\right)e^{-\gamma x_2}\right]\\ &+Z_{01}Z_{02}(G_{12}+j\omega C_{12})\left(e^{\gamma(x_0+a)}+\Gamma_L e^{-\gamma(x_0+a)}\right)\\ &\times\left[\left(1-\Gamma_{NE}e^{-2\gamma(l_2-x_1)}\right)e^{-\gamma x_1}-\left(1-\Gamma_{NE}e^{-2\gamma(l_2-x_2)}\right)e^{-\gamma x_2}\right]\Big\}\quad \mathrm{x} \ge \text{-}\mathrm{x}_1\end{aligned} \tag{32b}$$

E. Total Solution to the Transmission Line Equations for an Electrically Large Coupling Region

The total solution for the victim voltage response is given by the superposition principle in (22). The voltage response in the victim circuit is directly related to the voltages and currents in the aggressor circuit in addition to the mutual coupling parameters seen in (4) and (5). The aggressor voltages and currents when the culprit is electrically long can be found in (23). The victim voltage due to distributed voltage sources in (5a) when the coupling region is electrically large can be found from (11), (13), and (15) as,

$$V_{2,v}(x) = -(R_{12} + j\omega L_{12})\frac{V_S}{2}\frac{1}{Z_{01}+Z_S}\frac{e^{-\gamma l_1}}{1-\Gamma_L\Gamma_S e^{-2\gamma l_1}}\frac{e^{\gamma a}}{1-\Gamma_{NE}\Gamma_{FE}e^{-2\gamma l_2}}$$
$$\times\left\{\begin{array}{ll}
\left\{(x_2 - x_1)\left(\Gamma_{FE} + \Gamma_L e^{-2\gamma a}\right) + \frac{1}{2\gamma}\left(1 + \Gamma_L\Gamma_{FE}e^{-2\gamma(x_1+x_2+a)}\right)\left(e^{2\gamma x_1} - e^{2\gamma x_2}\right)\right\} & \\
\times\left(\Gamma_{\mathrm{NE}}e^{-2\gamma l_2}e^{-\gamma x} + e^{\gamma x}\right) & x \le -x_2 \\
 & \\
\left\{(x_2 + x)\left(1 + \Gamma_L\Gamma_{NE}e^{-2\gamma(a+l_2)}\right) + \frac{1}{2\gamma}\left(\Gamma_L e^{2\gamma(x-x_2-a)} + \Gamma_{NE}e^{-2\gamma l_2}\right)\left(e^{-2\gamma x} - e^{2\gamma x_2}\right)\right\} & \\
\times\left(\mathrm{e}^{-\gamma x} + \Gamma_{FE}e^{\gamma x}\right) & \\
+\left\{-(x + x_1)\left(\Gamma_{FE} + \Gamma_L e^{-2\gamma a}\right) + \frac{1}{2\gamma}\left(1 + \Gamma_L\Gamma_{FE}e^{2\gamma(x-x_1-a)}\right)\left(e^{2\gamma x_1} - e^{-2\gamma x}\right)\right\} & \\
\times\left(\Gamma_{\mathrm{NE}}e^{-2\gamma l_2}e^{-\gamma x} + e^{\gamma x}\right) & -\mathrm{x}_2 < x < -x_1 \\
 & \\
\left\{\left(x_2 - x_1\right)\left(1 + \Gamma_L\Gamma_{NE}e^{-2\gamma(a+l_2)}\right)\right. & \\
\left.+\frac{1}{2\gamma}\left(\Gamma_L e^{-2\gamma(x_1+x_2+a)} + \Gamma_{NE}e^{-2\gamma l_2}\right)\left(e^{2\gamma x_1} - e^{2\gamma x_2}\right)\right\}\left(\mathrm{e}^{-\gamma x} + \Gamma_{FE}e^{\gamma x}\right). & x \ge -x_1
\end{array}\right. \tag{33}$$

The victim voltage due to distributed current sources in (5b) can be found from (18)-(19) as,

$$V_{2,i}(x) = -(G_{12} + j\omega C_{12})V_S\frac{Z_{01}}{Z_{01}+Z_S}\frac{e^{-\gamma l_1}}{1-\Gamma_L\Gamma_S e^{-2\gamma l_1}}\frac{Z_{02}}{2}\frac{e^{\gamma a}}{1-\Gamma_{NE}\Gamma_{FE}e^{-2\gamma l_2}}$$
$$\times\left\{\begin{array}{ll}
\left\{(x_2 - x_1)\left(\Gamma_{FE} + \Gamma_L e^{-2\gamma a}\right) + \frac{1}{2\gamma}\left(1 + \Gamma_L\Gamma_{FE}e^{-2\gamma(x_1+x_2+a)}\right)\left(e^{2\gamma x_2} - e^{2\gamma x_1}\right)\right\} & \\
\times\left(\Gamma_{\mathrm{NE}}e^{-2\gamma l_2}e^{-\gamma x} + e^{\gamma x}\right) & x \le -x_2 \\
 & \\
\left\{(x_2 + x)\left(1 + \Gamma_L\Gamma_{NE}e^{-2\gamma(a+l_2)}\right) + \frac{1}{2\gamma}\left(\Gamma_L e^{2\gamma(x-x_2-a)} + \Gamma_{NE}e^{-2\gamma l_2}\right)\left(e^{2\gamma x_2} - e^{-2\gamma x}\right)\right\} & \\
\times\left(\mathrm{e}^{-\gamma x} + \Gamma_{FE}e^{\gamma x}\right) & \\
+\left\{-(x + x_1)\left(\Gamma_{FE} + \Gamma_L e^{-2\gamma a}\right) + \frac{1}{2\gamma}\left(1 + \Gamma_L\Gamma_{FE}e^{2\gamma(x-x_1-a)}\right)\left(e^{-2\gamma x} - e^{2\gamma x_1}\right)\right\} & \\
\times\left(\Gamma_{\mathrm{NE}}e^{-2\gamma l_2}e^{-\gamma x} + e^{\gamma x}\right) & -\mathrm{x}_2 < x < -x_1 \\
 & \\
\left\{\left(x_2 - x_1\right)\left(1 + \Gamma_L\Gamma_{NE}e^{-2\gamma(a+l_2)}\right)\right. & \\
\left.+\frac{1}{2\gamma}\left(\Gamma_L e^{-2\gamma(x_1+x_2+a)} + \Gamma_{NE}e^{-2\gamma l_2}\right)\left(e^{2\gamma x_2} - e^{2\gamma x_1}\right)\right\}\left(\mathrm{e}^{-\gamma x} + \Gamma_{FE}e^{\gamma x}\right). & x \ge -x_1
\end{array}\right. \tag{34}$$

The total voltage in the victim circuit outside the coupling region can be written from (22) and (33)-(34) as,

$$\begin{aligned} V_2(x) = {} & \frac{V_S}{2}\frac{1}{Z_{01}+Z_S}\frac{e^{-\gamma l_1}}{1-\Gamma_L\Gamma_S e^{-2\gamma l_1}}\frac{e^{\gamma(a+x)}}{1-\Gamma_{NE}\Gamma_{FE}e^{-2\gamma l_2}}\left(1+\Gamma_{\mathrm{NE}}e^{-2\gamma(l_2+x)}\right) \\ & \times\{-\left[R_{21}+j\omega L_{21}+Z_{01}Z_{02}\left(G_{21}+j\omega C_{21}\right)\right]\left[\left(x_2-x_1\right)\left(\Gamma_{FE}+\Gamma_L e^{-2\gamma a}\right)\right] \\ & +\left[R_{21}+j\omega L_{21}-Z_{01}Z_{02}\left(G_{21}+j\omega C_{21}\right)\right]\left[\frac{1}{2\gamma}\left(1+\Gamma_L\Gamma_{FE}e^{-2\gamma(x_1+x_2+a)}\right)\left(e^{2\gamma x_2}-e^{2\gamma x_1}\right)\right]\Bigg\} \\ & \text{for x} \le \text{-x}_2 \end{aligned} \qquad (35a)$$

$$\begin{aligned} V_2(x) = {} & \frac{V_S}{2}\frac{1}{Z_{01}+Z_S}\frac{e^{-\gamma l_1}}{1-\Gamma_L\Gamma_S e^{-2\gamma l_1}}\frac{e^{-\gamma(x-a)}}{1-\Gamma_{NE}\Gamma_{FE}e^{-2\gamma l_2}}\left(1+\Gamma_{\mathrm{FE}}e^{2\gamma x}\right) \\ & \times\{-\left[R_{21}+j\omega L_{21}+Z_{01}Z_{02}\left(G_{21}+j\omega C_{21}\right)\right]\left[\left(x_2-x_1\right)\left(1+\Gamma_L\Gamma_{NE}e^{-2\gamma(a+l_2)}\right)\right] \\ & +\left[R_{21}+j\omega L_{21}-Z_{01}Z_{02}\left(G_{21}+j\omega C_{21}\right)\right] \\ & \times\left[\frac{1}{2\gamma}\left(\Gamma_L e^{-2\gamma(x_1+x_2+a)}+\Gamma_{NE}e^{-2\gamma l_2}\right)\left(e^{2\gamma x_2}-e^{2\gamma x_1}\right)\right] \\ & \text{for x} \ge \text{-x}_1. \end{aligned} \qquad (35b)$$

Although the mathematics for finding the voltage in the victim circuit was based on the presumption that the signal lines were electrically long, the integral formulation is also applicable when the signal lines are electrically small. When the aggressor circuit is electrically small, the voltage and current in the aggressor circuit is approximately the same along the length of the line. Evaluation of the integral formulation remains the same. The final result for the victim voltage, however, is more compact when the lines are electrically small due to a greater simplicity in the voltage and current expressions for the aggressor circuit.

F. Maximum Crosstalk Estimation

The crosstalk between the aggressor and victim circuits at the near-end and far-end loads can be evaluated using (35), though the resulting expression does not provide the worst case crosstalk at all frequencies. The maximum crosstalk can be found through mathematical manipulations that find a maximum envelope for crosstalk given in (35). These manipulations vary with the electrical length of the aggressor circuit and the coupling region. When the aggressor is electrically small, the maximum victim voltages can be extracted from the magnitude of (35). When the aggressor circuit is electrically large, modifications to (35) are required. Equation (35) is written in a product of sums format. Thus, the maximum envelope for (35) can be approximated as the multiplication of the maximum envelopes for each of the individual products. Maximum values are approximated by modifying addition and subtraction operations to maximize the value of numerators and minimize the value of denominators, within the bounds of parameter values. Many of the terms in (35) are of the form $1 \pm \Gamma e^{\pm \gamma l}$. At maximum or minimum, the exponential quantity becomes real and is then of the form $1 \pm \Gamma e^{\pm \alpha l}$.

The mathematical manipulations required to find the maximum crosstalk can be illustrated with an example. One term in the far-end crosstalk expression derived from (35b) is $\left(\left(1+\Gamma_{\mathrm{FE}}\right)/\left(1-\Gamma_{NE}\Gamma_{FE}e^{-2\gamma l_2}\right)\right)e^{\gamma a}$. The denominator of this term is minimized when the product $\Gamma_{NE}\Gamma_{FE}e^{-2\gamma l_2}$ is a positive, real number. The numerator maximum can be found without significant overprediction by taking the magnitude of $1+\Gamma_{FE}$ and using $\left|e^{\gamma a}\right| = e^{\alpha a}$. The maximum envelope of this example term can then be defined as $\left(\left(\left|1+\Gamma_{\mathrm{FE}}\right|\right)/\left(1-\left|\Gamma_{NE}\right|\left|\Gamma_{FE}\right|e^{-2\alpha l_2}\right)\right)e^{\alpha a}$. Similarly, the maximum voltages at the victim loads can be found as a function of the aggressor electrical length and the coupling region electrical length with the piecewise expressions shown as follows:

$$\begin{aligned} V_{NE,\max} \approx & \left| \frac{V_S}{2} \frac{1}{Z_{01}+Z_S} \left(x_2 - x_1\right) \frac{e^{-\gamma l_1}}{1-\Gamma_L \Gamma_S e^{-2\gamma l_1}} \frac{1+\Gamma_{NE}}{1-\Gamma_{NE}\Gamma_{FE}e^{-2\gamma l_2}} e^{\gamma\left(x_0 - l_2\right)} \right| \\ & \times \left| \left(R_{12} + j\omega L_{12}\right)\left(e^{\gamma\left(x_0+a\right)} - \Gamma_L e^{-\gamma\left(x_0+a\right)}\right)\left(1-\Gamma_{FE}e^{-2\gamma x_0}\right) \right. \\ & \left. - Z_{01}Z_{02}\left(G_{12} + j\omega C_{12}\right)\left(e^{\gamma\left(x_0+a\right)} + \Gamma_L e^{-\gamma\left(x_0+a\right)}\right)\left(1+\Gamma_{FE}e^{-2\gamma x_0}\right) \right| \\ & \text{for } a+b \le \frac{\lambda}{10} \end{aligned} \tag{36a}$$

$$\begin{aligned} V_{NE,\max} \approx & \frac{\left|V_S\right|}{2} \frac{1}{\left|Z_{01}+Z_S\right|} \frac{e^{-\alpha l_1}}{1-\left|\Gamma_L\right|\left|\Gamma_S\right|e^{-2\alpha l_1}} \frac{\left|1+\Gamma_{\mathrm{NE}}\right|}{1-\left|\Gamma_{NE}\right|\left|\Gamma_{FE}\right|e^{-2\alpha l_2}} e^{\alpha\left(a-l_2\right)} \\ & \times \left\{ \left|R_{12} + j\omega L_{12} + Z_{01}Z_{02}\left(G_{12} + j\omega C_{12}\right)\right| \left[\left(x_2 - x_1\right)\left(\left|\Gamma_{FE}\right| + \left|\Gamma_L\right|e^{-2\alpha a}\right)\right] \right. \\ & + \left|R_{12} + j\omega L_{12} - Z_{01}Z_{02}\left(G_{12} + j\omega C_{12}\right)\right| \\ & \left. \times \left[\frac{1}{2\left|\gamma\right|} \left(1 + \left|\Gamma_L\right|\left|\Gamma_{FE}\right|e^{-2\alpha\left(x_1+x_2+a\right)}\right) \left|e^{2\gamma x_2} - e^{2\gamma x_1}\right| \right] \right\} \\ & \text{for } a+b > \frac{\lambda}{10} \text{ and } x_2 - x_1 < \frac{\lambda}{4} \end{aligned} \tag{36b}$$

$$
\begin{aligned}
V_{NE,\max} \approx{} & \frac{|V_S|}{2}\frac{1}{|Z_{01}+Z_S|}\frac{e^{-\alpha l_1}}{1-|\Gamma_L||\Gamma_S|e^{-2\alpha l_1}}\frac{|1+\Gamma_{\mathrm{NE}}|}{1-|\Gamma_{NE}||\Gamma_{FE}|e^{-2\alpha l_2}}e^{\alpha(a-l_2)} \\
& \times\Big\{|R_{12}+j\omega L_{12}+Z_{01}Z_{02}(G_{12}+j\omega C_{12})|\left[(x_2-x_1)\left(|\Gamma_{FE}|+|\Gamma_L|e^{-2\alpha a}\right)\right] \\
& +|R_{12}+j\omega L_{12}-Z_{01}Z_{02}(G_{12}+j\omega C_{12})| \\
& \times\left[\frac{1}{2|\gamma|}\left(1+|\Gamma_L||\Gamma_{FE}|e^{-2\alpha(x_1+x_2+a)}\right)e^{2\alpha x_1}\left(e^{n\lambda\alpha/2}+1\right)\right]\Big\} \\
& \text{for } x_2-x_1=\frac{n\lambda}{4} \text{ and } x_2-x_1\ge\frac{\lambda}{4}
\end{aligned}
\tag{36c}
$$

$$
\begin{aligned}
V_{FE,\max} \approx{} & \left|\frac{V_S}{2}\frac{1}{Z_{01}+Z_S}(x_2-x_1)\frac{e^{-\gamma l_1}}{1-\Gamma_L\Gamma_S e^{-2\gamma l_1}}\frac{1+\Gamma_{FE}}{1-\Gamma_{NE}\Gamma_{FE}e^{-2\gamma l_2}}e^{-\gamma x_0}\right| \\
& \times\Big|(R_{12}+j\omega L_{12})\left(e^{\gamma(x_0+a)}-\Gamma_L e^{-\gamma(x_0+a)}\right)\left(1-\Gamma_{NE}e^{-2\gamma(l_2-x_0)}\right) \\
& +Z_{01}Z_{02}(G_{12}+j\omega C_{12})\left(e^{\gamma(x_0+a)}+\Gamma_L e^{-\gamma(x_0+a)}\right)\left(1+\Gamma_{NE}e^{-2\gamma(l_2-x_0)}\right)\Big| \\
& \text{for } a+b\le\frac{\lambda}{10}
\end{aligned}
\tag{37a}
$$

$$
\begin{aligned}
V_{FE,\max} \approx{} & \frac{|V_S|}{2}\frac{1}{|Z_{01}+Z_S|}\frac{e^{-\alpha l_1}}{1-|\Gamma_L||\Gamma_S|e^{-2\alpha l_1}}\frac{|1+\Gamma_{\mathrm{FE}}|}{1-|\Gamma_{NE}||\Gamma_{FE}|e^{-2\alpha l_2}}e^{\alpha a} \\
& \times\Big\{|R_{12}+j\omega L_{12}+Z_{01}Z_{02}(G_{12}+j\omega C_{12})|\left[(x_2-x_1)\left(1+|\Gamma_L||\Gamma_{NE}|e^{-2\alpha(a+l_2)}\right)\right] \\
& +|R_{12}+j\omega L_{12}-Z_{01}Z_{02}(G_{12}+j\omega C_{12})| \\
& \times\left[\frac{1}{2|\gamma|}\left(|\Gamma_L|e^{-2\alpha(x_1+x_2+a)}+|\Gamma_{NE}|e^{-2\alpha l_2}\right)\left|e^{2\gamma x_2}-e^{2\gamma x_1}\right|\right]\Big\} \\
& \text{for } a+b>\frac{\lambda}{10} \text{ and } x_2-x_1<\frac{\lambda}{4}
\end{aligned}
\tag{37b}
$$

$$
\begin{aligned}
V_{FE,\max} \approx{} & \frac{|V_S|}{2}\frac{1}{|Z_{01}+Z_S|}\frac{e^{-\alpha l_1}}{1-|\Gamma_L||\Gamma_S|e^{-2\alpha l_1}}\frac{|1+\Gamma_{\mathrm{FE}}|}{1-|\Gamma_{NE}||\Gamma_{FE}|e^{-2\alpha l_2}}e^{\alpha a} \\
& \times\Big\{|R_{12}+j\omega L_{12}+Z_{01}Z_{02}(G_{12}+j\omega C_{12})|\left[(x_2-x_1)\left(1+|\Gamma_L||\Gamma_{NE}|e^{-2\alpha(a+l_2)}\right)\right] \\
& +|R_{12}+j\omega L_{12}-Z_{01}Z_{02}(G_{12}+j\omega C_{12})| \\
& \times\left[\frac{1}{2|\gamma|}\left(|\Gamma_L|e^{-2\alpha(x_1+x_2+a)}+|\Gamma_{NE}|e^{-2\alpha l_2}\right)e^{2\alpha x_1}\left(e^{n\lambda\alpha/2}+1\right)\right]\Big\} \\
& \text{for } x_2-x_1=\frac{n\lambda}{4} \text{ and } x_2-x_1\ge\frac{\lambda}{4}
\end{aligned}
\tag{37c}
$$

where

$$\gamma=\alpha+j\beta \tag{38}$$

where λ is the wavelength of the signal in the propagating medium and n is a positive, odd integer. The subscripts NE and FE represent the near-end and far-end position of the victim loads relative to the aggressor source.

Equation (36) and (37) confirm on a mathematical basis that the maximum crosstalk can be minimized by: reducing the aggressor source voltage, minimizing the coupling region length, using loads well matched to the transmission line characteristic impedance in the aggressor and victim circuits, and decreasing capacitive, inductive, and common impedance coupling mechanisms. The first piecewise expression for the near-end and far-end maximum voltages, (36a) and (37a), were derived from a formulation where the aggressor circuit was electrically small. This formulation was used instead of the electrically large formulation presented in (35) to provide better insight into the crosstalk response and to minimize the possibility of overpredicting the maximum crosstalk. The remaining piecewise expressions were derived from the electrically large aggressor circuit formulation in (35). The second piecewise expression in both equations, (36b) and (37b), are given when the aggressor circuit is electrically large, but the coupling region is less than one quarter wavelength. The last piecewise expression in both equations, (36c) and (37c), is evaluated when the coupling region is greater than one quarter wavelength. To predict the maximum values of crosstalk, (36c) and (37c) are evaluated at discrete frequency points where the coupling region is odd, integer quarter wavelengths long. This unique evaluation constraint removes undulations in the maximum crosstalk response due to the electrical length of the coupling region.

III. ANALYTIC VALIDATION

The validity of (35), from which (36) and (37) were derived, can be shown indirectly by demonstrating that it can be reduced to simpler formulas found in the literature under the correct conditions. For the case where circuits are electrically small, (35) can be reduced to the well-known crosstalk equations found in [6], as shown below. The voltage and current on the aggressor circuit can be written as (23a) and (23b). When the aggressor circuit is electrically small, the voltage and current are approximately the same along the length of the transmission line and satisfy $V_1(x) \approx V_1(-x_0)$ and

$I_1(x) \approx I_1(-x_0)$. The voltage at the near-end and far-end loads of the victim circuit due to an equivalent lumped voltage source at a position $-x_0$ can be found from (13) and (15) where $v(\xi) = V_N \delta(\xi + x_0)$. At the near-end $x = -l_2$, and at the far-end $x = 0$. Using these relationships the voltages at the near-end and far-end of the victim circuit can be written as,

$$V_{v,NE} = -\frac{V_{N,NE}}{2} \frac{(1+\Gamma_{NE})\left(1-\Gamma_{FE}e^{-2\gamma x_0}\right)}{1-\Gamma_{NE}\Gamma_{FE}e^{-2\gamma l_2}} e^{\gamma(-l_2+x_0)} \tag{39a}$$

$$V_{v,FE} = \frac{V_{N,FE}}{2} \frac{(1+\Gamma_{FE})\left(1-\Gamma_{NE}e^{-2\gamma(l_2-x_0)}\right)}{1-\Gamma_{NE}\Gamma_{FE}e^{-2\gamma l_2}} e^{-\gamma x_0} \tag{39b}$$

where, $V_{N,NE}$ and $V_{N,FE}$ is the lumped voltage source in the victim transmission line that creates the victim near-end and far-end responses, respectively. When the coupling region is electrically large, $V_{N,NE} \neq V_{N,FE}$ and the analysis of the near-end and far-end responses are completed separately. Similarly, the voltage at the near-end and far-end loads of the victim circuit due to an equivalent lumped current source at a position $-x_0$ can be found from (19) where $i(\xi) = I_N \delta(\xi + x_0)$. At the near-end $x = -l_2$, and at the far-end $x = 0$. Using these relationships the voltages at the near-end and far-end of the victim circuit can be written as,

$$V_{i,NE} = \frac{I_{N,NE}Z_{02}}{2} \frac{(1+\Gamma_{NE})\left(1+\Gamma_{FE}e^{-2\gamma x_0}\right)}{1-\Gamma_{NE}\Gamma_{FE}e^{-2\gamma l_2}} e^{\gamma(-l_2+x_0)} \tag{40a}$$

$$V_{i,FE} = \frac{I_{N,FE}Z_{02}}{2} \frac{(1+\Gamma_{FE})\left(1+\Gamma_{NE}e^{-2\gamma(l_2-x_0)}\right)}{1-\Gamma_{NE}\Gamma_{FE}e^{-2\gamma l_2}} e^{-\gamma x_0} \tag{40b}$$

where, $I_{N,NE}$ and $I_{N,FE}$ is the lumped current source in the victim transmission line that creates the victim near-end and far-end responses, respectively. When the coupling region is electrically large, $I_{N,NE} \neq I_{N,FE}$ and the analysis of the near-end and far-end responses are completed separately. Although (35) was formulated based on distributed voltage and current sources in the victim circuit, (35) can be re-arranged as a superposition of responses due to equivalent lumped sources. The near-end and far-end voltages in the victim circuit can be evaluated from (41)-(42).

$$V_{NE} = V_{v,NE} + V_{i,NE} \tag{41a}$$

$$V_{FE} = V_{v,FE} + V_{i,FE} \tag{41b}$$

$$\begin{aligned} V_{N,NE} = & -\frac{e^{\gamma(a-x_0)}}{1-\Gamma_{FE}e^{-2\gamma x_0}} \frac{\left(R_{12} + j\omega L_{12}\right)I_1(-x_0)}{e^{-\gamma(-x_0-a)} - \Gamma_L e^{\gamma(-x_0-a)}} \\ & \times\left[\frac{1}{2\gamma}\left(1+\Gamma_L\Gamma_{FE}e^{-2\gamma(x_1+x_2+a)}\right)\left(e^{2\gamma x_2} - e^{2\gamma x_1}\right) - \left(x_2 - x_1\right)\left(\Gamma_{FE} + \Gamma_L e^{-2\gamma a}\right)\right] \end{aligned} \tag{42a}$$

$$\begin{aligned} I_{N,NE} = & -\frac{e^{\gamma(a-x_0)}}{1+\Gamma_{FE}e^{-2\gamma x_0}} \frac{\left(G_{12} + j\omega C_{12}\right)V_1(-x_0)}{e^{-\gamma(-x_0-a)} + \Gamma_L e^{\gamma(-x_0-a)}} \\ & \times\left[\frac{1}{2\gamma}\left(1+\Gamma_L\Gamma_{FE}e^{-2\gamma(x_1+x_2+a)}\right)\left(e^{2\gamma x_2} - e^{2\gamma x_1}\right) + \left(x_2 - x_1\right)\left(\Gamma_{FE} + \Gamma_L e^{-2\gamma a}\right)\right] \end{aligned} \tag{42b}$$

$$\begin{aligned} V_{N,FE} = & \frac{e^{-\gamma(-x_0-a)}}{1-\Gamma_{NE}e^{-2\gamma(l_2-x_0)}} \frac{\left(R_{12} + j\omega L_{12}\right)I_1(-x_0)}{e^{-\gamma(-x_0-a)} - \Gamma_L e^{\gamma(-x_0-a)}} \\ & \times\left[\frac{1}{2\gamma}\left(\Gamma_L e^{-2\gamma(x_1+x_2+a)} + \Gamma_{NE}e^{-2\gamma l_2}\right)\left(e^{2\gamma x_2} - e^{2\gamma x_1}\right) - \left(x_2 - x_1\right)\left(1+\Gamma_L\Gamma_{NE}e^{-2\gamma(a+l_2)}\right)\right] \end{aligned} \tag{42c}$$

$$\begin{aligned} I_{N,FE} = & -\frac{e^{-\gamma(-x_0-a)}}{1+\Gamma_{NE}e^{-2\gamma(l_2-x_0)}} \frac{\left(G_{12} + j\omega C_{12}\right)V_1(-x_0)}{e^{-\gamma(-x_0-a)} + \Gamma_L e^{\gamma(-x_0-a)}} \\ & \times\left[\frac{1}{2\gamma}\left(\Gamma_L e^{-2\gamma(x_1+x_2+a)} + \Gamma_{NE}e^{-2\gamma l_2}\right)\left(e^{2\gamma x_2} - e^{2\gamma x_1}\right) + \left(x_2 - x_1\right)\left(1+\Gamma_L\Gamma_{NE}e^{-2\gamma(a+l_2)}\right)\right] \end{aligned} \tag{42d}$$

If the transmission lines are assumed to be lossless, where $\gamma = j\beta$ but R_{12} is kept to account for common impedance coupling, the transmission lines are also assumed to be electrically small, and the operating frequency is sufficiently low that all of the exponential terms are equal to one in (23) and (39)-(42), then the source equations simplify to,

$$V_{N,NE} = V_{N,FE} = -\left(x_2 - x_1\right)\left(R_{12} + j\omega L_{12}\right)I_1(-x_0) \tag{43a}$$

$$I_{N,NE} = I_{N,FE} = -(x_2 - x_1)(G_{12} + j\omega C_{12})V_1(-x_0). \tag{43b}$$

The voltage and current in the aggressor circuit can be simplified from (23) as

$$V_1(-x_0) \approx \frac{Z_L}{Z_S + Z_L} V_S \tag{44a}$$

$$I_1(-x_0) \approx \frac{1}{Z_S + Z_L} V_S . \tag{44b}$$

Then the near-end and far-end voltages, derived from (35), can be written as a summation of inductive ($M_{NE/FE}^{IND}$), capacitive ($M_{NE/FE}^{CAP}$), and common impedance ($M_{NE/FE}^{CI}$) coupling mechanisms as in [6]. Thus, (35) is validated for the case where transmission lines are approximately lossless, electrically small, and the operating frequency is sufficiently small.

IV. SIMULATIONS AND MEASUREMENTS

Equations (35)-(37) were validated through multiple simulations and measurements. The exact formulation in (35) was validated by applying the finite difference method to the weak coupling transmission line equations in (3)-(5). These low-level simulations showed agreement between the simulated results and (35) to within fractions of a dB over the entire simulation frequency range. Further details about these simulations are provided in Appendix A and Appendix B. Hspice simulations with *w*-element models that described the transmission line characteristics in the aggressor and victim circuits were also performed, as will be illustrated later. In both the measurements and the Hspice simulations the weak coupling condition was achieved through the design of the aggressor and victim circuit per-unit-length parameter ratios. The weak coupling condition allows the coupling from the victim back to the aggressor to be ignored and implies the following relationships [6]:

$$R_{11}I_1(x) + j\omega L_{11}I_1(x) >> R_{12}I_2(x) + j\omega L_{12}I_2(x) \tag{45a}$$

$$G_{11}V_1(x) + j\omega C_{11}V_1(x) >> G_{12}V_2(x) + j\omega C_{12}V_2(x). \tag{45b}$$

Assuming the voltages and currents are of the same magnitude in both the aggressor and victim circuits, the real and imaginary parts of (45) show that the weak coupling assumption is valid when $l_{11}/l_{12} >> 1$, $|(c_{11}+c_{12})/-c_{12}| >> 1$, $(r_1+r_{11})/r_{12} >> 1$, and $|(g_{11}+g_{12})/-g_{12}| >> 1$. These per-unit-length parameter ratios defining weak coupling are similar to conditions that have been derived by others [3], [6], [11], [26].

The measurement setup to validate (35)-(37) consisted of a printed circuit board (PCB) with six sets of coupled traces as shown in Fig. 5. The use of a PCB rather than a wiring harness or similar setup allowed precise specification of system geometry. The two layer PCB was fabricated with a 59 mil thick Isola FR402 dielectric and consisted of 1 oz. copper traces that were 116 mils wide. Six cases were tested as shown in Table I. Parameters for the test cases are defined in Fig. 1. The aggressor and victim traces were separated by 120 mils for Case 1-3 and Case 5-6 to satisfy the weak coupling conditions implied by (45) in the coupling region. Case 4 had a 20 mil separation distance in the coupling region and did not satisfy the weak coupling conditions implied by (45). The aggressor and victim traces were separated by 634 mils at the thru-hole SMA connectors.

Single-ended traces were placed at the bottom of the PCB to facilitate substrate and connector parasitic characterization measurements. The SMA connector parasitic model used was a shunt 1.1 pF capacitance with a series 0.8 nH inductance. The per-unit-length parameters for the geometries on the PCB were extracted from a signal integrity tool, Hyperlynx, for $\varepsilon_r = 4.7$ and $\tan\delta = 0.015$. These parameters were used in *w*-element models in Hspice. An example simulation without connector parasitics for Case 1 and a modified form of Case 1 is shown in Fig. 6 and Fig. 7, respectively. Connector parasitics were not included in the simulations to reduce simulation complexity. The modified Case 1 simulation used all of the same layout parameters as Case 1 except for a 500 mil trace separation in the coupling region. The loads for both simulations were defined as $Z_S = 30 + j\omega(100e-9)$, $Z_L = 75 + 1/[j\omega(30e-12)]$, $Z_{NE} = 45 + j\omega(10e-9)$, and $Z_{FE} = 75 + 1/[j\omega(5e-12)]$.

Fig. 6 and Fig. 7 show that there is better agreement between the Hspice simulations and the analytical results above 3 GHz when there is a greater separation of the traces in the coupling region. This trend occurs because the weak coupling

TABLE I. Measurement Setup Dimensions (Mils)

Case #	b	l_2	x_2	x_1	a	Trace Separation
Case 1	14853	14640	11320	3320	213	120
Case 2	14853	14640	9320	5320	213	120
Case 3	14853	14640	12320	8320	213	120
Case 4	14894	14640	11320	3320	254	20
Case 5	12533	12320	8000	2000	2213	120
Case 6	14853	12320	10320	4320	-107	120

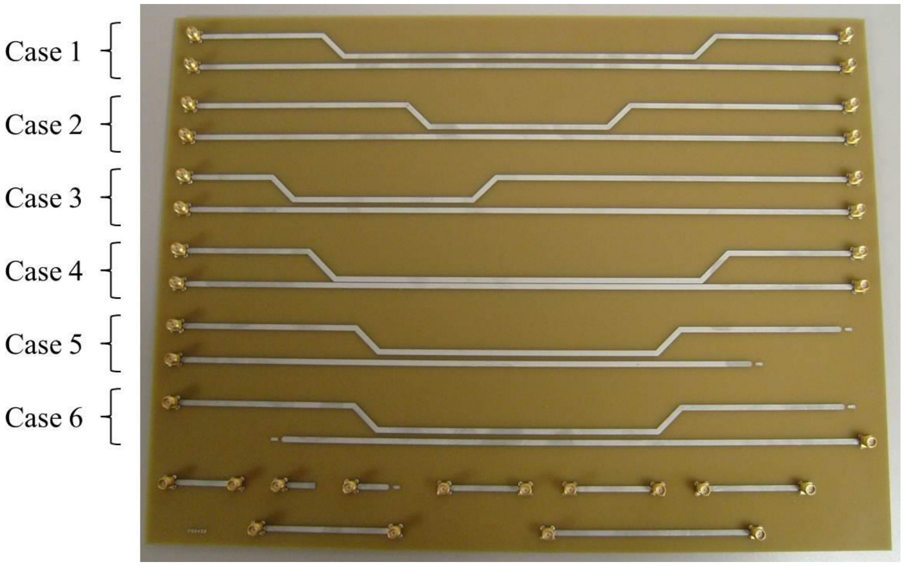

Fig. 5. Coupled microstrip PCB used to validate the maximum crosstalk equations. The total PCB size was 12” x 16”. Traces were made long to facilitate electrically long crosstalk measurements at low frequencies.

assumption is better satisfied with increasing trace separation. A comparison of the per-unit-length parameter ratios used to quantify weak coupling for these two simulations at 3 GHz is shown in Table II. An additional weak coupling condition for inhomogeneous media exists that cannot be deduced from (45). Reference [26] lists a condition in (15) that illustrates frequency dependence in the weak coupling assumption for lossless, inhomogeneous media. Rewriting this equation according to parameters given in Fig. 1 and (2), this condition is given by [26]

$$\omega(x_2 - x_1)\frac{|C_{21}L_{11} + L_{21}C_{11}|}{2\sqrt{L_{11}C_{11} + L_{21}C_{21}}} << 1 \cdot \tag{46}$$

Neglecting the transmission line losses in the Case 1 and modified Case 1 simulations, (46) was found to equal one at 4 and 19 GHz, respectively, which corresponds to the loss of accuracy between (35) and the simulated response. A condition similar to (46) that includes transmission line losses would fully explain the divergence in results in Fig. 6, but this derivation is outside the scope of this paper.

Crosstalk measurements were taken for the coupled trace cases illustrated in Fig. 5 using a two port network analyzer. The top microstrip trace and bottom microstrip trace for each coupled pair was considered as the aggressor circuit and victim circuit, respectively. The SMA jacks on the left of the PCB were dedicated to aggressor source and victim near-end load connections. The SMA jacks on the right of the PCB were dedicated to aggressor load and victim far-end load connections. Z_L and Z_{FE} were varied to study the near-end crosstalk response as a function of load impedance. Similarly, Z_L and Z_{NE} were varied to study the far-end crosstalk response. Three load combinations were measured for each crosstalk response and included two matched loads, two shorts, and two opens.

The measured crosstalk responses for Case 1 are illustrated in Fig. 8-Fig. 10. The coupling length was approximately one wavelength long at 793 MHz. Thus, the coupling length was electrically long for most of the measurement frequency range. Fig. 8-Fig. 10 show that the maximum crosstalk estimations given by (36) and (37) predict the crosstalk envelope within a few decibels. Initial attempts to compare the maximum crosstalk expressions in (36) and (37) with those in [24] with meaningful results were unsuccessful for the measurement setup of Fig. 5. This is due in part to the inhomogeneous nature of the test setup in Fig. 5. It can be shown that the equations in [24] can be derived from (35) using a homogeneous medium relationship.

A divergence between the analytical modeling and the crosstalk measurement in Fig. 8-Fig. 10 can be seen starting around 3 GHz. This discrepancy is due mostly to the weak coupling assumption not being well satisfied from a frequency dependent condition similar to (46). This assertion is supported by the data in Fig. 6 and Fig. 7. Some

TABLE II. WEAK COUPLING RATIOS FOR TWO CASE 1 SIMULATIONS AT 3 GHZ

Simulation Case	l_{11}/l_{12}	$(c_{11}+c_{12})/c_{12}$	$(r_1+r_{11})/r_{12}$	$(g_{11}+g_{12})/g_{12}$
Original	11	37	26	152
Modified	69	796	82	2337

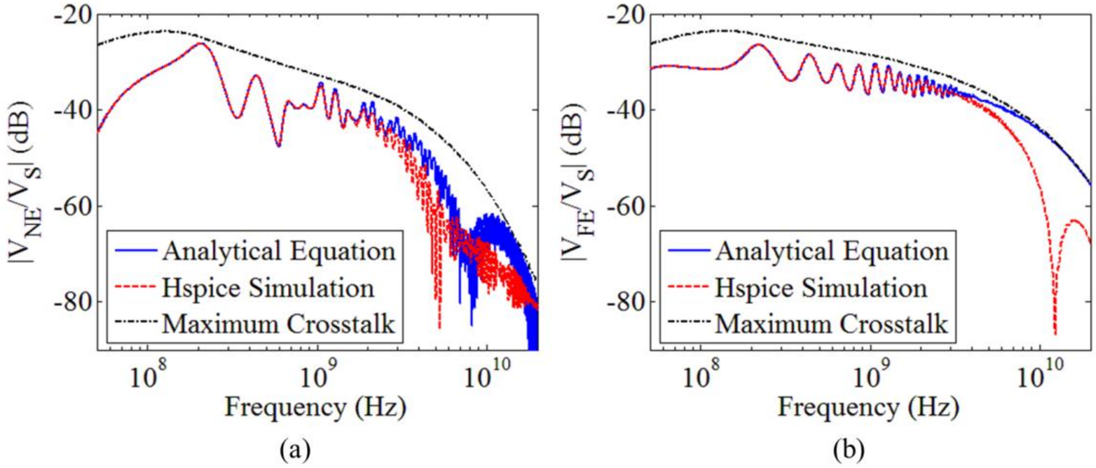

Fig. 6. Crosstalk example for the Case 1 configuration without SMA connector parasitics. (a) Near-end crosstalk. (b) Far-end crosstalk. The separation between traces in the coupling region was 120 mil. The analytical equation is given by (35a) and (35b) and the maximum crosstalk estimate is given by (36) and (37) for (a) and (b), respectively.

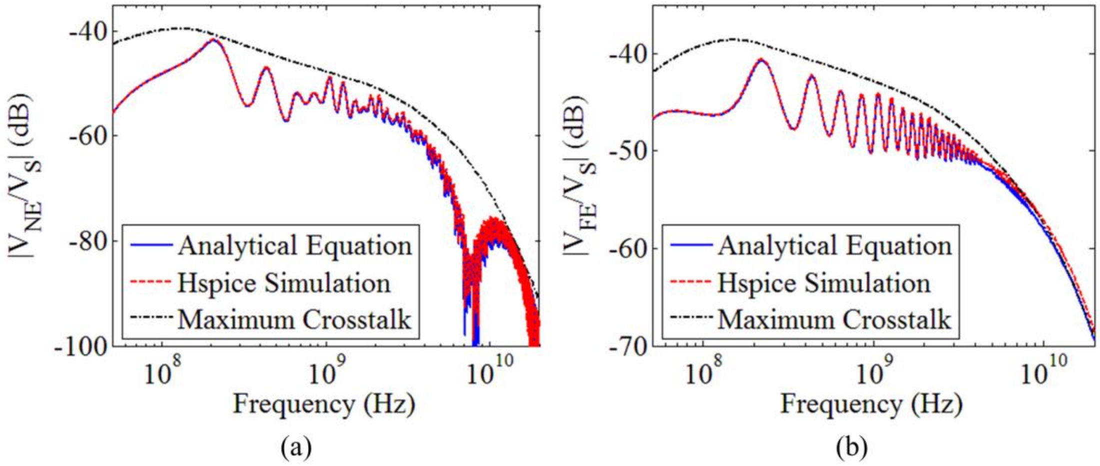

Fig. 7. Crosstalk example for the modified Case 1 configuration without SMA connector parasitics. (a) Near-end crosstalk. (b) Far-end crosstalk. The separation between traces in the coupling region was 500 mil. The analytical equation is given by (35a) and (35b) and the maximum crosstalk estimate is given by (36) and (37) for (a) and (b), respectively.

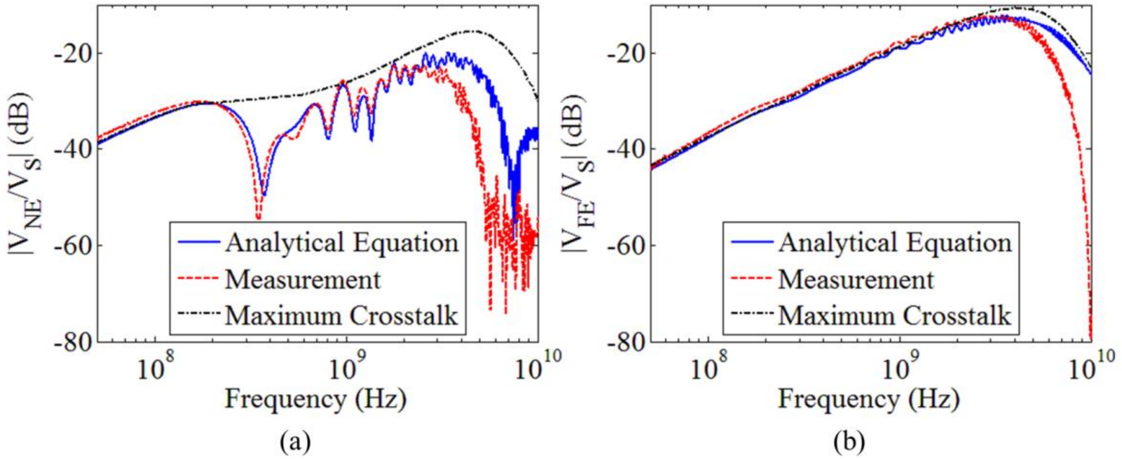

Fig. 8. Crosstalk example for the Case 1 configuration with SMA connector parasitics. (a) Near-end crosstalk. (b) Far-end crosstalk. Matched loads were used for the ports not connected to the network analyzer on the PCB. The maximum crosstalk curves are predicted from (36) and (37).

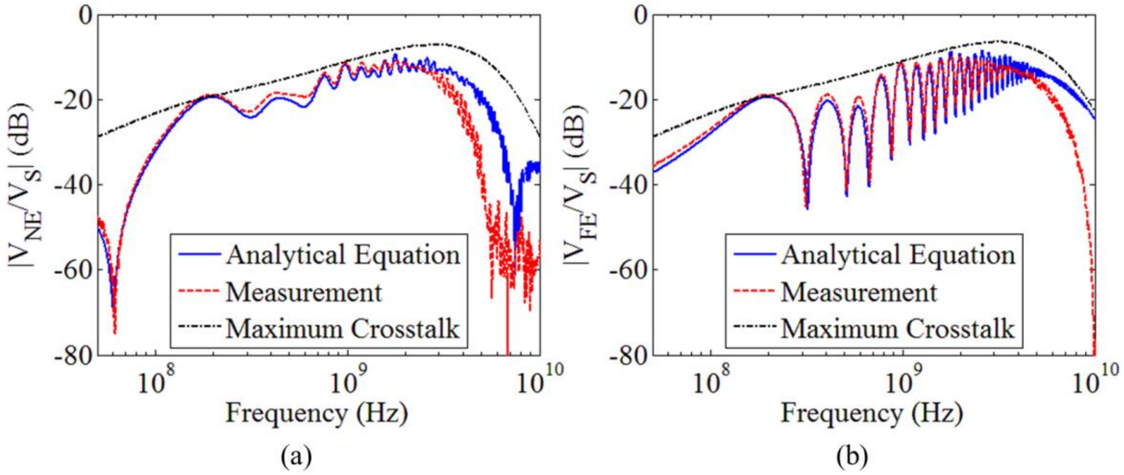

Fig. 9. Crosstalk example for the Case 1 configuration with SMA connector parasitics. (a) Near-end crosstalk. (b) Far-end crosstalk. The ports not connected to the network analyzer on the PCB were left open. The maximum crosstalk curves are predicted from (36) and (37).

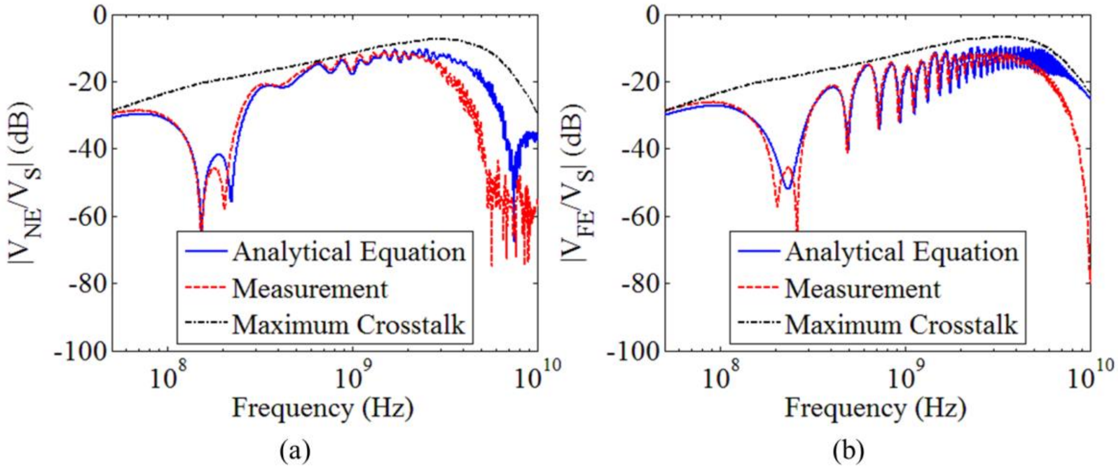

Fig. 10. Crosstalk example for the Case 1 configuration with SMA connector parasitics. (a) Near-end crosstalk. (b) Far-end crosstalk. Shorts were used for the ports not connected to the network analyzer on the PCB. The maximum crosstalk curves are predicted from (36) and (37).

additional divergence in the results may also be caused by an inadequate SMA connector parasitic model above 3 GHz and by higher order mode effects. Despite the difference in measured and analytically predicted results above 3 GHz, the maximum crosstalk curves still adequately predict the maximum crosstalk to relatively high frequency. The other test cases on the PCB were tested with similar results. Although the maximum crosstalk formulas were derived on the basis of weak coupling, these formulas may still give reasonable results in cases where the weak coupling assumption is not strictly met. The measured crosstalk responses for Case 4, which does not satisfy the weak coupling conditions implied by (45), are shown in Fig. 11-Fig. 13.

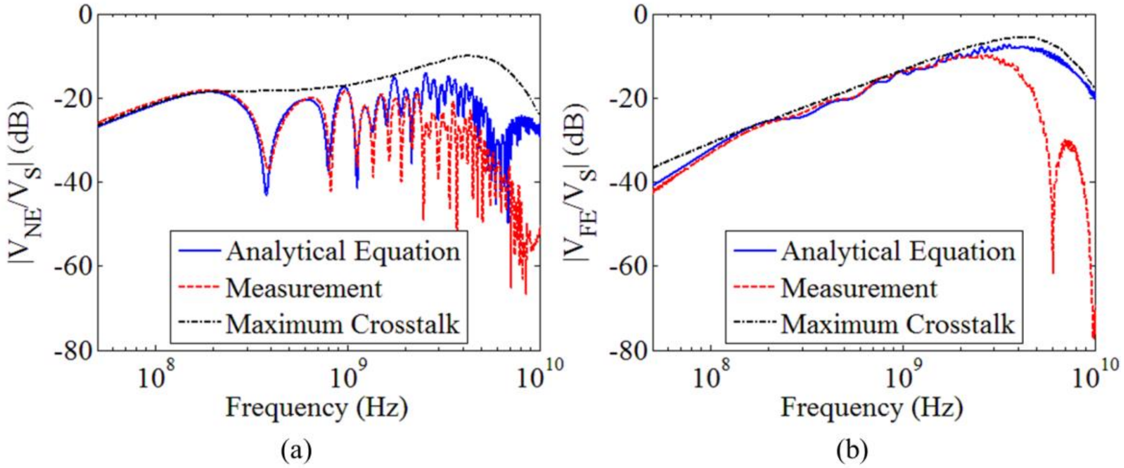

Fig. 11. Crosstalk example for the Case 4 configuration with SMA connector parasitics. (a) Near-end crosstalk. (b) Far-end crosstalk. Matched loads were used for the ports not connected to the network analyzer on the PCB. The maximum crosstalk curves are predicted from (36) and (37).

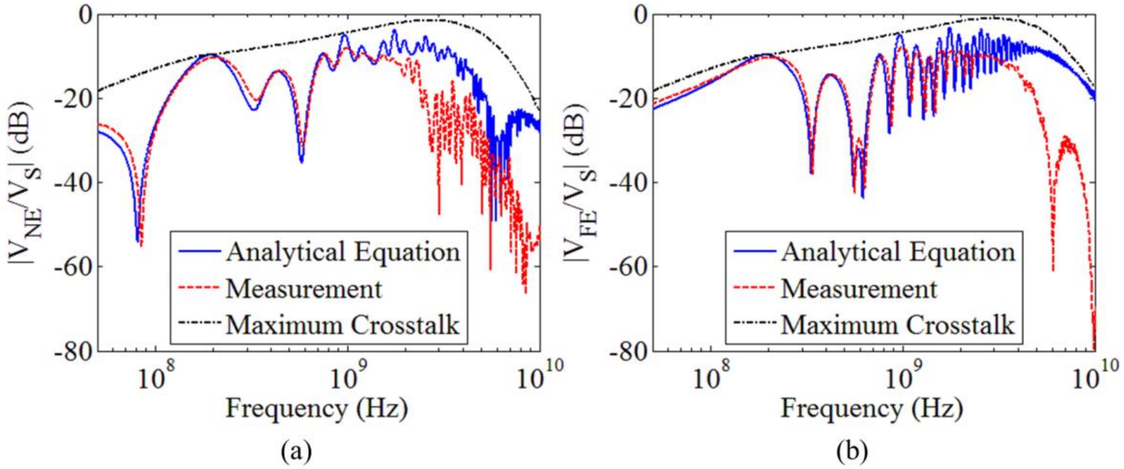

Fig. 12. Crosstalk example for the Case 4 configuration with SMA connector parasitics. (a) Near-end crosstalk. (b) Far-end crosstalk. The ports not connected to the network analyzer on the PCB were left open. The maximum crosstalk curves are predicted from (36) and (37).

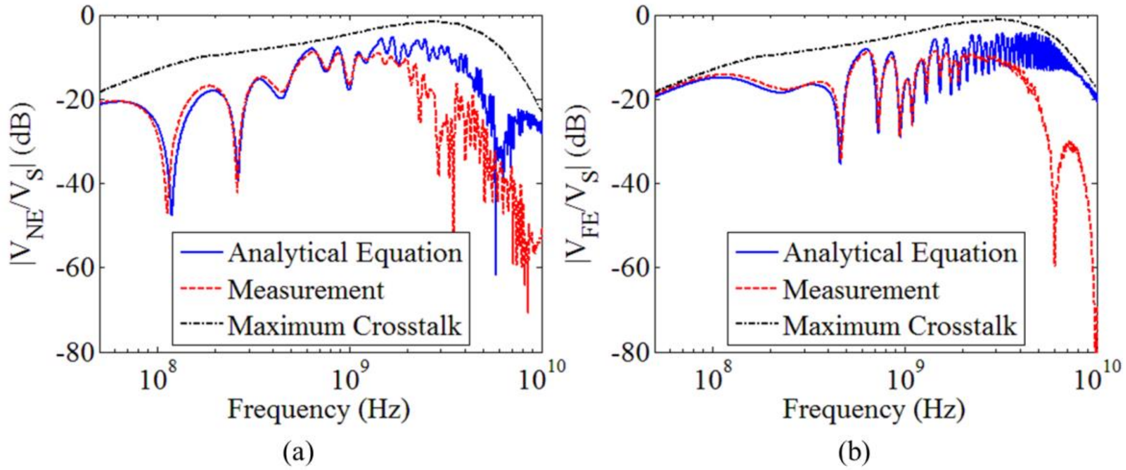

Fig. 13. Crosstalk example for the Case 4 configuration with SMA connector parasitics. (a) Near-end crosstalk. (b) Far-end crosstalk. Shorts were used for the ports not connected to the network analyzer on the PCB. The maximum crosstalk curves are predicted from (36) and (37).

V. CONCLUSION

Equations for estimating the maximum crosstalk in a three-conductor transmission line have been presented and validated against a well-known crosstalk formulation and validated against simulated and measured data. These formulas are based on the weak coupling assumption where the transmission line system has a single coupling region with a uniform cross section. These equations may be expanded to systems with more than three conductors through the application of the superposition principle. If weak coupling is assumed among all conductors in such a system, a first-order approach to find the maximum crosstalk estimate would be to formulate a three-conductor transmission line problem as in Fig. 1 for each aggressor. The maximum crosstalk could then be formulated as the summation of (36) at the near-end, and (37) at the far-end for all of the three-conductor transmission line problems. This approach would neglect higher order coupling effects where a signal could propagate and couple among multiple aggressor lines before coupling to a victim line. Transmission line losses and resistive transmission line terminations in many cases could make these higher order coupling effects negligible. This superposition approach could also be used for systems that have more than one coupling region. Caution should be used, however, as the resulting maximum crosstalk expression may suffer from over prediction problems.

The newly presented formulas can model the maximum crosstalk for transmission lines in lossy, inhomogeneous media where the transmission lines may have unique and arbitrary lengths. Measurements and simulations show that the maximum crosstalk formulas capture the envelope of the near-end and far-end victim voltages well, often within a few decibels. Future work may include estimation of maximum crosstalk for transmission lines without the weak coupling assumption, for transmission lines with non-uniform cross sections, and for systems containing more than two transmission lines. These equations are also well suited for evaluation of signal integrity in systems where transmission line parameters are not well known and crosstalk sensitivity analysis is needed.

REFERENCES

[1] A. Feller, H. R. Kaupp, and J. J. Digiacome, “Crosstalk and reflections in high-speed digital systems,” in *Proc. Fall Joint Comp. Conf.*, 1965, pp. 511-525.

[2] R. E. Matick, “Coupled transmission lines and directional couplers,” in *Transmission Lines for Digital and Communication Networks*. New York, NY, USA: McGraw-Hill, 1969, ch. 7, pp. 268-309.

[3] C. R. Paul, “Solution of the transmission-line equations for three-conductor lines in homogeneous media,” *IEEE Trans. Electromagn. Compat.*, vol. EMC-20, no. 1, pp. 216-222, Feb. 1978.

[4] C. R. Paul, “On the superposition of inductive and capacitive coupling in crosstalk-prediction models,” *IEEE Trans. Electromagn. Compat.*, vol. EMC-24, no. 3, pp. 335-343, Aug. 1982.

[5] C. R. Paul, “Derivation of common impedance coupling from the transmission-line equations,” *IEEE Trans. Electromagn. Compat.*, vol. 34, no. 3, pp. 315-319, Aug. 1992.

[6] C. R. Paul, “Crosstalk,” in *Introduction to Electromagnetic Compatibility,* 2nd ed. Hoboken, NJ: Wiley, 2006, ch. 9, pp. 559-711.

[7] R. G. Olsen, “A simple model for weakly coupled lossy transmission lines of finite length,” *IEEE Trans. Electromagn. Compat.*, vol. EMC-26, no. 2, pp. 79-83, May 1984.

[8] C. R. Paul, “Computation of crosstalk in a multiconductor transmission line,” *IEEE Trans. Electromagn. Compat.*, vol. EMC-23, no. 4, pp. 352-358, Nov. 1981.

[9] C. R. Paul, *Analysis of Multiconductor Transmission Lines*, 2nd ed. Hoboken, NJ, USA: Wiley, 2008, ch. 3 and ch. 10, pp. 89-109, and pp. 544-577.

[10] C. R. Paul, “Literal solutions for time-domain crosstalk on lossless transmission lines,” *IEEE Trans. Electromagn. Compat.*, vol. 34, no. 4, pp. 433-444, Nov. 1992.

[11] C. R. Paul, “Solution of the transmission-line equations under the weak-coupling assumption,” *IEEE Trans. Electromagn. Compat.*, vol. 44, no. 3, pp. 413-423, Aug. 2002.

[12] C. Gordon and K. M. Roselle, “Estimating crosstalk in multiconductor transmission lines,” *IEEE Trans. Compon. Packag. Manuf. Technol. B*, vol. 19, no. 2, pp. 273-277, May 1996.

[13] W. Shi and J. Fang, “Evaluation of closed-form crosstalk models of coupled transmission lines,” *IEEE Trans. Adv. Packag.*, vol. 22, no. 2, pp. 174-181, May 1999.

[14] Y.-Z. Xie, F. G. Canavero, T. Maestri, and Z.-J. Wang, “Crosstalk analysis of multiconductor transmission lines based on distributed analytical representation and iterative technique,” *IEEE Trans. Electromagn. Compat.*, vol. 52, no. 3, pp. 712-727, Aug. 2010.

[15] M. Khalaj-Amirhosseini, “Analysis of coupled or single nonuniform transmission lines using the method of moments,” *Int. J. RF Microw. Comput.-Aided Eng.*, vol. 18, no. 4, pp. 376-382, Jul. 2008.

[16] M. Khalaj-Amirhosseini, “An approximated closed form solution for nonuniform transmission lines,” in *Proc. Asia Pacific Microw. Conf.*, Singapore, 2009, pp. 1310-1314.

[17] Y. Kami and R. Sato, “Coupling model of crossing transmission lines,” *IEEE Trans. Electromagn. Compat.*, vol. 28, no. 4, pp. 204-210, Nov. 1986.

[18] Y. Kami and R. Sato, “Crosstalk of finite-length transmission lines in arbitrary directions on the same ground plane,” in *Proc. IEEE Int. Symp. Electromagn. Compat.*, Anaheim, CA, USA, Aug. 1992, pp. 247-250.

[19] M. Wu, D. G. Beetner, T. H. Hubing, H. Ke, and S. Sun, “Statistical prediction of “reasonable worst-case” crosstalk in cable bundles,” *IEEE Trans. Electromagn. Compat.*, vol. 51, no. 3, pp. 842-851, Aug. 2009.

[20] A. Ciccolella and F. G. Canavero, “Stochastic prediction of wire coupling interference,” in *Proc. IEEE Int. Symp. Electromagn. Compat.*, Atlanta, GA, USA, Aug. 1995, pp. 51-56.

[21] D. Bellan and S. A. Pignari, “Estimation of crosstalk in nonuniform cable bundles,” in *Proc. IEEE Int. Symp. Electromagn. Compat.*, Aug. 8-12, 2005, pp. 336-341.

[22] A. El-Zein and S. Chowdhury, “An analytical method for finding the maximum crosstalk in lossless-coupled transmission lines,” in *Proc. Dig. Tech. Papers IEEE/ACM Int. Conf. Comput.-Aided Design*, Santa Clara, CA, 1992, pp. 443-448.

[23] A. El-Zein and S. Chowdhury, “Maximum crosstalk in a transmission line system with linear time-invariant networks,” in *Proc. Int. Symp. Circuits and Syst.*, Chicago, IL, USA, 1993, pp. 2295-2298.

[24] X. Dong, H. Weng, D. G. Beetner, and T. H. Hubing, “Approximation of worst case crosstalk at high frequencies,” *IEEE Trans. Electromagn. Compat.*, vol. 53, no. 1, pp. 202-208, Feb. 2011.

[25] F. M. Tesche, M. V. Ianoz, and T. Karlsson, “Field coupling using transmission line theory,” in *EMC Analysis Methods and Computational Models*, 1st ed. New York, NY, USA: Wiley, 1997, ch. 7, pp. 321-394.

[26] D. J. Riley and L. D. Bacon, “On the limitation of the weak-coupling assumption for crosstalk analysis based on quasi-TEM propagation,” *IEEE Trans. Electromagn. Compat.*, vol. 32, no. 1, pp. 28-37, Feb. 1990.

II. Maximum Crosstalk Estimation in Lossless and Homogeneous Transmission Lines

Matthew S. Halligan and Daryl G. Beetner, *Senior Member*, IEEE

Abstract—In earlier papers, analytical formulas were derived to estimate the maximum crosstalk in the frequency domain for systems with electrically long signal lines. These formulas were developed to give designers intuitive feedback as to the causes for crosstalk problems and methods for maximum crosstalk reduction. In one of these papers the maximum crosstalk estimates are based on intuitive relationships for infinitely long transmission lines. While the resulting model is quite simple and easy to understand, its limitations are poorly understood. In another paper the maximum crosstalk estimates are based on a mathematically rigorous, integral formulation, but the resulting model is relatively complex. This rigorous model is derived assuming the signal lines are weakly coupled and the transmission line characteristic impedances are approximately the same over the entire lengths of the aggressor and victim circuits. The following paper illustrates how the less rigorously developed estimates, based on infinitely long transmission lines, may be derived from the mathematically rigorous maximum crosstalk estimates for lossless and homogeneous transmission lines in the frequency domain. The resulting derivation provides insight into the limitations and mathematical validity of the less rigorous estimates that are not available in the original paper. The mathematically rigorous maximum crosstalk estimates are shown to have fewer and less restrictive assumptions than the estimates based on infinitely long transmission lines. Measurements and simulations are presented that validate results and illustrate maximum crosstalk estimate limitations.

Index Terms—Cabling and transmission systems, crosstalk, frequency domain techniques, modeling techniques, transmission line theory

I. INTRODUCTION

Present design trends in commercial electronics are toward designs that are smaller, weigh less, and consume less power than designs of the past. One major implication of this trend is increased problems with crosstalk. Crosstalk is often evaluated through a combination of numerical simulations and rules of thumb and has been extensively studied in literature. Some crosstalk modeling approaches have included SPICE modeling methods for multiconductor transmission lines as in [1] and alternative modeling methods for multiconductor transmission lines with many conductors and non-uniform cross-sections as in [2]. Crosstalk reduction strategies have also been explored [3]-[4]. In [3], on-wafer measurements were performed and showed transmission line differential mode excitations had smaller crosstalk than transmission line common mode excitations and single-ended excitations. Conductor routing was investigated in [4] to reduce nearest neighbor crosstalk. Crosstalk has also been analyzed while considering "continuous-spectrum" currents and bound mode currents in a coupled, two microstrip line structure [5].

While most literature has focused on exact crosstalk formulations that capture every peak and valley in the crosstalk over frequency, design decisions are often better formulated from a maximum, worst case envelope perspective since the physical parameters for any transmission line system are never fully known. When the circuit becomes electrically large, in particular, small variations in transmission line parameters can cause large changes in the crosstalk at a given frequency, possibly making the difference between a system which passes or fails crosstalk requirements. Basing design decisions on a maximum crosstalk envelope rather than an exact model could lead to better design decisions since the maximum crosstalk envelope is generally less sensitive to transmission line parameter variations than an exact formulation. This bounding approach to design is also of interest to designers because passing this worst case performance limit eliminates the need for further design analysis and modifications. Worst case formulations are also often simpler than exact formulations, giving the designer a better opportunity to understand why crosstalk problems occur and how to fix them.

Several recent efforts have focused on the estimation of maximum crosstalk [6]-[10]. An effort was made in [8]-[9] to predict maximum crosstalk at “high frequencies”, where the signal lines were electrically large, in a homogeneous medium, and weak coupling was assumed. Although the results in [8] were shown to predict the crosstalk well, the maximum crosstalk formulations did not account for transmission line loss and lacked mathematical rigor. Mathematical derivations for new maximum crosstalk formulas were presented in [10] that addressed many of the shortcomings of [8]. The estimates in [10] were based on a mathematically rigorous, integral formulation where the transmission lines could be lossy and in an inhomogeneous medium. The estimates in [10] were formulated in the frequency domain where the signal lines were assumed to be weakly coupled, and the transmission line characteristic impedances were approximately the same over the entire lengths of the aggressor and victim circuits.

One objective of this paper is to show how the general maximum crosstalk estimates in [10] can be simplified for the specific case of lossless transmission lines and a homogeneous medium assumption. Another objective is to illustrate the limitations and mathematical validity of the estimates in [8] which are not available in the original paper. It is shown that the maximum crosstalk estimates in [8] can be derived from the formulas in [10] under the correct conditions. This paper provides rigorous derivations for the maximum crosstalk estimates in [8] which were originally formulated from an intuitive basis. It is shown that the mathematically rigorous crosstalk estimates in [10] provide a more general solution for the estimate of maximum crosstalk.

Derivations for the maximum crosstalk estimates based on the integral formulation in [10] for lossless and homogeneous transmission lines are first presented in Section II. Section III introduces an estimate based on lossless, homogeneous, and infinitely long transmission lines. Mathematical derivations for this estimate are also presented that are not available in [8]. An analytical comparison, and a measurement and simulation validation of the two maximum crosstalk estimates is presented in Section IV. Conclusions are given in Section V.

II. MAXIMUM CROSSTALK ESTIMATES FROM AN INTEGRAL FORMULATION

A detailed derivation of formulas for the maximum crosstalk estimates in weakly coupled transmission lines, including transmission line losses, can be found in [10]. The three conductor transmission line system in Fig. 1 was used as part of this derivation to develop maximum crosstalk expressions at frequencies where the signal lines were electrically long. This system consists of an aggressor circuit and a victim circuit, where the aggressor circuit is denoted as signal line one, and the victim circuit is denoted as signal line two. The primary quantity of interest is the voltage at the near-end and far-end loads of the victim circuit.

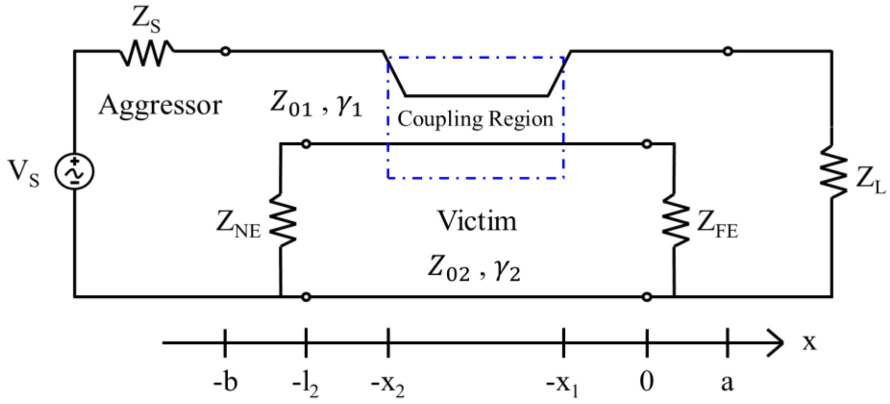

Fig. 1. Coupled three conductor transmission line system used to formulate an estimate of maximum crosstalk [10].

An integral formulation was used to solve for the voltage and current in the victim circuit in Fig. 1. Since the circuit is linear, superposition was used to find the total circuit response. The total circuit response consists of the response due to a distributed voltage source (related to inductive and common impedance coupling) and the response due to a distributed current source (related to capacitive and common impedance coupling). The responses from these sources were found separately. To minimize complexity, the propagation constant, γ, is assumed to be the same for both the aggressor and victim circuits. Weak coupling is also assumed where the voltages and currents in the aggressor circuit are not influenced by the voltages and currents in the victim circuit. The characteristic impedances, Z_{01} and Z_{02}, are assumed to be approximately the same over the entire lengths of the aggressor and victim circuits, respectively. The exact expressions for the victim near-end voltage and far-end voltage are [10]

$$\begin{aligned} V_{NE} &= \frac{V_S}{2} \frac{\left(1+\Gamma_{\mathrm{NE}}\right)}{\left(Z_{01}+Z_S\right)} \frac{e^{-\gamma l_1}}{\left(1-\Gamma_L \Gamma_S e^{-2\gamma l_1}\right)} \frac{e^{\gamma\left(a-l_2\right)}}{\left(1-\Gamma_{NE}\Gamma_{FE} e^{-2\gamma l_2}\right)} \\ &\times \Big\{ -\left[R_{12}+j\omega L_{12}+Z_{01}Z_{02}\left(G_{12}+j\omega C_{12}\right)\right]\left[\left(x_2-x_1\right)\left(\Gamma_{FE}+\Gamma_L e^{-2\gamma a}\right)\right] \\ &+\left[R_{12}+j\omega L_{12}-Z_{01}Z_{02}\left(G_{12}+j\omega C_{12}\right)\right]\left[\frac{1}{2\gamma}\left(1+\Gamma_L\Gamma_{FE} e^{-2\gamma\left(x_1+x_2+a\right)}\right)\left(e^{2\gamma x_2}-e^{2\gamma x_1}\right)\right]\Big\} \end{aligned} \tag{1a}$$

$$\begin{aligned} V_{FE} &= \frac{V_S}{2} \frac{\left(1+\Gamma_{\mathrm{FE}}\right)}{\left(Z_{01}+Z_S\right)} \frac{e^{-\gamma l_1}}{\left(1-\Gamma_L \Gamma_S e^{-2\gamma l_1}\right)} \frac{e^{\gamma a}}{\left(1-\Gamma_{NE}\Gamma_{FE} e^{-2\gamma l_2}\right)} \\ &\times \Big\{ -\left[R_{12}+j\omega L_{12}+Z_{01}Z_{02}\left(G_{12}+j\omega C_{12}\right)\right]\left[\left(x_2-x_1\right)\left(1+\Gamma_L\Gamma_{NE} e^{-2\gamma\left(a+l_2\right)}\right)\right] \\ &+\left[R_{12}+j\omega L_{12}-Z_{01}Z_{02}\left(G_{12}+j\omega C_{12}\right)\right] \\ &\times\left[\frac{1}{2\gamma}\left(\Gamma_L e^{-2\gamma\left(x_1+x_2+a\right)}+\Gamma_{NE} e^{-2\gamma l_2}\right)\left(e^{2\gamma x_2}-e^{2\gamma x_1}\right)\right]\Big\} \end{aligned} \tag{1b}$$

where,

$$\gamma = \alpha + j\beta \tag{2a}$$

$$l_1 = a + b \tag{2b}$$

$$\Gamma_L = \frac{Z_L - Z_{01}}{Z_L + Z_{01}} \tag{2c}$$

$$\Gamma_S = \frac{Z_S - Z_{01}}{Z_S + Z_{01}} \tag{2d}$$

$$\Gamma_{NE} = \frac{Z_{NE} - Z_{02}}{Z_{NE} + Z_{02}} \tag{2e}$$

$$\Gamma_{FE} = \frac{Z_{FE} - Z_{02}}{Z_{FE} + Z_{02}} \tag{2f}$$

and R_{21}, L_{21}, G_{21}, and C_{21} represent the transmission line per-unit-length coupling parameters in the coupling region. The subscripts NE and FE represent the near-end and far-end position of the victim loads relative to the aggressor source in Fig. 1.

If the transmission line system is lossless and homogeneous, (1) reduces to

$$\begin{aligned} V_{NE} &= \frac{V_S}{2}\frac{l_{21}}{l_{11}}\frac{Z_{01}}{\left(Z_{01}+Z_S\right)}\frac{e^{j\beta\left(a-l_2-l_1\right)}}{\left(1-\Gamma_L\Gamma_S e^{-j2\beta l_1}\right)}\frac{\left(1+\Gamma_{\mathrm{NE}}\right)}{\left(1-\Gamma_{NE}\Gamma_{FE}e^{-j2\beta l_2}\right)} \\ &\quad\times\left(1+\Gamma_L\Gamma_{FE}e^{-j2\beta\left(x_1+x_2+a\right)}\right)\left(e^{j2\beta x_2}-e^{j2\beta x_1}\right) \end{aligned} \tag{3a}$$

$$\begin{aligned} V_{FE} &= \frac{V_S}{2}\frac{l_{21}}{l_{11}}\frac{Z_{01}}{\left(Z_{01}+Z_S\right)}\frac{e^{j\beta\left(a-l_1\right)}}{\left(1-\Gamma_L\Gamma_S e^{-j2\beta l_1}\right)}\frac{\left(1+\Gamma_{\mathrm{FE}}\right)}{\left(1-\Gamma_{NE}\Gamma_{FE}e^{-j2\beta l_2}\right)} \\ &\quad\times\left(\Gamma_L e^{-j2\beta\left(x_1+x_2+a\right)}+\Gamma_{NE}e^{-j2\beta l_2}\right)\left(e^{j2\beta x_2}-e^{j2\beta x_1}\right) \end{aligned} \tag{3b}$$

where the per-unit-length parameters for inductance and capacitance in the coupling region are defined as [11]

$$\mathbf{L}=\begin{bmatrix} l_{11} & l_{12} \\ l_{21} & l_{22} \end{bmatrix} \qquad \mathbf{C}=\begin{bmatrix} c_{11}+c_{12} & -c_{12} \\ -c_{21} & c_{21}+c_{22} \end{bmatrix}. \tag{4}$$

The per-unit-length parameter matrices are symmetric for the system in Fig. 1 due to reciprocity. Equation (3) was derived using the relationship [12]

$$\frac{l_{21}}{l_{11}}=\frac{c_{21}}{c_{21}+c_{22}}, \tag{5}$$

which is valid in a homogeneous medium. Equation (3) can thus be alternatively written with a ratio of per-unit-length parameter capacitances rather than inductances.

The crosstalk between the aggressor and victim circuits at the near-end and far-end loads can be evaluated using (3), though the resulting expression does not provide the worst case crosstalk at all frequencies. The maximum crosstalk can be found through mathematical manipulations that find a maximum envelope for crosstalk given in (3). These manipulations vary with the electrical length of the aggressor circuit and the coupling region. When the aggressor is electrically small, the maximum voltages at the victim loads can be extracted from the magnitude of (3). When the aggressor circuit is electrically large, modifications to (3) are required. Equation (3) is written in a product of sums format. Thus, the maximum envelope for (3) can be approximated as the multiplication of the maximum envelopes for each of the individual products. Maximum values are approximated by modifying addition and subtraction operations to maximize the value of numerators and minimize the value of denominators, within the bounds of parameter values. Many of the terms in (3) are of the form $1 \pm \Gamma e^{\pm j\beta l}$. At maximum or minimum, the exponential quantity becomes real and the term is then of the form $1 \pm \Gamma$. The mathematical manipulations required to find the maximum crosstalk is illustrated in [10] with an example. The maximum voltages at the victim loads can be found as a function of the aggressor electrical length and the coupling region electrical lengths with the piecewise expressions as given in (6)-(7).

$$V_{NE,\max} \approx \left| V_S \omega l_{21} (x_2 - x_1) \frac{1}{(Z_{01} + Z_S)} \frac{(1 + \Gamma_{NE})}{\left(1 - \Gamma_L \Gamma_S e^{-j2\beta l_1}\right)} \frac{\left(1 + \Gamma_L \Gamma_{FE} e^{-j2\beta(2x_0 + a)}\right)}{\left(1 - \Gamma_{NE} \Gamma_{FE} e^{-j2\beta l_2}\right)} \right| \tag{6a}$$

$$\text{for } a + b \le \frac{\lambda}{10}$$

$$V_{NE,\max} \approx \frac{|V_S|}{2} \frac{l_{21}}{l_{11}} \frac{Z_{01}}{|Z_{01} + Z_S|} \frac{|1 + \Gamma_{\mathrm{NE}}|}{\left(1 - |\Gamma_L| |\Gamma_S|\right)} \frac{\left(1 + |\Gamma_L| |\Gamma_{FE}|\right)}{\left(1 - |\Gamma_{NE}| |\Gamma_{FE}|\right)} \left| e^{j2\beta x_2} - e^{j2\beta x_1} \right| \tag{6b}$$

$$\text{for } a + b > \frac{\lambda}{10} \text{ and } x_2 - x_1 < \frac{\lambda}{4}$$

$$V_{NE,\max} \approx |V_S| \frac{l_{21}}{l_{11}} \frac{Z_{01}}{|Z_{01} + Z_S|} \frac{|1 + \Gamma_{\mathrm{NE}}|}{\left(1 - |\Gamma_L| |\Gamma_S|\right)} \frac{\left(1 + |\Gamma_L| |\Gamma_{FE}|\right)}{\left(1 - |\Gamma_{NE}| |\Gamma_{FE}|\right)} \tag{6c}$$

$$\text{for } x_2 - x_1 \ge \frac{\lambda}{4}$$

$$V_{FE,\max} \approx \left| V_S \omega l_{21} (x_2 - x_1) \frac{1}{(Z_{01} + Z_S)} \frac{\left(\Gamma_L + \Gamma_{NE} e^{j2\beta(2x_0 + a - l_2)}\right)}{\left(1 - \Gamma_L \Gamma_S e^{-j2\beta l_1}\right)} \frac{(1 + \Gamma_{FE})}{\left(1 - \Gamma_{NE} \Gamma_{FE} e^{-j2\beta l_2}\right)} \right| \tag{7a}$$

$$\text{for } a + b \le \frac{\lambda}{10}$$

$$V_{FE,\max} \approx \frac{|V_S|}{2} \frac{l_{21}}{l_{11}} \frac{Z_{01}}{|Z_{01} + Z_S|} \frac{\left(|\Gamma_L| + |\Gamma_{NE}|\right)}{\left(1 - |\Gamma_L| |\Gamma_S|\right)} \frac{|1 + \Gamma_{\mathrm{FE}}|}{\left(1 - |\Gamma_{NE}| |\Gamma_{FE}|\right)} \left| e^{j2\beta x_2} - e^{j2\beta x_1} \right| \tag{7b}$$

$$\text{for } a + b > \frac{\lambda}{10} \text{ and } x_2 - x_1 < \frac{\lambda}{4}$$

$$V_{FE,\max} \approx |V_S| \frac{l_{21}}{l_{11}} \frac{Z_{01}}{|Z_{01} + Z_S|} \frac{\left(|\Gamma_L| + |\Gamma_{NE}|\right)}{\left(1 - |\Gamma_L| |\Gamma_S|\right)} \frac{|1 + \Gamma_{\mathrm{FE}}|}{\left(1 - |\Gamma_{NE}| |\Gamma_{FE}|\right)} \tag{7c}$$

$$\text{for } x_2 - x_1 \ge \frac{\lambda}{4}$$

where,

$$x_0 = \frac{x_1 + x_2}{2}, \tag{8}$$

and λ is the wavelength of the signal in the propagating medium.

The first piecewise expressions for the near-end and far-end maximum voltages, (6a) and (7a), were derived from a formulation where the aggressor circuit was electrically small. This formulation was used instead of the electrically large formulation presented in (3) to provide better insight into the crosstalk response and to minimize the possibility of over-predicting the maximum crosstalk. The remaining piecewise expressions were derived from the electrically large aggressor circuit formulation in (3). The second piecewise expressions in (6b) and (7b) are given when the aggressor circuit is electrically large, but the coupling region is less than one quarter wavelength. The last piecewise expressions in (6c) and (7c) are evaluated when the coupling region is greater than or equal to one quarter wavelength and is a modification to (6b) and (7b). When the coupling region length is equal to or larger than one quarter wavelength, the worst case value of $\left|e^{j2\beta x_2} - e^{j2\beta x_1}\right|$ is two. This worst case condition occurs when the coupling region length is an odd multiple of one quarter wavelength. It should be noted that (6) and (7) apply to transmission lines that are lossless and in a homogeneous medium. Application of these equations to media that are not homogeneous, where (5) is not approximately satisfied, can result in significant errors. For inhomogeneous or lossy media the reader should refer to the equations in [10].

III. MAXIMUM CROSSTALK ESTIMATES FROM INFINITELY LONG TRANSMISSION LINES

A. Introduction

A similar estimate of the maximum crosstalk based on lossless, infinitely long transmission lines was developed in [8]. To simplify the derivation, [8] defines crosstalk as a ratio of maximum voltages or currents in the victim and aggressor transmission lines, rather than at the loads as is typically done [12]. The crosstalk formulation in [8] assumes a majority of coupling occurs over a portion of the victim circuit length where coupling is greatest. The theory in [8] further assumes:

1. The geometry is uniform where coupling occurs.
2. The medium is homogeneous.
3. The transmission lines are weakly coupled.
4. The transmission lines are lossless.

A single, lumped voltage source or current source in the victim circuit is suggested in [8] to describe the coupling from the aggressor circuit. This representation reduces the transmission line system in Fig. 1 to a single transmission line system with a lumped source as in Fig. 2.

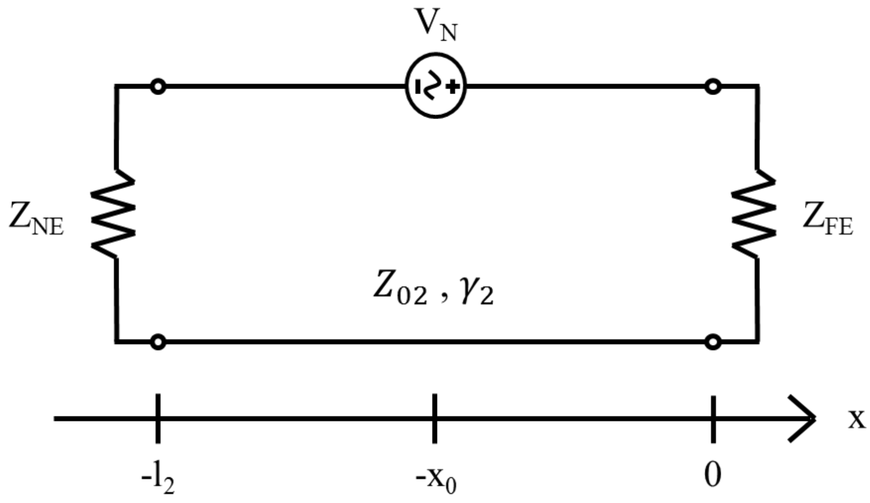

Fig. 2. Equivalent circuit model of weak inductive coupling to the victim circuit at a single location [8].

The ratio of the maximum voltage along the length of the victim transmission line to the maximum voltage in the aggressor transmission line was estimated in [8] by $V_{2,\max}/V_{1,\max} \approx l_{21}/l_{11}$ on intuitive grounds, based on the magnetic flux wrapping the aggressor and victim circuits. The worst case voltage induced at a specific location in the victim transmission line (assuming an infinite transmission line) would then be given by $|V_N| \approx V_{1,\max}(l_{21}/l_{11})$, where $V_{1,\max}$ denotes the maximum voltage along an infinitely long aggressor transmission line [8]. Using transmission line theory for the finite length transmission line in Fig. 2, the maximum voltage in the victim circuit can then be found as

$$V_{2,\max} \approx \frac{|V_N|}{2} \frac{\left(1+|\Gamma_{NE}|\right)\left(1+|\Gamma_{FE}|\right)}{\left(1-|\Gamma_{NE}||\Gamma_{FE}|\right)}. \tag{9}$$

Application of $|V_N| \approx V_{1,\max}\left(l_{21}/l_{11}\right)$ and the homogeneous medium relationship in (5) allows the maximum voltage in the victim circuit to then be represented by

$$V_{2,\max} \approx V_{1,\max} \frac{l_{21}}{l_{11}} \frac{\left(1+|\Gamma_{NE}|\right)\left(1+|\Gamma_{FE}|\right)}{2\left(1-|\Gamma_{NE}||\Gamma_{FE}|\right)}. \tag{10}$$

B. Mathematical Derivations

The ratio of the maximum voltages along the infinite transmission lines and the lumped voltage source V_N were developed in [8] from an intuitive basis. These quantities can be derived rigorously to show the validity and to better understand the limitations of the work in [8]. Consider two lossless, coupled transmission lines in a homogeneous medium, as shown in Fig. 1. The transmission lines are assumed to be infinite in length with a finite length coupling region. The voltage on the aggressor circuit can be written as

$$V_1(x) = V_S \frac{Z_{01}}{\left(Z_{01}+Z_S\right)} \frac{e^{-\gamma l_1}}{\left(1-\Gamma_L \Gamma_S e^{-2\gamma l_1}\right)} \left(e^{-\gamma(x-a)} + \Gamma_L e^{\gamma(x-a)}\right). \tag{11}$$

From (11), the maximum voltage along the aggressor circuit is

$$V_{1,\max} = \frac{1}{2}|V_S| \tag{12}$$

where all of the reflection coefficients are set equal to zero to satisfy the infinite transmission line length condition and where $\gamma = j\beta$ in the lossless case. The maximum voltage in the victim circuit is found as

$$V_{2,\max} = \max\{V_{2,mLHS}, V_{2,mSR}, V_{2,mRHS}\} \tag{13}$$

where, $V_{2,mLHS}$ is the maximum voltage in the victim circuit for $x < -x_2$, $V_{2,mSR}$ is the maximum voltage in the victim circuit for $-x_2 \le x \le -x_1$, and $V_{2,mRHS}$ is the maximum voltage in the victim circuit for $x > -x_1$. $V_{2,mLHS}$ and $V_{2,mRHS}$ are obtained from [10, eq. (18)] by taking the magnitude of the expression, applying the infinite transmission line condition, and applying the lossless transmission line condition. Similarly, $V_{2,mSR}$ is based on the total voltage response in the coupling region, which is found with the application of equations in [10, eq. (8), (10), (11), and (13)-(16)]. $V_{2,mSR}$ is found by taking the magnitude of the expression for the total voltage response, applying the infinite transmission line condition, and applying the lossless transmission line condition. The maximum voltage in the victim circuit is thus found to be

$$V_{2,mLHS} = \left| \frac{V_S}{4} \frac{e^{j\beta(a+x-l_1)}}{(Z_{01}+Z_S)} \frac{\omega}{\beta} (l_{21} + Z_{01}Z_{02}c_{21})\left(e^{j2\beta x_2} - e^{j2\beta x_1}\right) \right| \tag{14a}$$

$$\begin{aligned} V_{2,mSR} = & \left| -j \frac{V_S}{2} \frac{e^{-j\beta(-a+x+l_1)}}{(Z_{01}+Z_S)} \omega (l_{21} - Z_{01}Z_{02}c_{21})(x_2 + x) \right. \\ & \left. + \frac{V_S}{4} \frac{e^{j\beta(a+x-l_1)}}{(Z_{01}+Z_S)} \frac{\omega}{\beta} (l_{21} + Z_{01}Z_{02}c_{21})\left(e^{-j2\beta x} - e^{j2\beta x_1}\right) \right| \end{aligned} \tag{14b}$$

$$V_{2,mRHS} = \left| -j \frac{V_S}{2} \frac{e^{-j\beta(-a+x+l_1)}}{(Z_{01}+Z_S)} \omega (l_{21} - Z_{01}Z_{02}c_{21})(x_2 - x_1) \right| . \tag{14c}$$

To satisfy $\Gamma_S = 0$, $Z_S = Z_{01}$ in (14). The coupling region length must follow the relationship $x_2 = x_1 + n(\lambda/4)$, where n is a positive, odd integer for $V_{2,mLHS}$ to be maximum. Similarly, a location in the coupling region must be possible to satisfy $x = -x_1 - n(\lambda/4)$, where n is a positive, odd integer for $V_{2,mSR}$ to be maximum. Using the property where the propagation constant, $\gamma_1 = \gamma_2 = \gamma$, the phase velocity V_p in the victim or aggressor circuit can be written as $V_p = \sqrt{1/(l_{22}(c_{21} + c_{22}))}$. The characteristic impedances can be defined as $Z_{01} = l_{11} V_p$ and $Z_{02} = l_{22} V_p$. Assuming the transmission lines are in a homogeneous medium, (14) can be written as

$$V_{2,mLHS} = \frac{1}{2}\frac{l_{21}}{l_{11}}|V_S| = \frac{1}{2}\frac{c_{21}}{c_{21}+c_{22}}|V_S| \tag{15a}$$

$$V_{2,mSR} = V_{2,mLHS} = \frac{1}{2}\frac{l_{21}}{l_{11}}|V_S| = \frac{1}{2}\frac{c_{21}}{c_{21}+c_{22}}|V_S| \tag{15b}$$

$$V_{2,mRHS} = 0 \tag{15c}$$

where (5) was utilized for a homogeneous medium. Thus the maximum voltage in the victim circuit is

$$V_{2,\max} = \frac{1}{2}\frac{l_{21}}{l_{11}}|V_S| = \frac{1}{2}\frac{c_{21}}{c_{21}+c_{22}}|V_S| \tag{16}$$

and the ratio of the maximum voltages is

$$\frac{V_{2,\max}}{V_{1,\max}} = \frac{l_{21}}{l_{11}} = \frac{c_{21}}{c_{21}+c_{22}}, \tag{17}$$

as was found in [8] in an intuitive manner for coupled, infinite length, homogeneous, and lossless transmission lines.

The lumped voltage source V_N was also derived on intuitive grounds. This source was defined in [8] for finite length transmission lines using the relationship given in (17) and assuming infinitely long transmission lines (so that there would be a location at which this maximum coupling would occur). This voltage source can be derived more rigorously from the formulas presented in this paper and from [10] as follows. The victim circuit voltage for a lumped voltage source at a position $-x_0$ as in Fig. 2 for $x < -x_0$ and $x > -x_0$ is found from [10, eq. (10)-(11)] with $v(\xi) = V_N \delta(\xi + x_0)$. The voltages to the left and the right of the source can be written as,

$$V_{v,LHS}(x) = -\frac{V_{N,LHS}}{2}\frac{\left(1+\Gamma_{NE}e^{-2\gamma(l_2+x)}\right)\left(1-\Gamma_{FE}e^{-2\gamma x_0}\right)}{\left(1-\Gamma_{NE}\Gamma_{FE}e^{-2\gamma l_2}\right)e^{-\gamma(x+x_0)}} \tag{18a}$$

$$V_{v,RHS}(x) = \frac{V_{N,RHS}}{2}\frac{\left(1-\Gamma_{NE}e^{-2\gamma(l_2-x_0)}\right)\left(1+\Gamma_{FE}e^{2\gamma x}\right)}{\left(1-\Gamma_{NE}\Gamma_{FE}e^{-2\gamma l_2}\right)e^{\gamma(x+x_0)}} \tag{18b}$$

where, $V_{N,LHS}$ and $V_{N,RHS}$ are the lumped voltage sources in the victim transmission line that creates the victim responses in the $x < -x_0$ and $x > -x_0$ regions, respectively. The subscripts LHS and RHS indicate the position ranges $x < -x_0$ and $x > -x_0$ over which a variable is defined. The victim circuit voltage for a lumped current source at a position $-x_0$ for $x < -x_0$ and $x > -x_0$ can be found from [10, eq. (14)] where $i(\xi) = I_N \delta(\xi + x_0)$. The voltages to the left and the right of the source can be written as,

$$V_{i,LHS}(x) = \frac{I_{N,LHS}Z_{02}}{2}\frac{\left(1+\Gamma_{NE}e^{-2\gamma(l_2+x)}\right)\left(1+\Gamma_{FE}e^{-2\gamma x_0}\right)}{\left(1-\Gamma_{NE}\Gamma_{FE}e^{-2\gamma l_2}\right)e^{-\gamma(x+x_0)}} \tag{19a}$$

$$V_{i,RHS}(x) = \frac{I_{N,RHS}Z_{02}}{2}\frac{\left(1+\Gamma_{NE}e^{-2\gamma(l_2-x_0)}\right)\left(1+\Gamma_{FE}e^{2\gamma x}\right)}{\left(1-\Gamma_{NE}\Gamma_{FE}e^{-2\gamma l_2}\right)e^{\gamma(x+x_0)}} \tag{19b}$$

where, $I_{N,LHS}$ and $I_{N,RHS}$ is the lumped current source in the victim transmission line that creates the victim responses in the $x < -x_0$ and $x > -x_0$ regions, respectively. Comparing (18) and (19), an equivalent total lumped voltage source can be defined for each region as

$$V_{N,total:LHS} = V_{N,LHS} - \frac{I_{N,LHS}Z_{02}\left(1+\Gamma_{FE}e^{-2\gamma x_0}\right)}{1-\Gamma_{FE}e^{-2\gamma x_0}} \tag{20a}$$

$$V_{N,total:RHS} = V_{N,RHS} + \frac{I_{N,RHS}Z_{02}\left(1+\Gamma_{NE}e^{-2\gamma(l_2-x_0)}\right)}{1-\Gamma_{NE}e^{-2\gamma(l_2-x_0)}} \tag{20b}$$

where the total circuit voltage can be obtained by inserting (20a) for $V_{N,LHS}$ in (18a) and (20b) for $V_{N,RHS}$ in (18b). Mathematically equivalent lumped voltage and current sources can be found for an electrically large coupling region by equating equation forms. $V_{N,LHS}$

and $V_{N,RHS}$ are determined by equating $V_{2,v}(x)$ in [10, eq. (11)] with (18). Similarly, $I_{N,LHS}$ and $I_{N,RHS}$ are determined by equating $V_{2,i}(x)$ in [10, eq. (14)] with (19). If the transmission lines are lossless, the coupling region is $n(\lambda/4)$ in length where *n* is positive and odd in the worst case, and the transmission lines are in a homogeneous medium, then the magnitude of the maximum noise voltage can be determined from (20) as

$$\left|V_{N,\max LHS}\right| = \left| 2V_S \frac{l_{21}}{l_{11}} \frac{Z_{01}}{(Z_{01}+Z_S)} \frac{\left(1+\Gamma_L \Gamma_{FE} e^{-j2\beta(x_1+x_2+a)}\right)}{\left(1-\Gamma_{FE} e^{-j2\beta x_0}\right)\left(1-\Gamma_L \Gamma_S e^{-j2\beta l_1}\right)} e^{j\beta(a-x_0-l_1+2x_1)} \right| \tag{21a}$$

$$\left|V_{N,\max RHS}\right| = \left| -2V_S \frac{l_{21}}{l_{11}} \frac{Z_{01}}{(Z_{01}+Z_S)} \frac{\left(\Gamma_L e^{-j2\beta(x_1+x_2+a)} + \Gamma_{NE} e^{-j2\beta l_2}\right)}{\left(1-\Gamma_{NE} e^{-j2\beta(l_2-x_0)}\right)\left(1-\Gamma_L \Gamma_S e^{-j2\beta l_1}\right)} e^{-j\beta(-a-x_0+l_1-2x_1)} \right|. \tag{21b}$$

If the transmission lines are considered to be infinite in length, which forces the reflection coefficients to zero, then (21) reduces to

$$\left|V_{N,\max LHS}\right| = \left|V_S\right| \frac{l_{21}}{l_{11}} \tag{22a}$$

$$\left|V_{N,\max RHS}\right| = 0 \cdot \tag{22b}$$

Equation (22a) shows that $\left|V_N\right| \approx 2V_{1,\max}(l_{21}/l_{11})$ where $V_{1,\max}$ is given by (12) rather than $\left|V_N\right| \approx V_{1,\max}(l_{21}/l_{11})$ as suggested in [8]. The result of (22a) is, however, consistent with the defined lumped voltage source given in [9].

IV. MAXIMUM CROSSTALK ESTIMATE COMPARISON AND VALIDATION

The previous derivations show that while the equations in [8] can be found rigorously, these equations mix boundary conditions between infinite and finite transmission lines in the sense that (22a) is applied to finite length transmission lines when an infinite transmission line length assumption was used. This mix of boundary conditions is not strictly mathematically correct, however, it can be shown that the maximum crosstalk estimate in [8] does provide some useful results under the right conditions. Crosstalk measurements were performed in [8] at the victim circuit loads where at some frequencies it was assumed that the maximum victim voltage may occur at one of the loads. Using (22a) in (9) the maximum voltage along the length of the victim circuit is given by

$$V_{2,\max} \approx \frac{|V_S|}{2}\frac{l_{21}}{l_{11}}\frac{(1+|\Gamma_{NE}|)(1+|\Gamma_{FE}|)}{(1-|\Gamma_{NE}||\Gamma_{FE}|)} \tag{23}$$

where the measurements in [8] were used to validate (23). In all of these measurements $|\Gamma_S| \approx 0$ and $|\Gamma_L| \approx 1$. Under these conditions the mathematically rigorous maximum crosstalk estimates based on an integral formulation can be reduced to a similar form as (23). Since [8] assumes the coupling region length is maximally resonant in the worst case, a direct comparison may only be made among (6c), (7c), and (23). For $|\Gamma_S| = 0$ and $|\Gamma_L| = 1$, (6c) and (7c) reduce to

$$V_{NE,\max} \approx \frac{|V_S|}{2}\frac{l_{21}}{l_{11}}\frac{|1+\Gamma_{\mathrm{NE}}|(1+|\Gamma_{FE}|)}{(1-|\Gamma_{NE}||\Gamma_{FE}|)} \tag{24a}$$

$$V_{FE,\max} \approx \frac{|V_S|}{2}\frac{l_{21}}{l_{11}}\frac{(1+|\Gamma_{NE}|)|1+\Gamma_{\mathrm{FE}}|}{(1-|\Gamma_{NE}||\Gamma_{FE}|)}\,. \tag{24b}$$

The choice of $|1+\Gamma_{NE}|$ in (6c) and $|1+\Gamma_{FE}|$ in (7c) rather than $1+|\Gamma_{NE}|$ and $1+|\Gamma_{FE}|$ was made to reduce the error in the estimates when the near-end and far-end reflection coefficients are largely negative and real (e.g., a short termination). For small reflection coefficients, real and positive reflection coefficients, and complex reflection coefficients that are largely positive and real (e.g., matched terminations and large resistive terminations relative to the transmission line characteristic impedance), $|1+\Gamma| \approx 1+|\Gamma|$. Case 1 – Case 6 in [8] have terminations that satisfy $|1+\Gamma_{NE}| \approx 1+|\Gamma_{NE}|$ or $|1+\Gamma_{FE}| \approx 1+|\Gamma_{FE}|$ where at least one of the equations in (24) can be reduced to (23). This reduction provides additional validation for the maximum crosstalk estimates presented in [8] and [10] because the estimates are equivalent under the right assumptions.

A series of measurements and simulations were performed to evaluate the effectiveness of (6)-(7) and (23) in estimating the maximum crosstalk. The estimates were first evaluated for a two wire cable bundle simulation where per-unit-length parameters were extracted from a numerical cross-sectional analysis tool [13]. In this case the cable bundle was modeled above an infinitely large return plane where the signal wires were solid conductors 1.016 mm (40 mils) in diameter, were placed 14.986 mm (590 mils) above the return plane, and were separated by 59.944 mm (2360 mils). The wires and return plane were modeled as perfect electric conductors in a vacuum. The signal wires were weakly coupled and had a single-ended characteristic impedance of 250 Ω. Per-unit-length parameters from this cross-sectional analysis were: $l_{11} = l_{22} = 831.5\,\mathrm{nH}$, $l_{12} = l_{21} = 25.0\,\mathrm{nH}$, $c_{11} = c_{22} = 12.9\,\mathrm{pF}$, $c_{12} = c_{21} = 0.4\,\mathrm{pF}$. The cable bundle was modeled with the following dimensions (see Fig. 1): $b = 8.75\,\mathrm{m}$, $l_2 = 7.5\,\mathrm{m}$, $x_2 = 5.625\,\mathrm{m}$, $x_1 = 1.875\,\mathrm{m}$, $a = 1.25\,\mathrm{m}$. A variety of loads were simulated in the aggressor and victim circuits. Some of these test cases are given in Table I.

TABLE I. CABLE BUNDLE SIMULATION LOADING CONDITIONS

Case #	Z_S	Z_L	Z_{NE}	Z_{FE}
Case 1	250 Ω	1 MΩ (open)	250 Ω	750 Ω
Case 2	250 Ω	0 Ω (short)	750 Ω	250 Ω
Case 3	250 Ω	250 Ω	250 Ω	0 Ω (short)
Case 4	250 Ω	250 Ω	250 Ω	1 MΩ (open)
Case 5	0 Ω (short)	5 kΩ	250 Ω	250 Ω
Case 6	200 Ω	0 Ω	750 Ω‖47 pF	100 Ω + 1μH

The exact victim circuit load voltages were compared with the maximum crosstalk estimates proposed in (6)-(7) and (23). The victim circuit voltages were generated over frequency with a simulation that applied the finite difference method to the weak coupling transmission line equations. The results for the Case 1 – Case 6 simulations in Table I are shown in Fig. 3 – Fig. 7. In Fig. 3 – Fig. 5, the maximum crosstalk estimates (6c), (7c), and (23) were plotted along with the victim load voltages.

Fig. 3 shows the Case 1 and Case 2 near-end maximum crosstalk estimates where (6c), (7c), and (23) are equivalent because $|\Gamma_S| = 0$ and $|\Gamma_L| = 1$. Both methods predicted the maximum crosstalk well. Fig. 4 – Fig. 5 illustrate how moderate to severe errors in the maximum crosstalk estimation may occur when both the conditions, $|\Gamma_S| = 0$ and $|\Gamma_L| = 1$, are not satisfied as in the Case 3 – Case 5 simulations. A near-end maximum crosstalk estimate is shown in Fig. 4 and a far-end maximum crosstalk estimate is shown in Fig. 5. The difference between maximum crosstalk estimates in Fig. 4 and Fig. 5 are 6 dB and 26 dB, respectively. Fig. 6 – Fig. 7 show the near-end and far-end maximum crosstalk estimates using (6) and (7) for simulation Case 6. It can be seen that the maximum crosstalk estimate in both (6) and (7) perform better than (23) for the general case.

Measurements were also performed on an eight layer printed circuit board (PCB) with two coupled stripline traces in layer five of the PCB reported in [14]-[16] to validate the proposed estimates. A picture of the measurement setup is shown in Fig. 8. The PCB was fabricated from Nelco N4000-6 FR4 substrates with $\varepsilon_r = 4.1$ and $\tan\delta = 0.017$. The measured symmetric stripline structure had a total dielectric height of 914.40 μm

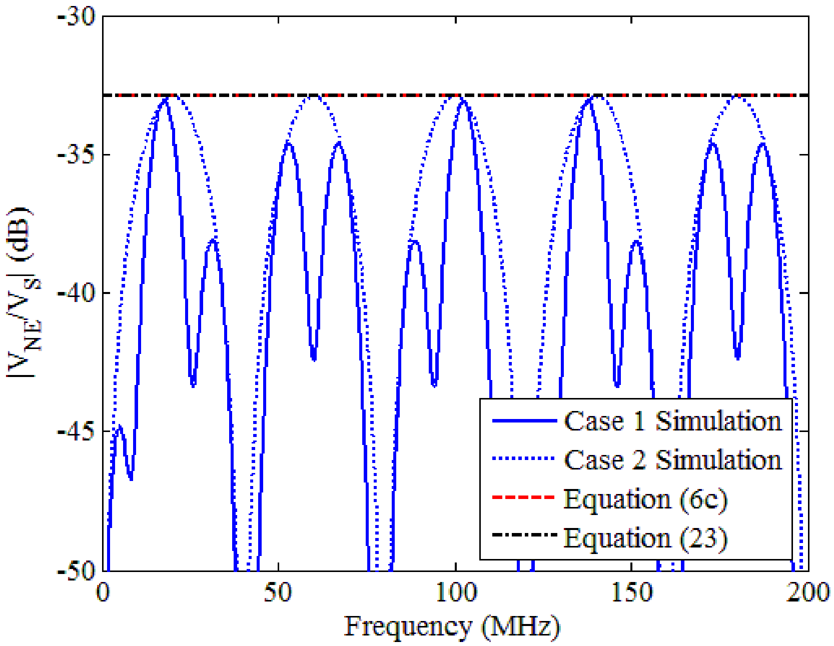

Fig. 3. Cable bundle crosstalk example for the Case 1 and Case 2 loading conditions in Table I. The near-end maximum crosstalk estimates (6c) and (23) are equivalent under these loading conditions.

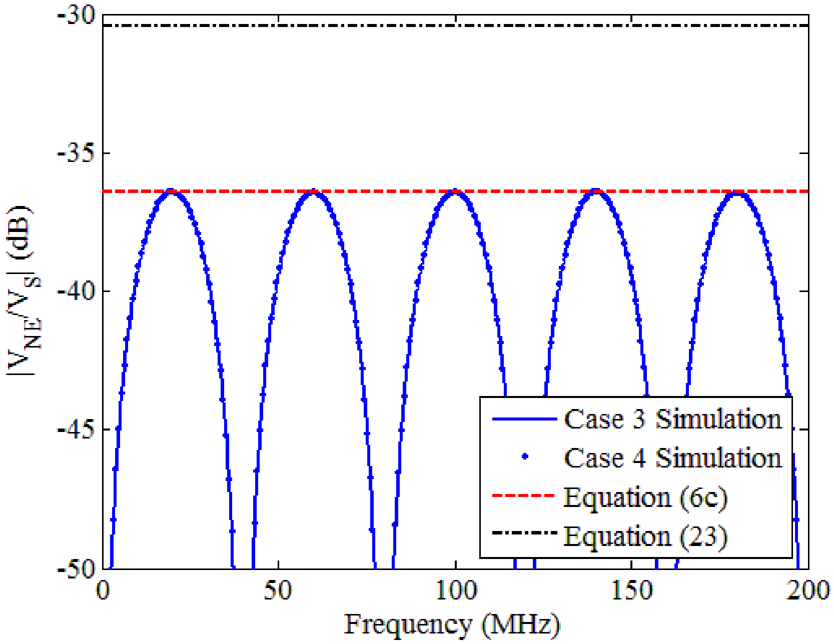

Fig. 4. Cable bundle crosstalk example for the Case 3 and Case 4 loading conditions. The near-end maximum crosstalk estimates (6c) and (23) differ by 6 dB under these loading conditions.

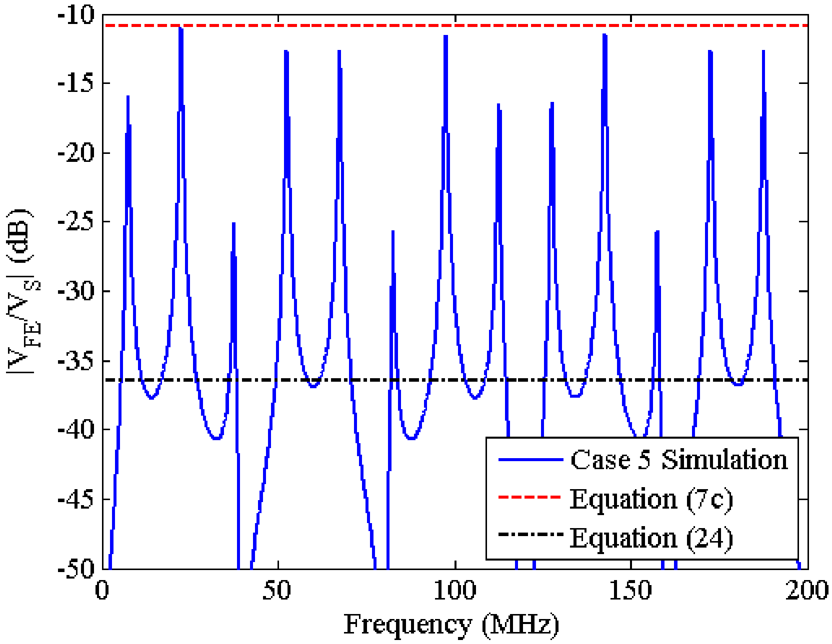

Fig. 5. Cable bundle crosstalk example for the Case 5 loading conditions in Table I. The far-end maximum crosstalk estimates (7c) and (23) differ by 26 dB under these loading conditions.

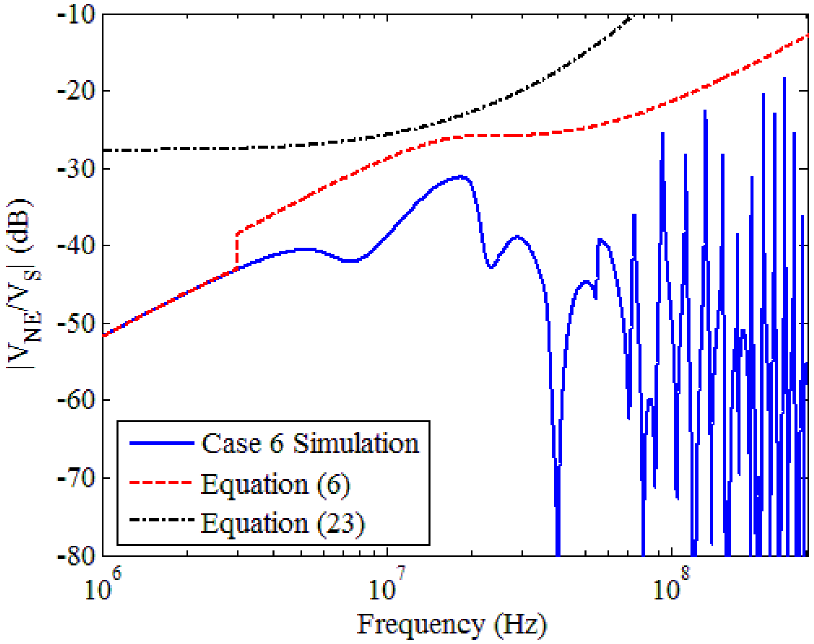

Fig. 6. Cable bundle crosstalk example for the Case 6 loading conditions. The near-end maximum crosstalk estimates are predicted from the full piecewise expression in (6) and (23).

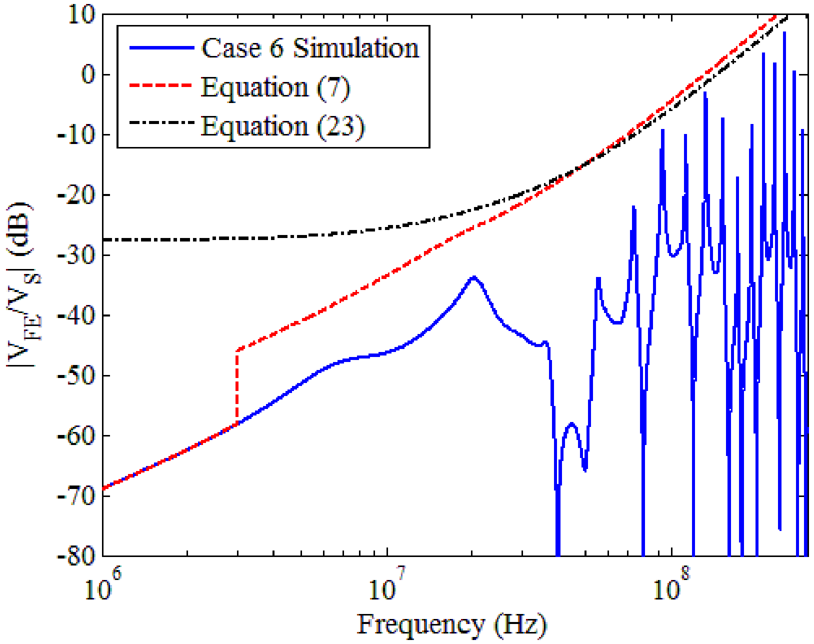

Fig. 7. Cable bundle crosstalk example for the Case 6 loading conditions in Table I. The far-end maximum crosstalk estimates are predicted from the full piecewise expression in (7) and (23).

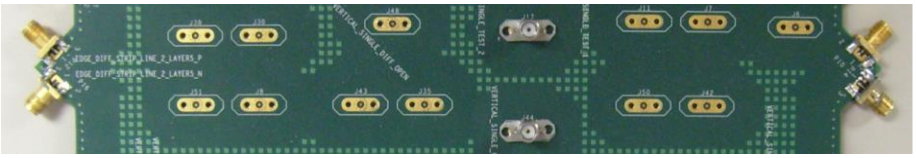

Fig. 8. Coupled stripline measurement setup used to validate the maximum crosstalk equations.

(36 mils) between the reference planes and a 30.48 μm (1.2 mil) copper thickness for the signal traces and reference planes. The trace widths were 347.98 μm (13.7 mils), and the traces were separated by 419.10 μm (16.5 mils) in the coupling region. The circuit dimensions were as follows (see Fig. 1): $b = 241.51\,\text{mm}\,(9508.3\,\text{mils})$, $l_2 = 241.51\,\text{mm}\,(9508.3\,\text{mils})$, $x_2 = 234.19\,\text{mm}\,(9220.1\,\text{mils})$, $x_1 = 7.32\,\text{mm}\,(288.3\,\text{mils})$, and $a = 0\,\text{mm}\,(0\,\text{mils})$. Per-unit-length parameters for the measurement were extracted from the signal integrity tool Hyperlynx based on the PCB stack-up information. These parameters were then used in *w*-element simulation models in Synopsys Hspice to simulate the crosstalk.

Crosstalk measurements were performed using a two port network analyzer. End-launch SMA connectors were used to interface with the stripline traces to mitigate connector parasitic effects. Notches were cut into the PCB at the board edges to facilitate the end-launch SMA connections. The loads at the two free ports in the measurements were varied to study the impacts on the near-end and far-end crosstalk as a function of load impedance. Port terminations tested included matched loads (50 Ω), shorts (8.8 nH), and opens (2.5 pF). A series 275 pH inductance was used as the SMA connector parasitic model. Some of the test cases evaluated are given in Table II.

TABLE II. PCB MEASUREMENT LOADING CONDITIONS

Case #	Z_S	Z_L	Z_{NE}	Z_{FE}
Case 1	50 Ω	8.8 nH (short)	50 Ω	8.8 nH (short)
Case 2	50 Ω	2.5 pF (open)	2.5 pF (open)	50 Ω
Case 3	50 Ω	50 Ω	50 Ω	8.8 nH (short)
Case 4	50 Ω	50 Ω	8.8 nH (short)	50 Ω

Comparisons of the estimates proposed in (6)-(7), (23), and (19)-(20) in [10] for the test cases in Table II, are shown in Fig. 9 – Fig. 12. The simulated and measured crosstalk was plotted in addition to the maximum crosstalk estimates. The near-end crosstalk was measured in Case 1 and Case 3, whereas the far-end crosstalk was measured in Case 2 and Case 4. Fig. 9 – Fig. 10 show cases where the maximum crosstalk estimates in (6c), (7c), and (23) are equivalent because $\left|\Gamma_S\right| = 0$ and $\left|\Gamma_L\right| = 1$. Fig. 11 – Fig. 12 show that errors in the maximum crosstalk estimation in (23) may occur when both conditions, $\left|\Gamma_S\right| = 0$ and $\left|\Gamma_L\right| = 1$, are not satisfied. As Fig. 4 – Fig. 7 and Fig. 11 – Fig. 12 show, an underestimation or overestimation of the maximum crosstalk by (23) is possible when $\left|\Gamma_S\right| \neq 0$ and $\left|\Gamma_L\right| \neq 1$. Above a few GHz, the lossless estimates in (6c) and (7c) significantly over-predict the maximum crosstalk. This is mostly caused by transmission line losses which are only accounted in (19c) and (20c) in [10] and are prevalent in the PCB above a few GHz. A divergence between the simulated and measured results above a few GHz is also seen in Fig. 9 – Fig. 12. This divergence is likely due to inadequate connector parasitic and per-unit-length parameter models. Despite the simulated and measured results divergence, these figures illustrate maximum crosstalk estimates can be reasonably formulated to relatively high frequencies when transmission line characteristics are not perfectly known.

Although (23) has been validated in [8] and in this paper through analysis, measurements, and simulations, the estimates in (6)-(7) have several features which make them more attractive for lossless and homogeneous transmission lines. Equation (23) is less general than (6)-(7), where assumptions are made for the reflection coefficients of the aggressor circuit that may not occur in practice. Assumptions are also made for the victim circuit terminations when measuring the maximum crosstalk at the victim loads. Equation (23) is based on the crosstalk definition where crosstalk is defined either as a ratio of maximum voltages or currents in the victim and aggressor circuits. A crosstalk definition using the source voltage of the aggressor and victim load voltages as in (6)-(7) is believed to be more useful in general. Another limitation of (23) is it greatly over-predicts the maximum crosstalk when the coupling region length in Fig. 1 is much less than one quarter wavelength as shown in Fig. 6 – Fig. 7 and Fig. 11 – Fig. 12. Equations

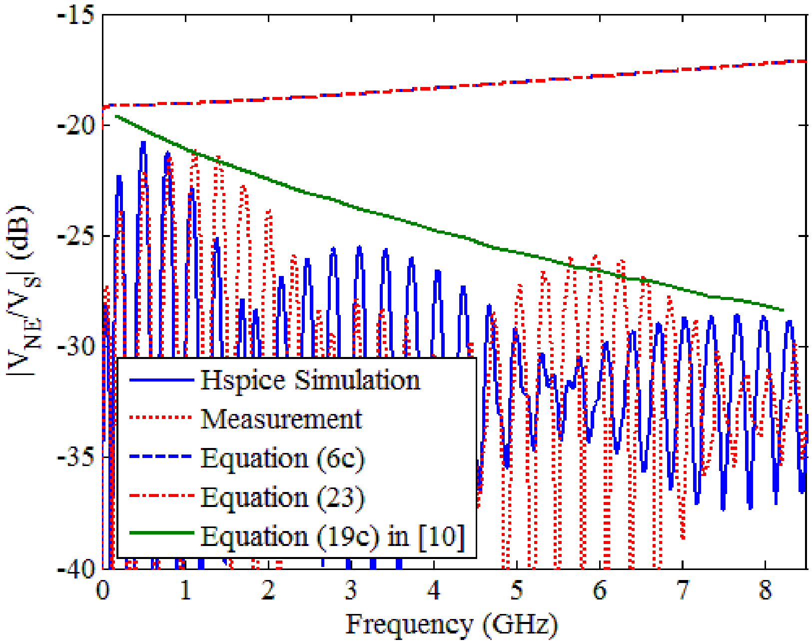

Fig. 9. Coupled stripline crosstalk example for the Case 1 loading conditions in Table II. The near-end maximum crosstalk estimates (6c) and (23) are equivalent under these loading conditions.

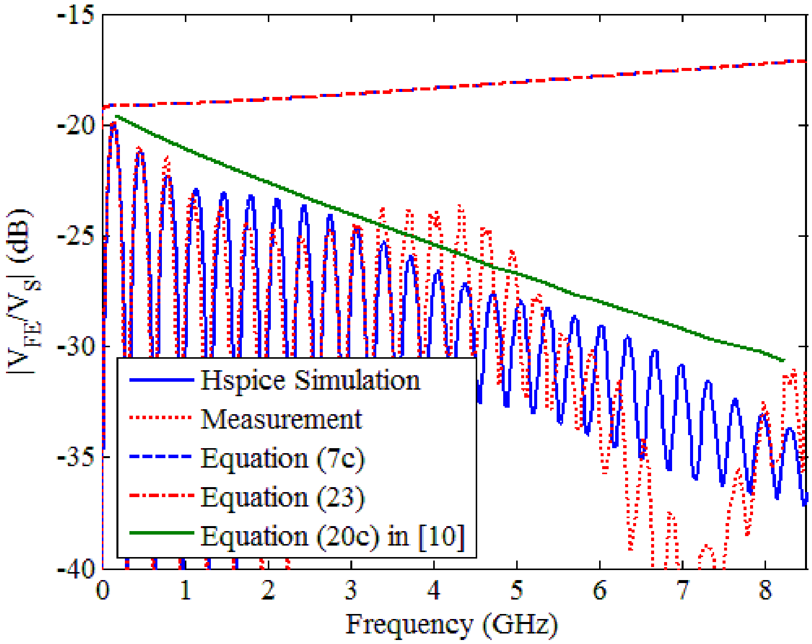

Fig. 10. Coupled stripline crosstalk example for the Case 2 loading conditions in Table II. The far-end maximum crosstalk estimates (7c) and (23) are equivalent under these loading conditions.

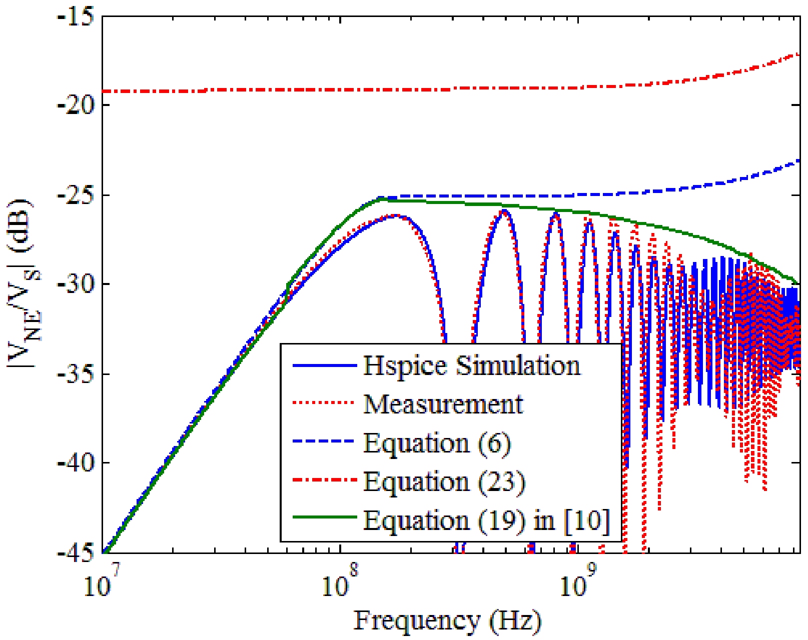

Fig. 11. Coupled stripline crosstalk example for the Case 3 loading conditions in Table II. The near-end maximum crosstalk estimates are predicted from the full piecewise expression in (6) and (23). The near-end maximum crosstalk estimates (6c) and (23) differ by 6 dB under these loading conditions.

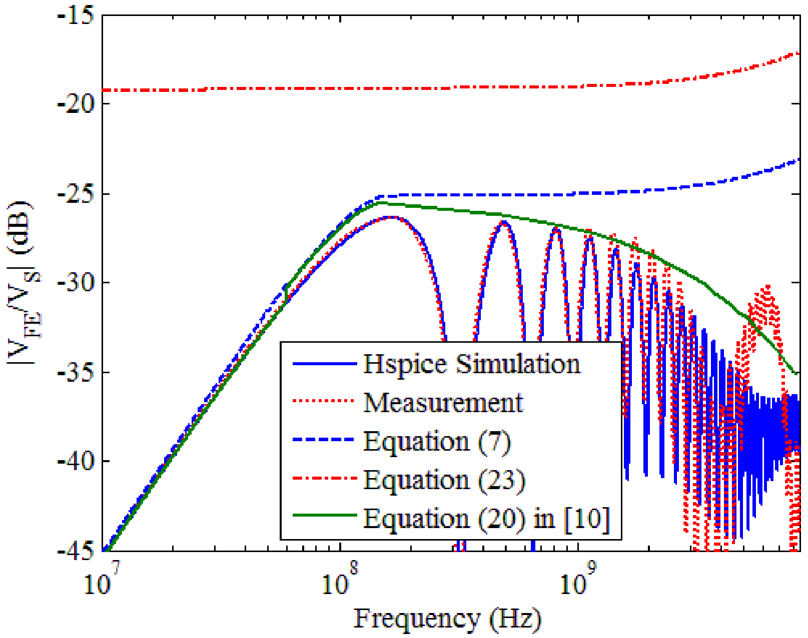

Fig. 12. Coupled stripline crosstalk example for the Case 4 loading conditions in Table II. The far-end maximum crosstalk estimates are predicted from the full piecewise expression in (7) and (23). The far-end maximum crosstalk estimates (7c) and (23) differ by 6 dB under these loading conditions.

(6)-(7) extend the maximum crosstalk estimates as a function of the aggressor circuit and coupling region lengths to facilitate less maximum crosstalk estimate over-prediction. If information is not available about the coupling region length, which, could be the case in a practical measurement, (6c) and (7c) may be used to estimate the maximum crosstalk over all frequencies. The main advantage of (23) is its simplicity, which may aid understanding and analysis.

V. CONCLUSION

Equations for estimating the maximum crosstalk in the frequency domain and in a three conductor, lossless, and homogeneous transmission line have been presented based on an integral formulation. These formulas are based on the weak coupling assumption where the transmission line system has a single coupling region with a uniform cross-section. The newly presented formulas can model the maximum crosstalk where the transmission lines may have unique and arbitrary lengths. Derivations on another maximum crosstalk estimate for finite length transmission lines based on a relationship for infinitely long transmission lines were also presented. These derivations illustrate that the previously published estimate, though relatively simple to understand and shown to predict the maximum crosstalk well, mixes boundary conditions between infinite and finite transmission lines which is not strictly mathematically correct. Despite the mixing of boundary conditions, the previous maximum crosstalk estimate is demonstrated to be equivalent to the integral formulation based estimate under some restrictive conditions. These conditions may not occur in a practical setup making the previous formulation more prone to errors. The integral formulation based maximum crosstalk estimates were shown to be more robust because they can estimate the maximum crosstalk with fewer and less restrictive assumptions. Future work may include estimation of maximum crosstalk for transmission lines without the weak coupling assumption, for transmission lines with non-uniform cross-sections, and for systems containing more than two transmission lines.

REFERENCES

[1] A. Tripathi and V. K. Tripathi, "A configuration-oriented SPICE model for multiconductor transmission lines in an inhomogeneous medium," *IEEE Trans. Microw. Theory Techn.*, vol. 46, no. 12, pp. 1997-2005, Dec. 1998.

[2] S. Sercu and L. Martens, "High-frequency circuit modeling of large pin count packages," *IEEE Trans. Microw. Theory Techn.*, vol. 45, no. 10, pp. 1897-1904, Oct. 1997.

[3] D. E. Bockelman and W. R. Eisenstadt, "Direct measurement of crosstalk between integrated differential circuits," *IEEE Trans. Microw. Theory Techn.*, vol. 48, no. 8, pp. 1410-1413, Aug. 2000.

[4] R. H. Voelker, "Transposing conductors in signal buses to reduce nearest-neighbor crosstalk," *IEEE Trans. Microw. Theory Techn.*, vol. 43, no. 5, pp. 1095-1099, May 1995.

[5] J. Bernal, F. Mesa, and D. R. Jackson, "Crosstalk between two microstrip lines excited by a gap voltage source," *IEEE Trans. Microw. Theory Techn.*, vol. 52, no. 8, pp. 1770-1780, Aug. 2004.

[6] A. El-Zein and S. Chowdhury, "An analytical method for finding the maximum crosstalk in lossless-coupled transmission lines," in *Dig. Tech. Papers 1992 IEEE/ACM Int. Conf. Computer-Aided Design*, Santa Clara, CA, pp. 443-448.

[7] A. El-Zein and S. Chowdhury, "Maximum crosstalk in a transmission line system with linear time-invariant networks," in *Proc. 1993 Int. Symp. Circuits and Systems*, Chicago, IL, pp. 2295-2298.

[8] X. Dong, H. Weng, D. G. Beetner, and T. H. Hubing, "Approximation of worst case crosstalk at high frequencies," *IEEE Trans. Electromagn. Compat.*, vol. 53, no. 1, pp. 202-208, Feb. 2011.

[9] X. Dong, "Estimation, modeling and identification of electromagnetic crosstalk and emissions in automotive and integrated circuit applications," Ph.D. dissertation, Dept. Elect. Eng., Univ. Missouri-Rolla, Rolla, 2005.

[10] M. S. Halligan and D. G. Beetner, "Maximum crosstalk estimation in weakly coupled transmission lines," *IEEE Trans. Electromagn. Compat.*, vol. 56, no. 3, pp. 736-744, June 2014.

[11] C. R. Paul, *Analysis of Multiconductor Transmission Lines*, 2nd ed. Hoboken, NJ: Wiley, 2008, ch 3, pp. 89-109.

[12] C. R. Paul, "Crosstalk," in *Introduction to Electromagnetic Compatibility*, 2nd ed. Hoboken, NJ: Wiley, 2006, ch 9, pp.559-711.

[13] Fast Electromagnetic Analysis Suite (FEMAS). [Online]. Available: http://www.ems-plus.com/FEMAS_main.html

[14] J. Zhang, J. L. Drewniak, D. J. Pommerenke, and Z. Yang, "Influence of an extended stub at connector ports on signal launches and TRL de-embedding," in *Proc. IEEE Int. Symp. Electromagn. Compat.*, Portland, OR, Aug. 2006, pp. 172-177.

[15] J. Zhang, "Characterization and modeling for multi-gigabit signaling," Ph.D. dissertation, Dept. Elect. Eng., Univ. Missouri-Rolla, Rolla, 2007.

[16] J. Zhang, J. L. Drewniak, D. J. Pommerenke, M. Y. Koledintseva, R. E. DuBroff, W. Cheng, Z. Yang, Q. B. Chen, and A. Orlandi, "Causal RLGC(*f*) models for transmission lines from measured *S*-parameters," *IEEE Trans. Electromagn. Compat.*, vol. 52, no. 1, pp. 189-198, Feb. 2010.

III. Electromagnetic Radiation Resulting From PCB/High-Density Connector Interfaces

Bruce Archambeault, *Fellow, IEEE*, Sam Connor, *Senior Member, IEEE*, Matthew S. Halligan, James L. Drewniak, *Fellow, IEEE*, and Albert E. Ruehli, *Life Fellow, IEEE*

Abstract—Professor Clayton Paul made many contributions to the field of electromagnetic compatibility as a researcher, teacher, and mentor. Among these contributions, he provided a seminal push in characterizing, understanding, and quantifying the coupling and radiation physics of electromagnetic interference (EMI). An overview of these original contributions that were driven by industry problems and needs is given here. His work emphasized physics and formulation in order to provide quantitative solutions and design directions. These ideas are applied to a current industry challenge in understanding and quantifying EMI that results at the interface between high-speed, high-density connectors and printed circuit boards.

Index Terms—Antenna mode, common mode, electromagnetic radiation, printed circuit board (PCB) connectors.

I. INTRODUCTION

Unintentional radiation is of concern in the design of electronics to avoid interference with other equipment and to meet regulatory requirements. The quote on the dedication page of Professor Clayton Paul's well-known book *Introduction to Electromagnetic Compatibility*, *"For every difficult problem there is always a simple answer and most of them are wrong,"* is a suitable reflection on the challenges in understanding and quantifying electromagnetic interference (EMI) from high-speed digital electronics [1]. Radiated EMI can be broken down into a noise source, radiating structure, and a coupling path. The noise source and radiating structure, i.e., cables or seams, penetrations and openings in enclosures are straightforward to identify in any given product application. However, the coupling path will often be subtle and complex, and comprises the parasitic path in the layout – IC, package, printed circuit board (PCB), enclosure, cabling, for coupling currents and fields to unintentional radiators. The physics of the EMI coupling path when the coupling region is electrically small is based on current continuity and conservation of charge. Ott noted that "…a signal ground is a low-impedance (hopefully) path for current to return to the source…" [2]. (To allow for magnetic-field coupling to a loop with no source, a corollary is that current must flow in a loop.) For the EMI coupling path, the currents are unintentional, but current continuity and conservation of charge still apply, and these currents must flow in a loop as well. The unintentional current paths are comprised of both conduction currents, which are carried by electrons, and, displacement currents, which are carried by a time-changing electric-flux density.

A well-developed knowledge of unintentional radiation was incomplete into the 1980s. The powerful numerical electromagnetic (EM) modeling capabilities as well as easy-to-use network and spectrum analyzers that are available today for discovering and identifying the EMI coupling path through modeling, or two-port transfer function methods did not exist. Diagramming an EMI problem was typically a combination of one or more "liver-shape" objects, a line to represent the cable and a (+) and (–) across somewhere identified as the "common-mode" source. These sketches can look more like the beginning of a Far Side cartoon than a discussion of physics and engineering. The current on the cable was referred to as "common-mode" current, and there may be no indication of a complete current path or the current return for these "common-mode" currents.

Professor Paul's formal graduate education was in the controls area, and in the late 1980s, he brought the habits of the area for mathematical formulation, rigor, and logic, together with his knowledge of electromagnetic physics, to provide a seminal push for developing a better understanding and quantifying unintentional radiation in electronics. He had already made significant contributions to crosstalk in cable assemblies and was an IEEE Fellow (1987) "*for contributions to the understanding and solution of crosstalk problems in cable assemblies*." Professor Paul's contributions toward understanding and quantifying EMI are overviewed here. Only the work and ideas with colleagues and students relevant to the EMI area are articulated. A comprehensive history or literature review of the subject is not intended.

Early 8-bit microprocessors produced in 1974 and 1975 that provided the spark for the PC conflagration had nominal clock rates of 1-2 MHz. At these frequencies, unintentional radiation was dominated by cables exiting from the electronics [3], and these were ineffective radiators, since they were electrically very short. At low-megahertz clock rates, managing unintentional radiation was often a matter of shielding and filtering at the connector/cable interface. The details of the electromagnetic physics of the coupling between the noise source in the electrical/electronic design and the radiating cable were not important as long as the specifications could be met with straightforward mitigation approaches of "grounding," shielding, and filtering. In the mid-1980s though, the pressure for integrating electromagnetic compatibility (EMC) into the product design from the beginning began to increase as design cycles decreased, and cost pressures and design densities increased. EMI solutions implemented at the end of the design cycle resulted in product delays, as well as added cost. The need for eliminating the trial-and-error process of EMC retrofits to meet EMI compliance was growing. However, knowledge of the EMI coupling physics that could be related directly and quantitatively to the circuit layout was in general lacking.

Professor Paul's published work in EMI focused on both efforts to make quantitative calculations as well as to understand and demonstrate the underlying physics experimentally. He observed in an early paper that "…given two printed circuit boards which have identical function and components but different land patterns, the board having the lower levels of ground drop will also have lower levels of radiated emissions" [4]. He proceeded in this paper to develop a lumped element model to quantify the EMI coupling path resulting from nonzero impedance of the current return using Ruehli's concept of partial inductance [5]. A sketch, reproduced in Fig. 1 from a subsequent paper clearly identifies the physics associated with this coupling path as resulting from two parallel current paths, one for the intended return current and the other for the radiating current on the cable [6]. Professor Paul cites, "…the "return path" for these common-mode currents is via displacement current …" and represents the displacement current that is due to a time-changing electric flux density as a capacitor in his sketch [6], [7]. The L_{ground} is calculated from partial inductance concepts in [4], and in the PCB layout is the inductance of the conductor comprising the intended return path for the intentional

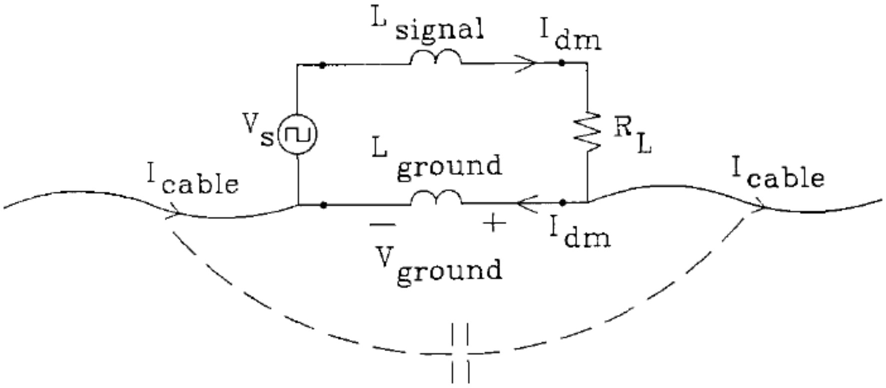

Fig. 1. Original sketch from [6] identifying the physics associated with illumination and EMI from cables as a result of nonzero impedance (inductance) in a signal return conductor.

signal current I_{DM}. For this coupling path, the unintentional currents on the cable result from a low impedance electrical connection between the signal-return conductors of the intended circuit, and extended conductors in the cable connected to the traces or area fills on the PCB. In those days of single- and double-sided PCBs, the signal current return path would have been routed on traces or irregular area fills and denoted as “GND” or ground on the circuit schematic. The currents going off the PCB in a cable, power and signal currents, would have a current return in the cable that would be attached to the “GND” of the PCB. This extended conductor comprised the antenna for the unintentional radiation. In Fig. 1, the intended signal return current is also labeled as I_{DM}, but enforcing Kirchhoff’s current law (KCL) at the node connecting R_L, the cable signal return conductor, and the circuit signal return conductor on the PCB GND is actually $I_{DM} - I_{cable}$. Paul notes in another paper that KCL applies, and, hence, includes the radiating current on the cable [7]. In that paper, it was demonstrated that $I_{DM} >> I_{cable}$, and the current on the reference structure shown in Fig. 1 is approximated as I_{DM}. Fig. 1 and [6] from which it is extracted also reflect Paul’s close collaborations with industry and habit to work toward applying research outcomes to practical design. In [6], where the conductor for the signal return current is electrically small, the voltage $V_{ground} \approx j\omega L_{ground} I_{DM}$ can be calculated and used as a source in a dipole antenna model for approximate EMI calculations, and L_{ground} used directly for comparison between design layouts for the PCB signal return.

Paul demonstrated “that predictions of radiated emissions based solely on differential-mode (DM) [transmission-line (TL)] currents will generally bear no resemblance to measured levels of radiated emissions…” rather that the “…common-mode (antenna) currents can be the dominant radiation mechanism from lands on PCB’s…” though the common-mode antenna currents can be orders of magnitude smaller than the signal DM TL currents [7]. In these statements, he uses language common to EMI engineers denoting the radiating currents as “common-mode” and the signal currents as “differential mode,” but was also careful to identify the physics that evokes an analytical model of a folded dipole antenna [8], both in language and in the diagram in [7, Fig. 1] by identifying the signal currents as (non-radiating) TL currents and the radiating currents as antenna currents.

A series of papers by Professor Paul, colleagues, and students in the early 1990s focused on the relationship between asymmetry and imbalance in the geometry of a PCB layout, as well as interconnect cables and radiated emissions [9]-[13]. The work was a careful theoretical assessment addressing imbalances in the source and load locations, as well as in the layout geometry itself [9]-[12]. The source, load, and layout geometry were divided into a symmetric portion, a symmetric mode model (SMM), and a remaining portion, an asymmetric mode model (AMM) that included all the asymmetries and imbalances, which when put together using superposition would produce the same electromagnetic field. Hardin and Paul [10] observed from the particular geometry reproduced in Fig. 2 that they considered experimentally and numerically over the frequency range 30-200 MHz “…that the AMM is the dominant cause of emissions above 80 MHz (by as much as 20 dB)…” and “that common-mode or asymmetrical currents on transmission line structures are often the dominant contributors to the total radiated emissions of a structure. The symmetric or differential-mode currents on these transmission line structures are often not the dominant contributor to the total radiated emissions of the structure….” The layout and routing of the asymmetric structure will include portions or all of the intended signal path but will also include unintentional current on extended reference conductors as discussed above, or conductors in proximity,

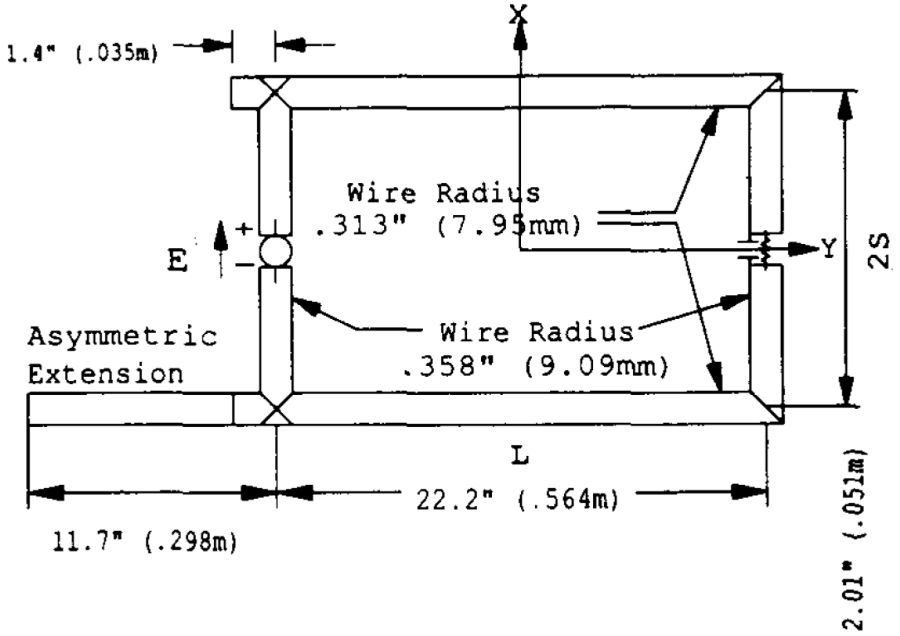

Fig. 2. Geometry used in [10] for numerical and experimental demonstration of the decomposition of a signal path with extended reference structures into symmetric and asymmetric components and quantifying and comparing the EMI associated with each.

e.g., coupling from a signal trace that runs adjacent to a heatsink and capacitively couples to the heatsink. This study was also among the early efforts on EMI modeling using numerical methods, in this case an integral equation formulation with method of moments discretization that used the MININEC code [14]. Jerse and Paul continued to expand this idea further to include a hybrid multiconductor TL (MTL)/radiation formulation using MTL theory and the partial element equivalent circuit (PEEC) method [15]. This approach had the advantage that while PEEC is a full-wave EM formulation that includes radiation, a SPICE-compatible model is extracted that requires no matrix solution of the integral equation formulation as necessary when discretizing the integral equation with the method of moments.

In this paper, a method to analyze the radiation properties of a PCB/connector structure is presented based on network parameters. A discussion of current modes in differential system designs is first presented in Section II. Section III highlights mode conversion mechanisms and their quantification in mixed-mode *S*-parameters. A PCB/connector geometry under study is presented in Section IV. Section V outlines the mathematical details to perform radiated power analysis with network parameters. The radiation properties of the PCB/connector structure presented in Section IV are shown in Section VI. Section VII contains an example calculation of radiated power for digital signals and illustrates individual radiated power contributions.

II. TRANSMISSION LINE AND ANTENNA CURRENTS AT PCB/CONNECTOR INTERFACES

As data rates increase there is a trend to move from single-ended signals to differential signals in order to maintain high signal fidelity. Furthermore, well-balanced currents in a TL differential signal pair can potentially be a better design for reducing unintended radiated emissions or EMI. These are currents with the signal current and signal-return current on a symmetric, balanced pair with a net zero return current on a reference structure (so-called “ground”). At data rates and frequencies where the signal routing is no longer electrically short, these are the odd-mode TL currents for a three-conductor set comprising two signal conductors and one reference conductor. In the EMC literature, this is typically denoted the DM, though there is a factor of $1/\sqrt{2}$ between these definitions. An illustration of these TL-DM currents is shown in Fig. 3 and can be found in [16].

The TL common-mode (TL-CM) currents on a balanced differential signal pair are similar to single-ended signal currents; in that, they can result in a coupling path leading to significant EMI. These currents are those signal currents that have a signal return current that uses a common reference structure. These are the even-mode TL currents for a three-conductor set and will be denoted herein as the TL common-mode currents. An illustration of these TL-CM currents is shown in Fig. 3 can be found in [16].

The reference structure in a printed circuit layout with plug-in modules or attached cables will be of significant electrical extent, and typically extend beyond the footprint of the signal conductor as depicted in the drawing of Fig. 1. The unintentional current on the extended reference conductor leads to unintended radiation. The extended reference structures comprise the effective antenna and the unintentional current on these conductors that result in radiation or contribute to EMI are referred to herein as common-mode antenna currents. The CM antenna currents wind up on external data cables

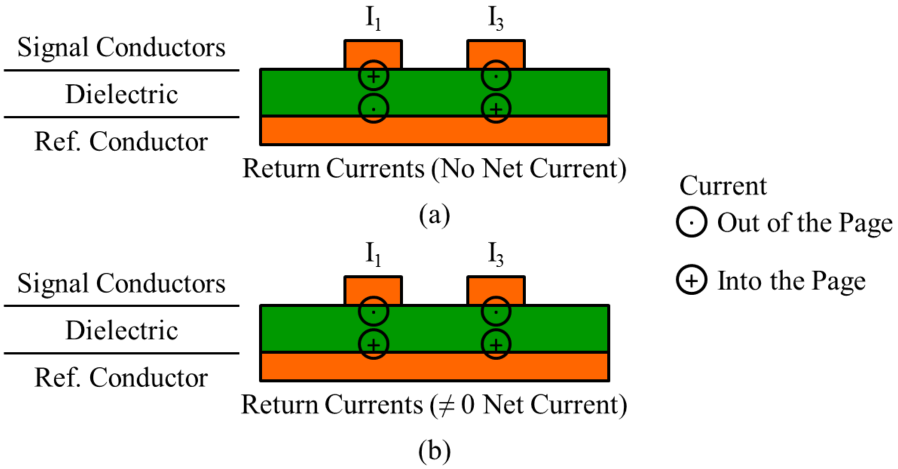

Fig. 3. (a) Odd-mode or differential-mode currents in a coupled, microstrip printed circuit board. (b) Even-mode or common-mode currents in a coupled, microstrip printed circuit board.

(shielded or unshielded), heatsinks, and extended ground-reference planes on PCBs connected by connectors, among many other possibilities.

It is necessary to understand the radiation physics for high-density PCB connectors and to be able to quantify the radiated emissions performance in order to provide design direction at the silicon and board levels, as well as to determine potential EMI mitigation approaches. Present connector design specifications are dominated by signal integrity. Furthermore, the EMI coupling physics at the PCB/connector interface are not well quantified for providing design approaches for the connector or on the PCB. As data rates have increased, significant challenges result in real-world designs where products can fail radiated emissions requirements due to inadequate understanding of the EMI coupling physics and design approaches for mitigating the radiation either in the connector or on the board, or both. A methodology is proposed here for comparing connector radiated emissions performance so that EMI performance can be balanced along with signal integrity and cost in identifying a suitable high-speed connector for a system design.

III. SCATTERING AT THE PCB/CONNECTOR INTERFACE IN DIFFERENTIAL-MODE SIGNALING

Differential signals in high-speed digital printed circuits are most often routed edge-coupled. In order to achieve a 100 Ω TL DM characteristic impedance with a typical material dielectric constant $3.3 < \varepsilon_r < 4.5$, the signal pair on the PCB is weakly coupled [17]. The modal TL DM voltage V_{DM} and the CM voltage V_{CM} are defined in terms of the single-ended voltages V_1 and V_2 as

$$V_{DM} = V_2 - V_1 \tag{1}$$

$$V_{CM} = \frac{1}{2}\left(V_2 + V_1\right). \tag{2}$$

A nonzero TL common-mode signal can arise in a differential signaling system through signal asymmetries in the time-domain waveforms of V_1 and V_2, geometry asymmetries in the routing, or material asymmetries. Waveform asymmetries include amplitude mismatches between V_1 and V_2, rise- and fall-time mismatches, or time offsets between the transitions of the two single-ended signals (skew). Geometry asymmetries include any non-mirror image routing of the V_1 and V_2 traces such as one trace over a reference plane while the companion trace is not, one is closer to a reference plane edge, pairs routed through connectors with asymmetric ground reference structures, and asymmetric placement of vias connected to the ground reference in PCBs that are near the signal traces or signal vias. At every point along the propagation path where the translational invariance of the differential pair and reference cross-section as shown in Fig. 3 is disrupted by a geometry asymmetry, there will be scattering between the TL differential- and common-modes. Geometry asymmetries also include electrical length differences between the V_1 and V_2 signal propagation paths, such as pairs routed through right-angle connector pins with different lengths, e.g., backplane connectors. Material asymmetries, e.g., one trace over a glass fiber bundle, while the companion trace is not, the so-called "glass weave effect," will also contribute to the TL common-mode signal.

The TL-DM and TL-CM voltages are uncoupled over a propagation length where the cross-sectional geometry is translationally invariant. If a pure TL-DM voltage, with no TL-CM voltage, is incident on the PCB/connector interface, where the translational invariance of the TL geometry set on the PCB is interrupted, scattering results. The incident TL-DM voltage is scattered into transmitted (onto the connector) and reflected (from the connector) TL-DM voltages. Because of the geometry asymmetry in the right-angle connectors considered here, scattering of the incident TL-DM into a reflected TL-CM and transmitted TL-CM also occurs at the PCB/connector interface to match the continuity of current and continuity of voltage boundary conditions at the PCB/connector interface.

The mixed-mode *S*-parameter matrix that characterizes the scattering due to the discontinuity in the geometry from the PCB to the connector is [18]

$$\left[\tilde{S}^{MM}\right]=\begin{bmatrix} S_{dd11} & S_{dd12} & S_{dc11} & S_{dc12} \\ S_{dd21} & S_{dd22} & S_{dc21} & S_{dc22} \\ S_{cd11} & S_{cd12} & S_{cc11} & S_{cc12} \\ S_{cd21} & S_{cd22} & S_{cc21} & S_{cc22} \end{bmatrix}. \tag{3}$$

For an incident TL-DM, S_{dd11} is the reflected TL-DM at mixed-mode Port 1 and S_{dd21} is the transmitted TL-DM to mixed-mode Port 2. The parameters for the TL-CM are analogous. The scattering between the modes is characterized by the S_{dcij} and S_{cdij} terms. For example, S_{cd11} characterizes the reflected TL-CM wave that results from an incident TL-DM wave and S_{cd21} is the transmitted TL-CM wave to mixed-mode Port 2 that results from the incident TL-DM wave. Further, because the geometry of the differential pair within the connector is not translationally invariant, it is expected that there will be coupling between the TL-DM and the TL-CM as the wave propagates through the connector.

The mixed-mode *S*-parameters are network parameters and characterize the voltage waves at the ports on either side of the connector. However, since the geometry of the differential signal pair is imbalanced, radiation also occurs as the wave propagates through the connector [10]. Currently, the detailed physics and a quantitative model for the radiation in terms of the coupling of the TL-DM and TL-CM to antenna currents on the connector are unknown. However, as a first step for providing design guidance it is sufficient to quantify this radiation using network parameters and power conservation. The radiation as a function of the incident waveform can then be quantified.

IV. PCB/CONNECTOR GEOMETRY

The paper presented here for modeling the radiation for a PCB/connector interface focused on a connector design in which the differential pair signal conductors had wide reference conductor blades on three sides, as shown in Fig. 4. The connector geometry in the study was loosely based on commercially available 100 Ω differential characteristic impedance designs. This signal/reference layout strategy is one approach used in commercial connector designs, though the geometry shown is simplified for EM modeling purposes and is not intended to match any specific commercial product. The connector design under study consisted of two wafer layers that contained signal blades and signal reference blades whose cross-sectional layout is given in Fig. 4(b). Only two wafers were modeled to minimize the complexity of the problem. A full-wave EM modeling tool (CST Microwave Studio) was used to simulate the connector geometry. This style of high-speed connector is typically a press-fit connector with through-hole vias on the PCB into which the connector pins are pressed. However, in the simplified model, no through-hole vias were included and only the strip transition from a microstrip differential pair to the connector was modeled.

The radiation from a PCB/connector structure is dependent upon both the connector PCB return plane dimensions and the connector dimensions. Two different structures were simulated to determine the dominant geometry features in the connector radiated power response, as shown in Fig. 4(a). Thirteen magnetic field circulation integrals were placed around the connector structure as shown in Fig. 4(a) to calculate the CM antenna currents. The left structure in Fig. 4(a) is denoted as the “connector only” case and was simulated to determine the radiation due to the connector itself. A small PCB area around the connector footprint was modeled with the connector geometry so that the PCB to connector transitions and the associated scattering remained in the

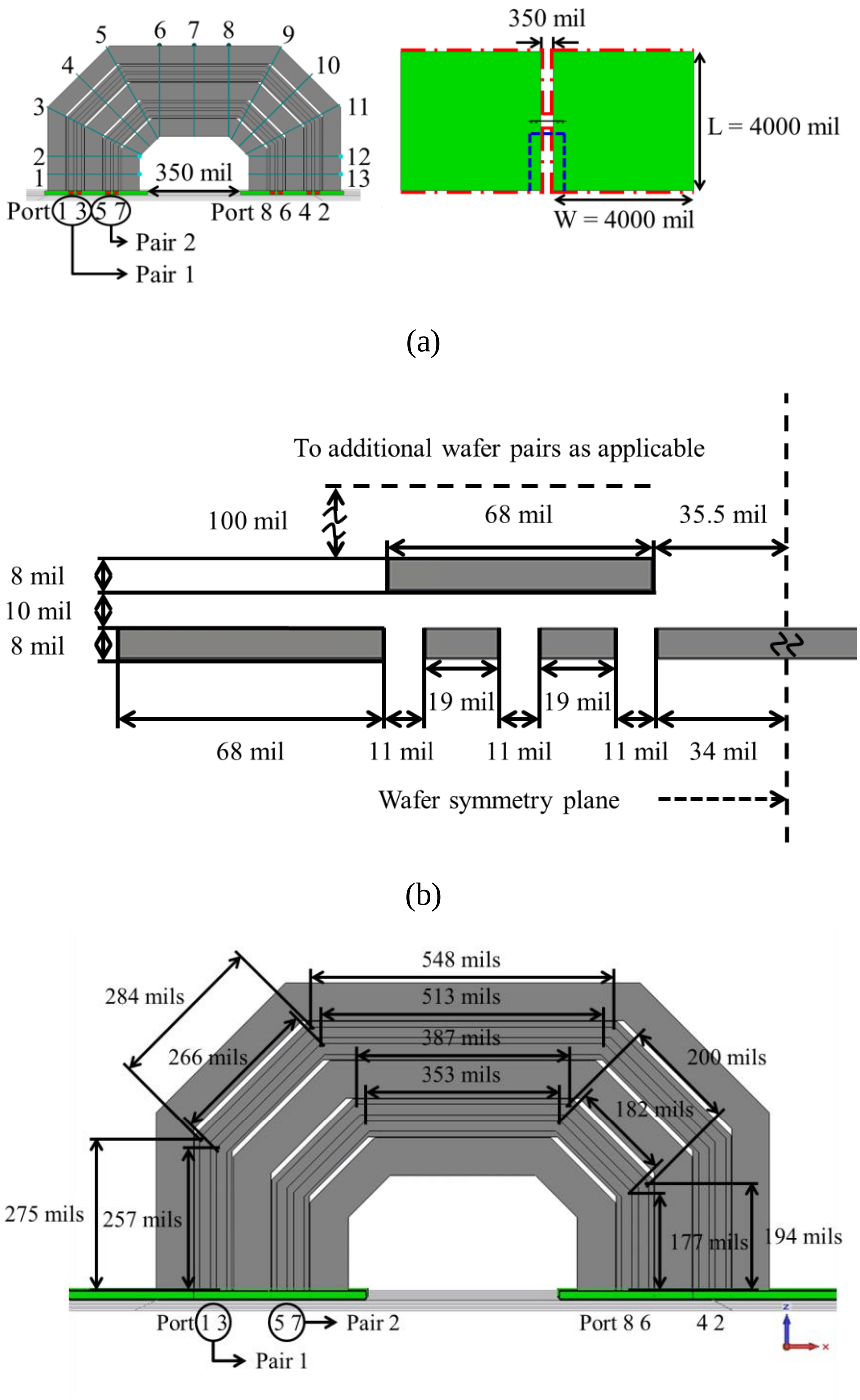

(a)

(b)

(c)

Fig. 4. (a) Left PCB/connector structure is the simulated “connector only” case. The right PCB/connector structure is the simulated “large PCB plane” case. These simulations were formulated without conductor and dielectric losses. The connector consisted of two differential signaling pairs. (b) Wafer cross-sectional layout for the connector of (a). The connector in (a) consisted of two wafer layers. (c) Front connector wafer signal blades layout for the connector in (a).

problem. The PCB area footprint for the connector only case as shown in Fig. 4(a) was 101 mils × 390 mils, and the transition was from a 99 Ω differential characteristic impedance microstrip line to the 102 Ω differential characteristic impedance connector. The signal reference conductors in the connector were modeled to electrically connect to the signal return reference for the microstrip lines in the small PCB area footprint. The right structure in Fig. 4(a) is denoted as the "large PCB plane" case and was simulated to determine radiation due to larger PCB return planes. The sources and geometry of the transition from the PCB to the connector remained the same as the previous connector only case, and only the reference planes for the PCB microstrip geometry were extended as shown in Fig. 4(a). The radiation due to illumination of the large PCB reference planes was identified by the difference in radiation responses in these two cases. The connector was placed in the middle of the PCB edges as shown in Fig. 4(a).

The structures in Fig. 4 have many features that are the same. Additional physical layout details for the simulated structures in Fig. 4(a) that are the same are given in Fig. 4(b) and (c). The microstrip traces were 42 mils long and were on a substrate with 4.3 relative permittivity and 14.45 mils thickness. The substrate completely covered the PCB return planes and did not extend beyond the return plane dimensions. The PCB signal conductors had a 0.7 mil thickness. Fig. 4(b) illustrates the cross-sectional layout of the connector wafers and Fig. 4(c) depicts the layout of the signal blades in the front connector wafer. In Fig. 4(c), only unique connector dimensions are denoted; all other dimensions may be found by structure symmetry.

The objective of modeling the PCB/connector geometry was to identify the geometry features that contributed to the radiation as well as quantify the radiation from the network parameters. The signal traces for both simulations shown in Fig. 4(a) were fed with discrete face ports on the PCB microstrip traces, and the PCB/connector structure was modeled in air with PML absorbing boundary conditions. The discrete face port impedances were set to 50 Ω. Time-domain simulations were performed and the *S*-parameters of the PCB/connector geometry were extracted in CST Microwave Studio from the time-domain signals.

V. RADIATED POWER CALCULATIONS USING NETWORK PARAMETERS

The radiated power resulting from signals through the connector can be calculated either from the fields or with conservation of power using network parameters. The electric and magnetic fields over a surface enclosing the PCB/connector geometry are calculated in the full-wave simulations and can be used to calculate the radiated power. In general, this calculation method is unsuitable for design because it can be computer memory intensive and the computations can be time consuming. Further, the spatial variation of the fields are unneeded for typical design choices related to connector performance and to provide guidance on the differential signal time-waveform balance that might impact EMI. An alternative approach to the calculation is to use *S*-parameters generated from full-wave simulations to calculate the radiated power. This radiated power calculation from network parameters at ports has the advantage of a much faster simulation time than the radiated power calculations using the electric and magnetic fields. However, the time-domain simulations must be run sufficiently long that the radiation aspects of the problem are captured from the network *S*-parameters. Terminating the simulations too early in the time history may provide sufficient *S*-parameter results for signal integrity purposes, but insufficient for radiation calculations.

Design discovery for radiation attributes is readily facilitated using the network parameter and power conservation approach. The important attributes are those geometry features that impact the *S*-parameters including the transition from the PCB to the connector and the specifics of the connector geometry itself. Also, quantifying the radiation with the differential signal time-waveform imbalance is readily done using the network parameters.

Radiated power can be calculated using incident port voltages and single-ended *S*-parameters as [16]

$$P_{rad,total} = \left(1/\left(2Z_0\right)\right)\left[\overline{V}^{+}\right]^{t}\left(\left[\tilde{I}\right] - \left[\tilde{S}^{SE}\right]^{t}\left[\tilde{S}^{SE}\right]\right)\left[\overline{V}^{+}\right] \tag{4}$$

where, Z_0 is the port characteristic impedance, $\left[\overline{V}^+\right]$ is the incident voltage vector, t denotes the complex conjugate transpose, $\left[\tilde{I}\right]$ is the identity matrix, and $\left[\tilde{S}^{SE}\right]$ is the single-ended *S*-parameter matrix at ports on the PCBs. The ports on the PCBs must have a well-defined voltage and current, and so must be sufficiently removed from the transition of the signal on the PCB to the connector so that a transverse electromagnetic (TEM) mode exists. The location can be quantified such that $\left|\overline{E}_{axial}\right| / \left|\overline{E}_{transverse}\right| << 1$, where $\overline{E}_{axial}$ is the field along the propagation direction and $\overline{E}_{transverse}$ is the transverse field, which is the only component for a TEM mode. The total radiated power can also be represented in a modal form using mixed-mode *S*-parameters [18].

The total radiated power from the PCB/connector geometry can be written in the modal domain as the superposition of radiated power from an incident wave that is purely a TL DM and an incident wave that is purely a TL CM, in addition to a term with the product of $V_{CM}^+ V_{DM}^+$. The total radiated power using modal quantities can then be written as

$$P_{rad,total} = P_{rad,V_{DM}^+} + P_{rad,V_{CM}^+} + P_{rad,product}\,. \tag{5}$$

The notation is not meant to suggest that there is radiation from a TL DM signal or a TL CM signal, but rather identifies the radiation resulting from the modal TL incident wave.

A single pair of signal conductors in a PCB/connector geometry with single-ended and mixed-mode port assignments is shown in Fig. 5. From (1) and (2), writing the incident voltage at single-ended Port 1 as $V_1^+ = V_{CM}^+ - (1/2)V_{DM}^+$ and the incident voltage at single-ended Port 3 as $V_3^+ = V_{CM}^+ + (1/2)V_{DM}^+$, it follows that the incident voltage vector $\left[\overline{V}^+\right]$ is given by

$$\left[\overline{V}^+\right] = \left[\left(V_{CM}^+ - \frac{1}{2}V_{DM}^+\right) \quad 0 \quad \left(V_{CM}^+ + \frac{1}{2}V_{DM}^+\right) \quad 0\right]^T \tag{6}$$

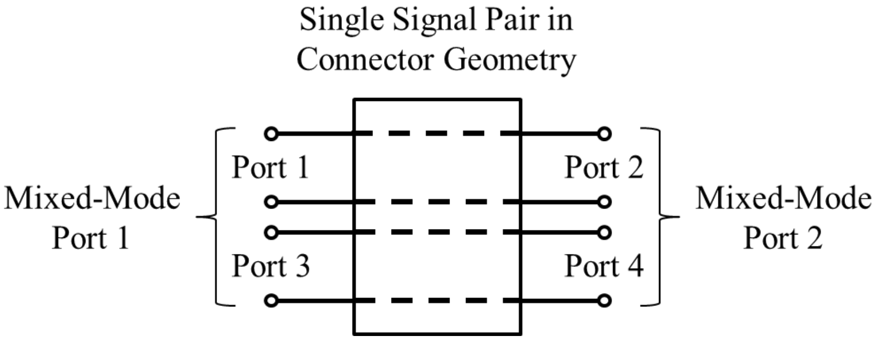

Fig. 5. Single-ended and mixed-mode port assignments for a single signal pair in a connector.

where T is the transpose. The radiated power from (4) can then be written as

$$P_{rad,total} = \left(1/\left(2Z_0\right)\right)\left(\left[\overline{B}\right]^t\left[\tilde{D}\right]\left[\overline{B}\right] + \left[\overline{C}\right]^t\left[\tilde{D}\right]\left[\overline{C}\right] + \left[\overline{B}\right]^t\left[\tilde{D}\right]\left[\overline{C}\right] + \left[\overline{C}\right]^t\left[\tilde{D}\right]\left[\overline{B}\right]\right) \tag{7}$$

$$\left[\overline{B}\right] = \left[\left(-(1/2)V_{DM}^{+}\right) \quad 0 \quad \left((1/2)V_{DM}^{+}\right) \quad 0\right]^T \tag{8a}$$

$$\left[\overline{C}\right] = \left[V_{CM}^{+} \quad 0 \quad V_{CM}^{+} \quad 0\right]^T \tag{8b}$$

$$\begin{aligned}\left[\tilde{D}\right] &= \left[\tilde{I}\right] - \left[\tilde{S}^{SE}\right]^t\left[\tilde{S}^{SE}\right] \\ &= \left[\tilde{I}\right] - \left[\tilde{M}\right]^T\left[\tilde{S}^{MM}\right]^t\left[\tilde{S}^{MM}\right]\left[\tilde{M}\right]\end{aligned} \tag{8c}$$

$$\left[\tilde{M}\right] = \frac{1}{\sqrt{2}}\begin{bmatrix} 1 & 0 & -1 & 0 \\ 0 & 1 & 0 & -1 \\ 1 & 0 & 1 & 0 \\ 0 & 1 & 0 & 1 \end{bmatrix}. \tag{8d}$$

The radiated power due to the DM incident waves is given by

$$\begin{aligned}P_{rad,V_{DM}^{+}} &= \left(1/\left(2Z_0\right)\right)\left[\overline{B}\right]^t\left[\tilde{D}\right]\left[\overline{B}\right] \\ &= \left(1/Z_0\right)\left|(1/2)V_{DM}^{+}\right|^2\left(1 - \left|S_{dd11}\right|^2 - \left|S_{dd21}\right|^2 - \left|S_{cd11}\right|^2 - \left|S_{cd21}\right|^2\right)\end{aligned} \tag{9}$$

where $-|S_{dd11}|$ in decibels is the TL-DM return loss, $-|S_{dd21}|$ in decibels is the TL-DM insertion loss, $-|S_{cd11}|$ in decibels is the TL-DM to TL-CM return loss (incident TL-DM that gets reflected into the TL-CM), and $-|S_{cd21}|$ in decibels is the TL-DM to TL-CM insertion loss (incident TL-DM that gets scattered into a transmitted TL-CM). The radiated power due to the TL-CM incident waves is given by

$$\begin{aligned} P_{rad,V_{CM}^{+}} &= \left(1/(2Z_0)\right)\left[\overline{C}\right]^t\left[\tilde{D}\right]\left[\overline{C}\right] \\ &= \left(1/Z_0\right)\left|V_{CM}^{+}\right|^2\left(1-|S_{cc11}|^2-|S_{cc21}|^2-|S_{dc11}|^2-|S_{dc21}|^2\right) \end{aligned} \tag{10}$$

where $-|S_{cc11}|$ in decibels is the TL-CM return loss, $-|S_{cc21}|$ in decibels is the TL-CM insertion loss, $-|S_{dc11}|$ in decibels is the TL-CM to TL-DM return loss, and $-|S_{dc21}|$ in decibels is the TL-CM to TL-DM insertion loss. The radiated power in the product term $V_{CM}^{+}V_{DM}^{+}$ is given by

$$\begin{aligned} P_{rad,\,product} &= \left(1/(2Z_0)\right)\left(\left[\overline{B}\right]^t\left[\tilde{D}\right]\left[\overline{C}\right]+\left[\overline{C}\right]^t\left[\tilde{D}\right]\left[\overline{B}\right]\right) \\ &= \left(1/(2Z_0)\right)V_{CM}^{+}V_{DM}^{+*}\left(S_{cc11}S_{cd11}^{*}+S_{cc21}S_{cd21}^{*}+S_{dc11}S_{dd11}^{*}+S_{dc21}S_{dd21}^{*}\right) \\ &\quad+\left(1/(2Z_0)\right)V_{DM}^{+}V_{CM}^{+*}\left(S_{dd11}S_{dc11}^{*}+S_{dd21}S_{dc21}^{*}+S_{cd11}S_{cc11}^{*}+S_{cd21}S_{cc21}^{*}\right) \end{aligned} \tag{11}$$

and is real as is necessary.

The modal radiated power expressions (5)-(11) assume that the TL coupling between signal pairs in multiple pair connectors is negligible, since the formulas were derived for a single signal pair. For cases where the coupling among signal pairs is nonnegligible, (4) still holds. If desired, a portion of the *S*-parameter matrix may be used in (4) rather than the full matrix representing the entire PCB/connector geometry with multiple signal pairs. A reduced *S*-parameter matrix must retain data for the ports that are fed and ports that have significant coupling to the feed ports.

VI. RADIATION FROM THE PCB/CONNECTOR ASSEMBLY

The radiated power calculated from the mixed-mode *S*-parameters when the outermost and innermost signal pairs were excited as shown in Fig. 4 are illustrated in Fig. 6 and Fig. 7, respectively. The outermost signal pair is denoted as “Pair 1” and the innermost signal pair as “Pair 2” in Fig. 6 and Fig. 7. The calculated radiated powers are shown when the incident waves were a TL CM excitation and a TL DM excitation. The modal excitations were created from 1 V single-ended incident port voltages. The radiated power resonances below 3 GHz only occurred for the TL common-mode excitation with the large PCB plane case of Fig. 4(a), as seen in Fig. 6(a) and Fig. 7(a). For the TL common-mode excitation, the dominant antenna structure was related to the PCB reference plane dimensions below 3 GHz, whereas above 3 GHz the dominant antenna structure was the connector geometry itself, as described later.

There were two primary resonant geometry features in the TL common-mode response below 3 GHz. The first resonance frequency at 0.49 GHz was created by the length of the PCB return perimeter and a path length through the connector as shown by the dashed-dotted line in the right structure of Fig. 4(a). The second resonance frequency at 1.14 GHz was influenced by the placement of the connector along the length of the PCB-PCB gap, where the resonance was dictated by the length of the gap as shown by the dashed line in the right structure of Fig. 4(a). The gap width was 350 mils, and though the E-field across the gap was not highly varying, attempts at modeling it as a narrow gap with constant fields fed at a well-defined port for frequencies well into the gigahertz range were unsuccessful. The 1.14 GHz resonance was minimally influenced by the gap width and remained fixed in frequency so long as a gap existed. When the gap between PCBs was eliminated with a continuous plane, the 0.49 and 1.14 GHz resonances were eliminated from the radiated power response.

Both resonances below 3 GHz occurred when the indicated resonant lengths in the right structure of Fig. 4(a) were approximately $\lambda/2$ in length. For the right geometry in Fig. 4(a), the indicated lengths were approximately 13367 mils and 5367 mils. Using the free-space wave velocity, the predicted resonances were 0.44 and 1.10 GHz. Some of the discrepancies between the predicted resonances and the actual resonances at 0.49 and 1.14 GHz can be attributed to length assignments for the CM antenna current flow paths

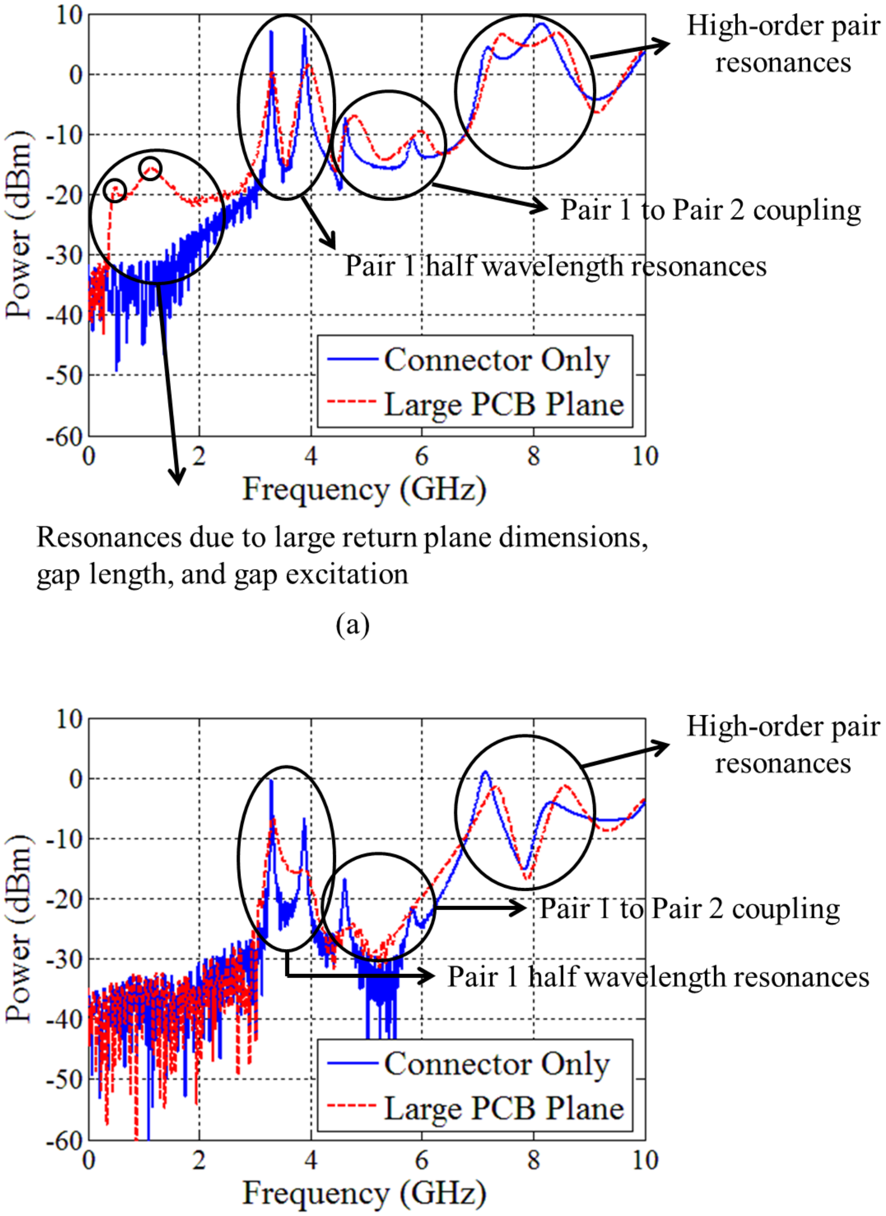

(a)

(b)

Fig. 6. Radiated power when the outermost signal pair, Pair 1, was fed and all other ports were matched for the PCB/connector structures of Fig. 4(a). Incident single-ended port voltages were 1 V. (a) TL CM excitation. (b) TL DM excitation.

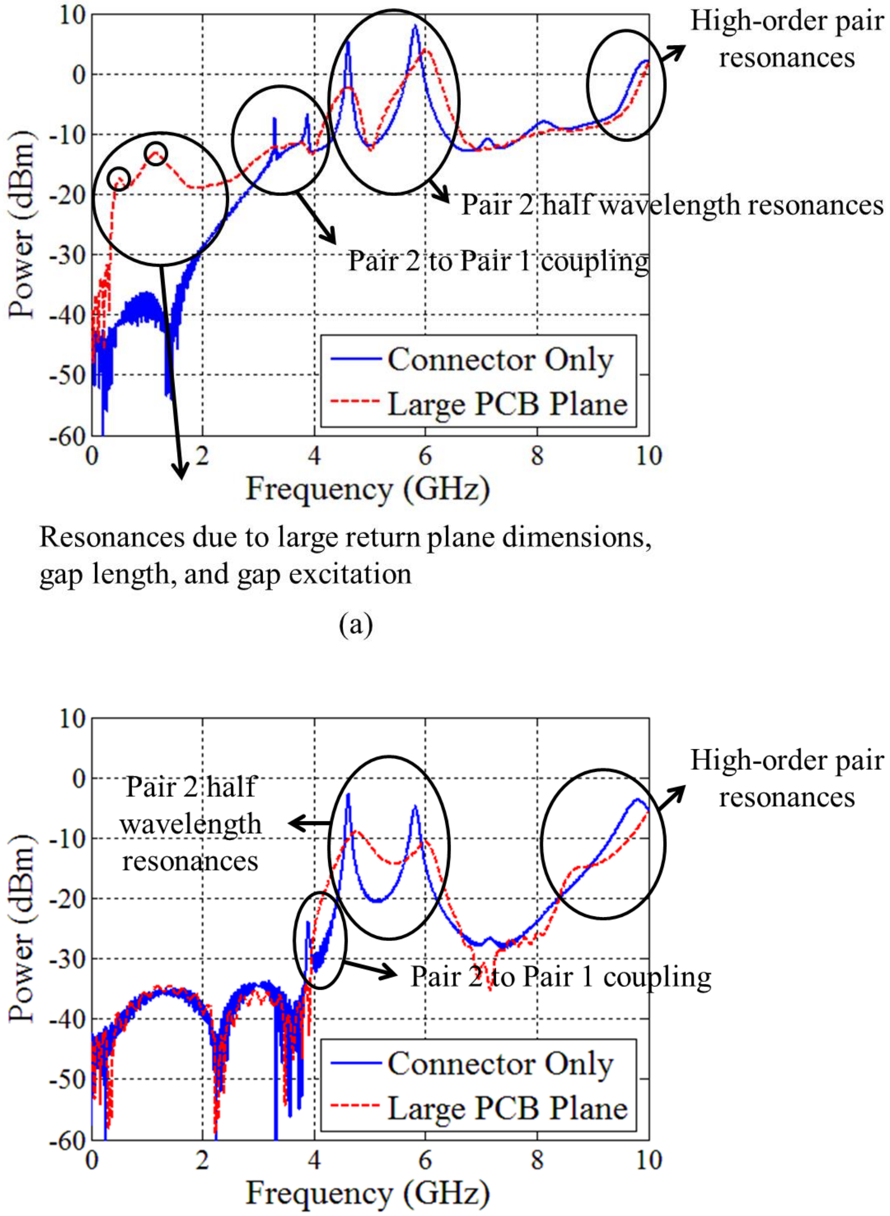

(a)

(b)

Fig. 7. Radiated power when the innermost signal pair, Pair 2, was fed and all other ports were matched for the PCB/connector structures of Fig. 4(a). Incident single-ended port voltages were 1 V. (a) TL CM excitation. (b) TL DM excitation.

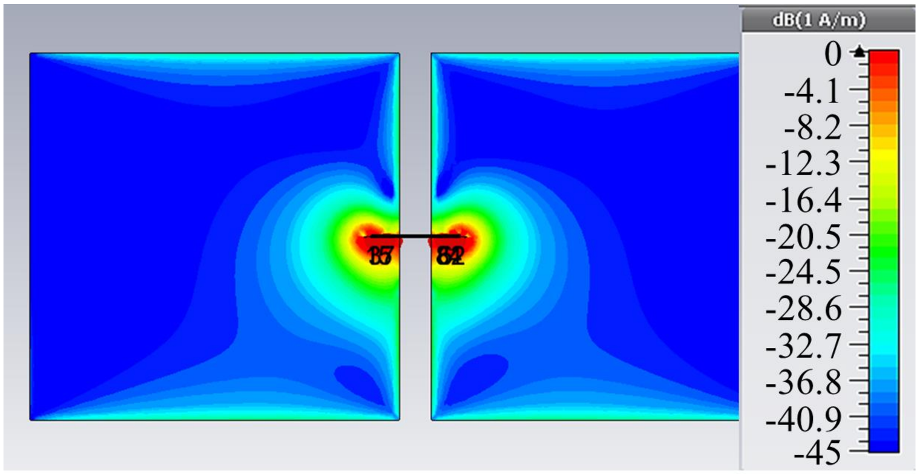

Fig. 8. Surface current density plot at 0.49 GHz when Pair 1 was fed with a TL CM excitation and all other ports were matched.

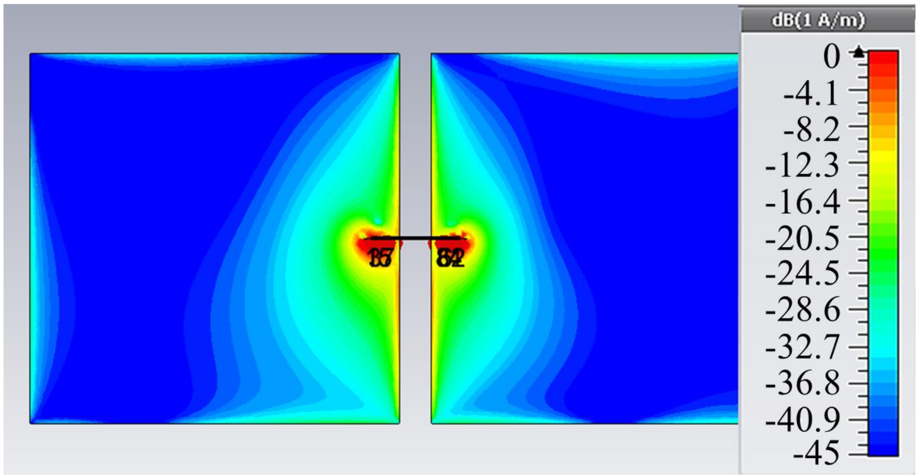

Fig. 9. Surface current density plot at 1.14 GHz when Pair 1 was fed with a TL CM excitation and all other ports were matched.

in the connector geometry and the low quality factor of the resonances. The surface current density in the PCB/connector structure at the 0.49 GHz and 1.14 GHz resonant frequencies are given in Fig. 8 and Fig. 9, respectively. These plots illustrate the CM antenna currents on the PCB return planes that contribute significantly to the connector/PCB radiated power.

A series of simulations were performed to study the proposed dominant geometry features in the radiated power response. The basic structure on the right in Fig. 4(a) was used and the simulations were run when individual return planes had widths of W =

2000, 3000, and 4000 mils. The results from this series of simulations are shown in Fig. 10, where Pair 2 was fed and all other ports were matched. The first low-frequency resonance near 0.5 GHz increased in frequency as the width of the PCB return plane decreased. The second low frequency resonance near 1.2 GHz remained relatively fixed in frequency as expected since the length of the PCB-PCB gap and the connector position were unchanged. The radiated power remained relatively unchanged above 3 GHz, independent of the plane width geometry variation, because the response was dominated by the connector structure only.

The resonances in the radiated power above 3 GHz as seen in Fig. 6 and Fig. 7 are due to CM antenna currents on the connector blades, independent of the modal excitation. These resonances are due to the electrical lengths of particular geometry feature(s) in the connector design and groupings of these resonances can be easily referenced to signal pairs that drive TL currents on the associated resonant reference blades. The first set of resonances for Pair 1 was at 3.30 and 3.89 GHz and for Pair 2 was at 4.63 and 5.83 GHz.

Magnetic field circulation integrals were placed about contours that encircle the connector structure as shown in Fig. 4(a) to find the CM antenna current as a function of connector angular position. The circulation integrals were arranged about the connector relative to the innermost reference blade. The integrals were placed at the midpoints and ends of each straight conductor in the innermost reference blade. The CM antenna currents were calculated at both Pair 1 half wavelength resonances (3.30 and 3.89 GHz) and at a high-order resonance (7.17 GHz) as shown in Fig. 11. The CM antenna currents form approximately a $\lambda/2$ and λ distribution along the connector arc at the half wavelength resonances and at the high-order resonance, respectively.

The radiated power resonances can be approximately predicted from the edge lengths of the reference blades that are closest to the resonant signal pair in question and on the same layer as the signal pair. The inner edge of the left return blade and the outer edge of the right return blade for Pair 1 are 1745 and 1483 mils. The $\lambda/2$ resonant frequencies for these lengths are 3.38 and 3.98 GHz, respectively, which are close to the actual 3.30 and 3.89 GHz resonances. The inner edge of the left return blade and the outer edge of the right return blade for Pair 2 are 1257 and 996 mils. The $\lambda/2$ resonant frequencies for these lengths are 4.70 and 5.93 GHz, respectively, which are near the 4.63 and 5.83 GHz resonances.

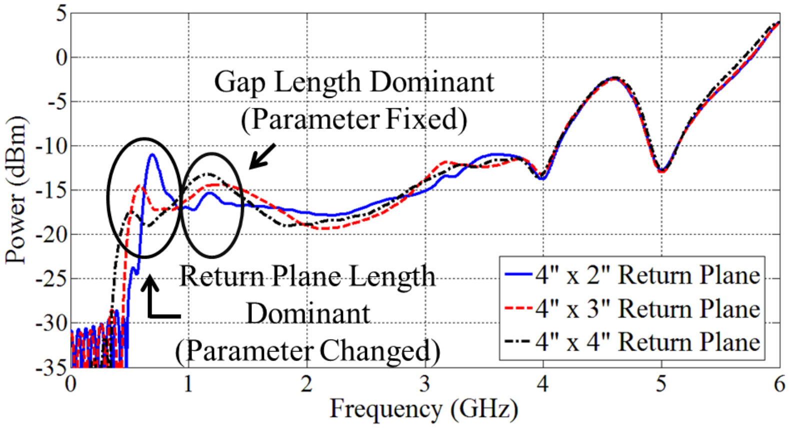

Fig. 10. Connector TL common-mode radiated power response for varying return plane width when Pair 2 was fed. Incident single-ended port voltages were 1 V and all non-source ports were matched.

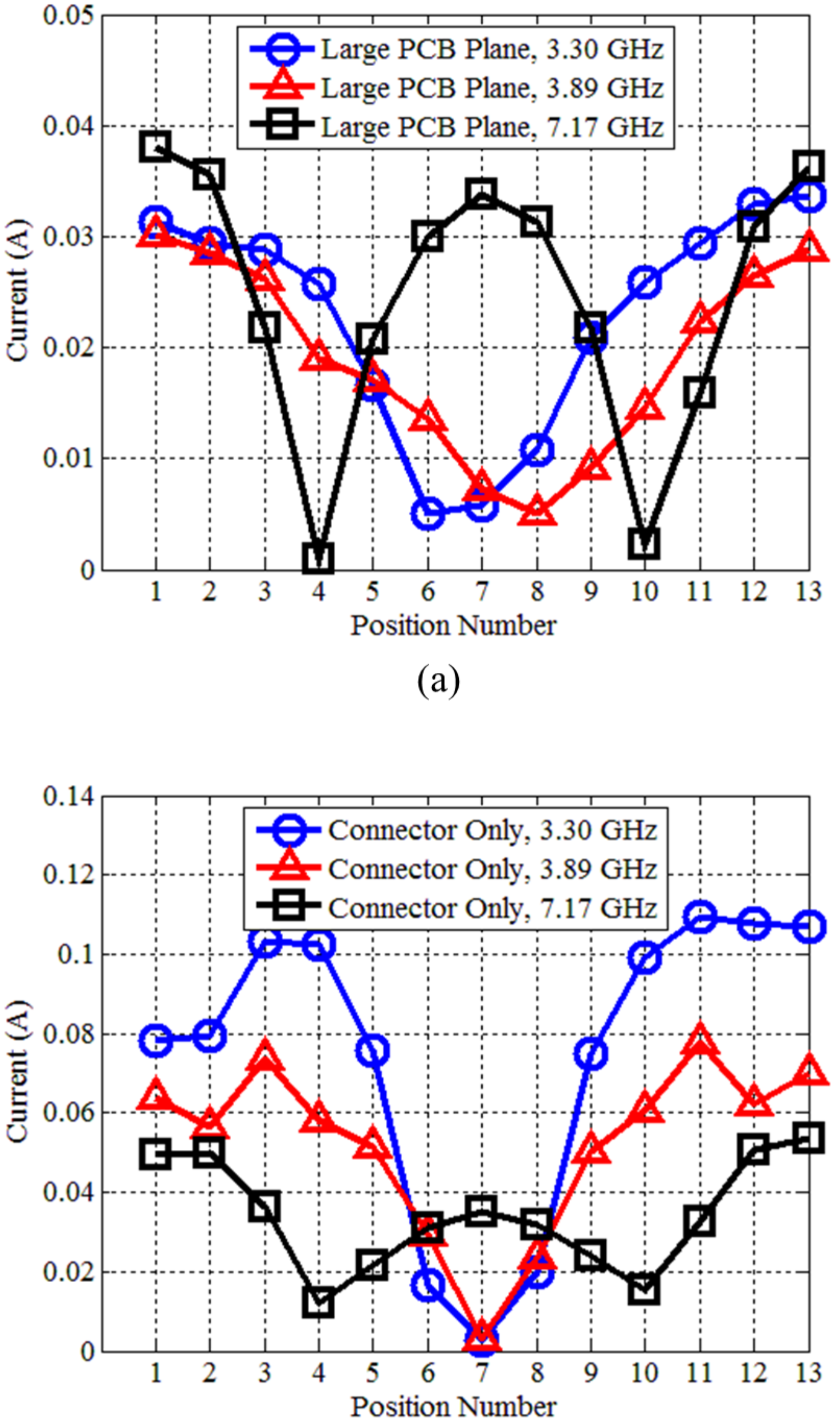

(a)

(b)

Fig. 11. Connector CM antenna currents at 3.30, 3.89, and 7.17 GHz resonances when Pair 1 was fed with a TL common-mode excitation. Incident single-ended port voltages were 1 V. (a) Right connector structure of Fig. 4(a). (b) Left connector structure of Fig. 4(a).

VII. RADIATION CALCULATIONS WITH A DIGITAL SIGNAL

An analysis is given in this section to illustrate the level of the radiated emissions with the right PCB/connector structure in Fig. 4(a). Single-ended time-domain incident voltage waveforms V_1^+ and V_3^+ with amplitudes of 500 mV and with rise- and fall-times of 52.5 ps are used in this example. The incident voltage waveforms are shown in Fig. 12. An offset skew of 50 ps was added to V_3^+, which is 10% of the unit interval. The incident TL differential- and common-mode voltages have peak amplitudes of 1 V and 383 mV, respectively. The time-domain signals were converted to the frequency-domain using a fast Fourier transform, and the modal radiated powers were calculated using (9)-(11). The contributions for the individual terms P_{rad,V_{DM}^+}, P_{rad,V_{CM}^+}, and $P_{rad,product}$ are shown in Fig. 13(a) where Pair 1 in the PCB/connector structure was fed. The radiated power for incident TL-CM voltages is 10-20 dB greater than the radiated power for incident TL-DM voltages over most of the simulated frequency range.

It is useful to convert radiated power into an electric field quantity so comparisons may be made to the Federal Communications Commission (FCC) Class B Limit and to provide a reference on the radiation level. Typical high-speed designs using the type of connector in Fig. 4 are often contained within a shielded enclosure and contain many wafers with a wide variety of signals. Thus, the following calculations serve only as a reference and not a prediction of the actual EMI in an application. In the far-field, the electric field in free space can be calculated as [1]

$$|E(r,\theta,\varphi)| = \frac{\sqrt{60 D_{\max} P_{rad}}}{r} \tag{12}$$

where $D_{\max}$ is the maximum directivity of the antenna structure, P_{rad} is the radiated power, and r is the distance from the radiator. The electric field for the present example was calculated from (12) and is compared to the FCC Class B Limit at three meters in Fig. 13(b), using a factor of one for the maximum directivity.

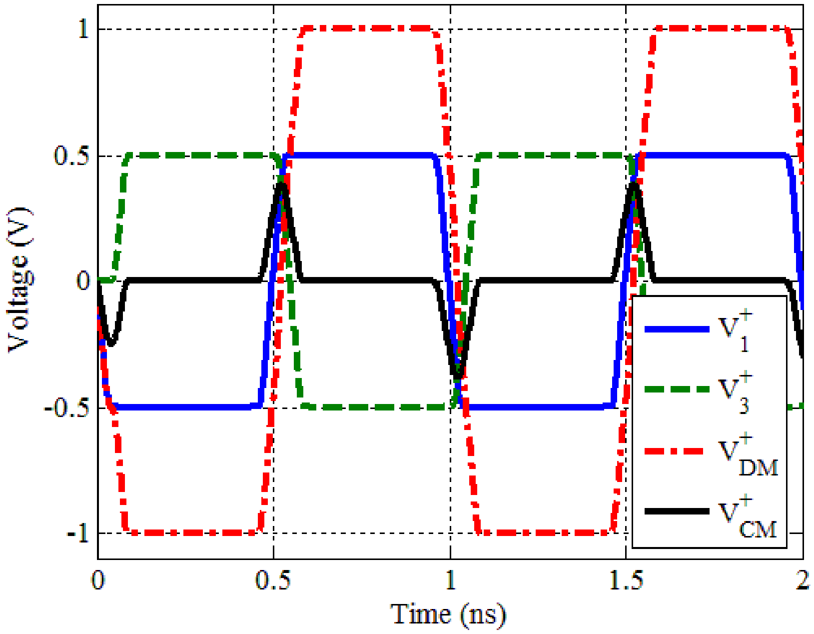

Fig. 12. Time-domain incident port voltages in the single-ended and modal domains applied to Port 1 and Port 3 of the right PCB/connector structure in Fig. 4(a).

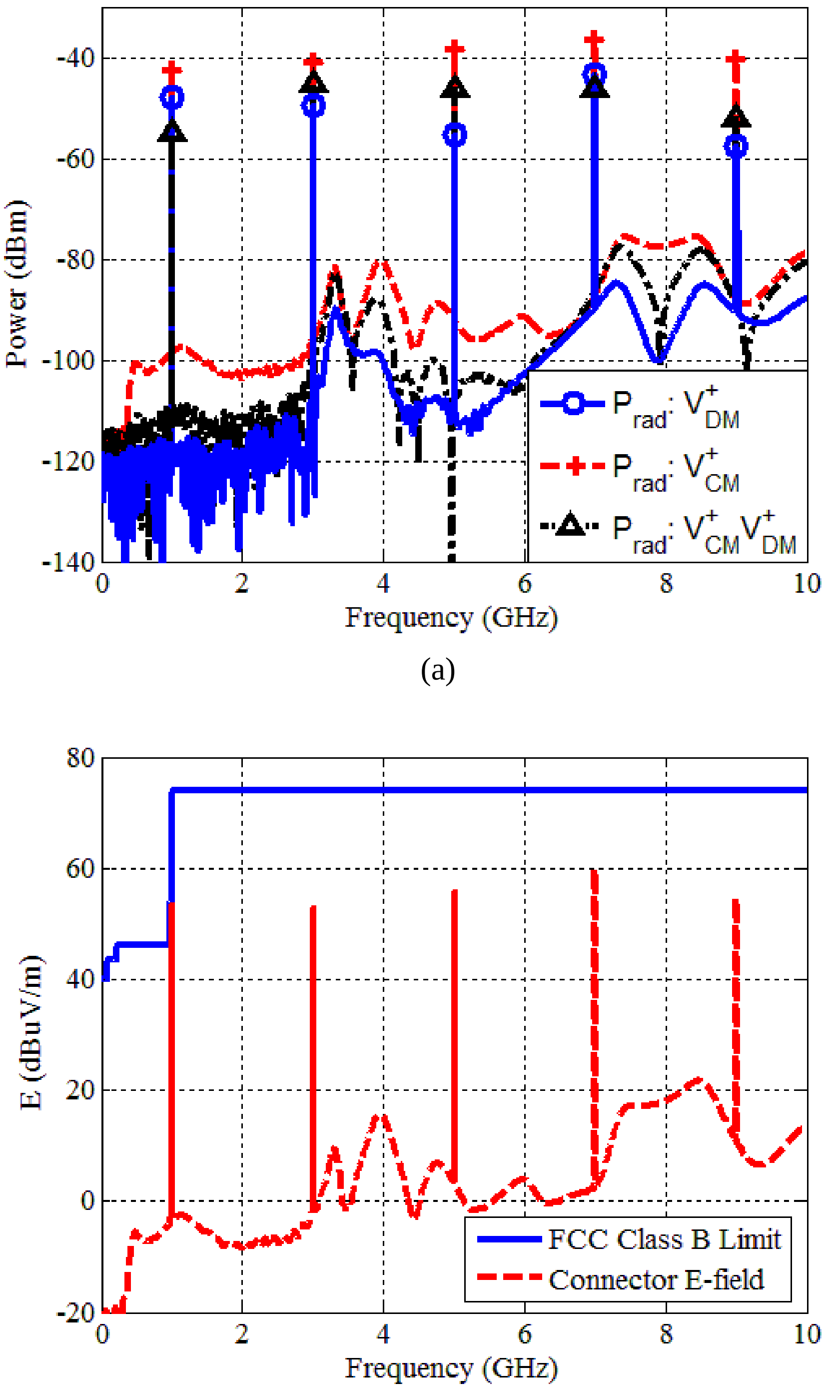

(a)

(b)

Fig. 13. (a) Connector frequency-domain modal radiated power. The solid trace represents the radiated power due to the DM incident voltages. The dashed trace represents the radiated power due to the CM incident voltages. The dashed-dotted trace represents the radiated power due to the CM and DM incident voltage product. (b) Connector radiated electric field comparison with FCC Class B Limit at three meters.

VIII. CONCLUSION

Clayton Paul, working together with industry colleagues, provided a seminal push toward developing a better understanding of EMI coupling paths and radiation physics. Aspects of these core ideas are being used in the present study to understand and quantify the EMI physics in PCB/connector interfaces for high-speed digital applications. Three distinct radiation modes were found. The first mode consists of a radiating structure comprised of PCB reference planes driven by signals through the connector. This mode produces half-wavelength dipole type current on the PCB reference planes. The radiation is significant with a TL common-mode excitation, even with ground references on three sides of the signal pair in the connector. Another radiation mode is associated with the gap between the PCBs that the connector spans. At the resonance frequency of 1.14 GHz, the 350 mil gap is electrically small, and the radiation physics corresponded to those of a slot antenna that include the ground reference path through the connector. Finally, at frequencies where the connector signal path lengths are not electrically short, resonances associated with integer half-wavelength antenna-mode current distributions result in significant radiation. The coupling of TL modes to a radiating antenna mode is unknown at present.

The radiation was calculated using *S*-parameters, and expressions were developed using mixed-mode *S*-parameters to quantify the radiation in terms of the TL DM and TL CM incident voltages. The formulation facilitates calculations for determining signal balance for minimizing the radiation. These calculations were also used to provide a simple example of the level of the radiation. In particular, for a single signal pair, the radiation was within a few decibels of the FCC Class B Limit, and can well exceed the limit at the antenna-mode resonance frequencies of the PCB geometry.

Extensive work remains to characterize and quantify the radiation physics for a propagating signal along a connector. Additional research is needed to develop a better understanding of coupling from TL modes to a radiation mode, e.g. [19], and to relate coupling to a radiation mode with the geometry in more than the rudimentary manner provided at present. A suitable formulation of the physics is needed to better engineer high-speed connectors for determining tradeoffs between signal integrity and EMI across the connector. Further work is also needed to understand and quantify the effects of many simultaneous signals, and numerous wafers (10-50 is common) in the connector geometry, so that expectations of shielding performance for the product enclosure can be specified.

Professor Paul made many contributions to the field of EMC. The second quote on the acknowledgement page of his EMC book [1]

> *"When you can measure what you are speaking about and express it in numbers you know something about it; but when you cannot measure it, when you cannot express it in numbers your knowledge is of meagre and unsatisfactory kind; it may be the beginning of knowledge but you have scarcely progressed in your thoughts to the stage of science whatever the matter may be."* – Lord Kelvin

is a fitting summary of the approach he adapted for his scientific work.

REFERENCES

[1] C. R. Paul, *Introduction to Electromagnetic Compatibility*, 2nd ed. Hoboken, NJ, USA: Wiley, 2006.

[2] H. W. Ott, "Ground – a path for current flow," *EMC Technol.*, pp. 44-48, Jan./Mar. 1983.

[3] C. R. Paul and D. R. Bush, "Radiated emissions from common-mode currents," in *Proc. 1987 IEEE Int. Symp. Electromagn. Compat.*, Atlanta, GA, USA, Aug. 25-27, 1987, pp. 197-203.

[4] C. R. Paul, "Modeling electromagnetic interference properties of printed circuit boards," *IBM J. Res. Develop.*, vol. 33, no. 1, pp. 33-50, Jan. 1989.

[5] C. L. Holloway, E. F. Kuster, A. E. Ruehli and G. Antonini, "Partial and internal inductance: Two of Clayton. R. Paul's many passions", *IEEE Trans. Electromagn. Compat.*, 2013, to be published.

[6] R. F. German, H. W. Ott, and C. R. Paul, "Effect of an image plane on printed circuit board radiation," in *Proc. 1990 IEEE Int. Symp. Electromagn. Compat.*, Washington, DC, USA, Aug. 21-23, 1990, pp. 284-291.

[7] C. R. Paul, "A comparison of the contributions of common-mode and differential-mode currents in radiated emission," *IEEE Trans. Electromagn. Compat.*, vol. 31, no. 2, pp. 189-193, May 1989.

[8] W. L. Stutzman and G. A. Thiele, "Resonant antennas: Wires and patches," in *Antenna Theory and Design*, 2nd ed. Hoboken, NJ, USA: Wiley, 1998, ch. 5, sec. 2, pp. 175-180.

[9] K. B. Hardin, C. R. Paul, and K. Naishadham, "Direct prediction of common-mode currents," in *Proc. 1991 IEEE Int. Symp. Electromagn. Compat.*, Cherry Hill, NJ, USA, Aug. 12-16, 1991, pp. 67-71.

[10] K. B. Hardin and C. R. Paul, "Decomposition of radiating structures using the ideal structure extraction methods (ISEM)," *IEEE Trans. Electromagn. Compat.*, vol. 35, no. 2, pp. 264-273, May 1993.

[11] K. B. Hardin, "Decomposition of radiating structures to directly predict asymmetric-mode radiation," Ph.D. dissertation, Dept. Elect. Eng., Univ. Kentucky, Lexington, USA, 1991.

[12] T. W. Nuteson, K. Naishadham, K. B. Hardin, and C. R. Paul, "Asymmetry-symmetry decomposition: a new technique for efficient analysis of coupled antennas," in *Proc. 1992 IEEE Int. Symp. Antennas and Propag.*, Chicago, IL, USA, Jul. 18-25, 1992, pp. 204-207.

[13] S. K. Das, W. T. Smith, and C. R. Paul, "Radiated emissions of interconnect cables," in *Proc. 1992 IEEE Int. Symp. Electromagn. Compat.*, Anaheim, CA, USA, Aug. 17-21, 1992, pp. 423-427.

[14] J. W. Rockway, J. C. Logan, D. W. S. Tam, and S. T. Li, *The MININEC Microcomputer Analysis of Wire Antennas*. Dedham, MA, USA: Artech House, 1988.

[15] T. A. Jerse and C. R. Paul, "A hybrid method for efficiently estimating common-mode radiation from transmission-line structures," in *Proc. IEEE Int. Symp. Electromagn. Compat.*, Atlanta, GA, USA, Aug. 14-18, 1995, pp. 145-149.

[16] D. M. Pozar, *Microwave Engineering*, 4th ed. Hoboken, NJ, USA: Wiley, 2012, pp. 178–188, 348.

[17] C. R. Paul, *Analysis of Multiconductor Transmission Lines,* 2nd ed. Hoboken, NJ, USA: Wiley, 2008.

[18] D. E. Bockelman and W. R. Eisenstadt, “Combined differential and common-mode scattering parameters: theory and simulation,” *IEEE Trans. Microw. Theory Tech.*, vol. 43, no. 7, pp. 1530-1539, Jul. 1995.

[19] A. Vukicevic, F. Rachidi, M. Rubinstein, and S. V. Tkachenko, “On the evaluation of antenna-mode currents along transmission lines,” *IEEE Trans. Electromagn. Compat.*, vol. 48, no. 4, pp. 693-700, Nov. 2006.

IV. Quantifying High-Density Connector Radiation in a Lossy Multi-Signal Environment

Matthew S. Halligan, Xinxin Tian, Xiao Li, Sam Connor, *Senior Member, IEEE,* Daryl G. Beetner, *Senior Member, IEEE,* James L. Drewniak, *Fellow, IEEE*

Abstract—A method is presented to quantify the radiated power in a high-density connector. This method is based on network parameters and the principle of conservation of power. Unlike previous work, which assumed only radiated losses were present, the proposed method is able to characterize the radiated power in environments that contain material losses and when there are multiple signals at the printed circuit board (PCB)/connector interface. The power losses are quantified through the definition of power loss constant matrices that can be used to find the power losses for arbitrary input excitations when the matrices are entirely known. The power loss constant matrices can be calculated through multiple single port and two port excitations for an *N*-port connector. The formulation of these excitations is dictated by the non-linear properties of the power loss calculation. Simulations and measurements are presented that validate the proposed power loss calculation methodology, and practical simulation problems related to finding the full power loss constant matrices are discussed.

Index Terms—Connectors, electromagnetic radiation, printed circuit board connectors, radiated power, scattering parameters

I. INTRODUCTION

Connector design has become an increasingly complex, engineering challenge for printed circuit board (PCB) applications due to ever increasing data rates and the miniaturization of circuit designs. The connectors implemented in today’s multi-PCB systems often require a tremendous amount of signal line density while also requiring minimal signal degradation through crosstalk and material losses. Connector design requirements of the past were often dominated by signal integrity and mechanical requirements with little regard to electromagnetic interference (EMI). Slower data rates allowed these connectors to be ineffective radiators due to their small size relative to even the smallest operating wavelength. Thus, EMI from the connectors themselves could often be ignored with little consequence. The electrically small connectors were often part of a much larger and more efficient dipole-like radiating structure consisting of attached PCBs, cables, or enclosures [1]-[4]. The radiation resulting from these dipole-like structures, however, could not be ignored. A common design approach to minimize radiation facilitated by the electrically small connectors was to reduce the return inductance of these connectors so the feed voltage of the dipole-like structure was reduced [3], [4].

The radiation physics of connectors today are different from the past due to increasing data rates, presently on the order of several Gbps or more [5]. Many connectors are now electrically large and have been shown to radiate effectively [6]-[9]. The connectors themselves can now comprise the majority of the radiating antenna structure due to significant, high-frequency spectral content in data signals. These electrically large connectors require more innovative solutions to mitigate EMI, and more robust methods to quantify radiation from connectors than provided in the literature at present. Much research on electromagnetic radiation due to connectors is based on the current and voltage driven models presented in [2]. Many studies have explored radiation effects through experimental methods with finite-difference time-domain simulations, common mode current measurements, and EM fields measurements [10]-[15]. Radiation performance was evaluated indirectly through transfer impedance measurements as in [16]-[19], and through connector inductance measurements and calculations [20]-[22]. Analytical formulations for connector inductances were also used in [20]-[22] to estimate the radiated electric field from a few common PCB/connector structures directly.

Full-wave electromagnetic simulations are an important tool for discovering the radiation physics from connectors as radiation physics discovery is often limited in measurements. One significant challenge in industry is the lack of robust connector simulation models and simulation methods to quantify the radiation from high-density connectors (connectors containing 10’s or even 100’s of signal lines) where input signals can be easily modified. Much of the literature focuses on computationally small problems with significant geometry simplifications from a realistic product to ease the computational and geometry creation burden [23]-[27]. While simplified structures can provide some insight into the general radiation physics, subtle but important details in the actual geometry of high-density connectors has been shown to significantly alter the radiation properties of PCB/connector structures [7]-[9]. Many simulation methods at present have limited flexibility for evaluating electromagnetic radiation changes with different signaling conditions. Changes to signal pin assignments, signal pin terminations, or input signal characteristics often require many additional simulations with significant computation times.

The purpose of this paper is to develop a simulation method to quantify radiation from practical, high-density PCB/connector structures that enables flexibility in the evaluation of radiation mitigation solutions. The proposed method is based on power loss calculations with network parameters and field data in full-wave simulations. Unlike previous simulation studies, the proposed method is formulated to predict connector radiation in typical, lossy environments where signals on multiple signal lines can be present at a PCB/connector interface. The mathematical basis for and experimental validations of the radiated power loss calculation are shown in Section II. Practical simulation issues for the proposed radiated power calculation are discussed in Section III. Conclusions are given in Section IV.

II. POWER LOSS CALCULATIONS FROM NETWORK PARAMETERS

Radiation from PCB/connector interfaces was investigated in [6] using network parameters. In this simulation study, the radiated power was calculated from network parameters assuming the only loss mechanism was due to electromagnetic radiation. Material loss, or power loss in conductors and dielectrics, was not included in the simulations, and the radiated power was obtained using conservation of power. While the proposed method in [6] is useful for low loss PCB/connector interfaces, many practical interfaces have material loss that cannot be neglected and that can actually reduce the total radiated power from these interfaces. Application of the radiated power formula in [6] with non-negligible material loss can result in a large overestimation of the true radiated power as shown in [7], [8]. Modifications to the theory in [6] can be applied, however, to correctly predict the radiated power as will be shown. This work expands upon the connector radiation modeling concepts presented in [6] by also quantifying the radiation in the presence of multiple signals at a PCB/connector interface.

The practical connector model used to guide this study is shown in Fig. 1. This full-wave connector model was designed in CST Microwave Studio and is based on a commercial connector designed for differential signaling. Details on the connector model generation are provided in [7]-[8]. The modeled connector consists of three identical wafers placed next to one another where each wafer consists of a slice A and a slice B. The signal conductors and return conductors in each slice are alternated for properly designed signal referencing and to minimize crosstalk within the connector. Small six layer PCBs were included in the connector model to enable 125 mil long, 50 Ω single-ended stripline feed structures for each signal line in the connector. The stripline feeds are asymmetric with a 48.3 mil total dielectric thickness between the return planes and a 7.95 mil separation distance from the signal traces to the nearest return plane. Layers two and five are signal layers in the PCB. The PCB dimensions are 505 mils x 715 mils x 111 mils, where all the signal layers and return layers have 1.35 mil conductor thicknesses. All conductors were modeled as perfected electric conductors and the modeled dielectrics in the PCB and connector were modeled with losses. The relative permittivity and the loss tangent of the connector plastic was modeled as $\varepsilon_r = 3.1$ and $\tan\delta = 0.02$, respectively. The PCB FR4 substrates were modeled with a relative permittivity of $\varepsilon_r = 4.3$ and a loss tangent of $\tan\delta = 0.025$. A total of 96 signal ports were defined, and discrete face ports were defined at the end of each stripline trace with 50 Ω reference impedances. The PCB/connector structure was modeled in air with PML absorbing boundary conditions. Additional details about a similar connector model, the actual connector geometry, and the simulation details are given in [7]-[8].

A. Power Loss as a Function of Loss Constant Matrices

The total power loss at a PCB/connector interface can be written as a summation of radiated power loss and material power loss as

$$P_{loss,total} = P_{rad,total} + P_{mat,total}, \tag{1}$$

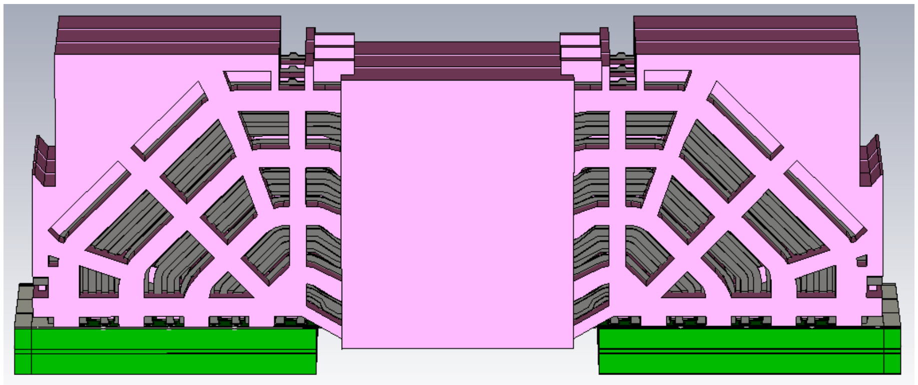

Fig. 1. Full-wave connector model used to formulate methods to quantify PCB/connector interface radiation.

where, $P_{loss,total}$ is the total power loss, $P_{rad,total}$ is the total radiated power, and $P_{mat,total}$ is the total material loss. From [6], scattering parameters can be used to calculate the total power loss as

$$P_{loss,total} = (1/2)[\bar{a}]^H\left([\tilde{I}]-[\tilde{S}]^H[\tilde{S}]\right)[\bar{a}] \tag{2}$$

where $[\bar{a}]$ is an incident power wave vector with units of $\sqrt{Watt}$ and is based on generalized scattering parameters [28], H denotes the complex conjugate transpose, $[\tilde{I}]$ is the identity matrix, and $[\tilde{S}]$ is the single-ended S-parameter matrix at ports with well-defined voltages and currents that define transverse electromagnetic wave propagation. The total radiated power and the total material loss in (1) cannot be separated from the total power loss without additional external information. In full-wave simulations, field monitors can separate these two loss mechanisms using the calculated fields. In measurements, the radiated power can be measured directly.

The total power loss in (1) is dependent on PCB/connector geometry (which dictates the PCB/connector S-parameters) and the incident waves at the connector ports as shown in (2). Although the expressions for $P_{rad,total}$ and $P_{mat,total}$ as a function of geometry and incident waves are not specified in (1), it is postulated that they take a similar form to that of $P_{loss,total}$. For convenience, a general power loss equation that can represent any of the power losses is defined as

$$P_{loss} = (1/2)[\bar{a}]^H [\bar{a}] - (1/2)[\bar{a}]^H [\tilde{P}_{const}][\bar{a}], \tag{3}$$

where, $[\tilde{P}_{const}]$ is a frequency dependent power loss constant matrix and is defined by

$$[\tilde{P}_{const}] = \begin{bmatrix} P_{1,1} & P_{1,2} & \cdots & P_{1,n} \\ P_{2,1} & P_{2,2} & \cdots & P_{2,n} \\ \vdots & \vdots & \ddots & \vdots \\ P_{n,1} & P_{n,2} & \cdots & P_{n,n} \end{bmatrix} = \begin{bmatrix} P_{1,1} & P_{1,2} & \cdots & P_{1,n} \\ P_{1,2}^* & P_{2,2} & \cdots & P_{2,n} \\ \vdots & \vdots & \ddots & \vdots \\ P_{1,n}^* & P_{2,n}^* & \cdots & P_{n,n} \end{bmatrix}. \tag{4}$$

The matrix, $[\tilde{P}_{const}]$, is termed as a “power loss constant matrix” with reference that the matrix is used to quantify power loss in (3). Physically this matrix quantifies the total power received from all ports. The total power loss, the total radiated power, and the total material loss can be written in the same form as (3) as shown in (5)-(7).

$$P_{loss,total} = (1/2)[\bar{a}]^H [\bar{a}] - (1/2)[\bar{a}]^H [\tilde{P}_{loss,const}][\bar{a}] \tag{5}$$

$$P_{rad,total} = (1/2)[\bar{a}]^H [\bar{a}] - (1/2)[\bar{a}]^H [\tilde{P}_{rad,const}][\bar{a}] \tag{6}$$

$$P_{mat,total} = (1/2)[\bar{a}]^H [\bar{a}] - (1/2)[\bar{a}]^H [\tilde{P}_{mat,const}][\bar{a}] \tag{7}$$

Comparing (2) and (5) the total power loss constant matrix is defined as

$$[\tilde{P}_{loss,const}] = [\tilde{S}]^H [\tilde{S}], \tag{8}$$

whereas, the radiated power constant matrix, $[\tilde{P}_{rad,const}]$, and the material loss constant matrix, $[\tilde{P}_{mat,const}]$, are unknown in general. The power loss constant matrices fully characterize the power loss in any system with ports. Once the power loss constant matrices are known, radiation and signal integrity performance may be evaluated with customizable input signaling and port termination conditions. The radiated power constant matrix and the material loss constant matrix can be found in full-wave simulations with the right port excitations and field monitors as will be illustrated.

B. *Properties of the Power Loss Calculation and Port Excitation Solutions for the Power Loss Constants*

In general, the power losses in (5)-(7) can be written as a summation of power losses for all possible two port combinations in an *N*-port connector. To illustrate this point, consider a three port network where all three ports are fed with incident power waves a_x, a_y, a_z where,

$$[\overline{a}] = \begin{bmatrix} a_x \\ a_y \\ a_z \end{bmatrix} = \begin{bmatrix} a_x \\ 0 \\ 0 \end{bmatrix} + \begin{bmatrix} 0 \\ a_y \\ 0 \end{bmatrix} + \begin{bmatrix} 0 \\ 0 \\ a_z \end{bmatrix} = [\overline{A}] + [\overline{B}] + [\overline{C}]. \tag{9}$$

The general power loss equation in (3) can then be written as

$$\begin{aligned} P_{loss} &= (1/2)([\overline{A}]+[\overline{B}]+[\overline{C}])^H([\overline{A}]+[\overline{B}]+[\overline{C}]) - (1/2)([\overline{A}]+[\overline{B}]+[\overline{C}])^H[\widetilde{P}_{const}]([\overline{A}]+[\overline{B}]+[\overline{C}]) \\ &= (1/2)\left\{ |a_x|^2 + |a_y|^2 + |a_z|^2 - sum\left(\begin{bmatrix} [\overline{A}]^H[\widetilde{P}_{const}][\overline{A}] & [\overline{A}]^H[\widetilde{P}_{const}][\overline{B}] & [\overline{A}]^H[\widetilde{P}_{const}][\overline{C}] \\ [\overline{B}]^H[\widetilde{P}_{const}][\overline{A}] & [\overline{B}]^H[\widetilde{P}_{const}][\overline{B}] & [\overline{B}]^H[\widetilde{P}_{const}][\overline{C}] \\ [\overline{C}]^H[\widetilde{P}_{const}][\overline{A}] & [\overline{C}]^H[\widetilde{P}_{const}][\overline{B}] & [\overline{C}]^H[\widetilde{P}_{const}][\overline{C}] \end{bmatrix} \right) \right\} \end{aligned} \tag{10}$$

where, the *sum* function is the summation of all elements in the 3x3 matrix in this example. It can be seen that (10) contains the power losses for all possible two port excitations in a three port network. Thus, the values in $[\widetilde{P}_{rad,const}]$ and $[\widetilde{P}_{mat,const}]$ can be found by solving for the power loss constants for all possible two port combinations.

The types of excitations to find the power loss constants for a two port combination are greatly influenced by the non-linearity of the power loss calculation. In the case of (10), if $a_x \neq 0$, $a_y \neq 0$, and $a_z = 0$, then the power loss for this two port excitation is given by

$$P_{loss,pxpy} = (1/2)\left\{|a_x|^2 + |a_y|^2 - [\bar{A}]^H [\tilde{P}_{const}][\bar{A}] - [\bar{B}]^H [\tilde{P}_{const}][\bar{B}] - [\bar{A}]^H [\tilde{P}_{const}][\bar{B}] - [\bar{B}]^H [\tilde{P}_{const}][\bar{A}]\right\}. \tag{11}$$

In contrast, when port *x* and port *y* are fed independently, the power losses are given by

$$P_{loss,px} = (1/2)\left\{|a_x|^2 - [\bar{A}]^H [\tilde{P}_{const}][\bar{A}]\right\} \tag{12a}$$

$$P_{loss,py} = (1/2)\left\{|a_y|^2 - [\bar{B}]^H [\tilde{P}_{const}][\bar{B}]\right\}. \tag{12b}$$

It can be seen from (11) and (12) that $P_{loss,px} + P_{loss,py} \neq P_{loss,pxpy}$ which indicates that the power loss calculation is not linear. To further illustrate the non-linearity of the power loss calculation, a series of simulations were performed with the connector in Fig. 1. The longest differential pair in slice A of the middle wafer was excited with a common-mode excitation with 1 W total input power, and all other ports were terminated in matched loads. The radiated power was then calculated in the full-wave simulation. Next, the signal lines in the excited differential pair were fed independently with 0.5 W, and the calculated radiated powers were added. A comparison of these two radiated power calculations is shown in Fig. 2. It can be seen that radiated power for the simultaneous port excitation is not equal to a linear superposition of the individual excitations. Thus, calculating the radiated power loss and the material power loss for a simultaneous, multi-port excitation requires single port and well-designed two port excitations to find the full $[\tilde{P}_{rad,const}]$ and $[\tilde{P}_{mat,const}]$ matrices.

The excitations required to solve the unknown power loss constants can be found by investigating the power loss for a general two port excitation. Since the power losses for an *N*-port network can be written based on two port excitations, relationships obtained for a two port excitation can be used to determine parameters for an *N*-port network. When feeding a port *x* and a port *y*, where $x \neq y$, the incident power wave vector and a general power loss constant matrix can be written as

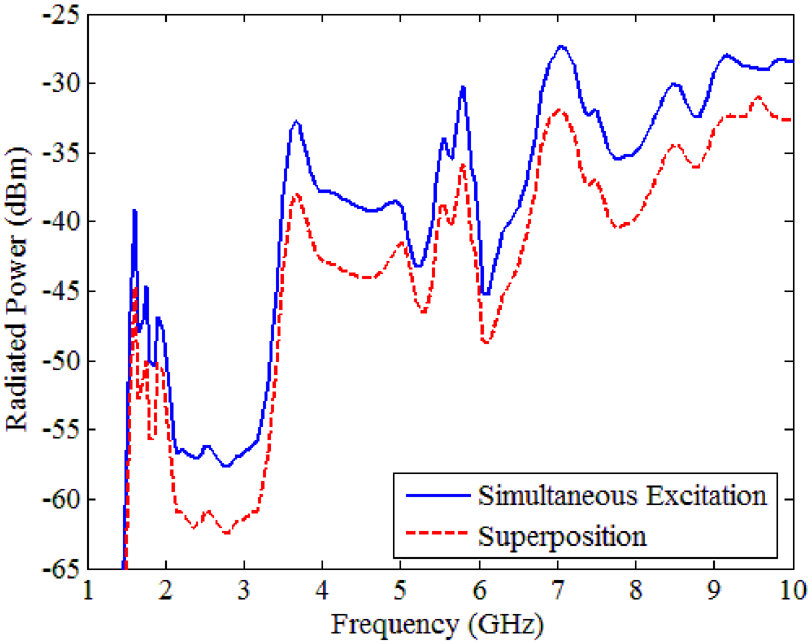

Fig. 2. A radiated power calculation example illustrating the non-linear property of the power loss calculations for the connector in Fig. 1.

$$[\bar{a}] = \begin{bmatrix} a_x \\ a_y \end{bmatrix} \tag{13a}$$

$$[\tilde{P}_{const}] = \begin{bmatrix} P_{x,x} & P_{x,y} \\ P_{y,x} & P_{y,y} \end{bmatrix}. \tag{13b}$$

The general power loss in (3) can then be written as

$$\begin{aligned} P_{loss,pxpy} = {} & (1/2)|a_x|^2 + (1/2)|a_y|^2 - (1/2)|a_x|^2 (P_{x,x}) - (1/2)|a_y|^2 (P_{y,y}) \\ & - (1/2) a_x^* a_y (P_{x,y}) - (1/2) a_x a_y^* (P_{y,x}), \end{aligned} \tag{14}$$

where, * denotes the complex conjugate. Elements on the diagonal of the power loss constant matrix in (4) and (13b) are solved from single port excitations and are purely real. These diagonal elements can be found when ports are excited one at a time as would be the case in a traditional S-parameter simulation or a measurement. The diagonal elements in the power loss constant matrix in (13b) can be found from

$$P_{x,x} = 1 - \frac{2P_{loss,pxpy}}{\left|a_x\right|^2} \text{ for } a_x \neq 0, a_y = 0 \tag{15a}$$

$$P_{y,y} = 1 - \frac{2P_{loss,pxpy}}{\left|a_y\right|^2} \text{ for } a_x = 0, a_y \neq 0 \cdot \tag{15b}$$

Off-diagonal elements in the power loss constant matrix in (4) and (13b) are solved from two port excitations and are complex valued. For the power loss to be purely real, the power loss constant matrix must satisfy reciprocity with a complex conjugate transpose, or, $\left[\tilde{P}_{const}\right] = \left[\tilde{P}_{const}\right]^H$. This property can be illustrated from the two port power loss expression in (14) as follows. Consider the last two terms in (14) with the minus sign factored out as shown in (16).

$$P_{terms,pxpy} = (1/2)a_x^* a_y \left(P_{x,y}\right) + (1/2)a_x a_y^* \left(P_{y,x}\right) \tag{16}$$

If $a_x = a + jb$, $a_y = c + jd$, $P_{x,y} = e + jf$, and $P_{y,x} = g + jh$, then (16) reduces to

$$\begin{aligned} P_{terms,pxpy} &= (1/2)(a - jb)(c + jd)(e + jf) + (1/2)(a + jb)(c - jd)(g + jh) \\ &= (1/2)\{(ac + bd)(e + g) + (bc - ad)(f - h)\} \\ &\quad + j(1/2)\{(ad - bc)(e - g) + (ac + bd)(f + h)\}. \end{aligned} \tag{17}$$

For (17) to be real, $P_{y,x} = P_{x,y}^*$ so $g = e$ and $h = -f$. Equation (17) then reduces to

$$P_{terms,pxpy} = e(ac + bd) + f(bc - ad) \tag{18}$$

or, more generally,

$$\begin{aligned} P_{terms,pxpy} &= \mathrm{Re}\{P_{x,y}\}\left(\mathrm{Re}\{a_x\}\mathrm{Re}\{a_y\} + \mathrm{Im}\{a_x\}\mathrm{Im}\{a_y\}\right) \\ &\quad + \mathrm{Im}\{P_{x,y}\}\left(\mathrm{Im}\{a_x\}\mathrm{Re}\{a_y\} - \mathrm{Re}\{a_x\}\mathrm{Im}\{a_y\}\right). \end{aligned} \tag{19}$$

It is also observed that the total power loss constant matrix follows $\left[\tilde{P}_{const}\right]=\left[\tilde{P}_{const}\right]^H$ since, $\left[\tilde{P}_{loss,const}\right]=\left[\tilde{S}\right]^H\left[\tilde{S}\right]$ and $\left[\tilde{P}_{loss,const}\right]^H=\left(\left[\tilde{S}\right]^H\left[\tilde{S}\right]\right)^H=\left[\tilde{S}\right]^H\left[\tilde{S}\right]$ as is expected.

The real and imaginary parts of the complex power loss constant $P_{x,y}$ in (14) can be found from two linearly independent excitations after the real power loss constants, $P_{x,x}$ and $P_{y,y}$, have been evaluated from (15). Both the real and imaginary parts of $P_{x,y}$ satisfy the equation,

$$\begin{bmatrix} A_{11} & A_{12} \\ A_{21} & A_{22} \end{bmatrix}\begin{bmatrix} \mathrm{Re}\{P_{x,y}\} \\ \mathrm{Im}\{P_{x,y}\} \end{bmatrix}=\begin{bmatrix} B_1 \\ B_2 \end{bmatrix} \tag{20}$$

where,

$$A_{11}=\mathrm{Re}\{a_x\}_{exc1}\,\mathrm{Re}\{a_y\}_{exc1}+\mathrm{Im}\{a_x\}_{exc1}\,\mathrm{Im}\{a_y\}_{exc1} \tag{21a}$$

$$A_{12}=\mathrm{Im}\{a_x\}_{exc1}\,\mathrm{Re}\{a_y\}_{exc1}-\mathrm{Re}\{a_x\}_{exc1}\,\mathrm{Im}\{a_y\}_{exc1} \tag{21b}$$

$$A_{21}=\mathrm{Re}\{a_x\}_{exc2}\,\mathrm{Re}\{a_y\}_{exc2}+\mathrm{Im}\{a_x\}_{exc2}\,\mathrm{Im}\{a_y\}_{exc2} \tag{21c}$$

$$A_{22}=\mathrm{Im}\{a_x\}_{exc2}\,\mathrm{Re}\{a_y\}_{exc2}-\mathrm{Re}\{a_x\}_{exc2}\,\mathrm{Im}\{a_y\}_{exc2} \tag{21d}$$

$$B_1=-P_{loss,\,pxpy,exc1}+\frac{1}{2}|a_x|^2_{exc1}+\frac{1}{2}|a_y|^2_{exc1}-\frac{1}{2}|a_x|^2_{exc1}\left(P_{x,x}\right)-\frac{1}{2}|a_y|^2_{exc1}\left(P_{y,y}\right) \tag{22a}$$

$$B_2=-P_{loss,\,pxpy,exc2}+\frac{1}{2}|a_x|^2_{exc2}+\frac{1}{2}|a_y|^2_{exc2}-\frac{1}{2}|a_x|^2_{exc2}\left(P_{x,x}\right)-\frac{1}{2}|a_y|^2_{exc2}\left(P_{y,y}\right) \tag{22b}$$

and *exc1* and *exc2* denote two different excitation cases. Two excitations that solve for the real and imaginary parts of $P_{x,y}$ directly in frequency-domain simulations are a common-mode excitation ($a_{x,exc1}=1,\ a_{y,exc1}=1$) and a phase shifted excitation ($a_{x,exc2}=j$, $a_{y,exc2}=1$). Using these excitations (20) reduces to

$$\mathrm{Re}\{P_{x,y}\}=1-P_{loss,\,pxpy,exc1}-\frac{1}{2}\left(P_{x,x}\right)-\frac{1}{2}\left(P_{y,y}\right) \tag{23a}$$

$$\mathrm{Im}\{P_{x,y}\}=1-P_{loss,\,pxpy,exc2}-\frac{1}{2}\left(P_{x,x}\right)-\frac{1}{2}\left(P_{y,y}\right). \tag{23b}$$

It should be noted that a common-mode excitation ($a_x = 1,\ a_y = 1$) and a differential-mode excitation ($a_x = 1,\ a_y = -1$) were not chosen to solve for $P_{x,y}$ in (20) because these two excitations are not linearly independent in reference to (20). Assuming prior single port excitations were performed, a common-mode excitation and a differential-mode excitation will only yield the real part of a complex power loss constant.

Although the preceding analysis is in the frequency-domain, time-domain simulations may also be used to quantify the power losses at a PCB/connector interface. In time-domain simulations, only port incident wave magnitudes and time shifts are defined directly. The phase of an input signal is only defined through the Fourier transform properties $x(t) \leftrightarrow X(f)$ and $x(t-t_0) \leftrightarrow X(f)e^{-j2\pi f t_0}$ where a phase shift is defined by $\theta = -2\pi f t_0$ [29]. A common-mode excitation can be specified for a time-domain, two-port excitation when there is no time shift for both excitations. A phase shifted excitation where the two port excitations are out of phase by 90° cannot be defined for all frequencies in a time-domain solver, but the only requirement to solve for $P_{x,y}$ is that the two, two port excitations be linearly independent in (20). An example choice of two excitation sets for a time-domain simulation is given in (24). Suppose that excitation one and excitation two are given by

$$a_{x,exc1} = \left|a_{x,exc1}\right|,\ a_{y,exc1} = \left|a_{y,exc1}\right| \tag{24a}$$

$$a_{x,exc2} = \left|a_{x,exc2}\right|,\ a_{y,exc2} = \left|a_{y,exc2}\right|(\cos\theta + j\sin\theta) \tag{24b}$$

where, the phase in $a_{y,exc2}$ is created from a time delay t_0. Applying (24) to (20), the determinant of $[A]$ in (20) is given by,

$$\det[A] = -\left|a_{x,exc1}\right|\left|a_{y,exc1}\right|\left|a_{x,exc2}\right|\left|a_{y,exc2}\right|\sin\theta \tag{25}$$

and is zero when $\theta = -n\pi$ where n is a positive integer. It then follows that $P_{x,y}$ cannot be solved in general from the excitations in (24) at discrete frequencies given by

$f = n/(2t_0)$. Thus, the time delay that defined the phase in (24b) must be carefully chosen so the calculation of $P_{x,y}$ can be performed over any frequency band of interest. For some broadband simulations a third, two-port excitation with a different time delay than in (24b) may be necessary to calculate $P_{x,y}$ at frequencies that are inappropriate for the excitations in (24).

C. *Power Loss Relationships for Total Power Loss, Radiated Power Loss, and Material Power Loss*

Relationships among $[\tilde{P}_{loss,const}]$, $[\tilde{P}_{rad,const}]$ and $[\tilde{P}_{mat,const}]$ in (5)-(7) can also be derived from a general two port excitation. If a port *x* and a port *y* are fed where $x \neq y$ and the incident power wave vector is given by (13a), then the matrices for the power loss constants can be written as,

$$[\tilde{P}_{loss,const}] = \begin{bmatrix} P_{lx,x} & P_{lx,y} \\ P^*_{lx,y} & P_{ly,y} \end{bmatrix} \tag{26a}$$

$$[\tilde{P}_{rad,const}] = \begin{bmatrix} P_{rx,x} & P_{rx,y} \\ P^*_{rx,y} & P_{ry,y} \end{bmatrix} \tag{26b}$$

$$[\tilde{P}_{mat,const}] = \begin{bmatrix} P_{mx,x} & P_{mx,y} \\ P^*_{mx,y} & P_{my,y} \end{bmatrix}. \tag{26c}$$

From (1), (5)-(7), and (26), the diagonal elements in the power loss constant matrices follow

$$-P_{lx,x} + P_{rx,x} + P_{mx,x} = 1 \tag{27a}$$

$$-P_{ly,y} + P_{ry,y} + P_{my,y} = 1 \tag{27b}$$

where $a_x \neq 0$ and $a_y = 0$ was applied to find (27a) and $a_x = 0$ and $a_y \neq 0$ was applied to find (27b). Similarly, the real and imaginary parts of the complex power loss constants are related by

$$\mathrm{Re}\{P_{rx,y}\}+\mathrm{Re}\{P_{mx,y}\}=\mathrm{Re}\{P_{lx,y}\} \tag{28a}$$

$$\mathrm{Im}\{P_{rx,y}\}+\mathrm{Im}\{P_{mx,y}\}=\mathrm{Im}\{P_{lx,y}\} \tag{28b}$$

which can be condensed to

$$P_{rx,y}+P_{mx,y}=P_{lx,y}\,. \tag{28c}$$

A common-mode excitation ($a_x = 1,\ a_y = 1$) was applied to find (28a) and a phase shifted excitation ($a_x = j,\ a_y = 1$) was applied to find (28b). Combining (27) and (28), the power loss constant matrices are related generally for an *N*-port connector by

$$\left[\tilde{P}_{loss,const}\right]=\left[\tilde{P}_{rad,const}\right]+\left[\tilde{P}_{mat,const}\right]-\left[\tilde{I}\right]. \tag{29}$$

D. A Multi-signal Power Loss Quantification Example

A series of full-wave time-domain simulations were performed with the connector shown in Fig. 1. The simulations were designed so the power losses may be characterized when the two longest pairs in slice A of the second wafer were fed and all other ports were matched. A far-field monitor was defined in CST Microwave Studio so the radiated power could be calculated from the fields on the bounding box of the calculation domain. An S-parameter simulation was first performed to characterize the total power loss, and a full S-parameter matrix containing information about all 96 ports in the connector was obtained. In addition, the single port excitation radiated powers were calculated and recorded during the S-parameter simulation. Next, custom simulations were performed where two port combinations of the feed ports for the differential pairs under study were excited. Common-mode and time-delay excitations as indicated in (24a) and (24b), respectively, were performed to facilitate the calculation of the real and imaginary parts of the complex radiated power loss constants. The time-delay excitation used a 45 ps delay to optimize the calculation of the complex radiated power loss constants over 1

GHz – 10 GHz. The S-parameters and the radiated power data for all the excitations were post-processed using (15), (20), and (29) to calculate the total power loss constant matrix, the radiated power loss constant matrix, and the material power loss constant matrix.

To validate the proposed power loss calculation method, the radiated power loss and the material power loss were evaluated for a random excitation where both signal pairs were fed. A full-wave simulation was performed to calculate the radiated power directly from the fields on the bounding box of the calculation domain. The non-zero port excitations are given by

$$[\bar{a}_{sub}] = \begin{bmatrix} a_{41} \\ a_{43} \\ a_{45} \\ a_{47} \end{bmatrix} = \begin{bmatrix} 1.67\angle -2\pi f\left(18e-12\right) \\ 0.44\angle -2\pi f\left(3e-12\right) \\ 0.51\angle -2\pi f\left(34e-12\right) \\ 1.11\angle -2\pi f\left(23e-12\right) \end{bmatrix}, \tag{30}$$

where, f is frequency in Hz, port 41 and port 43 are the feed ports for the shorter differential pair, and port 45 and port 47 are the feed ports for the longer differential pair. In this example the shortest signal conductor was excited by port 41 and the longest signal conductor was excited by port 47. The phases of the input excitations in (30) are defined according to the signal time delays indicated in parentheses. It should be noted that a partial incident wave vector is defined in (30). All other incident power waves not listed in (30) were zero since all other ports were matched. A comparison of the radiated power loss, the material power loss, and the total power loss for the excitation in (30) are shown in Fig. 3 using (5)-(7). It can be seen that the total power loss is dominated by the material losses as has been previously reported in [7], [8]. The radiated power calculated directly from the fields for the excitation in (30) is also shown in Fig. 3. The maximum deviation between the radiated power calculated from (6) and the direct calculation of the fields is 0.05 dB. An additional simulation was also performed with the excitation in (30) where power loss monitors were defined so the material power losses could be calculated directly from the fields in the lossy media. A comparison of the material power loss using the total power loss and the radiated power loss in (29) and the direct calculation is shown in Fig. 4. In the worst case the material power loss calculation differs by 0.2 dB or 3.8 %.

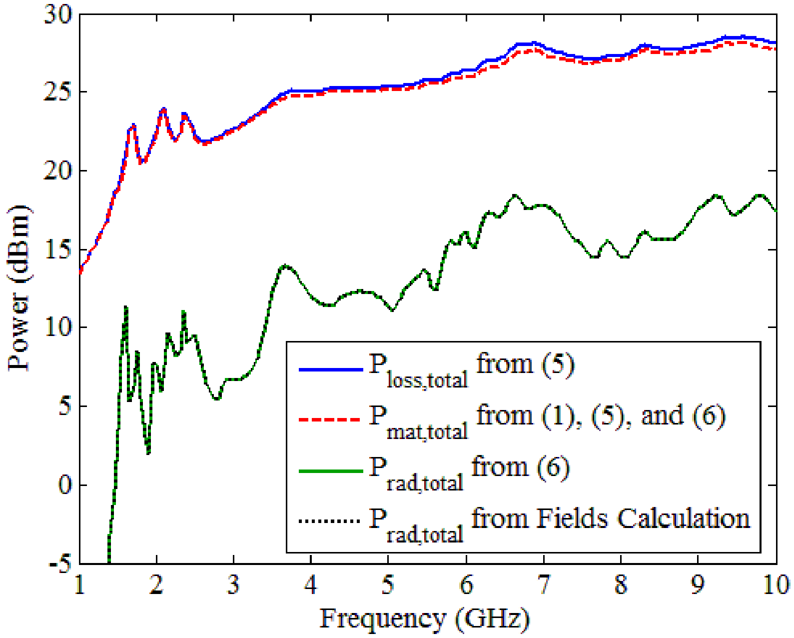

Fig. 3. Comparison of the total power loss, material power loss, and the radiated power loss for the random excitation in (30).

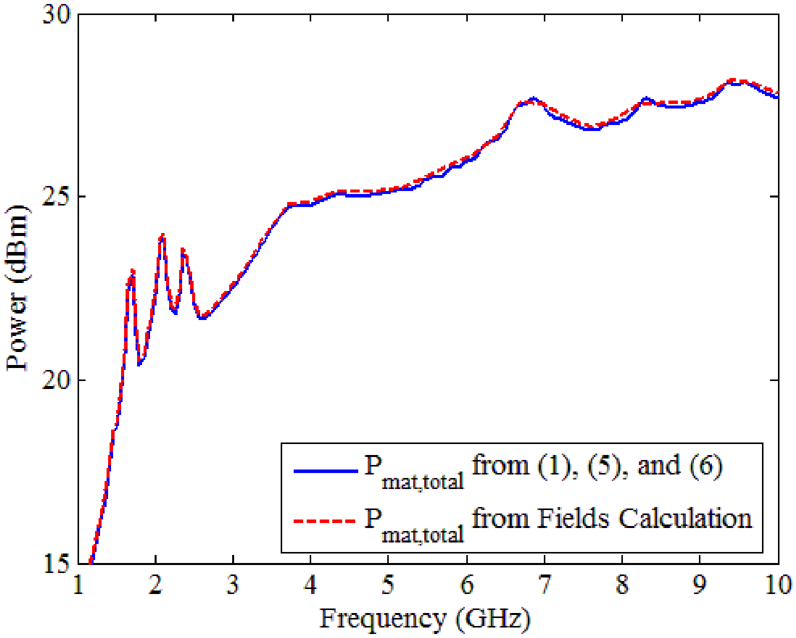

Fig. 4. Comparison of the material power loss calculations for the random excitation in (30).

E. Radiated Power Characterization with Reverberation Chamber Measurements

Although the focus of this paper is to develop a simulation method for power loss characterization at PCB/connector interfaces using full-wave simulations, the presented theory also applies to measurements. A series of reverberation chamber measurements were performed on the connector shown in Fig. 6(a) of [7] and Fig. 6 of [8]. The radiated power was characterized for the 3rd differential pair (from shortest to longest) in slice A of the middle wafer. The ports on the other end of the fed differential pair were terminated in matched loads and all other ports were left open. Five continuous wave radiated power measurements were performed in the reverberation chamber to quantify the radiated power loss constants. The characterization measurements consisted of two single-ended excitations, a common-mode excitation using a resistive power splitter with two connecting cables approximately the same length, and two phase shifted excitations that used a resistive power splitter and phase shifters. The phase shifted excitations utilized phase shifters to make the phase difference between the incident power wave excitations 90° near 6 GHz and 13 GHz in the two measurements. Two phase shifted measurements were required to quantify the complex power loss constant due to the large frequency range of the measurement (1-18 GHz). A 20 dB attenuator was connected to each excited port in all of the measurements to minimize multiple wave reflections in the measurements. The insertion loss and the phase progression of the cabling, power splitter, phase shifters, and attenuator chains were measured to facilitate proper calculation of the incident power waves at the PCB/connector ports. The data from the five radiated power measurements was used to calculate the radiated power loss constants when incident power waves were present at the fed differential pair. To validate the radiated power constant matrix calculation, a 6th radiated power measurement was performed. This additional measurement consisted of a two port excitation generated from a resistive power splitter and two unequal length cables. The difference in incident wave unwrapped phases varied from 31° to 541° over the measured frequency range. The radiated power was calculated using the radiated power loss constants and compared to the measurement with 0 dBm input power to the power splitter as shown in Fig. 5. The measured and calculated results agree to within fractions of a decibel over most of the frequency range and within a few decibels in the worst case near 2.5 GHz.

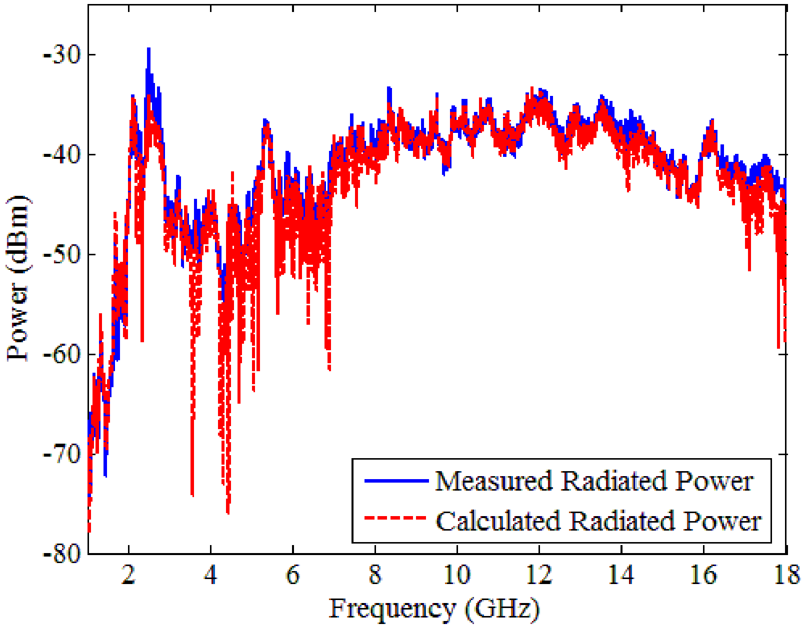

Fig. 5. Comparison of a measured and calculated radiated power loss for a continuous wave common-mode excitation with unequal cable lengths.

III. PRACTICAL ISSUES ARISING FROM SOLVING FOR THE POWER LOSS CONSTANT MATRICES

A. Computational Considerations in Solving for the Material and Radiated Power Losses

Power losses in a connector with known incident power waves can be evaluated once the power loss constant matrices are calculated from the methods presented in Section II. The total power loss constants can be calculated from S-parameters obtained through a traditional S-parameter simulation as in (8). The radiated power constants and the material power loss constants can be calculated with output data from full-wave simulations when appropriate field monitors are defined and the correct port excitations applied. Radiated power can be calculated using the fields at the PML boundaries enclosing a PCB/connector structure with data post-processing. Material power losses can also be calculated from the fields inside the lossy materials. In general, it is more desirable to solve for the total power loss constant matrix and only one of the remaining power loss constant matrices directly. Solving for all of the power loss constants directly with field information is potentially computationally intensive as well as computer memory intensive. Equation (29) can be used to find unknown power loss constants when two of the three power loss constant matrices are known.

Choosing to solve for either the radiated power loss constant matrix or the material power loss constant matrix directly from the fields is critical for large scale models. Finding the material power loss constants directly has the advantage that only single port excitation simulations are needed. The complex material loss constants can be evaluated from common-mode and phase shifted excitations defined with post-processing steps. One disadvantage of using (29) to calculate the radiated power loss constants is that the radiated power is only evaluated at relatively few frequency points as defined by the number of material power loss monitors in the simulation. In addition, each single port excitation requires a tremendous amount of hard drive space for practical connector models since the fields are saved everywhere in the computational domain.

An alternate simulation strategy is to solve for the radiated power loss constants directly with field information. This method has the advantage that the radiated power, which is often the desired quantity of interest, is found directly and can be defined with many frequency points. A moderate amount of hard drive space is required for practical connector models when compared to simulations calculating the material loss constants directly. Only field information on the bounding box of the computational domain must be saved for the radiated power calculation. Additional radiated powers for common-mode and phase shifted excitations can be calculated as post-processing steps from the single port simulations. Solving for the radiated power loss constants directly in many cases is the only practical choice to find the power loss constants due to hard drive space limitations and is preferred.

B. Computational Reduction Methods with Known Input Signaling and Worst Case Analysis

Although relatively little can be done to reduce computational model size to achieve accurate power loss characterization, the total number of simulations required to characterize power losses can be reduced with some input signaling assumptions and using worst case analysis. If the input signaling and terminations at a PCB/connector interface are known a priori to quantifying the power losses, then it is feasible that full power loss constant matrices are not needed to fully quantify the power losses. More specifically, power loss constants involving ports that do not have incident power waves do not need to be calculated since there are no power loss contributions from these port excitations. The total number of excitations required to fill the entire power loss constant matrices, assuming only two excitations are needed to solve for each unique complex loss constant, is N^2. If the entire power loss constant matrices are known, then the power losses may be quantified where incident power waves are present at all ports. Realistically, incident power waves may not be present at all ports since simultaneous, bidirectional transmission is not used with link protocols at present. In the worst case only half of a PCB/connector interface contains incident power waves due to signaling sources. It is possible for designated receive ports to have non-zero incident power waves caused by port termination mismatches; however, if all the receive ports are terminated with matched loads, then the minimum total number of excitations to fully characterize the power losses is reduced to $N^2 - 2N$. Further simulation reductions may also be realized if some of the signal lines are not used and if fixed transmit and receive port assignments are also implemented.

Worst case analysis can also reduce the total number of simulations required to characterize power losses and is useful when input signaling and termination information does not sufficiently reduce the total number of simulations. This type of analysis is an inexact method to characterize power losses within a connector and is less preferred over using input signaling and termination information to reduce the total number of simulations. In the worst case it is assumed that the incident power waves are configured for maximum total power loss, and the total power loss is solely due to radiated power loss. The radiated power loss in (6) can be modified to include worst case analysis and is written as,

$$P_{rad,total} \approx (1/2)[\bar{a}]^H[\bar{a}] - (1/2)[\bar{a}]^H\left[\tilde{P}^{\mathrm{mod}}_{rad,const}\right][\bar{a}] - (1/2)[|\bar{a}|]^T\left[\tilde{P}_{rad,const,wc}\right][|\bar{a}|] \qquad (31)$$

where, T is a non-conjugate transpose, $\left[\tilde{P}_{rad,const}^{\mathrm{mod}}\right]$ is the modified radiated power loss constant matrix, and $\left[\tilde{P}_{rad,const,wc}\right]$ is the worst case power loss constant matrix. $\left[\tilde{P}_{rad,const}^{\mathrm{mod}}\right]$ is equivalent in form to (4) except zeroes are in place of the off-diagonal elements chosen for worst case analysis. The diagonal of $\left[\tilde{P}_{rad,const,wc}\right]$ contains zeroes, and only the port combinations chosen for worst case analysis are non-zero. If, for example, all port combinations are chosen for worst case analysis, the modified radiated power loss constant matrix and the worst case power loss constant matrix are

$$\left[\tilde{P}_{rad,const}^{\mathrm{mod}}\right]=\begin{bmatrix} P_{r1,1} & 0 & \cdots & 0 \\ 0 & P_{r2,2} & \cdots & 0 \\ \vdots & \vdots & \ddots & \vdots \\ 0 & 0 & \cdots & P_{rn,n} \end{bmatrix} \tag{32}$$

$$\left[\tilde{P}_{rad,const,wc}\right]=\begin{bmatrix} 0 & P_{rwc1,2} & \cdots & P_{rwc1,n} \\ P_{rwc1,2} & 0 & \cdots & P_{rwc2,n} \\ \vdots & \vdots & \ddots & \vdots \\ P_{rwc1,n} & P_{rwc2,n} & \cdots & 0 \end{bmatrix} \tag{33}$$

$$P_{rwc1,2} = -\left(\left|\mathrm{Re}\left\{P_{l1,2}\right\}\right| + \left|\mathrm{Im}\left\{P_{l1,2}\right\}\right|\right) \tag{34a}$$

$$P_{rwc1,n} = -\left(\left|\mathrm{Re}\left\{P_{l1,n}\right\}\right| + \left|\mathrm{Im}\left\{P_{l1,n}\right\}\right|\right) \tag{34b}$$

$$P_{rwc2,n} = -\left(\left|\mathrm{Re}\left\{P_{l2,n}\right\}\right| + \left|\mathrm{Im}\left\{P_{l2,n}\right\}\right|\right) \tag{34c}$$

where, the P_l values in (34) are total power loss constants defined in (8).

The worst case radiated power constants in (33) are derived from the fundamental two port example given in (14). The last two terms in (14), which are expanded in (19), are the only terms that can cause variations in the power loss due to signal phase. In the worst case, it is assumed that these terms constructively add. If the incident power waves and the complex power loss constant are written in rectangular format where,

$$a_x = \left|a_x\right|\cos\theta_x + j\left|a_x\right|\sin\theta_x \tag{35a}$$

$$a_y = \left|a_y\right|\cos\theta_y + j\left|a_y\right|\sin\theta_y \tag{35b}$$

$$P_{x,y} = \mathrm{Re}\left\{P_{x,y}\right\} + j\,\mathrm{Im}\left\{P_{x,y}\right\}, \tag{35c}$$

then (19) becomes

$$\begin{aligned} &P_{terms,\,pxpy} = \\ &|a_x||a_y|\,\mathrm{Re}\{P_{x,y}\}(\cos\theta_x \cos\theta_y + \sin\theta_x \sin\theta_y) + |a_x||a_y|\,\mathrm{Im}\{P_{x,y}\}(\sin\theta_x \cos\theta_y - \cos\theta_x \sin\theta_y) \\ &P_{terms,\,pxpy} = \\ &|a_x||a_y|\left[\mathrm{Re}\{P_{x,y}\}\cos(\theta_x - \theta_y) + \mathrm{Im}\{P_{x,y}\}\sin(\theta_x - \theta_y)\right]. \end{aligned} \tag{36}$$

In the worst case (36) becomes

$$\min\{P_{terms,\,pxpy}\} \approx -|a_x||a_y|\left(|\mathrm{Re}\{P_{x,y}\}| + |\mathrm{Im}\{P_{x,y}\}|\right) \tag{37}$$

and, (14) reduces to

$$\begin{aligned} P_{loss,\,pxpy} &= (1/2)|a_x|^2 + (1/2)|a_y|^2 - (1/2)|a_x|^2(P_{x,x}) \\ &\quad - (1/2)|a_y|^2(P_{y,y}) + |a_x||a_y|\left(|\mathrm{Re}\{P_{x,y}\}| + |\mathrm{Im}\{P_{x,y}\}|\right). \end{aligned} \tag{38}$$

Equation (31) is derived from (38) for the *N*-port case.

Port combinations must be carefully chosen for worst case analysis so the radiated power is not largely over-predicted. The port combinations suitable for worst case analysis are those where the total power loss contribution by signal phase, in the worst case, is negligible compared to the radiated power loss contributions from single port excitations. Some details of the worst case analysis are readily illustrated with a fundamental two port example. Assume the full total power loss constant matrix is known and only the diagonal elements in the radiated power loss constant matrix are known. In the worst case, the radiated power loss can be written from (38) as,

$$P_{rad,\,wc,\,pxpy} \approx (1/2)|a_x|^2 + (1/2)|a_y|^2 - (1/2)\left(|a_x|^2(P_{rx,x}) + |a_y|^2(P_{ry,y})\right)[1 - \mathrm{term}\,1] \tag{39a}$$

$$\mathrm{term}\,1 = \frac{2|a_x||a_y|\left(|\mathrm{Re}\{P_{rx,y}\}| + |\mathrm{Im}\{P_{rx,y}\}|\right)}{|a_x|^2(P_{rx,x}) + |a_y|^2(P_{ry,y})} \tag{39b}$$

where the incident power waves are assumed to be non-zero. Since the complex radiated power loss constant, $P_{rx,y}$ is unknown, in the worst case the complex total power loss constant can be used where

$$P_{rad,wc,pxpy} \approx (1/2)|a_x|^2 + (1/2)|a_y|^2 - (1/2)\left(|a_x|^2\left(P_{rx,x}\right) + |a_y|^2\left(P_{ry,y}\right)\right)[1 - \text{term}\,2] \tag{40a}$$

$$\text{term}\,2 = \frac{2|a_x||a_y|\left(\left|\text{Re}\{P_{lx,y}\}\right| + \left|\text{Im}\{P_{lx,y}\}\right|\right)}{|a_x|^2\left(P_{rx,x}\right) + |a_y|^2\left(P_{ry,y}\right)} \tag{40b}$$

as indicated in (31). If $|a_x| \approx |a_y|$, then (40) reduces to

$$P_{rad,pxpy} \approx |a_x|^2 - (1/2)|a_x|^2\left(P_{rx,x} + P_{ry,y}\right)[1 - \text{term}\,2] \tag{41a}$$

$$\text{term}\,2 = \frac{2\left(\left|\text{Re}\{P_{lx,y}\}\right| + \left|\text{Im}\{P_{lx,y}\}\right|\right)}{P_{rx,x} + P_{ry,y}}. \tag{41b}$$

If $\text{term}\,2 \approx 0$ in (41b), this also implies that $\text{term}\,1 \approx 0$ under the same assumptions since $\text{term}\,2 \geq \text{term}\,1$. The condition $\text{term}\,2 \approx 0$ indicates that the two port combination is relatively uncoupled and suitable for worst case analysis since the coupling between ports is negligible even in the worst case. If $\text{term}\,2 \neq 0$, then the worst case analysis could significantly over-predict the radiated power. In this case it is advisable to perform the additional simulations to find the complex radiated power loss constant for the two port combination.

A similar analysis as the fundamental two port example may also be applied to an *N*-port PCB/connector structure to find suitable port combinations for worst case analysis. If all two port combinations are chosen for worst case analysis and the radiated power loss constant matrix is fully known, (31) can be alternatively written as

$$P_{rad,wc} \approx (1/2)[\bar{a}]^H[\bar{a}] - (1/2)\sum_{k=1}^{N}|a_k|^2 P_{rk,k} + \sum_{k=1}^{N-1}\sum_{m=k+1}^{N}|a_k||a_m|\left(\left|\text{Re}\{P_{rk,m}\}\right| + \left|\text{Im}\{P_{rk,m}\}\right|\right). \tag{42}$$

and represents a deterministic, maximum radiated power estimate independent of input signal phase. If the full total power loss constant matrix and the diagonal elements in the radiated power loss constant matrix are only known, as would be the case after a traditional S-parameter simulation, (42) can be rewritten with the complex total power loss constants as suggested in (31) as

$$P_{rad,wc} \approx (1/2)[\bar{a}]^H[\bar{a}] - (1/2)\sum_{k=1}^{N}|a_k|^2 P_{rk,k} + \sum_{k=1}^{N-1}\sum_{m=k+1}^{N}|a_k||a_m|\left(\left|\mathrm{Re}\{P_{lk,m}\}\right| + \left|\mathrm{Im}\{P_{lk,m}\}\right|\right). \tag{43}$$

If $|a_1| \approx |a_2| \approx \cdots \approx |a_N|$, as could be the case with traditional data traffic in a connector with the same logic levels, then (43) can be written as

$$P_{rad,wc} \approx (N/2)|a_1| - (1/2)|a_1|^2\left(\sum_{k=1}^{N} P_{rk,k}\right)[1-\mathrm{term}\,3] \tag{44a}$$

$$\mathrm{term}\,3 = \frac{2\sum_{k=1}^{N-1}\sum_{m=k+1}^{N}\left(\left|\mathrm{Re}\{P_{lk,m}\}\right| + \left|\mathrm{Im}\{P_{lk,m}\}\right|\right)}{\sum_{k=1}^{N} P_{rk,k}}. \tag{44b}$$

In the unlikely event that $\mathrm{term}\,3 \approx 0$ in (44b), all two port combinations are suitable for worst case analysis since the coupling between ports is negligible even in the worst case. Otherwise, additional data analysis is needed with the numerator terms in (44b) to find select two port combinations suitable for worst case analysis. A matrix can be formulated from the values in (44b) by

$$\mathrm{term}\,3_{\mathrm{matrix}}(k,m) = \frac{2\left(\left|\mathrm{Re}\{P_{lk,m}\}\right| + \left|\mathrm{Im}\{P_{lk,m}\}\right|\right)}{\sum_{h=1}^{N} P_{rh,h}} \tag{45}$$

where $k \neq m$, and the indices k and m only take on values in the upper triangular part of an *NxN* matrix. The upper triangular values in (45) can be concatenated into a vector named $\mathrm{term}\,3_{\mathrm{vect}}$ of length $0.5N(N-1)$. The values in $\mathrm{term}\,3_{\mathrm{vect}}$ should be sorted from smallest to largest while keeping track of the port excitation combinations. The contributions of successive worst case analyses can then be defined by

$$wc_{cont}(k) = \sum_{m=1}^{k} \mathrm{term3}_{\mathrm{vect}}(m) \quad 1 \leq k \leq 0.5N(N-1) \cdot \tag{46}$$

The port combinations eligible for worst case analysis can be found by using a search function with (46) to find the first index where the worst case analysis contribution is greater than a user specified limit. All port combinations associated with the power losses prior to the search result index can be used for worst case analysis.

IV. CONCLUSION

A method is proposed to quantify the power losses at a high-density PCB/connector interface. This method is based on network parameters and the conservation of power and can quantify power losses when material losses and multiple signals are present. The power losses are characterized through the definition of power loss constant matrices which are derived from well-designed single port and two port excitations for an *N*-port connector. Once found, the power loss constant matrices enable the evaluation of the radiated power loss, the material power loss, and the total power loss in a system with variable input signaling. This power loss characterization method allows designers to evaluate connector performance from EMI and signal integrity perspectives, as well as answer common design questions. The proposed method enables the evaluation of connector design modifications such as shielding, absorbing materials, and signal pin assignments and their relative effects on connector radiation. It also allows the direct evaluation of power losses in the frequency-domain which is not readily available when using a time-domain solver. Although the focus of this paper is the characterization of radiated power using simulations, the presented theory also applies to measurements as was shown in a reverberation chamber validation example. Despite using known input signaling information and worst case analysis, significant challenges remain to find full power loss constant matrices for large connectors with measurements due to the large number of measurements required. Future work includes the development of a statistical radiated power limit for high-density PCB/connector interfaces using the power loss constant matrices.

REFERENCES

[1] C. R. Paul and D. R. Bush, “Radiated emissions from common-mode currents,” in *Proc. 1987 IEEE Int. Symp. Electromagn. Compat.*, Atlanta, GA, Aug. 25-27, 1987, pp. 197-203.

[2] D. M. Hockanson, J. L. Drewniak, T. H. Hubing, T. P. Van Doren, F. Sha, and M. J. Wilhelm, “Investigation of fundamental EMI source mechanisms driving common-mode radiation from printed circuit boards with attached cables,” *IEEE Trans. Electromagn. Compat.*, vol. 38, no. 4, pp. 557-566, Nov. 1996.

[3] C. R. Paul, “Modeling electromagnetic interference properties of printed circuit boards,” *IBM J. Res. Develop.*, vol. 33, no. 1, pp. 33-50, Jan. 1989.

[4] R. F. German, H. W. Ott, and C. R. Paul, “Effect of an image plane on printed circuit board radiation,” in *Proc. 1990 IEEE Int. Symp. Electromagn. Compat.*, Washington, DC, Aug. 21-23, 1990, pp. 284-291.

[5] T.-L. Wu, F. Buesink, and F. Canavero, “Overview of signal integrity and EMC design technologies on PCB: fundamentals and latest progress,” *IEEE Trans. Electromagn. Compat.*, vol. 55, no. 4, pp. 624-638, Aug. 2013.

[6] B. Archambeault, S. Connor, M. S. Halligan, J. L. Drewniak, and A. E. Ruehli, “Electromagnetic radiation resulting from PCB/high-density connector interfaces,” *IEEE Trans. Electromagn. Compat.*, vol. 55, no. 4, pp. 614-623, Aug. 2013.

[7] X. Tian, M. S. Halligan, X. Li, K. Kim, H.-C. Chen, S. Connor, B. Archambeault, M. Cracraft, A. E. Ruehli, and J. L. Drewniak, “Modeling electromagnetic radiation at high-density PCB/connector interfaces,” submitted for publication.

[8] X. Tian, M. S. Halligan, X. Li, K. Kim, H.-C. Chen, S. Connor, and J. L. Drewniak, “Modeling and measurement of electromagnetic radiation from a practical PCB connector,” submitted for publication.

[9] H.-C. Chen, M. S. Halligan, S. Connor, X. Tian, X. Li, J. L. Drewniak, B. Archambeault, and T.-L. Wu, “Investigation of the radiated emission from high-speed/high density connector,” submitted for publication.

[10] L. K. C. Wong, “Backplane connector radiated emission and shielding effectiveness,” in *Proc. IEEE Int. Symp. Electromagn. Compat.*, Anaheim, CA, Aug. 1992, pp. 346-351.

[11] D. M. Hockanson, C.-W. Lam, J. L. Drewniak, T. H. Hubing, and T. P. Van Doren, “Experimental and numerical investigations of fundamental radiation mechanisms in PCB designs with attached cables,” in *Proc. IEEE Int. Symp. Electromagn. Compat.*, Santa Clara, CA, Aug. 1996, pp. 305-310.

[12] X. Ye, J. Nadolny, J. L. Drewniak, T. H. Hubing, T. P. Van Doren, and D. E. DuBroff, “EMI associated with inter-board connection for module-on-backplane and stacked-card configurations,” in *Proc. IEEE Int. Symp. Electromagn. Compat.*, Seattle, WA, Aug. 1999, pp. 797-802.

[13] D. Hockanson and S. Radu, “An investigation of the effects of PCB module orientation on radiated EMI,” in *Proc. IEEE Int. Symp. Electromagn. Compat.*, Seattle, WA, Aug. 1999, pp. 399-404.

[14] X. Ye, D. M. Hockanson, and J. L. Drewniak, “A common-mode current measurement technique for EMI performance evaluation of PCB structures,” in *Proc. Asia-Pacific Conf. Environmental Electromagnetics*, Shanghai, China, May 2000, pp. 389-394.

[15] X. Ye, J. L. Drewniak, J. Nadolny, and D. M. Hockanson, “High-performance inter-PCB connectors: analysis of EMI characteristics,” *IEEE Trans. Electromagn. Compat.*, vol. 44, no. 1, pp. 165-174, Feb. 2002.

[16] L. O. Hoeft and J. S. Hofstra, “Measured electromagnetic shielding performance of commonly used cables and connectors,” *IEEE Trans. Electromagn. Compat.*, vol. 30, no. 3, pp. 260-275, Aug. 1988.

[17] B. Vanlandschoot, L. Martens, L. Torren, and D. Morlion, “An improved triaxial cell for transfer impedance measurements on multipins backplane connectors,” in *Proc. IEEE Int. Symp. Electromagn. Compat.*, Austin, TX, Aug. 1997, pp. 141-144.

[18] L. O. Hoeft, J. L. Knighten, and M. Ahmad, “Measured surface transfer impedance of multi-pin Micro-D subminiature and LFH^{TM} connector assemblies at frequencies up to 1 GHz,” in *Proc. IEEE Int. Symp. Electromagn. Compat.*, vol. 2, Seattle, WA, Aug. 1999, pp. 577-582.

[19] L. Martens, A. Madou, L. Koné, B. Demoulin, P. Sjöberg, A. Anton, J. V. Koetsem, H. Hoffmann, and U. Schricker, “Comparison of test methods for the characterization of shielding of board-to-backplane and board-to-cable connectors,” *IEEE Trans. Electromagn. Compat.*, vol. 42, no. 4, pp. 427-440, Nov. 2000.

[20] M. Leone and V. Navrátil, “On the electromagnetic radiation of printed-circuit-board interconnections,” *IEEE Trans. Electromagn. Compat.*, vol. 47, no. 2, pp. 219-226, May 2005.

[21] M. Friedrich and M. Leone, “Network model for the analysis of radiated emissions from horizontal PCB submodules,” in *Proc. IEEE Int. Symp. Electromagn. Compat.*, Fort Lauderdale, FL, July 2010, pp. 631-636.

[22] M. Friedrich and M. Leone, “Inductive network model for the radiation analysis of electrically small parallel-plate structures,” *IEEE Trans. Electromagn. Compat.*, vol. 53, no. 4, pp. 1015-1024, Nov. 2011.

[23] K. Li, A. Tassoudji, S. Y. Poh, M. Tsuk, R. T. Shin, and J. A. Kong, “FD-TD analysis of electromagnetic radiation from modules-on-backplane configurations,” *IEEE Trans. Electromagn. Compat.*, vol. 37, no. 3, pp. 326-332, Aug. 1995.

[24] D. M. Hockanson, X. Ye, J. L. Drewniak, T. H. Hubing, T. P. Van Doren, and R. E. DuBroff, “FDTD and experimental investigation of EMI from stacked-card PCB configurations,” *IEEE Trans. Electromagn. Compat.*, vol. 43, no. 1, pp. 1-10, Feb. 2001.

[25] M. Valek, M. Leone, and F. Schmiedl, “Analysis of the electromagnetic radiation behavior of motherboard-subboard structures,” in *Proc. IEEE Int. Symp. Electromagn. Compat. and Electromagn. Ecology*, June 2005, pp. 175-178.

[26] Y. Toyota, A. Sadatoshi, T. Watanabe, K. Iokibe, R. Koga, and O. Wada, “Prediction of electromagnetic emissions from PCBs with interconnections through common-mode antenna model,” in *Proc. 18th Int. Zurich Symp. Electromagn. Compat.*, Munich, Germany, Sept. 2007, pp. 107-110.

[27] M. Torigoe, A. Sadatoshi, Y. Toyota, K. Iokibe, R. Koga, T. Watanabe, and O. Wada, “Prediction of the common-mode radiated emission from the board to board interconnection through common-mode antenna model,” in *Proc. IEEE Int. Symp. Electromagn. Compat.*, Detroit, MI, Aug. 2008, pp. 1-4.

[28] D. M. Pozar, *Microwave Engineering*, 3rd ed. Hoboken, NJ, USA: Wiley, 2005, pp. 181-182.

[29] G. E. Carlson, *Signal and Linear System Analysis*, 2nd ed. New York, NY, USA: Wiley, 1998, ch. 5, pp. 126-201.

V. Statistical Estimates of Maximum Radiated Power from High-Density Connectors

Matthew S. Halligan, Xiao Li, Xinxin Tian, Sam Connor, *Senior Member, IEEE,* Daryl G. Beetner, *Senior Member, IEEE,* James L. Drewniak, *Fellow, IEEE*

Abstract—A method to statistically estimate radiated emissions from high-density connectors is presented in this paper. The statistical formulations are based on the radiated power quantification method using power loss constant matrices and statistical bounding methods. Statistical limits for the maximum radiated power are proposed based on the Markov and Chebyshev inequalities where only low probability events are expected to exceed the limits in the worst case. The magnitude power spectra of the input signals to the connector are assumed to be known. The phases of the input signals are assumed to be independent uniformly distributed random variables. Incident power waves at the connector ports are defined as a function of the input power waves from the sources through a port connectivity matrix. Maximum radiated power limits are proposed that depend on the level of known information in the radiated power loss constant matrix. Simulations and measurements are presented that validate the proposed statistical maximum radiated power estimates.

Index Terms—Connectors, electromagnetic radiation, estimation, printed circuit board connectors, radiated power, scattering parameters, statistical analysis

I. INTRODUCTION

Electromagnetic radiation from printed circuit board (PCB) connectors is becoming a significant concern for industry as data rates increase. In the past, connectors alone were ineffective radiators since they were electrically small. These PCB connectors were often a part of a much larger unintentionally radiating structure consisting of PCBs, cables, or enclosures [1]-[4]. The connectors often facilitated the voltage difference between the two larger metallic structures through an inductive mechanism. With increasing data rates, however, PCB connectors have become electrically large and the connectors themselves have been shown to radiate effectively and, in some cases, to be the dominant radiators [5]-[9].

Radiation from connectors has been extensively studied in literature, though a majority of the literature focuses on cases where the connectors are electrically small. Many of the radiation studies are based on the current and voltage driven models in [2]. Additional efforts to quantify radiation from connectors have included finite-difference time-domain simulations [10]-[13], common mode current measurements [10]-[11], [13], electromagnetic fields measurements [13]-[14], transfer impedance measurements [15]-[16], and connector inductance measurements and calculations [17]-[18]. More recent efforts have focused on modeling connector radiation when connectors are electrically large [5]-[9].

In [9], a method was presented to quantify the radiated power from a high-density PCB/connector structure with material losses and multiple input signals. The method predicts PCB connector radiated power when input signals are known. Although deterministic evaluation is beneficial, in many cases the input signal characteristics are not known precisely and can be modeled as random variables. A statistical analysis can address this issue and can be formulated from the theory presented in [9]. The purpose of this paper is to expand on the foundations of [9] by developing statistical estimates of the maximum radiated power to quantify connector radiation performance. A review of the power loss calculations using power loss constant matrices is presented in Section II. The constraints for the defined statistical problem and bounding methods for power loss are discussed in Section III. Simulation and measurement results are provided in Section IV to validate the radiated power loss bounds defined in Section III. Conclusions are given in Section V.

II. POWER LOSS CALCULATIONS

A method to characterize power losses at a PCB/connector interface was presented in [9] using power loss constant matrices. This method is based on network parameters and the conservation of power and can be used to characterize any of the power losses (radiation, material, or total power loss). The general power loss equation is defined as [9]

$$P_{loss,gen} = (1/2)[\overline{a}]^H[\overline{a}] - (1/2)[\overline{a}]^H\left[\widetilde{P}_{const}\right][\overline{a}] \tag{1}$$

where $[\overline{a}]$ represents the inputs to the connector as an incident power wave vector with units of $\sqrt{Watt}$ and is based on generalized scattering parameters [19], H denotes the complex conjugate transpose, and $\left[\widetilde{P}_{const}\right]$ is a frequency dependent power loss constant matrix defined by

$$\left[\widetilde{P}_{const}\right] = \begin{bmatrix} P_{1,1} & P_{1,2} & \cdots & P_{1,n} \\ P_{2,1} & P_{2,2} & \cdots & P_{2,n} \\ \vdots & \vdots & \ddots & \vdots \\ P_{n,1} & P_{n,2} & \cdots & P_{n,n} \end{bmatrix} = \begin{bmatrix} P_{1,1} & P_{1,2} & \cdots & P_{1,n} \\ P_{1,2}^{*} & P_{2,2} & \cdots & P_{2,n} \\ \vdots & \vdots & \ddots & \vdots \\ P_{1,n}^{*} & P_{2,n}^{*} & \cdots & P_{n,n} \end{bmatrix}. \tag{2}$$

From (1), the total power loss, $P_{loss,total}$, the total radiated power, $P_{rad,total}$, and the total material loss, $P_{mat,total}$, can be written as [9]

$$P_{loss,total} = (1/2)[\overline{a}]^H[\overline{a}] - (1/2)[\overline{a}]^H\left[\widetilde{P}_{loss,const}\right][\overline{a}] \tag{3}$$

$$P_{rad,total} = (1/2)[\overline{a}]^H[\overline{a}] - (1/2)[\overline{a}]^H\left[\widetilde{P}_{rad,const}\right][\overline{a}] \tag{4}$$

$$P_{mat,total} = (1/2)[\overline{a}]^H[\overline{a}] - (1/2)[\overline{a}]^H\left[\widetilde{P}_{mat,const}\right][\overline{a}]. \tag{5}$$

The total power loss constant matrix can be found from single-ended network parameters using

$$\left[\widetilde{P}_{loss,const}\right] = \left[\widetilde{S}\right]^H\left[\widetilde{S}\right], \tag{6}$$

whereas, the radiated power constant matrix, $\left[\widetilde{P}_{rad,const}\right]$, and the material loss constant matrix, $\left[\widetilde{P}_{mat,const}\right]$, must be found from single- and two-port excitations. The diagonal elements in $\left[\tilde{P}_{rad,const}\right]$ and $\left[\tilde{P}_{mat,const}\right]$ are found from the single port excitations and the off-diagonal elements are found from the two-port common-mode and phase shifted excitations. $\left[\tilde{P}_{rad,const}\right]$ and $\left[\tilde{P}_{mat,const}\right]$ can be found through simulations or measurements as shown in [9].

III. DERIVATIONS ON A STATISTICAL RADIATED POWER ESTIMATE

One of the many benefits of the power loss characterization in (3)-(5) is the ability to quantify power losses in a PCB/connector structure when the incident power waves (the inputs) to the structure are known. Radiated power can be used to quantify PCB connector electromagnetic interference (EMI) performance. The radiated power formulation in (4) can be used to evaluate the radiated power deterministically or statistically. A statistical analysis of connector radiated power is of interest in this paper for a few reasons. First, the input excitations may not be fully known. In many cases the magnitude spectrum of the input signals will be known, but the phase spectrum will not. Uncertainties in the transmission line lengths from the sources to the PCB/connector structure interface as well as unknown relative timing characteristics of the sources can lead to an unknown phase spectrum. Another practical issue is that the radiated power loss constant matrix will often be incomplete for large connectors. Large connectors can contain as many as 10's or 100's of signal lines and the number of simulations or measurements required to find the entire radiated power loss constant matrix may not be feasible. For example, the total number of excitations required to fill the entire power loss constant matrix, assuming only two excitations are needed to solve for each unique complex loss constant, is n^2, where n is the number of ports defined at the PCB/connector interface. A worst case analysis can reduce the required number of excitations, however, these reductions alone are often not enough to make the calculation practical. A statistical evaluation of the radiated power can address these issues by utilizing limited radiated power loss constant information to predict a statistical estimate for the maximum radiated power in a systematic manner.

A statistical radiated power estimate can be derived from the general power loss equation in (1) with some slight modifications as will be shown. Because all of the power losses can be written in the same general form, the resulting formulas can be easily modified to describe the statistics for any of the power loss mechanisms. In the proposed statistical problem, the magnitude spectrum of all the incident power waves from the sources is assumed to be known and deterministic. The path lengths from the sources driving the PCB connector and the start-times of each incident signal from the sources are assumed to be unknown so that the phase of the incident signals are random variables (RVs) that are independent and uniformly distributed on $[-\pi, \pi)$ assuming phase wrapping. In an actual PCB connector, the incident power waves at the connector ports may not be independent from one another. For instance, a differential connector driven with differential transmitters will have incident wave dependencies on the positive and negative nets for each differential pair. Ideally, the positive and negative nets contain the same signal but with a phase difference of π radians. In addition, incident power wave dependencies may also exist when port terminations are not perfectly matched. Thus, a distinction must be made between incident waves at the connector ports and incident waves from independent sources. Known incident wave dependencies at the connector ports can be addressed in the proposed statistical problem by defining a port connectivity matrix that correlates the independent incident waves at the sources to the incident waves at the connector ports. The port connectivity matrix is defined by

$$[\bar{a}_c] = [\tilde{C}][\bar{a}_i], \tag{7}$$

where, $[\tilde{C}]$ is the port connectivity matrix, $[\bar{a}_i]$ is the independent incident power wave vector from the sources, and $[\bar{a}_c]$ is the incident power wave vector at the connector. The length of $[\bar{a}_c]$ is greater than $[\bar{a}_i]$ when differential signals are present, and $[\tilde{C}]$ can be built so that differential signals will have equal magnitude and opposite phase. The general power loss equation in (1) can be rewritten using (7) as

$$\begin{aligned} P_{loss,gen} &= (1/2)[\bar{a}_c]^H[\bar{a}_c] - (1/2)[\bar{a}_c]^H[\tilde{P}_{const}][\bar{a}_c] \\ &= (1/2)[\bar{a}_i]^H[\tilde{C}]^H[\tilde{C}][\bar{a}_i] - (1/2)[\bar{a}_i]^H[\tilde{C}]^H[\tilde{P}_{const}][\tilde{C}][\bar{a}_i]. \end{aligned} \tag{8}$$

The incident power wave vector used for the statistical problem can then be written as

$$[\bar{a}_i] = [|a_1|\angle\Theta_1 \quad |a_2|\angle\Theta_2 \quad \cdots \quad |a_n|\angle\Theta_n]^T \tag{9}$$

where T is the non-conjugate transpose and Θ_n is the phase RV for the nth incident wave. The probability density function (pdf) for the uniform RV Θ_n is given by [20]

$$f_{\Theta_n}(\theta_n) = \begin{cases} \dfrac{1}{2\pi} & -\pi \le \theta_n < \pi \\ 0 & else. \end{cases} \tag{10}$$

Since all of the incident wave phases are statistically independent, the joint pdf is a multiplication of the individual RV pdfs [20]. The joint pdf is given by

$$f_{\Theta_1,\Theta_2,\cdots,\Theta_n}(\theta_1,\theta_2,\cdots,\theta_n) = \begin{cases} \left(\dfrac{1}{2\pi}\right)^{\mathrm{n}} & -\pi \le \theta_1,\theta_2,\cdots,\theta_n < \pi \\ 0 & else. \end{cases} \tag{11}$$

The power loss in (8) is a function of *n* phase RVs. The cumulative distribution function (cdf) of the power loss can be found from (8) and (11) through integration, but the calculation is difficult due to the multi-dimensional nature of the statistical problem. Rather than evaluate the cdf of the power loss directly, statistical bounding methods can be used to formulate a maximum bound for the radiated power. Two common statistical bounding methods use the Markov inequality and the Chebyshev inequality, shown in (12) and (13) respectively [20]:

$$P[X \ge \gamma] \le \frac{\mu_X}{\gamma} \tag{12}$$

$$P[-\gamma + \mu_X \le X \le \gamma + \mu_X] \ge 1 - \frac{\sigma_X^2}{\gamma^2}. \tag{13}$$

Both inequalities apply to non-negative RVs (X), regardless of their distribution. The expected value or mean of the RV is denoted by μ_X, and the variance of the RV is denoted by σ_X^2. The scalar γ defines the statistical bound. In general, the Chebyshev inequality provides a tighter bound for RVs than the Markov inequality since the Chebyshev inequality uses the variance of the RV in addition to the mean. One possible bound for the Markov inequality is where $\gamma = 10\mu_X$. For this bound, the Markov inequality states the probability the RV X will be larger than or equal to $10\mu_X$ is less than or equal to 10%. Another bound can be defined from the Chebyshev inequality where $\gamma = 3\sigma_X$. The Chebyshev inequality states the probability the RV is within three standard deviations about the mean is greater than or equal to 89%. In the worst case, the remaining 11% could occur above the $\mu_X + 3\sigma_X$ limit curve.

Evaluating statistical bounds for the power loss based on (12)-(13) requires knowledge about the mean and variance of the power loss. The power loss mean and variance can be derived from the general power loss equation in (8) and with the constraints defined for the statistical problem. It can be shown that the power loss mean and variance are given by

$$\mu_{loss,gen} = \frac{1}{2}[\bar{a}_i]^H\left[\tilde{C}_{prod,diag}\right][\bar{a}_i] - \frac{1}{2}[\bar{a}_i]^H\left[\tilde{Q}_{diag}\right][\bar{a}_i] \tag{14}$$

$$\begin{aligned}\sigma^2_{loss,gen} = \frac{1}{4}\left[|\bar{a}_i|^2\right]^T\Bigg(&\left[\left|\tilde{C}_{prod,offdiag}\right|^2\right] + \left[\left|\tilde{Q}_{offdiag}\right|^2\right] \\ &- 2\left[\tilde{C}_{prod,offdiag}\right]\circ\left[\tilde{Q}_{offdiag}\right]^T\Bigg)\left[|\bar{a}_i|^2\right]\end{aligned} \tag{15}$$

$$\left[\tilde{C}_{prod}\right] = \left[\tilde{C}\right]^H\left[\tilde{C}\right] = \left[\tilde{C}_{prod,diag}\right] + \left[\tilde{C}_{prod,offdiag}\right] \tag{16}$$

$$\left[\tilde{Q}\right] = \left[\tilde{C}\right]^H\left[\tilde{P}_{const}\right]\left[\tilde{C}\right] = \left[\tilde{Q}_{diag}\right] + \left[\tilde{Q}_{offdiag}\right]. \tag{17}$$

The subscript *diag* and *offdiag* indicate matrices that contain nonzero diagonal elements only or nonzero off-diagonal elements only, respectively. The symbol $\circ$ denotes the Hadamard product or matrix element-wise multiplication operator. Equations (14)-(15) can be used to evaluate the mean and variance for any of the power losses (radiation, material, or total) when using the correct power loss constant matrix. A few important observations can be made about the mean and variance in (14)-(15). First, the mean of the power loss is a function of diagonal elements in the power loss constant matrix only when the connectivity matrix is an identity matrix. In many practical cases the diagonal power loss constants will be known, since these values are relatively easy to calculate through single-port simulations or measurements, and the mean can be calculated. Second, the power loss variance is a function of the off-diagonal elements of the power loss constant matrix, which can only be determined through a series of two-port excitations. If the two port excitations are not performed, the variance of the radiated power loss and the material power loss cannot be found.

A worst case estimate for the maximum variance of radiated power loss can be formulated, however, from relationships between the power loss means and variances. The total power loss at a PCB/connector interface can be written as a summation of radiated power loss and material power loss as

$$P_{loss,total} = P_{rad,total} + P_{mat,total} \,. \tag{18}$$

From (14), (15), and (18), the mean and the variances for the power losses are related as

$$\mu_{loss} = \mu_{rad} + \mu_{mat} \tag{19}$$

$$\begin{aligned} \sigma_{loss}^2 = \sigma_{rad}^2 + \sigma_{mat}^2 &+ \frac{1}{2}\left([\bar{a}_i]^H \left[\tilde{R}_{rad,diag}\right][\bar{a}_i]\right)\left([\bar{a}_i]^H \left[\tilde{R}_{mat,diag}\right][\bar{a}_i]\right) \\ &+ \frac{1}{2}\left[|\bar{a}_i|^2\right]^T \left(\left[\tilde{R}_{rad,offdiag}\right] \circ \left[\tilde{R}_{mat,offdiag}\right]^T\right)\left[|\bar{a}_i|^2\right] - 2\mu_{rad}\,\mu_{mat} \end{aligned} \tag{20}$$

$$\left[\tilde{R}\right] = \left[\tilde{C}_{prod}\right] - \left[\tilde{Q}\right] = \left[\tilde{R}_{diag}\right] + \left[\tilde{R}_{offdiag}\right] \tag{21}$$

where, the radiated power mean and material power loss mean are given by μ_{rad} and μ_{mat}, respectively. The radiated power and material power loss variance are represented by σ_{rad}^2 and σ_{mat}^2, respectively. From (20):

$$\sigma_{rad}^{2} = \sigma_{loss}^{2} - \sigma_{mat}^{2} + 2\mu_{rad}\,\mu_{mat} - \frac{1}{2}\left([\bar{a}_i]^H \left[\tilde{R}_{rad,diag}\right][\bar{a}_i]\right)\left([\bar{a}_i]^H \left[\tilde{R}_{mat,diag}\right][\bar{a}_i]\right) \\ - \frac{1}{2}\left[|\bar{a}_i|^2\right]^T \left(\left[\tilde{R}_{rad,offdiag}\right] \circ \left[\tilde{R}_{mat,offdiag}\right]^T\right)\left[|\bar{a}_i|^2\right] \tag{22}$$

Assuming $(1/2)\left[|\bar{a}_i|^2\right]^T \left(\left[\tilde{R}_{rad,offdiag}\right] \circ \left[\tilde{R}_{mat,offdiag}\right]^T\right)\left[|\bar{a}_i|^2\right]$ is non-negative, a worst case estimate of the radiated power variance is

$$\sigma_{rad,wc}^{2} = \sigma_{loss}^{2} + 2\mu_{rad}\,\mu_{mat} - \frac{1}{2}\left([\bar{a}_i]^H \left[\tilde{R}_{rad,diag}\right][\bar{a}_i]\right)\left([\bar{a}_i]^H \left[\tilde{R}_{mat,diag}\right][\bar{a}_i]\right). \tag{23}$$

This estimate can be used when only the diagonal elements in the radiated power loss constant matrix are known, and the port connectivity matrix is an identity matrix.

IV. VALIDATION

The connector model shown in Fig. 1 of [9] and shown in Fig. 1 of this paper was used to validate the derived statistics on the power losses. This full-wave connector model was created in CST Microwave Studio for a commercially available connector designed for differential signaling. Additional details about the connector model and the generation process are given in [7]-[9]. A series of full-wave time-domain simulations were performed to characterize the power losses for all the pairs in slice A of the second wafer. The radiated power loss constant matrix was calculated so that the radiated power can be found when feeding any of the pairs in slice A of the second wafer. A full S-parameter matrix containing information about all 96 ports in the connector was also obtained. To verify the radiated power loss constant matrix was calculated correctly, the radiated power loss was evaluated for a random excitation of all pairs in slice A of the second wafer and the radiated power loss found using (4) was compared to the value found through a full-wave simulation. The nonzero port excitations were given by

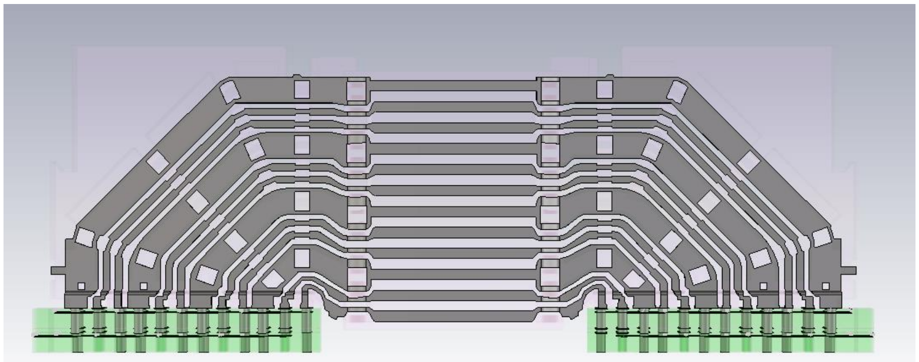

Fig. 1. Full-wave connector model used to validate statistical estimates for maximum radiated power. Radiated powers for all the differential pairs in Slice A of the middle wafer as shown were characterized in the simulation model.

$$[\bar{a}_{sub}] = \begin{bmatrix} a_{33} \\ a_{35} \\ a_{37} \\ a_{39} \\ a_{41} \\ a_{43} \\ a_{45} \\ a_{47} \end{bmatrix} = \begin{bmatrix} 1.90\angle -2\pi f\left(7e-12\right) \\ 0.46\angle -2\pi f\left(6e-12\right) \\ 1.21\angle -2\pi f\left(8e-12\right) \\ 0.97\angle -2\pi f\left(11e-12\right) \\ 1.78\angle -2\pi f\left(15e-12\right) \\ 1.52\angle -2\pi f\left(2e-12\right) \\ 0.91\angle -2\pi f\left(17e-12\right) \\ 0.34\angle -2\pi f\left(11e-12\right) \end{bmatrix}, \tag{24}$$

where, *f* is frequency in Hz, and the port numbers are indicated by the subscripts in the partial incident power wave vector. The shortest signal conductor was excited by port 33, and the longest signal conductor was excited by port 47. The phases of the input excitations in (24) are defined according to the signal time delays indicated in parentheses. It should be noted that (24) does not represent the full incident power wave vector. All other incident power waves were zero since all other ports were matched. A comparison of the radiated power loss, the material power loss, and the total power loss for the excitation in (24) are shown in Fig. 2 using (3)-(5). The maximum deviation between the radiated power calculated from (4) and the direct calculation of the fields is 0.03 dB. Fig. 2 shows that the radiated power calculated from the radiated power loss constant matrix is equivalent to the direct fields calculation.

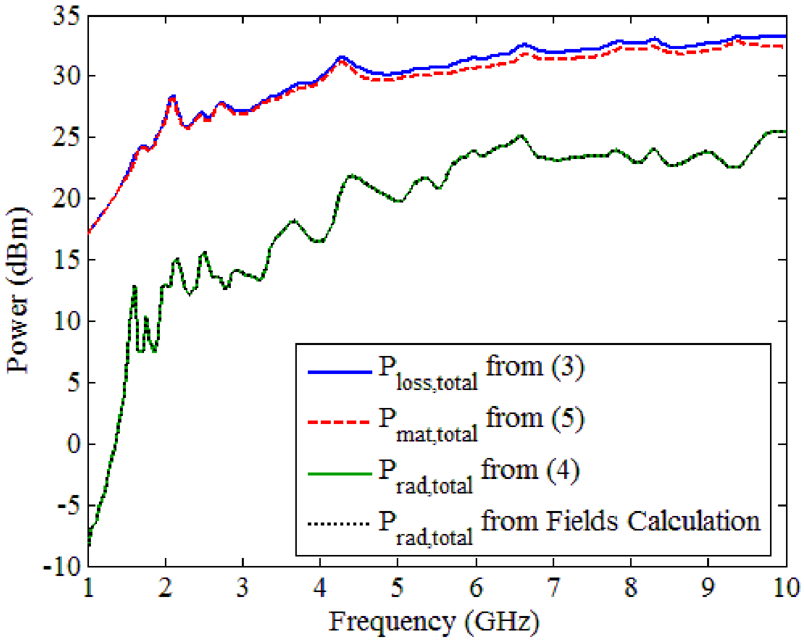

Fig. 2. Comparison of the total power loss, material power loss, and the radiated power loss for the random excitation in (24).

A. Simulation with Impulse Excitations

Statistical simulations were performed with the characterized connector model in Fig. 1 to validate (14)-(15), (19)-(20), and (23). A series of 1,000 statistical trials per frequency were performed and the radiated power calculated with the general power loss equation in (8). All odd ports between ports 33-47 were fed with 0.5 W over the entire frequency range (an impulse excitation) where the excitation phases were independently generated with a uniform distribution on $[-\pi,\pi)$. In the first set of simulations, the port connectivity matrix was assigned to be an identity matrix, which corresponds to independent, single-ended (SE) signaling. The mean and the variance of the radiated power were calculated from the statistical trials and compared to the mean and variance calculated from (14)-(15). The maximum difference between the means and the standard deviations were 0.12 dB and 0.36 dB, respectively. A worst case radiated power variance was also calculated from (23). Fig. 3 shows the mean and standard deviations derived from (14)-(15) and (23). The average difference between the radiated power standard deviation from (15) and the worst case standard deviation from (23) is 6.18 dB. The term in (22) containing $\left[\tilde{R}_{rad,offdiag}\right]$ and $\left[\tilde{R}_{mat,offdiag}\right]$ was confirmed to be positive as assumed in the worst case radiated power variance formulation. The mean and standard deviation of the radiated power were also calculated with randomly generated connectivity matrices with similar agreement.

Maximum radiated power bounds were generated with the Markov and Chebyshev inequalities in (12)-(13) using the radiated power mean and variances from (14)-(15), and (23). The maximum radiated power limit curve derived from the Markov inequality was defined as $P_{rad,\max} = 10\mu_{rad}$. Two limit curves were defined using the Chebyshev inequality. The first Chebyshev radiated power limit curve was defined as $P_{rad,\max} = \mu_{rad} + 3\sigma_{rad}$. The second limit curve, denoted as the worst case Chebyshev limit, was defined as $P_{rad,\max} = \mu_{rad} + 3\sigma_{rad,wc}$. The Markov, Chebyshev, and worst case Chebyshev limit curves were evaluated using the impulse excitation conditions defined previously. Fig. 4 provides a comparison of all these radiated power limit curves with respect to a radiated power limit curve derived from statistical trials. A limit curve where the radiated power was below the curve 89% of the time was found from the statistical trials. Both the Markov and Chebyshev limit curves overpredict the 89% trial curve because the Markov and Chebyshev inequalities predict RV bounds for *any* distribution of a non-negative RV [20]. It can be seen that the Chebyshev limit curve differs from the statistical trial 89% curve by only a couple decibels over most of the frequency range. When the Chebyshev limit cannot be calculated, a limit curve can be defined on a frequency by frequency basis by taking the minimum of the Markov and worst case Chebyshev limits. In Fig. 4, the worst-case limit would be defined by the Markov limit below 3 GHz and by the worst case Chebyshev limit above 3 GHz.

Another set of 1,000 statistical trials per frequency were performed to understand how the radiated power limit curves perform when the port connectivity matrix defines independent, differential-mode (DM) signaling. The port connectivity matrix was defined so that each differential pair shared a single independent incident wave source for all odd ports between ports 33-47. The positive and negative nets were defined to be out of phase by π radians in the connectivity matrix. Each port was fed with 0.5 W over the entire frequency range, and the independent, incident wave excitation phases were generated

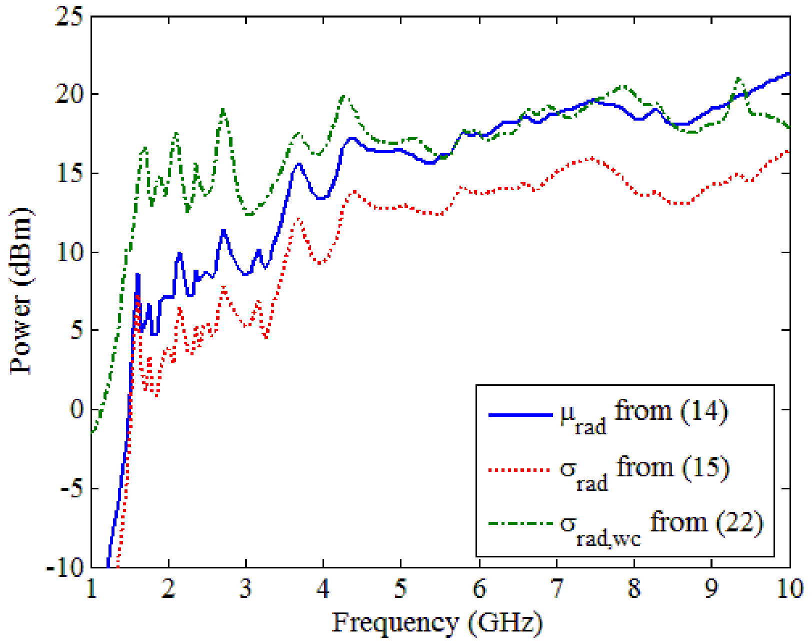

Fig. 3. Comparison of the radiated power mean, standard deviation, and worst case standard deviation for an impulse excitation and a single-ended signaling port connectivity matrix.

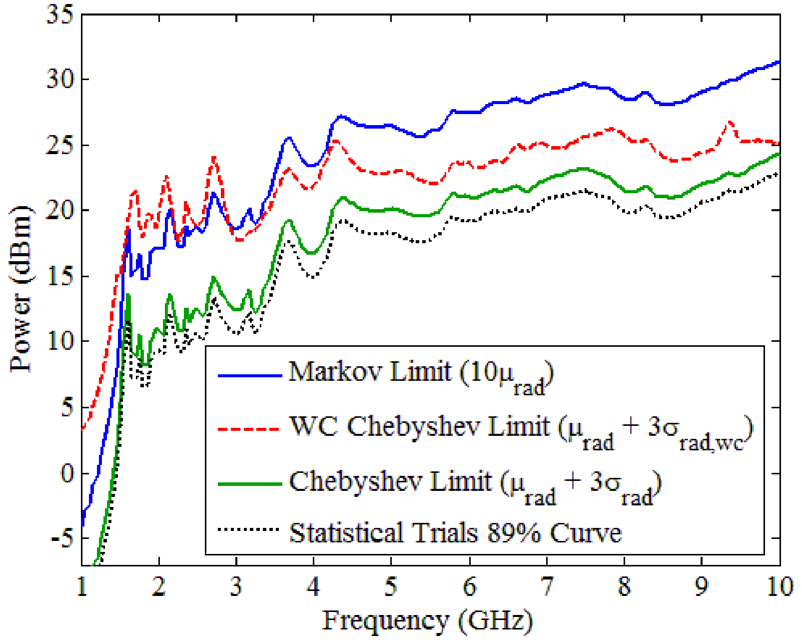

Fig. 4. Comparison of the maximum radiated power limit curves for an impulse excitation and single-ended signaling port connectivity matrix.

with a uniform distribution on $[-\pi,\pi)$. The layout of the port connectivity matrix can be illustrated with an example. For a four port network where ports 1 and 3 and ports 2 and 4 share the same independent incident power wave sources, the connectivity matrix would be defined as

$$[\tilde{C}]=\begin{bmatrix} 1 & 0 \\ 0 & 1 \\ -1 & 0 \\ 0 & -1 \end{bmatrix}. \tag{25}$$

The mean and the variance of the radiated power were calculated from the statistical trials and compared to the mean and variance calculated from (14)-(15). The maximum difference between the means and the standard deviations were 0.08 dB and 0.15 dB, respectively. A worst case radiated power variance was also calculated from (23). The Markov, Chebyshev, and worst case Chebyshev limit curves were evaluated using the impulse excitation conditions defined previously. Fig. 5 shows a comparison of all these radiated power limit curves with respect to a radiated power limit curve derived from statistical trials. In general, the worst case Chebyshev limit is smaller than the Markov limit over most of the frequency range in Fig. 5. The radiated power limit curves are smaller for the DM signaling case than the SE signaling case as seen when comparing Fig. 4 with Fig. 5.

Additional radiated power limit curves were formulated from the minimum of the Markov and worst case Chebyshev limits for the SE and DM signaling cases. These limit curves are compared to two unique trial excitations in Fig. 6. A SE trial excitation was formulated where the ports were fed with 0.5 W, and all the incident power waves had a zero degree phase. A DM trial excitation was generated where the ports were fed with 0.5 W, and the incident power waves were out of phase by π radians for each differential pair. All excited differential pairs were fed with the same differential excitation with no phase difference between the pairs. The SE excitation differs from the SE limit curve from 1.10 dB to 10.03 dB, and the DM excitation differs from the DM limit curve from 1.64 dB to 9.34 dB as seen in Fig. 6. One important point about the formulation of the DM limit curve is that the DM signaling connectivity matrix requires some off-diagonal

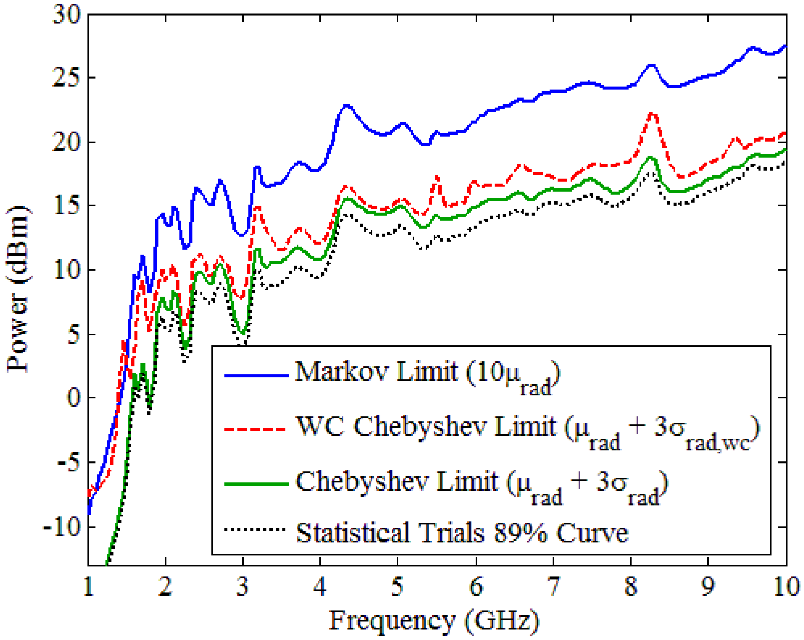

Fig. 5. Comparison of the maximum radiated power limit curves for an impulse excitation and a differential-mode signaling port connectivity matrix.

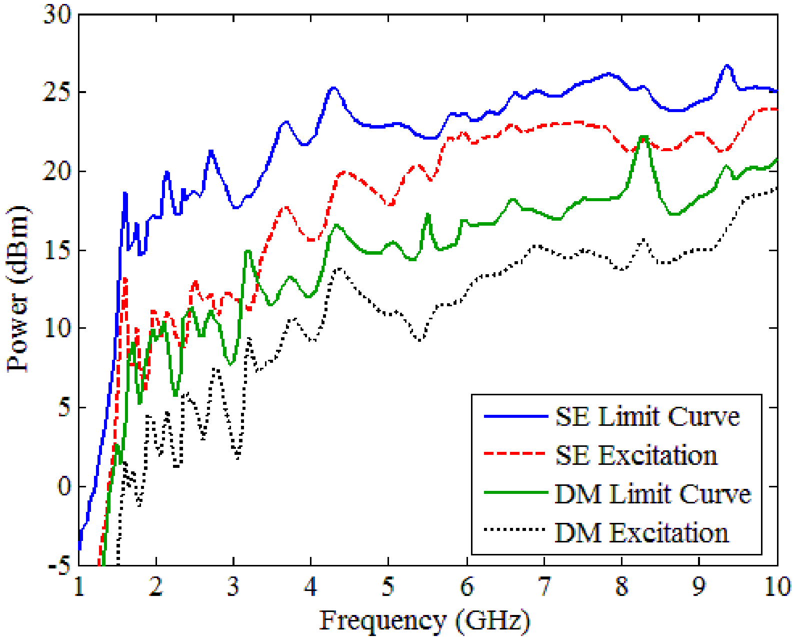

Fig. 6. Comparison of the spliced Markov and worst case Chebyshev limit curves using a single-ended signaling port connectivity matrix and a differential-mode signaling port connectivity matrix for impulse excitations. The SE and DM excitations represent cases where the independent incident waves are in phase with one another.

elements in the radiated power loss constant matrix to be known (i.e. for the differential pairs), to calculate the mean radiated power as in (14) and (17). If the necessary off-diagonal elements are unknown when DM signaling is employed, a question remains as to how to formulate a maximum radiated power limit from the known power loss information. One option is to use the SE radiated power limit curve. Another option is to construct a DM limit curve from the Markov and Chebyshev limits with the total power loss mean, μ_{loss}, and standard deviation, σ_{loss}. Fig. 7 shows a comparison of these two types of limit curves to the DM limit curve found using the full radiated power loss constant matrix. This figure shows that using the total power loss to estimate the statistical limit for radiated DM power substantially overestimates the radiated power. The DM radiation limit estimated in this way is even higher than the limit predicted for SE signals.

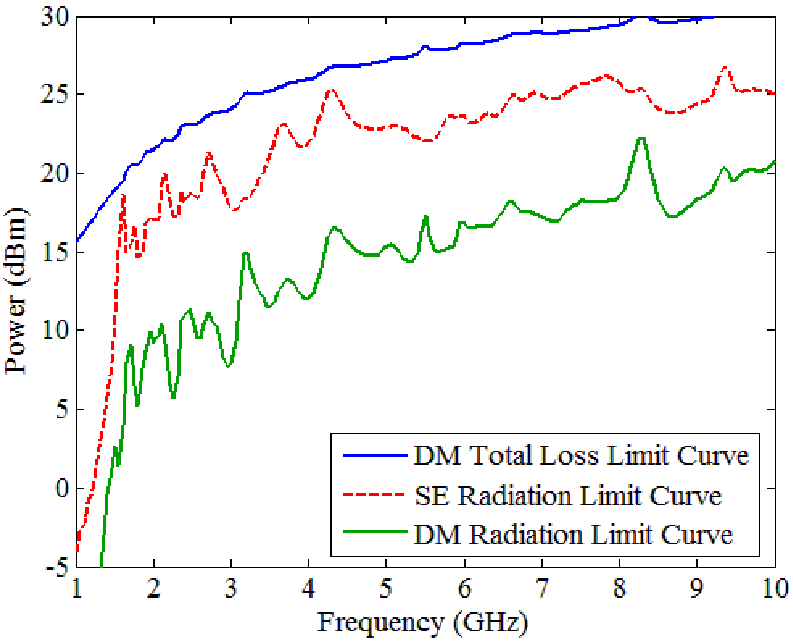

Fig. 7. Total power loss and radiated power loss limit curve comparison for differential-mode and single-ended signaling port connectivity matrices for an impulse excitation.

B. Simulation with Pseudo-Random Bit Sequences

Radiated power limit curves were also evaluated using pseudo-random bit sequences (PRBSs). These types of signals are of interest since they are often used to evaluate EMI performance of systems. A PRBS7 signal was designed with a 2 V total voltage maximum and a 0 V total voltage minimum at a matched load connected to the source. The PRBS7 signal was modeled as a series of trapezoidal pulses where the rise and fall time was 28 ps. The data rate of the bit stream was 4 Gbps. The PRBS7 signal was generated with shift registers where taps were placed at register six and register seven. The outputs of register six and register seven were fed into an exclusive-or gate, and the resulting output was fed into the first register of the shift register. All registers were initialized to the logic high state and the output of register seven was used as the source of the PRBS7 signal. A fast Fourier transform (FFT) was used to find the double-sided spectrum of the PRBS7 signal, and the total voltage spectrum was converted to a single-sided, incident power wave spectrum. All of the frequency-domain plots in this section show the envelope of the power spectrum rather than stem plots to improve figure clarity.

The connector model shown in Fig. 1 was used to validate the statistical formulas in Section III where all odd ports between ports 33-47 were fed with the PRBS7 signal, and all other ports were terminated with matched loads. A series of 1,000 statistical trials per frequency were performed and the radiated power was calculated with the general power loss equation in (8). In the first simulation study a SE signaling port connectivity matrix was used. The phases of the independent incident wave excitations were generated over frequency with a uniform distribution on $[-\pi,\pi)$. The mean and the variance of the radiated power were calculated from the statistical trials and compared to the mean and variance calculated from (14)-(15). The maximum difference between the means and the standard deviations were 0.17 dB and 0.35 dB, respectively. A worst case radiated power variance was also calculated from (23). Fig. 8 shows the mean and standard deviations derived from (14)-(15) and (23). The average difference between the radiated power standard deviation from (15) and the worst case standard deviation from (23) is 6.18 dB. The term in (22) containing $\left[\tilde{R}_{rad,offdiag}\right]$ and $\left[\tilde{R}_{mat,offdiag}\right]$ was confirmed to be positive as assumed in the worst case radiated power variance formulation. The Markov, Chebyshev, and the worst case Chebyshev limit curves were evaluated using the PRBS7 SE signaling conditions. Fig. 9 provides a comparison of all these radiated power limit curves with respect to a radiated power limit curve derived from statistical trials. Although the

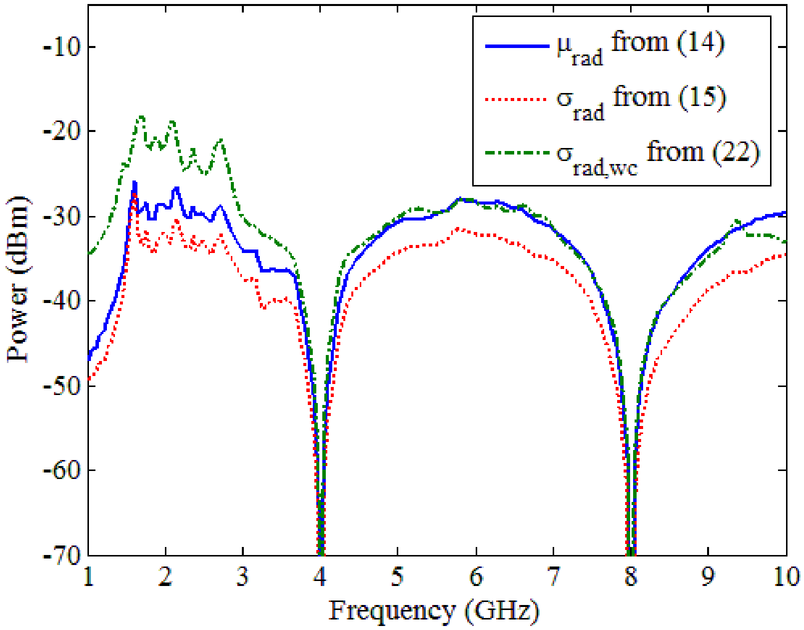

Fig. 8. Comparison of the radiated power mean, standard deviation, and worst case standard deviation for a PRBS7 excitation and a single-ended signaling port connectivity matrix.

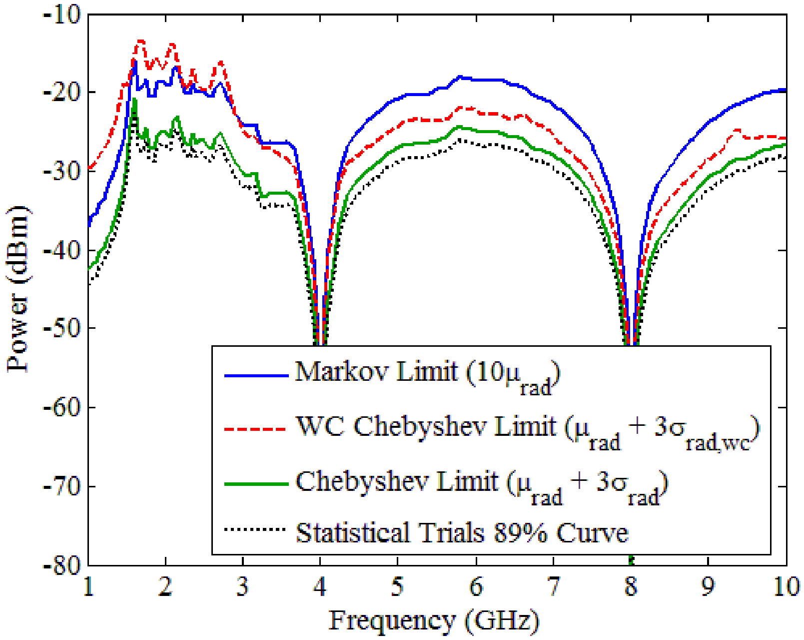

Fig. 9. Comparison of the maximum radiated power limit curves for a PRBS7 excitation and single-ended signaling port connectivity matrix.

Chebyshev limit curve differs from the statistical trial 89% curve by only a couple decibels over most of the frequency range, a limit curve consisting of the Markov and worst case Chebyshev limits may be found with incomplete radiated power loss constant matrices as discussed earlier.

Another set of 1,000 statistical trials per frequency were performed to show how the radiated power limit curves perform when the port connectivity matrix was defined for DM signaling. The port connectivity matrix was defined so that each differential pair shared a single independent incident wave source for all odd ports between ports 33-47. The positive and negative nets were defined to be out of phase by π radians in the connectivity matrix. Each port was fed with the PRBS7 signal, and the phases of the independent incident power waves were generated with a uniform distribution on $[-\pi,\pi)$. The mean and the variance of the radiated power were calculated from the statistical trials and compared to the mean and variance calculated from (14)-(15). The maximum difference between the means and the standard deviations were 0.11 dB and 0.22 dB, respectively. A worst case radiated power variance was also calculated from (23). The Markov, Chebyshev, and worst case Chebyshev limit curves were evaluated using the PRBS7 excitation conditions defined previously. Fig. 10 shows a comparison of all these radiated power limit curves with respect to a radiated power limit curve derived from the statistical trials. In general, the worst case Chebyshev limit is smaller than the Markov limit over most of the frequency range in Fig. 10. The radiated power limit curves are smaller for the DM signaling case than the SE signaling case as seen when comparing Fig. 9 with Fig. 10.

Additional radiated power limit curves were formulated from the minimum of the Markov and worst case Chebyshev limits for the SE and DM signaling cases. These limit curves are compared to two unique trial excitations in Fig. 11. A SE trial excitation was formulated where the ports were fed with the PRBS7 signal, and all the incident power waves had the same phase derived from the FFT of the time-domain PRBS7 signal. A DM trial excitation was generated where the ports were fed with the PRBS7 signal and the incident power waves were out of phase by π radians for each differential pair. All excited differential pairs were fed with the same differential excitation with no phase difference between the pairs. The SE excitation differs from the SE limit curve from 1.10

dB to 10.03 dB, and the DM excitation differs from the DM limit curve from 1.64 dB to 9.34 dB, the same as the impulse excitations as seen in Fig. 11.

A comparison of three radiated power limit curves is given in Fig. 12 to determine the best limit curve that approaches the DM signaling limit curve when only diagonal elements in the radiated power loss constant matrix are known. The motivation for Fig. 12 is the same as Fig. 7 with the impulse excitations. As before, the limit predicted for a DM signal using the total power loss, rather than diagonal elements in the power loss constant matrix, is even higher than the limit predicted for SE signals.

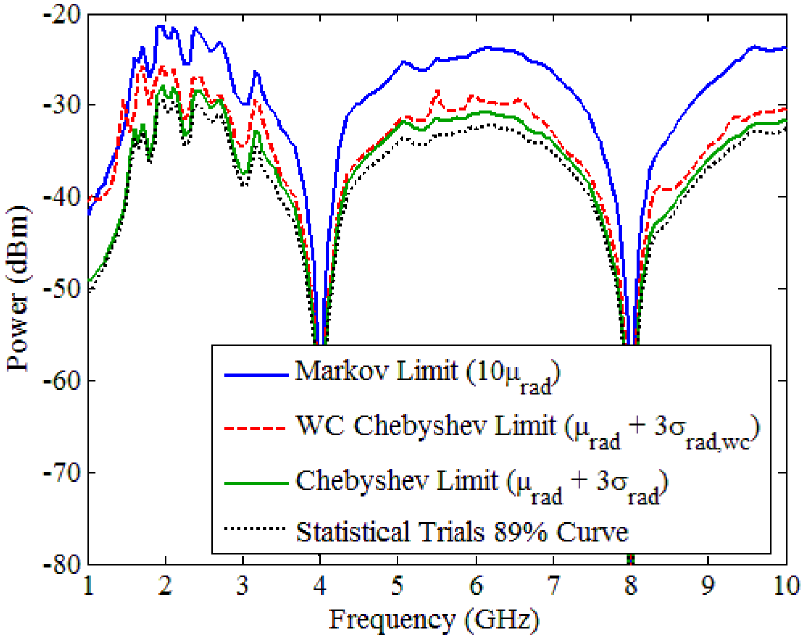

Fig. 10. Comparison of the maximum radiated power limit curves for a PRBS7 excitation and a differential-mode signaling port connectivity matrix.

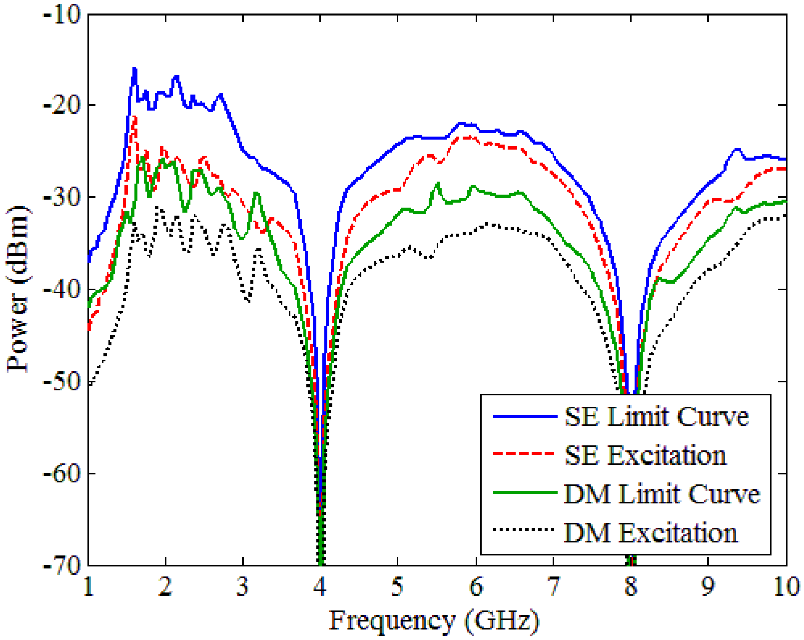

Fig. 11. Comparison of the spliced Markov and worst case Chebyshev limit curves using a single-ended signaling port connectivity matrix and a differential-mode signaling port connectivity matrix for PRBS7 excitations. The SE and DM excitations represent cases where the independent incident waves are in phase with one another.

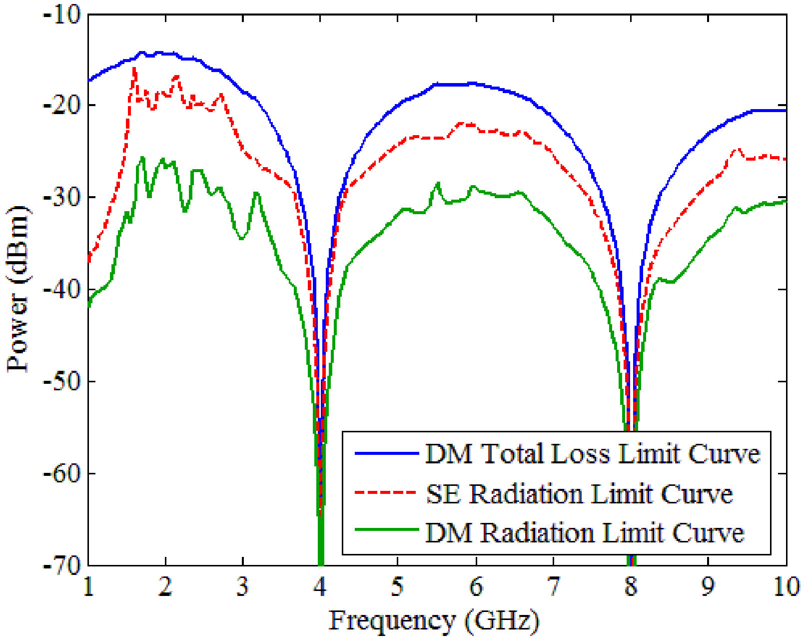

Fig. 12. Total power loss and radiated power loss limit curve comparison for differential-mode and single-ended signaling port connectivity matrices for a PRBS7 excitation.

C. Measurement with Pseudo-Random Bit Sequences

A series of reverberation chamber measurements were performed on the connector shown in Fig. 6(a) of [7], Fig. 6 of [8], and in Fig. 13 to characterize the radiated power for a single differential pair. The radiated power loss constants were found for the 3rd differential pair (from shortest to longest) in slice A of the middle wafer. The ports on the “receiving” end of the fed differential pair were terminated in matched loads and all other ports were left open. Continuous wave radiated power measurements were used to find the radiated power loss constants as described in [9]. A Tektronix BSA175C pattern generator with differential outputs was used in a reverberation chamber measurement to feed the differential pair with a PRBS7 signal. The pattern generator was configured with a 2 V total voltage maximum and a 0 V total voltage minimum output at a connected matched load. The data rate of the bit stream was 10.3125 Gbps. According to the pattern generator data sheet the typical rise time (10-90%) of the PRBS signal was 23 ps.

A spectrum analyzer was used to measure the radiated power and was configured with the following settings: 30 kHz resolution bandwidth, 1 GHz start frequency, 20 GHz stop frequency, 10 second sweep time, and 40 sweep averages. The sweep time was made sufficiently long so that multiple periods of the PRBS would be captured during the length of time the resolution bandwidth filter swept over any frequency. This setting ensured that the amplitude spectrum of the PRBS7 signal would be deterministic and would not vary with every frequency sweep.

The radiated power was predicted from the radiated power loss constant matrix where the PRBS7 signals for the positive and negative nets were modeled as a bit stream of trapezoidal pulses. The rise and fall times of the trapezoidal pulses were extrapolated from the data sheet typical value where the rise time was set to 28 ps and the fall time was set to 38 ps. An FFT was used to find the double-sided spectra of the PRBS7 signals for the positive and negative nets, and the total voltage spectra were converted to single-sided, incident power wave spectra. Equation (8) was used to find the radiated power where the port connectivity matrix was an identity matrix. A comparison of the measured radiated power and the radiated power envelope predicted using the deterministic PRBS signal is shown in Fig. 14. Above 12 GHz the calculated envelope overestimates the radiated power likely because the actual PRBS is not trapezoidal and damping in the actual waveform reduces the higher frequency spectral content.

Radiated power limit curves were calculated from the radiated power loss constant matrix and the simulated PRBS7 signal. A comparison of the SE signaling Markov limit, the SE signaling Chebyshev limit, and the DM calculated envelope from Fig. 14 is shown in Fig. 15. The SE signaling limit curves provide a bound for the radiated power assuming the radiation measurement were performed again with lossless and variable cable lengths. These curves also show the maximum radiated power limit is higher for SE signaling compared to DM signaling.

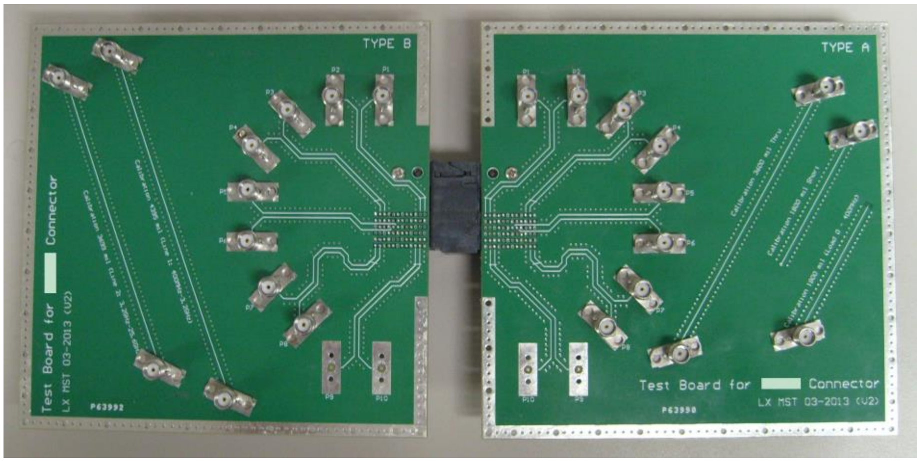

Fig. 13. PCB/connector pair used to measure radiated power. The PCBs were shorted with copper tape in the actual reverberation chamber measurement so that the radiated power from the connector was measured.

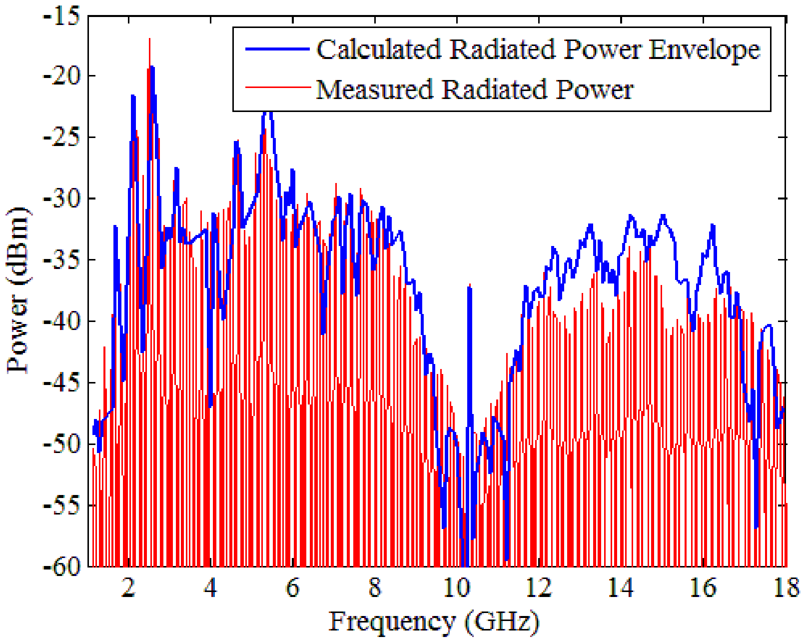

Fig. 14. Calculated radiated power envelope and measured radiated power for a differential pair fed with a differential PRBS7 signal.

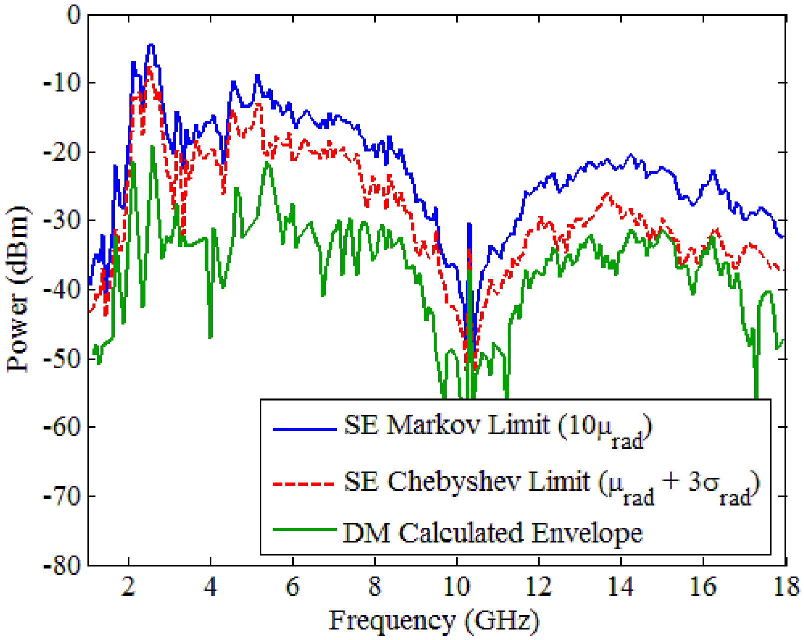

Fig. 15. Comparison of the singled-ended signaling radiated power limit curves with the deterministically calculated envelope for a differential PRBS7 signal.

V. CONCLUSION

Statistical estimates for maximum radiated power from a high-density connector are presented. These estimates are based on a power loss characterization technique using power loss constant matrices. Formulations are shown to provide practical, maximum radiated power estimates for large connectors where the entire radiated power loss constant matrix and the relative phase progression of the incident power wave signals may not be known. The statistical estimates are based on statistical bounding methods using the Markov and Chebyshev inequalities where the statistical problem assumes: a) known and deterministic magnitude spectra for the incident power waves at the PCB/connector interface, b) the incident power waves at the PCB/connector interface can be written as a linear function of independent incident power waves, and c) the independent incident power wave phases are uniformly distributed on $[-\pi,\pi)$. Maximum radiated power bounds are based on the radiated power mean and standard deviation which may require known diagonal and off-diagonal elements in the radiated power loss constant matrix. In many practical cases a radiated power limit can be defined as the minimum of a Markov and a worst case Chebyshev limit where the port connectivity matrix is an identity matrix. This limit can be used when the S-parameters of the PCB connector and only the diagonal elements in the radiated power loss constant matrix are known, as it assumes that all ports are driven SE (i.e. there are no DM signals). A tighter radiated power loss bound can be formulated with more complete radiated power loss constant matrices as is shown when comparing the traditional Chebyshev limit and the worst case Chebyshev limit. In most cases, a tighter radiated power limit can be formulated by performing additional two-port excitations to find off-diagonal elements in the radiated power loss constant matrix. Reductions in the number of independent incident power waves by defining incident power wave dependencies in the port connectivity matrix can also provide a tighter bound. Simulations and measurements are shown with impulse and PRBS signals to validate the statistical radiated power estimates. The maximum radiated power limit is illustrated to be higher for a port connectivity matrix representing SE signaling than for a port connectivity matrix representing DM signaling.

There are a few benefits to using a statistical approach for predicting a maximum radiated power limit over a worst-case deterministic approach. The first benefit is that this statistical approach has less severe over-prediction problems than a deterministic approach that uses worst case analysis to modify the radiated power equations. Another benefit is the modular nature of the presented statistical formulation. Additional information such as radiated power loss constant values or incident power wave dependencies can be incorporated into the radiated power limit calculation to provide an improved estimate should additional information be found. It is important to note that as the independent incident power waves are made dependent through definitions in the port connectivity matrix, the radiated power mean approaches the deterministic radiated power calculation result and the resulting radiated power variance approaches zero. An added benefit of the maximum radiated power limit estimation is that the presented formulation can be readily used to compare radiation performance from multiple PCB connectors, regardless of how they are driven.

REFERENCES

[1] C. R. Paul and D. R. Bush, “Radiated emissions from common-mode currents,” in *Proc. 1987 IEEE Int. Symp. Electromagn. Compat.*, Atlanta, GA, Aug. 25-27, 1987, pp. 197-203.

[2] D. M. Hockanson, J. L. Drewniak, T. H. Hubing, T. P. Van Doren, F. Sha, and M. J. Wilhelm, “Investigation of fundamental EMI source mechanisms driving common-mode radiation from printed circuit boards with attached cables,” *IEEE Trans. Electromagn. Compat.*, vol. 38, no. 4, pp. 557-566, Nov. 1996.

[3] C. R. Paul, “Modeling electromagnetic interference properties of printed circuit boards,” *IBM J. Res. Develop.*, vol. 33, no. 1, pp. 33-50, Jan. 1989.

[4] R. F. German, H. W. Ott, and C. R. Paul, “Effect of an image plane on printed circuit board radiation,” in *Proc. 1990 IEEE Int. Symp. Electromagn. Compat.*, Washington, DC, Aug. 21-23, 1990, pp. 284-291.

[5] B. Archambeault, S. Connor, M. S. Halligan, J. L. Drewniak, and A. E. Ruehli, “Electromagnetic radiation resulting from PCB/high-density connector interfaces,” *IEEE Trans. Electromagn. Compat.*, vol. 55, no. 4, pp. 614-623, Aug. 2013.

[6] H.-C. Chen, M. S. Halligan, S. Connor. X. Tian, X. Li, J. L. Drewniak, B. Archambeault, and T.-L. Wu, “Investigation of the radiated emission from high-speed/high density connector,” submitted for publication.

[7] X. Tian, M. S. Halligan, X. Li, K. Kim, H.-C. Chen, S. Connor, B. Archambeault, M. Cracraft, A. E. Ruehli, and J. L. Drewniak, “Modeling electromagnetic radiation at high-density PCB/connector interfaces,” submitted for publication.

[8] X. Tian, M. S. Halligan, X. Li, K. Kim, H.-C. Chen, S. Connor, and J. L. Drewniak, “Modeling and measurement of electromagnetic radiation from a practical PCB connector,” submitted for publication

[9] M. S. Halligan, X. Tian, X. Li, S. Connor, D. G. Beetner, and J. L. Drewniak, “Quantifying high-density connector radiation in a lossy multi-signal environment,” submitted for publication.

[10] D. M. Hockanson, C.-W. Lam, J. L. Drewniak, T. H. Hubing, and T. P. Van Doren, “Experimental and numerical investigations of fundamental radiation mechanisms in PCB designs with attached cables,” in *Proc. IEEE Int. Symp. Electromagn. Compat.*, Santa Clara, CA, Aug. 1996, pp. 305-310.

[11] X. Ye, J. Nadolny, J. L. Drewniak, T. H. Hubing, T. P. Van Doren, and D. E. DuBroff, “EMI associated with inter-board connection for module-on-backplane and stacked-card configurations,” in *Proc. IEEE Int. Symp. Electromagn. Compat.*, Seattle, WA, Aug. 1999, pp. 797-802.

[12] D. Hockanson and S. Radu, “An investigation of the effects of PCB module orientation on radiated EMI,” in *Proc. IEEE Int. Symp. Electromagn. Compat.*, Seattle, WA, Aug. 1999, pp. 399-404.

[13] X. Ye, J. L. Drewniak, J. Nadolny, and D. M. Hockanson, “High-performance inter-PCB connectors: analysis of EMI characteristics,” *IEEE Trans. Electromagn. Compat.*, vol. 44, no. 1, pp. 165-174, Feb. 2002.

[14] L. K. C. Wong, “Backplane connector radiated emission and shielding effectiveness,” in *Proc. IEEE Int. Symp. Electromagn. Compat.*, Anaheim, CA, Aug. 1992, pp. 346-351.

[15] L. O. Hoeft and J. S. Hofstra, “Measured electromagnetic shielding performance of commonly used cables and connectors,” *IEEE Trans. Electromagn. Compat.*, vol. 30, no. 3, pp. 260-275, Aug. 1988.

[16] B. Vanlandschoot, L. Martens, L. Torren, and D. Morlion, “An improved triaxial cell for transfer impedance measurements on multipins backplane connectors,” in *Proc. IEEE Int. Symp. Electromagn. Compat.*, Austin, TX, Aug. 1997, pp. 141-144.

[17] M. Leone and V. Navrátil, “On the electromagnetic radiation of printed-circuit-board interconnections,” *IEEE Trans. Electromagn. Compat.*, vol. 47, no. 2, pp. 219-226, May 2005.

[18] M. Friedrich and M. Leone, “Inductive network model for the radiation analysis of electrically small parallel-plate structures,” *IEEE Trans. Electromagn. Compat.*, vol. 53, no. 4, pp. 1015-1024, Nov. 2011.

[19] D. M. Pozar, *Microwave Engineering*, 3rd ed. Hoboken, NJ, USA: Wiley, 2005, pp. 181-182.

[20] A. Leon-Garcia, *Probability, Statistics, and Random Processes for Electrical Engineering*, 3rd ed. Upper Saddle River, NJ, USA: Pearson Prentice Hall, 2008, pp. 163, 181-183, 309-310.

SECTION

2. CONCLUSION

In the first paper of this dissertation, equations for estimating the maximum crosstalk in a three conductor transmission line are presented and validated against a well-known crosstalk formulation and validated against simulated and measured data. These formulas are based on the weak coupling assumption where the transmission line system has a single coupling region with a uniform cross section and are based in the frequency domain. These equations may be expanded to systems with more than three conductors through the application of the superposition principle. The newly presented formulas can model the maximum crosstalk for transmission lines in lossy, inhomogeneous media where the transmission lines may have unique and arbitrary lengths. Measurements and simulations show that the maximum crosstalk formulas capture the envelope of the near-end and far-end victim voltages well, often within a few decibels. The present equations are well suited for evaluation of signal integrity in systems where transmission line parameters are not well known and crosstalk sensitivity analysis is needed.

In the second paper, equations for estimating the maximum crosstalk in the frequency domain and in a three conductor, lossless, and homogeneous transmission line have been presented. The presented formulas are a simplified form of the equations in paper one that are based on an integral formulation. Derivations on another maximum crosstalk estimate for finite length transmission lines based on a relationship for infinitely long transmission lines are also presented. These derivations illustrate that the previously published estimate, though relatively simple to understand and shown to predict the maximum crosstalk well, mixes boundary conditions between infinite and finite transmission lines which is not strictly mathematically correct. Despite the mixing of boundary conditions, the previous maximum crosstalk estimate is demonstrated to be equivalent to the integral formulation based estimate under some restrictive conditions. These conditions may not occur in a practical setup making the previous formulation more prone to errors. The integral formulation based maximum crosstalk estimates are shown to be more robust because they can estimate the maximum crosstalk with fewer and less restrictive assumptions.

In the third paper, the radiation from a printed circuit board/connector interface was quantified using *S*-parameters without the presence of conductor and dielectric losses. The concept of using network parameters to calculate radiation from a printed circuit board/connector interface in the third paper served as a basis for the radiation calculations presented in the fourth and fifth papers of this dissertation. Three distinct radiation modes were found for the printed circuit board connector analyzed in the third paper. The first mode consists of a radiating structure comprised of printed circuit board reference planes driven by signals through the connector. This mode produces half-wavelength dipole type current on the printed circuit board reference planes. The radiation is significant with a transmission line common-mode excitation, even with ground references on three sides of the signal pair in a connector wafer. Another radiation mode is associated with the gap between the printed circuit boards that the connector spans. The radiation physics corresponded to those of a slot antenna that include the ground reference path through the connector. Lastly, at frequencies where the connector signal path lengths are not electrically short, resonances associated with integer half-wavelength antenna-mode current distributions result in significant radiation. Extensive work remains to develop a better understanding of coupling from transmission line modes to a radiation mode and to relate coupling to a radiation mode with the geometry in more than the rudimentary manner provided at present. A suitable formulation of the physics is needed to better engineer high-speed connectors for determining tradeoffs between signal integrity and electromagnetic interference across the connector.

In the fourth paper, a method is proposed to quantify the power losses at a high-density printed circuit board/connector interface. This method is based on network parameters and the conservation of power and can quantify power losses when material losses and multiple signals are present. The power losses are characterized through the definition of power loss constant matrices which are derived from well-designed single port and two port excitations for an *N*-port connector. Once found, the power loss constant matrices enable the evaluation of the radiated power loss, the material power loss, and the total power loss in a system with variable input signaling. This power loss characterization method allows designers to evaluate connector performance from EMI and signal integrity perspectives, as well as answer common design questions. The proposed method enables the evaluation of connector design modifications such as shielding, absorbing materials, and signal pin assignments and their relative effects on connector radiation. It also allows the direct evaluation of power losses in the frequency-domain which is not readily available when using a time-domain solver. Although the focus of this paper is the characterization of radiated power using simulations, the presented theory also applies to measurements as was shown in a reverberation chamber validation example. Despite using known input signaling information and worst case analysis, significant challenges remain to find full power loss constant matrices for large connectors with measurements due to the large number of measurements required.

In the fifth paper, statistical estimates for maximum radiated power from a high-density connector are presented. These estimates are based on a power loss characterization technique using power loss constant matrices. Formulations are shown to provide practical, maximum radiated power estimates for large connectors where the entire radiated power loss constant matrix and the relative phase progression of the incident power wave signals may not be known. The statistical estimates are based on statistical bounding methods using the Markov and Chebyshev inequalities where the statistical problem assumes: a) known and deterministic magnitude spectra for the incident power waves at the PCB/connector interface, b) the incident power waves at the PCB/connector interface can be written as a linear function of independent incident power waves, and c) the independent incident power wave phases are uniformly distributed on $[-\pi,\pi)$. Maximum radiated power bounds are based on the radiated power mean and standard deviation which may require known diagonal and off-diagonal elements in the radiated power loss constant matrix. In many practical cases a radiated power limit can be defined as the minimum of a Markov and a worst case Chebyshev limit where the port connectivity matrix is an identity matrix. This limit can be used when the S-parameters of the PCB connector and only the diagonal elements in the radiated power loss constant matrix are known, as it assumes that all ports are driven SE (i.e. there are no DM signals). A tighter radiated power loss bound can be formulated with more complete radiated power loss constant matrices as is shown when comparing the traditional Chebyshev limit and the worst case Chebyshev limit. In most cases, a tighter radiated power limit can be formulated by performing additional two-port excitations to find off-diagonal elements in the radiated power loss constant matrix. Reductions in the number of independent incident power waves by defining incident power wave dependencies in the port connectivity matrix can also provide a tighter bound. Simulations and measurements are shown with impulse and PRBS signals to validate the statistical radiated power estimates. The maximum radiated power limit is illustrated to be higher for a port connectivity matrix representing SE signaling than for a port connectivity matrix representing DM signaling.

There are a few benefits to using a statistical approach for predicting a maximum radiated power limit over a worst-case deterministic approach. The first benefit is that this statistical approach has less severe over-prediction problems than a deterministic approach that uses worst case analysis to modify the radiated power equations. Another benefit is the modular nature of the presented statistical formulation. Additional information such as radiated power loss constant values or incident power wave dependencies can be incorporated into the radiated power limit calculation to provide an improved estimate should additional information be found. It is important to note that as the independent incident power waves are made dependent through definitions in the port connectivity matrix, the radiated power mean approaches the deterministic radiated power calculation result and the resulting radiated power variance approaches zero. An added benefit of the maximum radiated power limit estimation is that the presented formulation can be readily used to compare radiation performance from multiple PCB connectors, regardless of how they are driven.

APPENDIX A

FINITE DIFFERENCE SIMULATION FORMULATION

I. PER-UNIT-LENGTH MODELS

Many of the analytical crosstalk expressions were validated by custom finite difference simulations. The finite difference simulation codes consisted mostly of solving the KVL and KCL equations formed by cascaded, electrically small transmission line circuits in the victim circuit. Instead of using the standard per-unit-length transmission line model found in most reference texts, a T-model was used as shown in Fig. 1. The T-model was used in the simulations due to its balanced structure since simulation accuracy was desired to be the same at both the near-end and far-end loads.

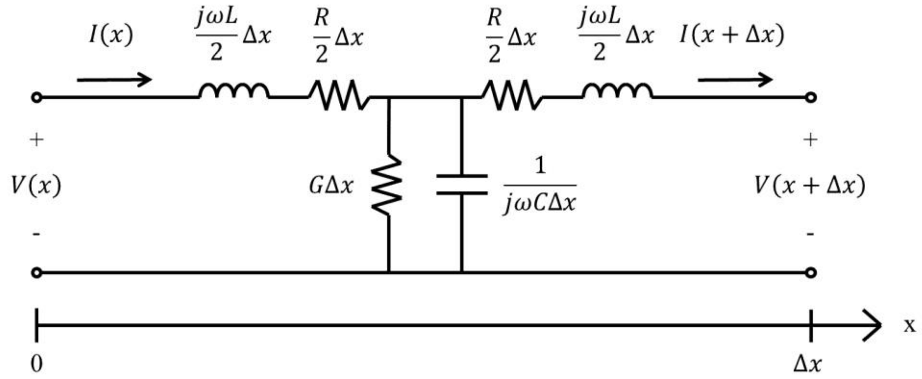

Fig. 1. Per-unit-length transmission line T-model.

The differential equations for the voltages and currents in the T-model are the same as those for the traditional per-unit-length transmission line model when the length of the per-unit-length section approaches zero. The derivations of the differential equations are given below. The two KVL equations from Fig. 1 can be written as,

$$-V(x)+I(x)\left[\frac{R+j\omega L}{2}\right]\Delta x+\left[I(x)-I(x+\Delta x)\right]\frac{1}{(G+j\omega C)\Delta x}=0 \tag{1a}$$

$$\left[I(x+\Delta x)-I(x)\right]\frac{1}{(G+j\omega C)\Delta x}+I(x+\Delta x)\left[\frac{R+j\omega L}{2}\right]\Delta x+V(x+\Delta x)=0\,. \tag{1b}$$

Inserting (1b) in (1a) reveals,

$$-V(x)+I(x)\left[\frac{R+j\omega L}{2}\right]\Delta x+I(x+\Delta x)\left[\frac{R+j\omega L}{2}\right]\Delta x+V(x+\Delta x)=0$$

$$\frac{V(x+\Delta x)-V(x)}{\Delta x}=-\frac{R+j\omega L}{2}\left[I(x+\Delta x)+I(x)\right]. \tag{2}$$

If a limit is taken where the per-unit-length section length approaches zero, then (2) reduces to,

$$\lim_{\Delta x\to 0}\frac{V(x+\Delta x)-V(x)}{\Delta x}=\lim_{\Delta x\to 0}-\frac{R+j\omega L}{2}\left[I(x+\Delta x)+I(x)\right]$$

$$\frac{dV(x)}{dx}=-RI(x)-j\omega LI(x). \tag{3}$$

The KCL equation from Fig. 1 can be written as,

$$-I(x)+I(x+\Delta x)+\frac{(G+j\omega C)\Delta x}{1+(G+j\omega C)\left(\frac{R+j\omega L}{2}\right)(\Delta x)^2}V(x)=0. \tag{4}$$

If a limit is taken where the per-unit length section length approaches zero then (4) reduces to,

$$\lim_{\Delta x\to 0}\frac{I(x+\Delta x)-I(x)}{\Delta x}=\lim_{\Delta x\to 0}\frac{-(G+j\omega C)}{1+(G+j\omega C)\left(\frac{R+j\omega L}{2}\right)(\Delta x)^2}V(x)$$

$$\frac{dI(x)}{dx}=-GV(x)-j\omega CV(x). \tag{5}$$

When a distributed voltage source is present in the victim circuit, voltage sources must be added to the T-model as shown in Fig. 2.

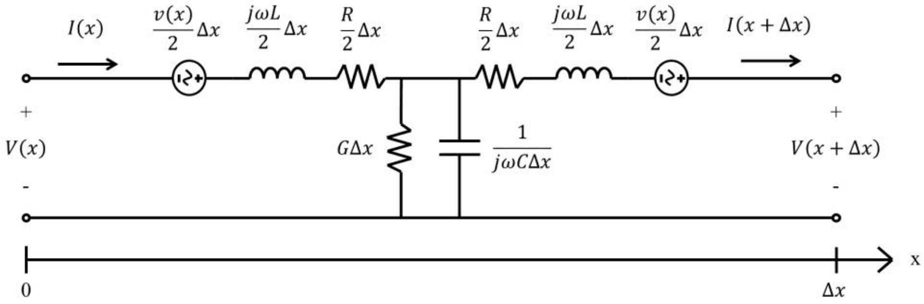

Fig. 2. Per-unit-length transmission line T-model with a distributed voltage source.

It can be shown that the differential equations for the voltages and currents in Fig. 2 when the length of the per-unit-length section approaches zero are,

$$\frac{dV(x)}{dx} = -RI(x) - j\omega LI(x) + v(x) \tag{6a}$$

$$\frac{dI(x)}{dx} = -GV(x) - j\omega CV(x). \tag{6b}$$

When a distributed current source is present in the victim circuit, a current source must be added to the T-model as shown in Fig. 3.

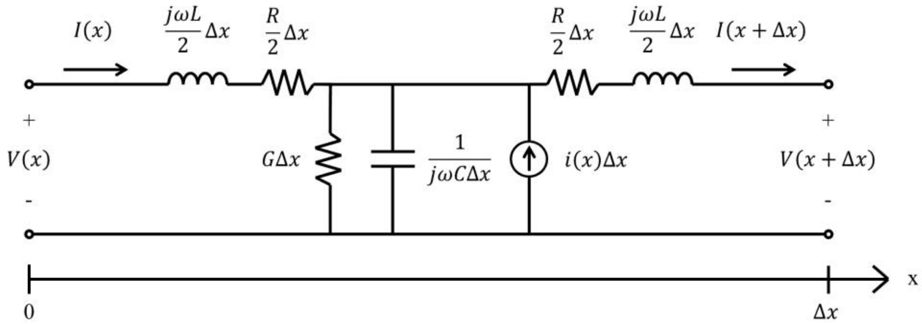

Fig. 3. Per-unit-length transmission line T-model with a distributed current source.

It can be shown that the differential equations for the voltages and currents in Fig. 3 when the length of the per-unit-length section approaches zero are,

$$\frac{dV(x)}{dx} = -RI(x) - j\omega LI(x) \tag{7a}$$

$$\frac{dI(x)}{dx} = -GV(x) - j\omega CV(x) + i(x). \tag{7b}$$

II. MATRIX EQUATIONS FOR DISTRIBUTED VOLTAGE SOURCES

The victim circuit was split into three distinct regions in the crosstalk analysis: a left hand side (LHS), a source region (SR), and a right hand side (RHS). These regions are indicated for the victim circuit in Fig. 4.

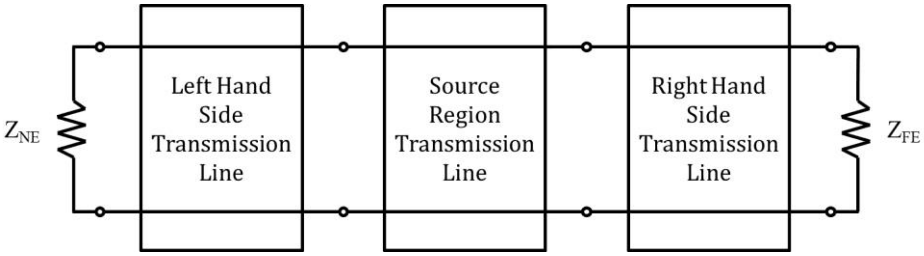

Fig. 4. Finite difference simulation victim circuit layout.

When considering distributed voltage sources in the source region, a series of KVL equation can be formulated in the victim circuit. These equations can be written using mesh currents and solved from a matrix of KVL equations. If a left hand side transmission line, source region transmission line, and right hand side transmission line exist, there are a total of seven unique equations that form the KVL matrix. The circuit at the victim near-end is shown in Fig. 5.

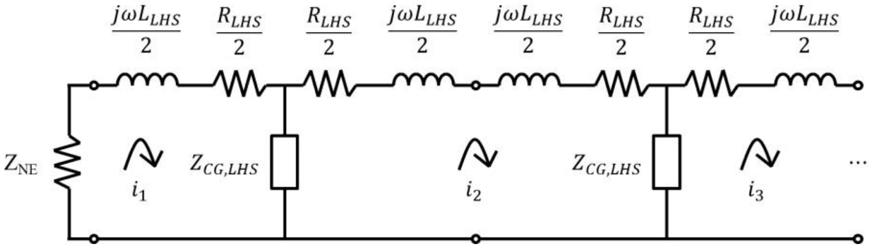

Fig. 5. Near-end victim finite difference circuit with mesh currents.

The near-end KVL equation is given by (8), and the general left hand side circuit KVL equation is given by (9). The circuit parameter definitions are defined to allow for different lengths for the per-unit-length transmission line sections.

$$\left(Z_{NE}+\frac{R_{LHS}+j\omega L_{LHS}}{2}+Z_{CG,LHS}\right)i_1+\left(-Z_{CG,LHS}\right)i_2=0 \tag{8}$$

$$\left(-Z_{CG,LHS}\right)i_1+\left(R_{LHS}+j\omega L_{LHS}+2Z_{CG,LHS}\right)i_2+\left(-Z_{CG,LHS}\right)i_3=0 \tag{9}$$

$$R_{LHS}=R\Delta x_{LHS} \tag{10a}$$

$$L_{LHS}=L\Delta x_{LHS} \tag{10b}$$

$$Z_{CG,LHS}=\frac{1}{j\omega C\Delta x_{LHS}+G\Delta x_{LHS}} \tag{10c}$$

The circuits at the LHS transition between the LHS and the SR circuits are shown in Fig. 6.

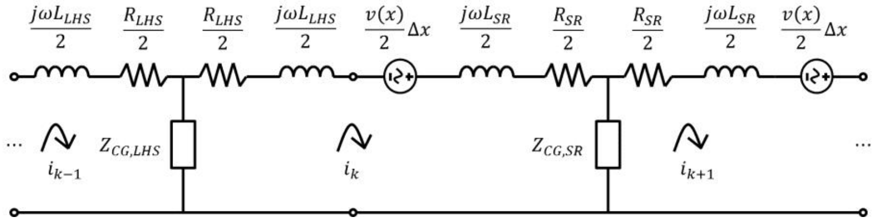

Fig. 6. LHS transition circuits with mesh currents.

The LHS transition KVL equation is given by (11), and the general source region circuit KVL equation is given by (12). There are k-1 per-unit-length transmission line sections in the left hand side transmission line region.

$$\begin{aligned}&\left(-Z_{CG,LHS}\right)i_{k-1}+\left(\frac{R_{LHS}+j\omega L_{LHS}}{2}+Z_{CG,LHS}+\frac{R_{SR}+j\omega L_{SR}}{2}+Z_{CG,SR}\right)i_k\\&\quad+\left(-Z_{CG,SR}\right)i_{k+1}=\frac{v(x)}{2}\Delta x_{SR}\end{aligned} \tag{11}$$

$$\left(-Z_{CG,SR}\right)i_k+\left(R_{SR}+j\omega L_{SR}+2Z_{CG,SR}\right)i_{k+1}+\left(-Z_{CG,SR}\right)i_{k+2}=v(x)\Delta x_{SR} \tag{12}$$

$$R_{SR} = R\Delta x_{SR} \tag{13a}$$

$$L_{SR} = L\Delta x_{SR} \tag{13b}$$

$$Z_{CG,SR} = \frac{1}{j\omega C\Delta x_{SR} + G\Delta x_{SR}} \tag{13c}$$

The circuits at the RHS transition between the SR and the RHS circuits are shown in Fig. 7.

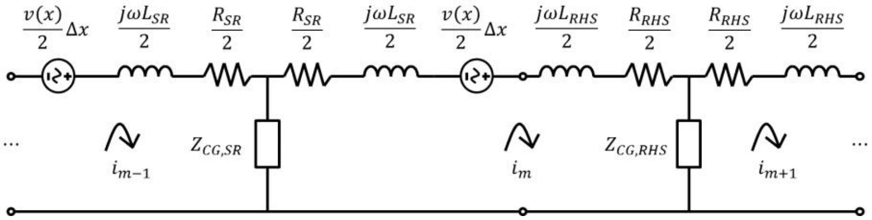

Fig. 7. RHS transition circuits with mesh currents.

The RHS transition KVL equation is given by (14). There are m-k per-unit-length transmission line sections in the source region transmission line region.

$$\begin{aligned}&\left(-Z_{CG,SR}\right)i_{m-1} + \left(\frac{R_{SR} + j\omega L_{SR}}{2} + Z_{CG,SR} + \frac{R_{RHS} + j\omega L_{RHS}}{2} + Z_{CG,RHS}\right)i_m \\ &\quad + \left(-Z_{CG,RHS}\right)i_{m+1} = \frac{v(x)}{2}\Delta x_{SR}\end{aligned} \tag{14}$$

$$R_{RHS} = R\Delta x_{RHS} \tag{15a}$$

$$L_{RHS} = L\Delta x_{RHS} \tag{15b}$$

$$Z_{CG,RHS} = \frac{1}{j\omega C\Delta x_{RHS} + G\Delta x_{RHS}} \tag{15c}$$

The circuit at the victim far-end is shown in Fig. 8.

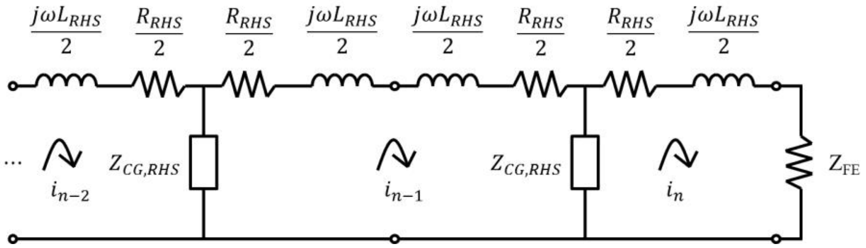

Fig. 8. Far-end victim finite difference circuit with mesh currents.

The general right hand side circuit KVL equation is given by (16) and the far-end KVL equation is given by (17). There are n-m per-unit-length transmission line sections in the right hand side transmission line region. In the overall victim circuit, there are n-1 per-unit-length transmission line sections.

$$\left(-Z_{CG,RHS}\right)i_{n-2} + \left(R_{RHS} + j\omega L_{RHS} + 2Z_{CG,RHS}\right)i_{n-1} + \left(-Z_{CG,RHS}\right)i_n = 0 \tag{16}$$

$$\left(-Z_{CG,RHS}\right)i_{n-1} + \left(Z_{FE} + \frac{R_{RHS} + j\omega L_{RHS}}{2} + Z_{CG,RHS}\right)i_n = 0 \tag{17}$$

The KVL matrix for the victim circuit can be written as shown in (18) and (19).

$$\left[KVL\ Z\right]\left[\bar{i}\right] = \left[\bar{v}\right] \tag{18}$$

$$\left[KVL\ Z\right] =$$

$$\begin{bmatrix}
A_1 & -Z_{CG,LHS} & 0 & \cdots & 0 & 0 & 0 & \cdots & 0 & 0 & 0 & \cdots & 0 \\
-Z_{CG,LHS} & B & -Z_{CG,LHS} & \cdots & 0 & 0 & 0 & \cdots & 0 & 0 & 0 & \cdots & 0 \\
\vdots & \ddots & \ddots & \ddots & 0 & 0 & 0 & \cdots & 0 & 0 & 0 & \cdots & 0 \\
0 & 0 & -Z_{CG,LHS} & B & -Z_{CG,LHS} & 0 & 0 & \cdots & 0 & 0 & 0 & \cdots & 0 \\
0 & 0 & 0 & -Z_{CG,LHS} & C & -Z_{CG,SR} & 0 & \cdots & 0 & 0 & 0 & \cdots & 0 \\
0 & 0 & 0 & 0 & -Z_{CG,SR} & D & -Z_{CG,SR} & \cdots & 0 & 0 & 0 & \cdots & 0 \\
\vdots & \vdots & \vdots & \vdots & \vdots & \ddots & \ddots & \ddots & 0 & 0 & 0 & \cdots & 0 \\
0 & 0 & 0 & 0 & 0 & 0 & -Z_{CG,SR} & D & -Z_{CG,SR} & 0 & 0 & \cdots & 0 \\
0 & 0 & 0 & 0 & 0 & 0 & 0 & -Z_{CG,SR} & E & -Z_{CG,RHS} & 0 & \cdots & 0 \\
0 & 0 & 0 & 0 & 0 & 0 & 0 & 0 & -Z_{CG,RHS} & F & -Z_{CG,RHS} & \cdots & 0 \\
\vdots & \vdots & \vdots & \vdots & \vdots & \vdots & \vdots & \vdots & \vdots & \ddots & \ddots & \ddots & 0 \\
0 & 0 & 0 & 0 & 0 & 0 & 0 & 0 & 0 & 0 & -Z_{CG,RHS} & F & -Z_{CG,RHS} \\
0 & 0 & 0 & 0 & 0 & 0 & 0 & 0 & 0 & 0 & 0 & -Z_{CG,RHS} & G_1
\end{bmatrix} \tag{19a}$$

$$\left[\bar{i}\right] = \left[i_1 \quad i_2 \quad i_3 \quad \cdots \quad i_{k-2} \quad i_{k-1} \quad i_k \quad i_{k+1} \quad i_{k+2} \quad \cdots \quad i_{m-2} \quad i_{m-1} \quad i_m \quad i_{m+1} \quad i_{m+2} \quad \cdots \quad i_{n-2} \quad i_{n-1} \quad i_n\right]^T \tag{19b}$$

$$[\bar{v}] = \begin{bmatrix} 0 & 0 & \cdots & 0 & \frac{v(x)}{2}\Delta x_{SR} & v(x)\Delta x_{SR} & \cdots & v(x)\Delta x_{SR} & \frac{v(x)}{2}\Delta x_{SR} & 0 & \cdots & 0 & 0 \end{bmatrix}^T \tag{19c}$$

$$A_1 = Z_{NE} + \frac{R_{LHS} + j\omega L_{LHS}}{2} + Z_{CG,LHS} \tag{19d}$$

$$B = R_{LHS} + j\omega L_{LHS} + 2Z_{CG,LHS} \tag{19e}$$

$$C = \frac{R_{LHS} + j\omega L_{LHS}}{2} + Z_{CG,LHS} + \frac{R_{SR} + j\omega L_{SR}}{2} + Z_{CG,SR} \tag{19f}$$

$$D = R_{SR} + j\omega L_{SR} + 2Z_{CG,SR} \tag{19g}$$

$$E = \frac{R_{SR} + j\omega L_{SR}}{2} + Z_{CG,SR} + \frac{R_{RHS} + j\omega L_{RHS}}{2} + Z_{CG,RHS} \tag{19h}$$

$$F = R_{RHS} + j\omega L_{RHS} + 2Z_{CG,RHS} \tag{19i}$$

$$G_1 = Z_{FE} + \frac{R_{RHS} + j\omega L_{RHS}}{2} + Z_{CG,RHS} \tag{19j}$$

If a source region transmission line and right hand side transmission line only exist, there are a total of five unique equations that form the KVL matrix. The KVL matrix for this case is similar to the KVL matrix where the LHS, SR, and RHS transmission line regions exist. The main difference resides in the KVL equation with the near-end load and the source region circuits. The circuit at the victim near-end is shown in Fig. 9, and the associated KVL matrix is shown in (20).

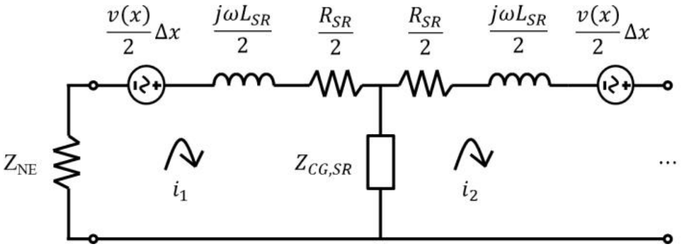

Fig. 9. Distributed voltage sources at the near-end.

$$[KVL\ Z] =$$

$$\begin{bmatrix} A_2 & -Z_{CG,SR} & 0 & \cdots & 0 & 0 & 0 & \cdots & 0 \\ -Z_{CG,SR} & D & -Z_{CG,SR} & \cdots & 0 & 0 & 0 & \cdots & 0 \\ \vdots & \ddots & \ddots & \ddots & 0 & 0 & 0 & \cdots & 0 \\ 0 & 0 & -Z_{CG,SR} & D & -Z_{CG,SR} & 0 & 0 & \cdots & 0 \\ 0 & 0 & 0 & -Z_{CG,SR} & E & -Z_{CG,RHS} & 0 & \cdots & 0 \\ 0 & 0 & 0 & 0 & -Z_{CG,RHS} & F & -Z_{CG,RHS} & \cdots & 0 \\ \vdots & \vdots & \vdots & \vdots & \vdots & \ddots & \ddots & \ddots & 0 \\ 0 & 0 & 0 & 0 & 0 & 0 & -Z_{CG,RHS} & F & -Z_{CG,RHS} \\ 0 & 0 & 0 & 0 & 0 & 0 & 0 & -Z_{CG,RHS} & G_1 \end{bmatrix} \tag{20a}$$

$$[\bar{i}] = [i_1 \quad i_2 \quad i_3 \quad \cdots \quad i_{m-2} \quad i_{m-1} \quad i_m \quad i_{m+1} \quad i_{m+2} \quad \cdots \quad i_{n-2} \quad i_{n-1} \quad i_n]^T \tag{20b}$$

$$[\bar{v}] = \left[\frac{v(x)}{2}\Delta x_{SR} \quad v(x)\Delta x_{SR} \quad \cdots \quad v(x)\Delta x_{SR} \quad \frac{v(x)}{2}\Delta x_{SR} \quad 0 \quad \cdots \quad 0 \quad 0 \right]^T \tag{20c}$$

$$A_2 = Z_{NE} + \frac{R_{SR} + j\omega L_{SR}}{2} + Z_{CG,SR} \tag{20d}$$

If the LHS, SR, and RHS transmission line regions exist, but the LHS transmission line region has only one per-unit-length section as shown below in Fig. 10, the KVL matrix must be modified to (21).

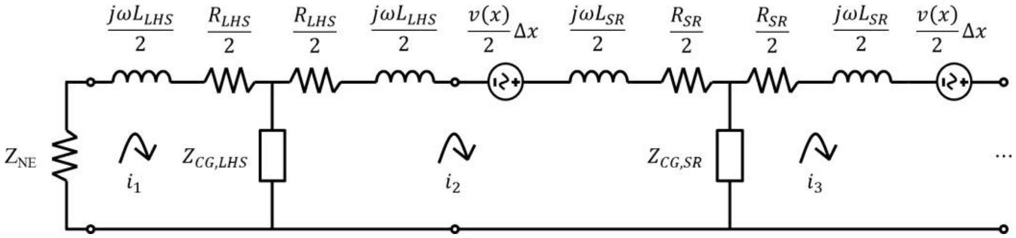

Fig. 10. Distributed voltage source close to the near-end.

$$[KVL\ Z] = \begin{bmatrix} A_1 & -Z_{CG,LHS} & 0 & 0 & \cdots & 0 & 0 & 0 & \cdots & 0 \\ -Z_{CG,LHS} & C & -Z_{CG,SR} & 0 & \cdots & 0 & 0 & 0 & \cdots & 0 \\ 0 & -Z_{CG,SR} & D & -Z_{CG,SR} & \cdots & 0 & 0 & 0 & \cdots & 0 \\ \vdots & \vdots & \ddots & \ddots & \ddots & 0 & 0 & 0 & \cdots & 0 \\ 0 & 0 & 0 & -Z_{CG,SR} & D & -Z_{CG,SR} & 0 & 0 & \cdots & 0 \\ 0 & 0 & 0 & 0 & -Z_{CG,SR} & E & -Z_{CG,RHS} & 0 & \cdots & 0 \\ 0 & 0 & 0 & 0 & 0 & -Z_{CG,RHS} & F & -Z_{CG,RHS} & \cdots & 0 \\ \vdots & \vdots & \vdots & \vdots & \vdots & \vdots & \ddots & \ddots & \ddots & 0 \\ 0 & 0 & 0 & 0 & 0 & 0 & 0 & -Z_{CG,RHS} & F & -Z_{CG,RHS} \\ 0 & 0 & 0 & 0 & 0 & 0 & 0 & 0 & -Z_{CG,RHS} & G_1 \end{bmatrix} \tag{21a}$$

$$[\bar{i}] = \begin{bmatrix} i_1 & i_2 & i_3 & i_4 & \cdots & i_{m-2} & i_{m-1} & i_m & i_{m+1} & i_{m+2} & \cdots & i_{n-2} & i_{n-1} & i_n \end{bmatrix}^T \tag{21b}$$

$$[\bar{v}] = \begin{bmatrix} 0 & \frac{v(x)}{2}\Delta x_{SR} & v(x)\Delta x_{SR} & \cdots & v(x)\Delta x_{SR} & \frac{v(x)}{2}\Delta x_{SR} & 0 & \cdots & 0 & 0 \end{bmatrix}^T \tag{21c}$$

If the LHS, SR, and RHS transmission line regions exist, but the SR transmission line region has only one per-unit-length section as shown below in Fig. 11, the KVL matrix must be modified to (22).

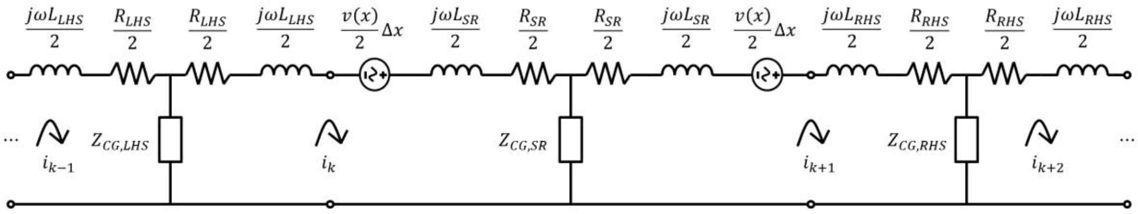

Fig. 11. Distributed voltage source single section.

$$[KVL\ Z] = \begin{bmatrix} A_1 & -Z_{CG,LHS} & 0 & \cdots & 0 & 0 & 0 & 0 & \cdots & 0 \\ -Z_{CG,LHS} & B & -Z_{CG,LHS} & \cdots & 0 & 0 & 0 & 0 & \cdots & 0 \\ \vdots & \ddots & \ddots & \ddots & 0 & 0 & 0 & 0 & \cdots & 0 \\ 0 & 0 & -Z_{CG,LHS} & B & -Z_{CG,LHS} & 0 & 0 & 0 & \cdots & 0 \\ 0 & 0 & 0 & -Z_{CG,LHS} & C & -Z_{CG,SR} & 0 & 0 & \cdots & 0 \\ 0 & 0 & 0 & 0 & -Z_{CG,SR} & E & -Z_{CG,RHS} & 0 & \cdots & 0 \\ 0 & 0 & 0 & 0 & 0 & -Z_{CG,RHS} & F & -Z_{CG,RHS} & \cdots & 0 \\ \vdots & \vdots & \vdots & \vdots & \vdots & \vdots & \ddots & \ddots & \ddots & 0 \\ 0 & 0 & 0 & 0 & 0 & 0 & 0 & -Z_{CG,RHS} & F & -Z_{CG,RHS} \\ 0 & 0 & 0 & 0 & 0 & 0 & 0 & 0 & -Z_{CG,RHS} & G_1 \end{bmatrix} \tag{22a}$$

$$[\bar{i}]=\begin{bmatrix} i_1 & i_2 & i_3 & \cdots & i_{k-2} & i_{k-1} & i_k & i_{k+1} & i_{k+2} & i_{k+3} & \cdots & i_{n-2} & i_{n-1} & i_n \end{bmatrix}^T \tag{22b}$$

$$[\bar{v}]=\begin{bmatrix} 0 & 0 & \cdots & 0 & \frac{v(x)}{2}\Delta x_{SR} & \frac{v(x)}{2}\Delta x_{SR} & 0 & \cdots & 0 & 0 \end{bmatrix}^T \tag{22c}$$

If the LHS, SR, and RHS transmission line regions exist, but the RHS transmission line region has only one per-unit-length section as shown in Fig. 12, the KVL matrix must be modified to (23).

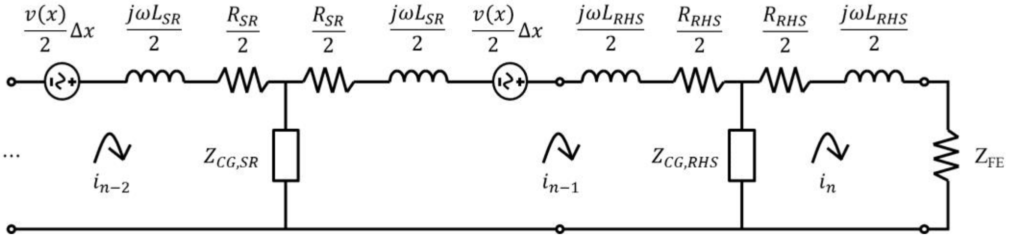

Fig. 12. Distributed voltage source close to the far-end.

$$[KVL\ Z]=$$

$$\begin{bmatrix}
A_1 & -Z_{CG,LHS} & 0 & \cdots & 0 & 0 & 0 & \cdots & 0 & 0 \\
-Z_{CG,LHS} & B & -Z_{CG,LHS} & \cdots & 0 & 0 & 0 & \cdots & 0 & 0 \\
\vdots & \ddots & \ddots & \ddots & 0 & 0 & 0 & \cdots & 0 & 0 \\
0 & 0 & -Z_{CG,LHS} & B & -Z_{CG,LHS} & 0 & 0 & \cdots & 0 & 0 \\
0 & 0 & 0 & -Z_{CG,LHS} & C & -Z_{CG,SR} & 0 & \cdots & 0 & 0 \\
0 & 0 & 0 & 0 & -Z_{CG,SR} & D & -Z_{CG,SR} & \cdots & 0 & 0 \\
\vdots & \vdots & \vdots & \vdots & \vdots & \ddots & \ddots & \ddots & 0 & 0 \\
0 & 0 & 0 & 0 & 0 & 0 & -Z_{CG,SR} & D & -Z_{CG,SR} & 0 \\
0 & 0 & 0 & 0 & 0 & 0 & 0 & -Z_{CG,SR} & E & -Z_{CG,RHS} \\
0 & 0 & 0 & 0 & 0 & 0 & 0 & 0 & -Z_{CG,RHS} & G_1
\end{bmatrix} \tag{23a}$$

$$[\bar{i}]=\begin{bmatrix} i_1 & i_2 & i_3 & \cdots & i_{k-2} & i_{k-1} & i_k & i_{k+1} & i_{k+2} & \cdots & i_{n-3} & i_{n-2} & i_{n-1} & i_n \end{bmatrix}^T \tag{23b}$$

$$[\bar{v}]=\begin{bmatrix} 0 & 0 & \cdots & 0 & \frac{v(x)}{2}\Delta x_{SR} & v(x)\Delta x_{SR} & \cdots & v(x)\Delta x_{SR} & \frac{v(x)}{2}\Delta x_{SR} & 0 \end{bmatrix}^T \tag{23c}$$

If a left hand side transmission line and a source region transmission line only exist, there are a total of five unique equations that form the KVL matrix. The KVL matrix for this case is similar to the KVL matrix where the LHS, SR, and RHS transmission line regions exist. The main difference resides in the KVL equation with the far-end load and the source region circuits. The circuit at the victim far-end is shown in Fig. 13, and the associated KVL matrix is shown in (24).

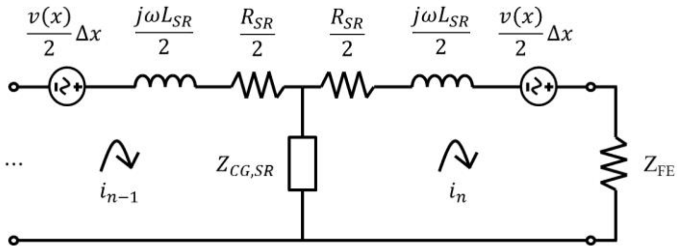

Fig. 13. Distributed voltage sources at the far-end.

$$[KVL\ Z] =$$

$$\begin{bmatrix} A_1 & -Z_{CG,LHS} & 0 & \cdots & 0 & 0 & 0 & \cdots & 0 \\ -Z_{CG,LHS} & B & -Z_{CG,LHS} & \cdots & 0 & 0 & 0 & \cdots & 0 \\ \vdots & \ddots & \ddots & \ddots & 0 & 0 & 0 & \cdots & 0 \\ 0 & 0 & -Z_{CG,LHS} & B & -Z_{CG,LHS} & 0 & 0 & \cdots & 0 \\ 0 & 0 & 0 & -Z_{CG,LHS} & C & -Z_{CG,SR} & 0 & \cdots & 0 \\ 0 & 0 & 0 & 0 & -Z_{CG,SR} & D & -Z_{CG,SR} & \cdots & 0 \\ \vdots & \vdots & \vdots & \vdots & \vdots & \ddots & \ddots & \ddots & 0 \\ 0 & 0 & 0 & 0 & 0 & 0 & -Z_{CG,SR} & D & -Z_{CG,SR} \\ 0 & 0 & 0 & 0 & 0 & 0 & 0 & -Z_{CG,SR} & G_2 \end{bmatrix} \tag{24a}$$

$$[\bar{i}] = [i_1 \quad i_2 \quad i_3 \quad \cdots \quad i_{k-2} \quad i_{k-1} \quad i_k \quad i_{k+1} \quad i_{k+2} \quad \cdots \quad i_{n-2} \quad i_{n-1} \quad i_n]^T \tag{24b}$$

$$[\bar{v}] = \left[0 \quad 0 \quad \cdots \quad 0 \quad \frac{v(x)}{2}\Delta x_{SR} \quad v(x)\Delta x_{SR} \quad \cdots \quad v(x)\Delta x_{SR} \quad \frac{v(x)}{2}\Delta x_{SR}\right]^T \tag{24c}$$

$$G_2 = Z_{FE} + \frac{R_{SR} + j\omega L_{SR}}{2} + Z_{CG,SR} \tag{24d}$$

III. MATRIX EQUATIONS FOR DISTRIBUTED CURRENT SOURCES

When considering distributed current sources in the source region, a series of KCL equations can be formulated in the victim circuit. These equations can be written using node voltages and the node voltages can be solved from a matrix of these KCL equations. If a left hand side transmission line, source region transmission line, and right hand side transmission line exist, there are a total of 11 unique equations that form the KCL matrix. The circuit at the victim near-end is shown in Fig. 14.

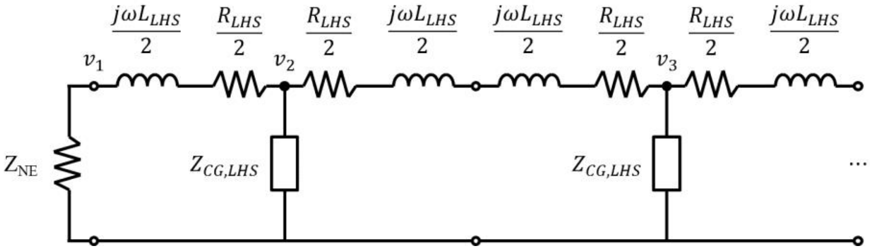

Fig. 14. Near-end victim finite difference circuit with node voltages.

The near-end KCL equations are given by (25) and (26). The general left hand side circuit KCL equation is given by (27). The circuit parameter definitions are defined to allow for different lengths for the per-unit-length transmission line sections. Additional parameter definitions are given in (10).

$$\left(\frac{1}{Z_{NE}}+\frac{2}{R_{LHS}+j\omega L_{LHS}}\right)v_1+\left(\frac{-2}{R_{LHS}+j\omega L_{LHS}}\right)v_2=0 \tag{25}$$

$$\left(\frac{-2}{R_{LHS}+j\omega L_{LHS}}\right)v_1+\left(\frac{3}{R_{LHS}+j\omega L_{LHS}}+\frac{1}{Z_{CG,LHS}}\right)v_2+\left(\frac{-1}{R_{LHS}+j\omega L_{LHS}}\right)v_3=0 \tag{26}$$

$$\left(\frac{-1}{R_{LHS}+j\omega L_{LHS}}\right)v_2+\left(\frac{2}{R_{LHS}+j\omega L_{LHS}}+\frac{1}{Z_{CG,LHS}}\right)v_3+\left(\frac{-1}{R_{LHS}+j\omega L_{LHS}}\right)v_4=0 \tag{27}$$

The circuits at the LHS transition between the LHS and the SR circuits are shown in Fig. 15.

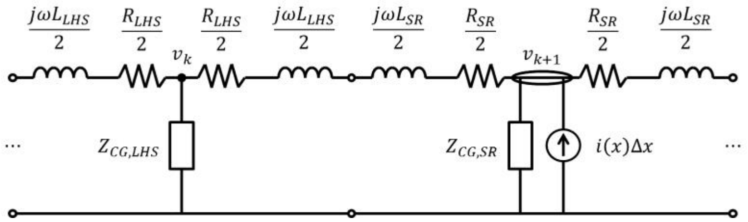

Fig. 15. LHS transition circuits with node voltages.

The LHS transition KCL equations are given by (28) and (29). The general source region circuit KCL equation is given by (30). There are k-1 per-unit-length transmission line sections in the left hand side transmission line region. Additional parameter definitions are given in (13).

$$\left(\frac{-1}{R_{LHS}+j\omega L_{LHS}}\right)v_{k-1}+\left(\frac{1}{R_{LHS}+j\omega L_{LHS}}+\frac{1}{Z_{CG,LHS}}+\frac{2}{R_{LHS}+j\omega L_{LHS}+R_{SR}+j\omega L_{SR}}\right)v_k + \left(\frac{-2}{R_{LHS}+j\omega L_{LHS}+R_{SR}+j\omega L_{SR}}\right)v_{k+1}=0 \tag{28}$$

$$\left(\frac{-2}{R_{LHS}+j\omega L_{LHS}+R_{SR}+j\omega L_{SR}}\right)v_k+\left(\frac{2}{R_{LHS}+j\omega L_{LHS}+R_{SR}+j\omega L_{SR}}+\frac{1}{Z_{CG,SR}}+\frac{1}{R_{SR}+j\omega L_{SR}}\right)v_{k+1} + \left(\frac{-1}{R_{SR}+j\omega L_{SR}}\right)v_{k+2}=i(x)\Delta x_{SR} \tag{29}$$

$$\left(\frac{-1}{R_{SR}+j\omega L_{SR}}\right)v_{k+1}+\left(\frac{2}{R_{SR}+j\omega L_{SR}}+\frac{1}{Z_{CG,SR}}\right)v_{k+2}+\left(\frac{-1}{R_{SR}+j\omega L_{SR}}\right)v_{k+3}=i(x)\Delta x_{SR} \tag{30}$$

The circuits at the RHS transition between the SR and the RHS circuits are shown below in Fig. 16.

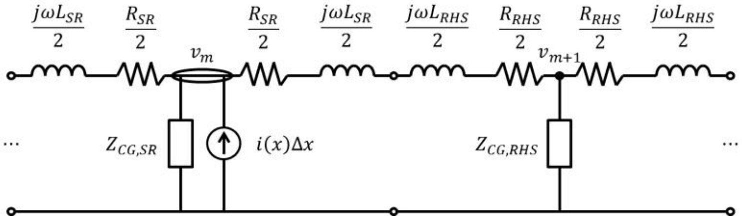

Fig. 16. RHS transition circuits with node voltages.

The RHS transition KCL equations are given by (31) and (32). There are m-k per-unit-length transmission line sections in the source region transmission line region. Additional parameter definitions are given in (15).

$$\left(\frac{-1}{R_{SR}+j\omega L_{SR}}\right)v_{m-1}+\left(\frac{1}{R_{SR}+j\omega L_{SR}}+\frac{1}{Z_{CG,SR}}+\frac{2}{R_{SR}+j\omega L_{SR}+R_{RHS}+j\omega L_{RHS}}\right)v_{m}$$
$$+\left(\frac{-2}{R_{SR}+j\omega L_{SR}+R_{RHS}+j\omega L_{RHS}}\right)v_{m+1}=i(x)\Delta x_{SR} \quad (31)$$

$$\left(\frac{-2}{R_{SR}+j\omega L_{SR}+R_{RHS}+j\omega L_{RHS}}\right)v_{m}+\left(\frac{2}{R_{SR}+j\omega L_{SR}+R_{RHS}+j\omega L_{RHS}}+\frac{1}{Z_{CG,RHS}}+\frac{1}{R_{RHS}+j\omega L_{RHS}}\right)v_{m+1}$$
$$+\left(\frac{-1}{R_{RHS}+j\omega L_{RHS}}\right)v_{m+2}=0 \quad (32)$$

The circuit at the victim far-end is shown below in Fig. 17.

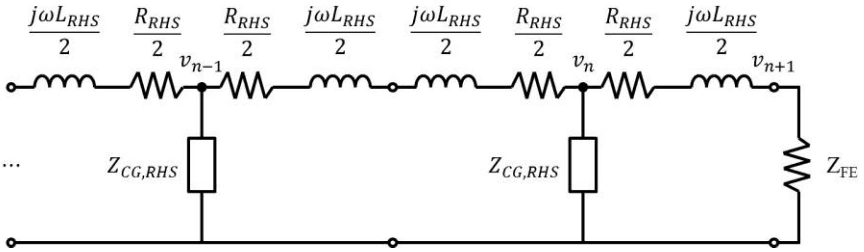

Fig. 17. Far-end victim finite difference circuit with node voltages.

The general right hand side circuit KCL equation is given by (33), and the far-end KCL equations are given by (34) and (35). There are n-m per-unit-length transmission line sections in the right hand side transmission line region. In the overall victim circuit, there are n-1 per-unit-length transmission line sections.

$$\left(\frac{-1}{R_{RHS}+j\omega L_{RHS}}\right)v_{n-2}+\left(\frac{2}{R_{RHS}+j\omega L_{RHS}}+\frac{1}{Z_{CG,RHS}}\right)v_{n-1}+\left(\frac{-1}{R_{RHS}+j\omega L_{RHS}}\right)v_{n}=0 \quad (33)$$

$$\left(\frac{-1}{R_{RHS}+j\omega L_{RHS}}\right)v_{n-1}+\left(\frac{3}{R_{RHS}+j\omega L_{RHS}}+\frac{1}{Z_{CG,RHS}}\right)v_{n}+\left(\frac{-2}{R_{RHS}+j\omega L_{RHS}}\right)v_{n+1}=0 \quad (34)$$

$$\left(\frac{-2}{R_{RHS}+j\omega L_{RHS}}\right)v_{n}+\left(\frac{2}{R_{RHS}+j\omega L_{RHS}}+\frac{1}{Z_{FE}}\right)v_{n+1}=0 \quad (35)$$

The KCL matrix can then be written as shown in (36) and (37).

$$\left[KVL\,Y\right]\left[\bar{v}\right]=\left[\bar{i}\right] \tag{36}$$

$$\left[KVL\,Y\right]=$$

$$\begin{bmatrix}
A & 2B & 0 & 0 & \cdots & 0 & 0 & 0 & 0 & \cdots & 0 & 0 & 0 & 0 & \cdots & 0 & 0\\
2B & C & B & 0 & \cdots & 0 & 0 & 0 & 0 & \cdots & 0 & 0 & 0 & 0 & \cdots & 0 & 0\\
0 & B & D & B & \cdots & 0 & 0 & 0 & 0 & \cdots & 0 & 0 & 0 & 0 & \cdots & 0 & 0\\
\vdots & \vdots & \ddots & \ddots & \ddots & 0 & 0 & 0 & 0 & \cdots & 0 & 0 & 0 & 0 & \cdots & 0 & 0\\
0 & 0 & 0 & B & D & B & 0 & 0 & 0 & \cdots & 0 & 0 & 0 & 0 & \cdots & 0 & 0\\
0 & 0 & 0 & 0 & B & E & F & 0 & 0 & \cdots & 0 & 0 & 0 & 0 & \cdots & 0 & 0\\
0 & 0 & 0 & 0 & 0 & F & G & H & 0 & \cdots & 0 & 0 & 0 & 0 & \cdots & 0 & 0\\
0 & 0 & 0 & 0 & 0 & 0 & H & J & H & \cdots & 0 & 0 & 0 & 0 & \cdots & 0 & 0\\
\vdots & \vdots & \vdots & \vdots & \vdots & \vdots & \vdots & \ddots & \ddots & \ddots & 0 & 0 & 0 & 0 & \cdots & 0 & 0\\
0 & 0 & 0 & 0 & 0 & 0 & 0 & 0 & H & J & H & 0 & 0 & 0 & \cdots & 0 & 0\\
0 & 0 & 0 & 0 & 0 & 0 & 0 & 0 & 0 & H & K & L & 0 & 0 & \cdots & 0 & 0\\
0 & 0 & 0 & 0 & 0 & 0 & 0 & 0 & 0 & 0 & L & M & N & 0 & \cdots & 0 & 0\\
0 & 0 & 0 & 0 & 0 & 0 & 0 & 0 & 0 & 0 & 0 & N & P & N & \cdots & 0 & 0\\
\vdots & \vdots & \vdots & \vdots & \vdots & \vdots & \vdots & \vdots & \vdots & \vdots & \vdots & \vdots & \ddots & \ddots & \ddots & 0 & 0\\
0 & 0 & 0 & 0 & 0 & 0 & 0 & 0 & 0 & 0 & 0 & 0 & 0 & N & P & N & 0\\
0 & 0 & 0 & 0 & 0 & 0 & 0 & 0 & 0 & 0 & 0 & 0 & 0 & 0 & N & Q & 2N\\
0 & 0 & 0 & 0 & 0 & 0 & 0 & 0 & 0 & 0 & 0 & 0 & 0 & 0 & 0 & 2N & R
\end{bmatrix} \tag{37a}$$

$$\left[\bar{v}\right]=\begin{bmatrix} v_1 & v_2 & v_3 & v_4 & \cdots & v_{k-2} & v_{k-1} & v_k & v_{k+1} & v_{k+2} & v_{k+3} & \cdots & v_{m-2} & v_{m-1} & v_m & v_{m+1} & v_{m+2} & v_{m+3} & \cdots & v_{n-2} & v_{n-1} & v_n & v_{n+1}\end{bmatrix}^T \tag{37b}$$

$$\left[\bar{i}\right]=\begin{bmatrix}0 & 0 & 0 & \cdots & 0 & 0 & i(x)\Delta x_{SR} & i(x)\Delta x_{SR} & \cdots & i(x)\Delta x_{SR} & i(x)\Delta x_{SR} & 0 & 0 & \cdots & 0 & 0 & 0\end{bmatrix}^T \tag{37c}$$

$$A=\frac{1}{Z_{NE}}+\frac{2}{R_{LHS}+j\omega L_{LHS}} \tag{37d}$$

$$B=\frac{-1}{R_{LHS}+j\omega L_{LHS}} \tag{37e}$$

$$C=\frac{3}{R_{LHS}+j\omega L_{LHS}}+\frac{1}{Z_{CG,LHS}} \tag{37f}$$

$$D=\frac{2}{R_{LHS}+j\omega L_{LHS}}+\frac{1}{Z_{CG,LHS}} \tag{37g}$$

$$E=\frac{1}{R_{LHS}+j\omega L_{LHS}}+\frac{1}{Z_{CG,LHS}}+\frac{2}{R_{LHS}+j\omega L_{LHS}+R_{SR}+j\omega L_{SR}} \tag{37h}$$

$$F=\frac{-2}{R_{LHS}+j\omega L_{LHS}+R_{SR}+j\omega L_{SR}} \tag{37i}$$

$$G = \frac{2}{R_{LHS} + j\omega L_{LHS} + R_{SR} + j\omega L_{SR}} + \frac{1}{Z_{CG,SR}} + \frac{1}{R_{SR} + j\omega L_{SR}} \tag{37j}$$

$$H = \frac{-1}{R_{SR} + j\omega L_{SR}} \tag{37k}$$

$$J = \frac{2}{R_{SR} + j\omega L_{SR}} + \frac{1}{Z_{CG,SR}} \tag{37l}$$

$$K = \frac{1}{R_{SR} + j\omega L_{SR}} + \frac{1}{Z_{CG,SR}} + \frac{2}{R_{SR} + j\omega L_{SR} + R_{RHS} + j\omega L_{RHS}} \tag{37m}$$

$$L = \frac{-2}{R_{SR} + j\omega L_{SR} + R_{RHS} + j\omega L_{RHS}} \tag{37n}$$

$$M = \frac{2}{R_{SR} + j\omega L_{SR} + R_{RHS} + j\omega L_{RHS}} + \frac{1}{Z_{CG,RHS}} + \frac{1}{R_{RHS} + j\omega L_{RHS}} \tag{37o}$$

$$N = \frac{-1}{R_{RHS} + j\omega L_{RHS}} \tag{37p}$$

$$P = \frac{2}{R_{RHS} + j\omega L_{RHS}} + \frac{1}{Z_{CG,RHS}} \tag{37q}$$

$$Q = \frac{3}{R_{RHS} + j\omega L_{RHS}} + \frac{1}{Z_{CG,RHS}} \tag{37r}$$

$$R = \frac{2}{R_{RHS} + j\omega L_{RHS}} + \frac{1}{Z_{FE}} \tag{37s}$$

If a source region transmission line and right hand side transmission line only exist, there are a total of eight unique equations that form the KCL matrix. The KCL matrix for this case is similar to the KCL matrix where the LHS, SR, and RHS transmission line regions exist. The main difference resides in the KCL equations with the near-end load and the source region circuits. The circuit at the victim near-end is shown in Fig. 18, and the associated KCL matrix is shown in (38).

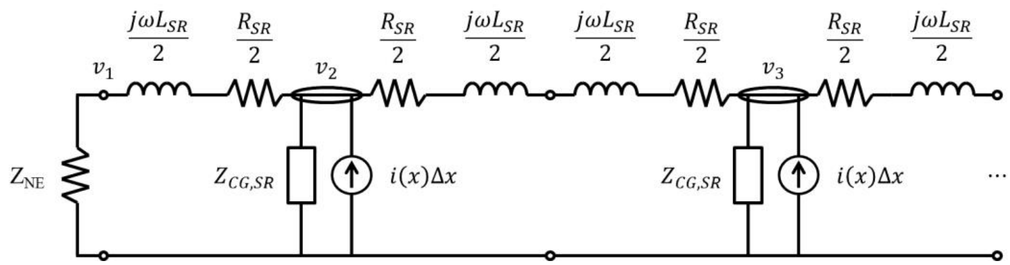

Fig. 18. Distributed current sources at the near-end.

$$[KVL\,Y] =$$

$$\begin{bmatrix}
A_2 & 2H & 0 & 0 & \cdots & 0 & 0 & 0 & 0 & \cdots & 0 & 0 \\
2H & C_2 & H & 0 & \cdots & 0 & 0 & 0 & 0 & \cdots & 0 & 0 \\
0 & H & J & H & \cdots & 0 & 0 & 0 & 0 & \cdots & 0 & 0 \\
\vdots & \vdots & \ddots & \ddots & \ddots & 0 & 0 & 0 & 0 & \cdots & 0 & 0 \\
0 & 0 & 0 & H & J & H & 0 & 0 & 0 & \cdots & 0 & 0 \\
0 & 0 & 0 & 0 & H & K & L & 0 & 0 & \cdots & 0 & 0 \\
0 & 0 & 0 & 0 & 0 & L & M & N & 0 & \cdots & 0 & 0 \\
0 & 0 & 0 & 0 & 0 & 0 & N & P & N & \cdots & 0 & 0 \\
\vdots & \vdots & \vdots & \vdots & \vdots & \vdots & \vdots & \ddots & \ddots & \ddots & 0 & 0 \\
0 & 0 & 0 & 0 & 0 & 0 & 0 & 0 & N & P & N & 0 \\
0 & 0 & 0 & 0 & 0 & 0 & 0 & 0 & 0 & N & Q & 2N \\
0 & 0 & 0 & 0 & 0 & 0 & 0 & 0 & 0 & 0 & 2N & R
\end{bmatrix} \tag{38a}$$

$$[\bar{v}] = \begin{bmatrix} v_1 & v_2 & v_3 & v_4 & \cdots & v_{m-2} & v_{m-1} & v_m & v_{m+1} & v_{m+2} & v_{m+3} & \cdots & v_{n-2} & v_{n-1} & v_n & v_{n+1} \end{bmatrix}^T \tag{38b}$$

$$[\bar{i}] = \begin{bmatrix} 0 & i(x)\Delta x_{SR} & i(x)\Delta x_{SR} & \cdots & i(x)\Delta x_{SR} & i(x)\Delta x_{SR} & 0 & 0 & \cdots & 0 & 0 & 0 \end{bmatrix}^T \tag{38c}$$

$$A_2 = \frac{1}{Z_{NE}} + \frac{2}{R_{SR} + j\omega L_{SR}} \tag{38d}$$

$$C_2 = \frac{3}{R_{SR} + j\omega L_{SR}} + \frac{1}{Z_{CG,SR}} \tag{38e}$$

If the LHS, SR, and RHS transmission line regions exist, but the LHS transmission line region has only one per-unit-length section as shown in Fig. 19, the KCL matrix must be modified to (39).

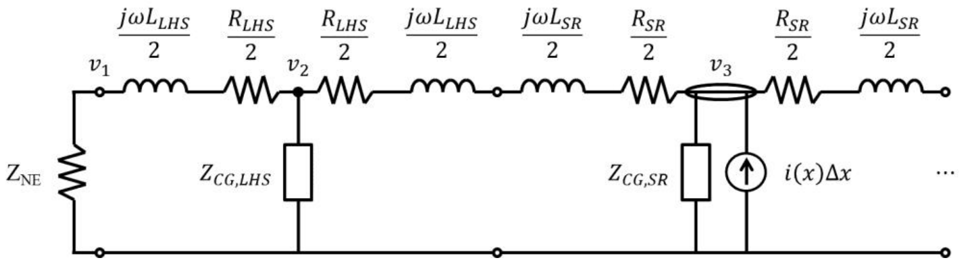

Fig. 19. Distributed current source close to the near-end.

$$[KVL\,Y] = \begin{bmatrix}
A & 2B & 0 & 0 & 0 & \cdots & 0 & 0 & 0 & 0 & \cdots & 0 & 0 \\
2B & E & F & 0 & 0 & \cdots & 0 & 0 & 0 & 0 & \cdots & 0 & 0 \\
0 & F & G & H & 0 & \cdots & 0 & 0 & 0 & 0 & \cdots & 0 & 0 \\
0 & 0 & H & J & H & \cdots & 0 & 0 & 0 & 0 & \cdots & 0 & 0 \\
\vdots & \vdots & \vdots & \ddots & \ddots & \ddots & 0 & 0 & 0 & 0 & \cdots & 0 & 0 \\
0 & 0 & 0 & 0 & H & J & H & 0 & 0 & 0 & \cdots & 0 & 0 \\
0 & 0 & 0 & 0 & 0 & H & K & L & 0 & 0 & \cdots & 0 & 0 \\
0 & 0 & 0 & 0 & 0 & 0 & L & M & N & 0 & \cdots & 0 & 0 \\
0 & 0 & 0 & 0 & 0 & 0 & 0 & N & P & N & \cdots & 0 & 0 \\
\vdots & \vdots & \vdots & \vdots & \vdots & \vdots & \vdots & \vdots & \ddots & \ddots & \ddots & 0 & 0 \\
0 & 0 & 0 & 0 & 0 & 0 & 0 & 0 & 0 & N & P & N & 0 \\
0 & 0 & 0 & 0 & 0 & 0 & 0 & 0 & 0 & 0 & N & Q & 2N \\
0 & 0 & 0 & 0 & 0 & 0 & 0 & 0 & 0 & 0 & 0 & 2N & R
\end{bmatrix} \tag{39a}$$

$$[\bar{v}] = \begin{bmatrix} v_1 & v_2 & v_3 & v_4 & v_5 & \cdots & v_{m-2} & v_{m-1} & v_m & v_{m+1} & v_{m+2} & v_{m+3} & \cdots & v_{n-2} & v_{n-1} & v_n & v_{n+1} \end{bmatrix}^T \tag{39b}$$

$$[\bar{i}] = \begin{bmatrix} 0 & 0 & i(x)\Delta x_{SR} & i(x)\Delta x_{SR} & \cdots & i(x)\Delta x_{SR} & i(x)\Delta x_{SR} & 0 & 0 & \cdots & 0 & 0 & 0 \end{bmatrix}^T \tag{39c}$$

If the LHS, SR, and RHS transmission line regions exist, but the SR transmission line region has only one per-unit-length section as shown in Fig. 20, the KCL matrix must be modified to (40).

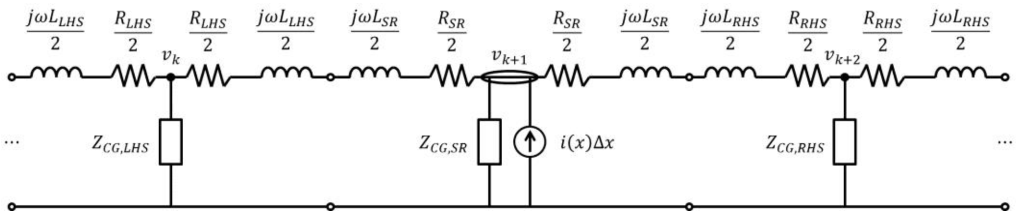

Fig. 20. Distributed current source single section.

$$[KVL\,Y] =$$

$$\begin{bmatrix}
A & 2B & 0 & 0 & \cdots & 0 & 0 & 0 & 0 & 0 & \cdots & 0 & 0 \\
2B & C & B & 0 & \cdots & 0 & 0 & 0 & 0 & 0 & \cdots & 0 & 0 \\
0 & B & D & B & \cdots & 0 & 0 & 0 & 0 & 0 & \cdots & 0 & 0 \\
\vdots & \vdots & \ddots & \ddots & \ddots & 0 & 0 & 0 & 0 & 0 & \cdots & 0 & 0 \\
0 & 0 & 0 & B & D & B & 0 & 0 & 0 & 0 & \cdots & 0 & 0 \\
0 & 0 & 0 & 0 & B & E & F & 0 & 0 & 0 & \cdots & 0 & 0 \\
0 & 0 & 0 & 0 & 0 & F & K_2 & L & 0 & 0 & \cdots & 0 & 0 \\
0 & 0 & 0 & 0 & 0 & 0 & L & M & N & 0 & \cdots & 0 & 0 \\
0 & 0 & 0 & 0 & 0 & 0 & 0 & N & P & N & \cdots & 0 & 0 \\
\vdots & \vdots & \vdots & \vdots & \vdots & \vdots & \vdots & \vdots & \ddots & \ddots & \ddots & 0 & 0 \\
0 & 0 & 0 & 0 & 0 & 0 & 0 & 0 & 0 & N & P & N & 0 \\
0 & 0 & 0 & 0 & 0 & 0 & 0 & 0 & 0 & 0 & N & Q & 2N \\
0 & 0 & 0 & 0 & 0 & 0 & 0 & 0 & 0 & 0 & 0 & 2N & R
\end{bmatrix} \tag{40a}$$

$$[\bar{v}] = [v_1 \;\; v_2 \;\; v_3 \;\; v_4 \;\; \cdots \;\; v_{k-2} \;\; v_{k-1} \;\; v_k \;\; v_{k+1} \;\; v_{k+2} \;\; v_{k+3} \;\; v_{k+4} \;\; \cdots \;\; v_{n-2} \;\; v_{n-1} \;\; v_n \;\; v_{n+1}]^T \tag{40b}$$

$$[\bar{i}] = [0 \;\; 0 \;\; 0 \;\; \cdots \;\; 0 \;\; 0 \;\; i(x)\Delta x_{SR} \;\; 0 \;\; 0 \;\; \cdots \;\; 0 \;\; 0 \;\; 0]^T \tag{40c}$$

$$K_2 = \frac{2}{R_{LHS} + j\omega L_{LHS} + R_{SR} + j\omega L_{SR}} + \frac{1}{Z_{CG,SR}} + \frac{2}{R_{SR} + j\omega L_{SR} + R_{RHS} + j\omega L_{RHS}} \tag{40d}$$

If the LHS, SR, and RHS transmission line regions exist, but the RHS transmission line region has only one per-unit-length section as shown in Fig. 21, the KCL matrix must be modified to (41).

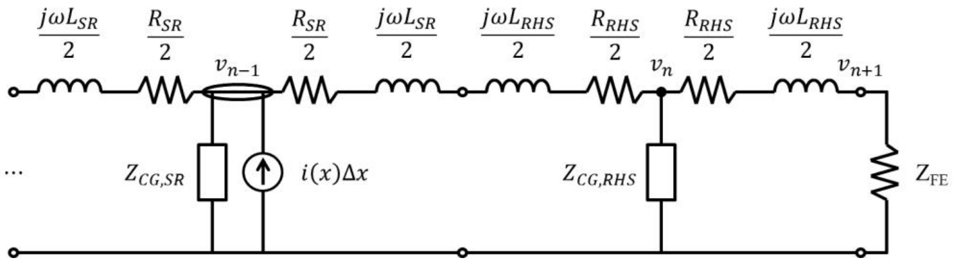

Fig. 21. Distributed current source close to the far-end.

$$[KVL\,Y] = \begin{bmatrix} A & 2B & 0 & 0 & \cdots & 0 & 0 & 0 & 0 & \cdots & 0 & 0 & 0 \\ 2B & C & B & 0 & \cdots & 0 & 0 & 0 & 0 & \cdots & 0 & 0 & 0 \\ 0 & B & D & B & \cdots & 0 & 0 & 0 & 0 & \cdots & 0 & 0 & 0 \\ \vdots & \vdots & \ddots & \ddots & \ddots & 0 & 0 & 0 & 0 & \cdots & 0 & 0 & 0 \\ 0 & 0 & 0 & B & D & B & 0 & 0 & 0 & \cdots & 0 & 0 & 0 \\ 0 & 0 & 0 & 0 & B & E & F & 0 & 0 & \cdots & 0 & 0 & 0 \\ 0 & 0 & 0 & 0 & 0 & F & G & H & 0 & \cdots & 0 & 0 & 0 \\ 0 & 0 & 0 & 0 & 0 & 0 & H & J & H & \cdots & 0 & 0 & 0 \\ \vdots & \vdots & \vdots & \vdots & \vdots & \vdots & \vdots & \ddots & \ddots & \ddots & 0 & 0 & 0 \\ 0 & 0 & 0 & 0 & 0 & 0 & 0 & 0 & H & J & H & 0 & 0 \\ 0 & 0 & 0 & 0 & 0 & 0 & 0 & 0 & 0 & H & K & L & 0 \\ 0 & 0 & 0 & 0 & 0 & 0 & 0 & 0 & 0 & 0 & L & M_2 & 2N \\ 0 & 0 & 0 & 0 & 0 & 0 & 0 & 0 & 0 & 0 & 0 & 2N & R \end{bmatrix} \tag{41a}$$

$$[\bar{v}] = \begin{bmatrix} v_1 & v_2 & v_3 & v_4 & \cdots & v_{k-2} & v_{k-1} & v_k & v_{k+1} & v_{k+2} & v_{k+3} & \cdots & v_{n-3} & v_{n-2} & v_{n-1} & v_n & v_{n+1} \end{bmatrix}^T \tag{41b}$$

$$[\bar{i}] = \begin{bmatrix} 0 & 0 & 0 & \cdots & 0 & 0 & i(x)\Delta x_{SR} & i(x)\Delta x_{SR} & \cdots & i(x)\Delta x_{SR} & i(x)\Delta x_{SR} & 0 & 0 \end{bmatrix}^T \tag{41c}$$

$$M_2 = \frac{2}{R_{SR} + j\omega L_{SR} + R_{RHS} + j\omega L_{RHS}} + \frac{1}{Z_{CG,RHS}} + \frac{2}{R_{RHS} + j\omega L_{RHS}} \tag{41d}$$

If a left hand side transmission line and a source region transmission line only exist, there are a total of eight unique equations that form the KCL matrix. The KCL matrix for this case is similar to the KCL matrix where the LHS, SR, and RHS transmission line regions exist. The main difference resides in the KCL equation with the far-end load and the source region circuits. The circuit at the victim far-end is shown in Fig. 22, and the associated KCL matrix is shown in (42).

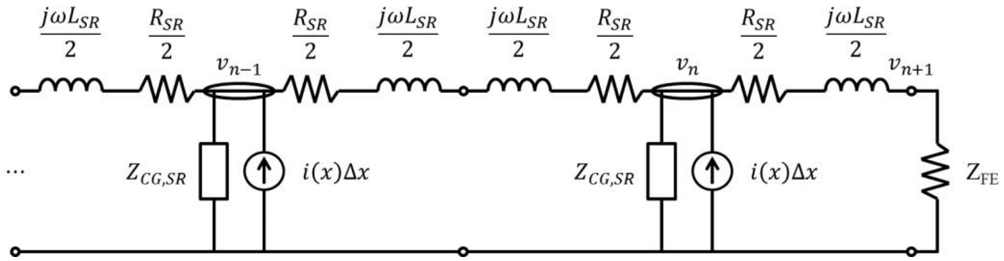

Fig. 22. Distributed current sources at the far-end.

$$[KVL\,Y] = \begin{bmatrix} A & 2B & 0 & 0 & \cdots & 0 & 0 & 0 & 0 & \cdots & 0 & 0 \\ 2B & C & B & 0 & \cdots & 0 & 0 & 0 & 0 & \cdots & 0 & 0 \\ 0 & B & D & B & \cdots & 0 & 0 & 0 & 0 & \cdots & 0 & 0 \\ \vdots & \vdots & \ddots & \ddots & \ddots & 0 & 0 & 0 & 0 & \cdots & 0 & 0 \\ 0 & 0 & 0 & B & D & B & 0 & 0 & 0 & \cdots & 0 & 0 \\ 0 & 0 & 0 & 0 & B & E & F & 0 & 0 & \cdots & 0 & 0 \\ 0 & 0 & 0 & 0 & 0 & F & G & H & 0 & \cdots & 0 & 0 \\ 0 & 0 & 0 & 0 & 0 & 0 & H & J & H & \cdots & 0 & 0 \\ \vdots & \vdots & \vdots & \vdots & \vdots & \vdots & \vdots & \ddots & \ddots & \ddots & 0 & 0 \\ 0 & 0 & 0 & 0 & 0 & 0 & 0 & 0 & H & J & H & 0 \\ 0 & 0 & 0 & 0 & 0 & 0 & 0 & 0 & 0 & H & Q_2 & 2H \\ 0 & 0 & 0 & 0 & 0 & 0 & 0 & 0 & 0 & 0 & 2H & R_2 \end{bmatrix} \tag{42a}$$

$$[\bar{v}] = \begin{bmatrix} v_1 & v_2 & v_3 & v_4 & \cdots & v_{k-2} & v_{k-1} & v_k & v_{k+1} & v_{k+2} & v_{k+3} & \cdots & v_{n-2} & v_{n-1} & v_n & v_{n+1} \end{bmatrix}^T \tag{42b}$$

$$[\bar{i}] = \begin{bmatrix} 0 & 0 & 0 & \cdots & 0 & 0 & i(x)\Delta x_{SR} & i(x)\Delta x_{SR} & \cdots & i(x)\Delta x_{SR} & i(x)\Delta x_{SR} & 0 \end{bmatrix}^T \tag{42c}$$

$$Q_2 = \frac{3}{R_{SR} + j\omega L_{SR}} + \frac{1}{Z_{CG,SR}} \tag{42d}$$

$$R_2 = \frac{2}{R_{SR} + j\omega L_{SR}} + \frac{1}{Z_{FE}} \tag{42e}$$

IV. MATRIX EQUATIONS FOR A LUMPED VOLTAGE SOURCE

The matrix equations for a victim circuit containing a single, lumped voltage source are similar to the case with distributed voltage sources. The main difference is with the KVL equations that interface with the source or source region. If a left hand side transmission line and right hand side transmission line exist, there are a total of five unique equations that form the KVL matrix. The KVL equations at the victim near-end are given by (8)-(9). These equations were originally derived for the distributed voltage sources case, however, these equations also apply to the lumped voltage source case. The circuits that transition between the LHS, the lumped voltage source, and the RHS are shown below in Fig. 23.

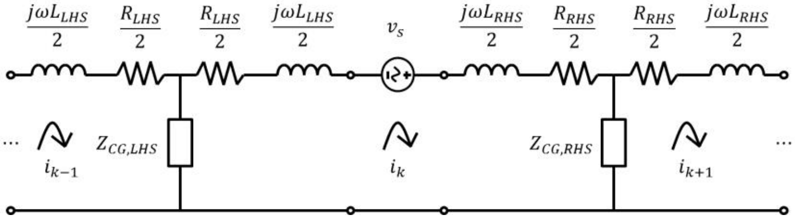

Fig. 23. Lumped voltage source transition with mesh currents

The KVL equation that involves the lumped voltage source is given by (43). There are k-1 per-unit-length transmission line sections in the left hand side transmission line region. For the lumped voltage source case, m = k and thus there is said to be zero per-unit-length transmission line sections in the source region transmission line region. Additional parameter definitions are given in (10) and (15).

$$\begin{aligned}&\left(-Z_{CG,LHS}\right)i_{k-1}+\left(\frac{R_{LHS}+j\omega L_{LHS}}{2}+Z_{CG,LHS}+\frac{R_{RHS}+j\omega L_{RHS}}{2}+Z_{CG,RHS}\right)i_k\\&\quad+\left(-Z_{CG,RHS}\right)i_{k+1}=v_s\end{aligned}\tag{43}$$

The KVL equations at the victim far-end are given by (16)-(17). These equations were originally derived for the distributed voltage sources case, however, these equations also apply to the lumped voltage source case. The KVL matrix can be written as shown in (44). Additional parameter definitions are given in (19).

$$[KVL\ Z] =$$

$$\begin{bmatrix} A_1 & -Z_{CG,LHS} & 0 & \cdots & 0 & 0 & 0 & \cdots & 0 \\ -Z_{CG,LHS} & B & -Z_{CG,LHS} & \cdots & 0 & 0 & 0 & \cdots & 0 \\ \vdots & \ddots & \ddots & \ddots & 0 & 0 & 0 & \cdots & 0 \\ 0 & 0 & -Z_{CG,LHS} & B & -Z_{CG,LHS} & 0 & 0 & \cdots & 0 \\ 0 & 0 & 0 & -Z_{CG,LHS} & C_2 & -Z_{CG,RHS} & 0 & \cdots & 0 \\ 0 & 0 & 0 & 0 & -Z_{CG,RHS} & F & -Z_{CG,RHS} & \cdots & 0 \\ \vdots & \vdots & \vdots & \vdots & \vdots & \ddots & \ddots & \ddots & 0 \\ 0 & 0 & 0 & 0 & 0 & 0 & -Z_{CG,RHS} & F & -Z_{CG,RHS} \\ 0 & 0 & 0 & 0 & 0 & 0 & 0 & -Z_{CG,RHS} & G_1 \end{bmatrix} \quad (44a)$$

$$[\bar{i}] = \begin{bmatrix} i_1 & i_2 & i_3 & \cdots & i_{k-2} & i_{k-1} & i_k & i_{k+1} & i_{k+2} & \cdots & i_{n-2} & i_{n-1} & i_n \end{bmatrix}^T \quad (44b)$$

$$[\bar{v}] = \begin{bmatrix} 0 & 0 & \cdots & 0 & v_s & 0 & \cdots & 0 & 0 \end{bmatrix}^T \quad (44c)$$

$$C_2 = \frac{R_{LHS} + j\omega L_{LHS}}{2} + Z_{CG,LHS} + \frac{R_{RHS} + j\omega L_{RHS}}{2} + Z_{CG,RHS} \quad (44d)$$

If the lumped voltage source is placed at the near-end such that there is no left hand side transmission line region as shown in Fig. 24, the KVL matrix must be modified to (45).

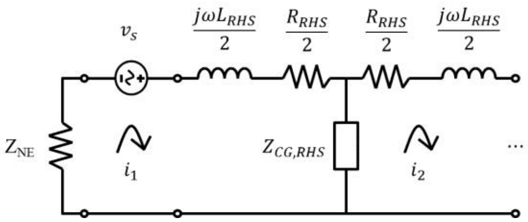

Fig. 24. Lumped voltage source at the near-end.

$$[KVL\ Z] = \begin{bmatrix} A_3 & -Z_{CG,RHS} & 0 & \cdots & 0 \\ -Z_{CG,RHS} & F & -Z_{CG,RHS} & \cdots & 0 \\ \vdots & \ddots & \ddots & \ddots & 0 \\ 0 & 0 & -Z_{CG,RHS} & F & -Z_{CG,RHS} \\ 0 & 0 & 0 & -Z_{CG,RHS} & G_1 \end{bmatrix} \tag{45a}$$

$$[\bar{i}] = \begin{bmatrix} i_1 & i_2 & i_3 & \cdots & i_{n-2} & i_{n-1} & i_n \end{bmatrix}^T \tag{45b}$$

$$[\bar{v}] = \begin{bmatrix} v_s & 0 & \cdots & 0 & 0 \end{bmatrix}^T \tag{45c}$$

$$A_3 = Z_{NE} + \frac{R_{RHS} + j\omega L_{RHS}}{2} + Z_{CG,RHS} \tag{45d}$$

If the lumped voltage source is placed at the near-end such that there is only one per-unit-length section in the left hand side transmission line region as shown in Fig. 25, the KVL matrix must be modified to (46).

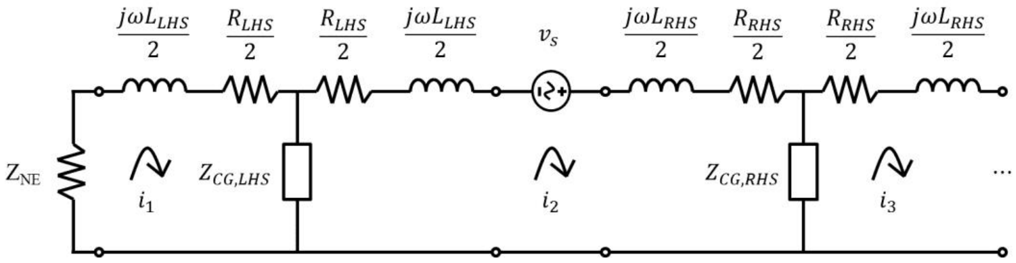

Fig. 25. Lumped voltage source close to the near-end.

$$[KVL\ Z] = \begin{bmatrix} A_1 & -Z_{CG,LHS} & 0 & 0 & \cdots & 0 \\ -Z_{CG,LHS} & C_2 & -Z_{CG,LHS} & 0 & \cdots & 0 \\ 0 & -Z_{CG,RHS} & F & -Z_{CG,RHS} & \cdots & 0 \\ \vdots & \vdots & \ddots & \ddots & \ddots & 0 \\ 0 & 0 & 0 & -Z_{CG,RHS} & F & -Z_{CG,RHS} \\ 0 & 0 & 0 & 0 & -Z_{CG,RHS} & G_1 \end{bmatrix} \tag{46a}$$

$$[\bar{i}] = \begin{bmatrix} i_1 & i_2 & i_3 & i_4 & \cdots & i_{n-2} & i_{n-1} & i_n \end{bmatrix}^T \tag{46b}$$

$$[\bar{v}] = \begin{bmatrix} 0 & v_s & 0 & \cdots & 0 & 0 \end{bmatrix}^T \tag{46c}$$

If the lumped voltage source is placed at the far-end such that there is only one per-unit-length section in the right hand side transmission line region as shown in Fig. 26, the KVL matrix must be modified to (47).

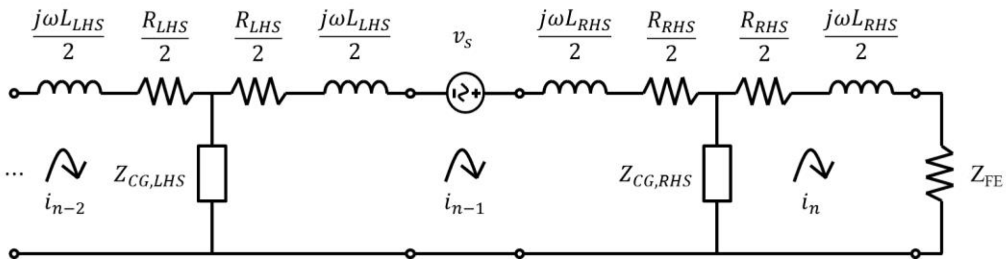

Fig. 26. Lumped voltage source close to the far-end.

$$[KVL\ Z] =$$

$$\begin{bmatrix} A_1 & -Z_{CG,LHS} & 0 & \cdots & 0 & 0 \\ -Z_{CG,LHS} & B & -Z_{CG,LHS} & \cdots & 0 & 0 \\ \vdots & \ddots & \ddots & \ddots & 0 & 0 \\ 0 & 0 & -Z_{CG,LHS} & B & -Z_{CG,LHS} & 0 \\ 0 & 0 & 0 & -Z_{CG,LHS} & C_2 & -Z_{CG,RHS} \\ 0 & 0 & 0 & 0 & -Z_{CG,RHS} & G_1 \end{bmatrix} \tag{47a}$$

$$[\bar{i}] = \begin{bmatrix} i_1 & i_2 & i_3 & \cdots & i_{n-3} & i_{n-2} & i_{n-1} & i_n \end{bmatrix}^T \tag{47b}$$

$$[\bar{v}] = \begin{bmatrix} 0 & 0 & \cdots & 0 & v_s & 0 \end{bmatrix}^T \tag{47c}$$

If the lumped voltage source is placed at the far-end such that there is no right hand side transmission line region as shown below in Fig. 27, the KVL matrix must be modified to (48).

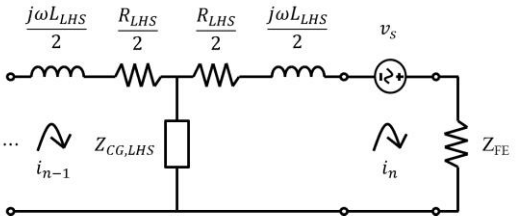

Fig. 27. Lumped voltage source at the far-end.

$$[KVL\ Z] =$$

$$\begin{bmatrix} A_1 & -Z_{CG,LHS} & 0 & \cdots & 0 \\ -Z_{CG,LHS} & B & -Z_{CG,LHS} & \cdots & 0 \\ \vdots & \ddots & \ddots & \ddots & 0 \\ 0 & 0 & -Z_{CG,LHS} & B & -Z_{CG,LHS} \\ 0 & 0 & 0 & -Z_{CG,LHS} & G_3 \end{bmatrix} \tag{48a}$$

$$[\bar{i}] = \begin{bmatrix} i_1 & i_2 & i_3 & \cdots & i_{n-2} & i_{n-1} & i_n \end{bmatrix}^T \tag{48b}$$

$$[\bar{v}] = \begin{bmatrix} 0 & 0 & \cdots & 0 & v_s \end{bmatrix}^T \tag{48c}$$

$$G_3 = Z_{FE} + \frac{R_{LHS} + j\omega L_{LHS}}{2} + Z_{CG,LHS} \tag{48d}$$

V. MATRIX EQUATIONS FOR A LUMPED CURRENT SOURCE

The matrix equations for a victim circuit containing a single, lumped current source are similar to the case with distributed current sources. Instead of implementing KCL equations for the lumped current source case, it is possible to implement KVL equations. If a left hand side transmission line and right hand side transmission line exist, there are a total of six unique equations that form the KVL matrix. The KVL equations at the victim near-end are given by (8)-(9). These equations were originally derived for the distributed voltage sources case, however, these equations also apply to the lumped current source case. The circuits that transition between the LHS, the lumped current source, and the RHS are shown below in Fig. 28.

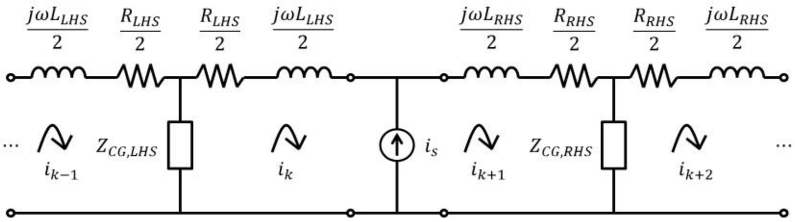

Fig. 28. Lumped current source transition with mesh currents.

The KVL equations that involve the lumped current source are given by (49) and (50). There are k-1 per-unit-length transmission line sections in the left hand side transmission line region. Additional parameter definitions are given in (10) and (15).

$$\begin{aligned}&\left(-Z_{CG,LHS}\right)i_{k-1}+\left(\frac{R_{LHS}+j\omega L_{LHS}}{2}+Z_{CG,LHS}\right)i_k+\left(\frac{R_{RHS}+j\omega L_{RHS}}{2}+Z_{CG,RHS}\right)i_{k+1}\\&\quad+\left(-Z_{CG,RHS}\right)i_{k+2}=0\end{aligned}\tag{49}$$

$$\left(-1\right)i_k+i_{k+1}=i_s\tag{50}$$

The KVL equations at the victim far-end are given by (16)-(17). These equations were originally derived for the distributed voltage sources case, however, these equations also apply to the lumped current source case. The KVL matrix can be written as shown in (51). Additional parameter definitions are given in (19).

$$\left[KVL\ Z\right]=$$
$$\begin{bmatrix}A_1 & -Z_{CG,LHS} & 0 & \cdots & 0 & 0 & 0 & 0 & \cdots & 0\\ -Z_{CG,LHS} & B & -Z_{CG,LHS} & \cdots & 0 & 0 & 0 & 0 & \cdots & 0\\ \vdots & \ddots & \ddots & \ddots & 0 & 0 & 0 & 0 & \cdots & 0\\ 0 & 0 & -Z_{CG,LHS} & B & -Z_{CG,LHS} & 0 & 0 & 0 & \cdots & 0\\ 0 & 0 & 0 & -Z_{CG,LHS} & C_3 & E_2 & -Z_{CG,RHS} & 0 & \cdots & 0\\ 0 & 0 & 0 & 0 & -1 & 1 & 0 & 0 & \cdots & 0\\ 0 & 0 & 0 & 0 & 0 & -Z_{CG,RHS} & F & -Z_{CG,RHS} & \cdots & 0\\ \vdots & \vdots & \vdots & \vdots & \vdots & \vdots & \ddots & \ddots & \ddots & 0\\ 0 & 0 & 0 & 0 & 0 & 0 & 0 & -Z_{CG,RHS} & F & -Z_{CG,RHS}\\ 0 & 0 & 0 & 0 & 0 & 0 & 0 & 0 & -Z_{CG,RHS} & G_1\end{bmatrix}\tag{51a}$$

$$\left[\bar{i}\right]=\begin{bmatrix}i_1 & i_2 & i_3 & \cdots & i_{k-2} & i_{k-1} & i_k & i_{k+1} & i_{k+2} & i_{k+3} & \cdots & i_{n-2} & i_{n-1} & i_n\end{bmatrix}^T\tag{51b}$$

$$\left[\bar{v}\right]=\begin{bmatrix}0 & 0 & \cdots & 0 & 0 & i_s & 0 & \cdots & 0 & 0\end{bmatrix}^T\tag{51c}$$

$$C_3 = \frac{R_{LHS} + j\omega L_{LHS}}{2} + Z_{CG,LHS} \tag{51d}$$

$$E_2 = \frac{R_{RHS} + j\omega L_{RHS}}{2} + Z_{CG,RHS} \tag{51e}$$

If the lumped current source is placed at the near-end such that there is no left hand side transmission line region as shown in Fig. 29, the KVL matrix must be modified to (52).

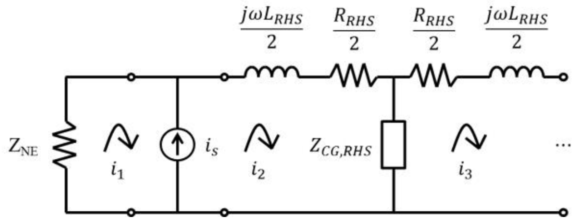

Fig. 29. Lumped current source at the near-end.

$$[KVL\ Z] =$$

$$\begin{bmatrix} Z_{NE} & E_2 & -Z_{CG,RHS} & 0 & \cdots & 0 \\ -1 & 1 & 0 & 0 & \cdots & 0 \\ 0 & -Z_{CG,RHS} & F & -Z_{CG,RHS} & \cdots & 0 \\ \vdots & \vdots & \ddots & \ddots & \ddots & 0 \\ 0 & 0 & 0 & -Z_{CG,RHS} & F & -Z_{CG,RHS} \\ 0 & 0 & 0 & 0 & -Z_{CG,RHS} & G_1 \end{bmatrix} \tag{52a}$$

$$[\bar{i}] = \begin{bmatrix} i_1 & i_2 & i_3 & i_4 & \cdots & i_{n-2} & i_{n-1} & i_n \end{bmatrix}^T \tag{52b}$$

$$[\bar{v}] = \begin{bmatrix} 0 & i_s & 0 & \cdots & 0 & 0 \end{bmatrix}^T \tag{52c}$$

If the lumped current source is placed at the near-end such that there is only one per-unit-length section in the left hand side transmission line region as shown in Fig. 30, the KVL matrix must be modified to (53).

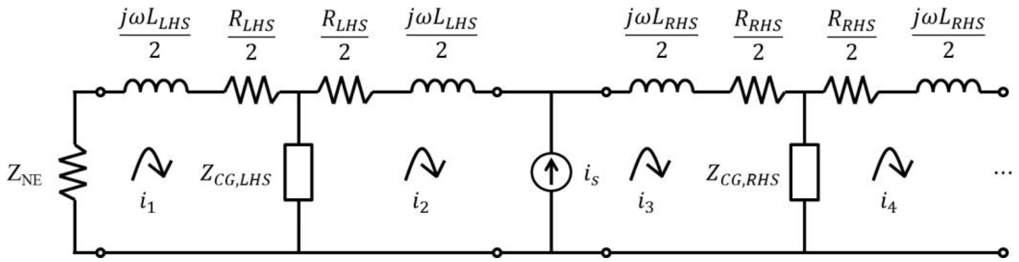

Fig. 30. Lumped current source close to the near-end.

$$[KVL\ Z] =$$

$$\begin{bmatrix} A_1 & -Z_{CG,LHS} & 0 & 0 & 0 & \cdots & 0 \\ -Z_{CG,LHS} & C_3 & E_2 & -Z_{CG,RHS} & 0 & \cdots & 0 \\ 0 & -1 & 1 & 0 & 0 & \cdots & 0 \\ 0 & 0 & -Z_{CG,RHS} & F & -Z_{CG,RHS} & \cdots & 0 \\ \vdots & \vdots & \vdots & \ddots & \ddots & \ddots & 0 \\ 0 & 0 & 0 & 0 & -Z_{CG,RHS} & F & -Z_{CG,RHS} \\ 0 & 0 & 0 & 0 & 0 & -Z_{CG,RHS} & G_1 \end{bmatrix} \tag{53a}$$

$$[\bar{i}] = \begin{bmatrix} i_1 & i_2 & i_3 & i_4 & i_5 & \cdots & i_{n-2} & i_{n-1} & i_n \end{bmatrix}^T \tag{53b}$$

$$[\bar{v}] = \begin{bmatrix} 0 & 0 & i_s & 0 & \cdots & 0 & 0 \end{bmatrix}^T \tag{53c}$$

If the lumped current source is placed at the far-end such that there is only one per-unit-length section in the right hand side transmission line region as shown in Fig. 31, the KVL matrix must be modified to (54).

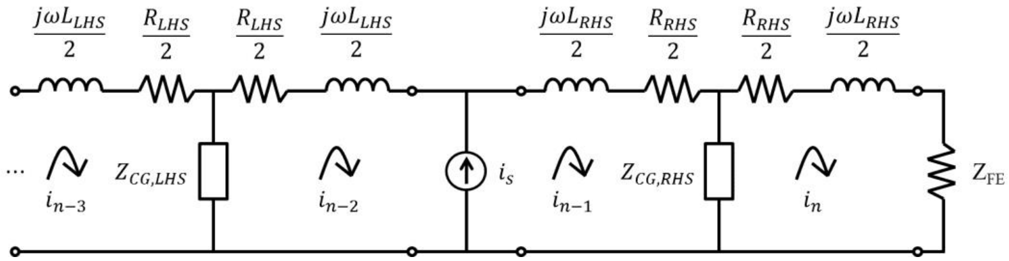

Fig. 31. Lumped current source close to the far-end.

$$[KVL\ Z] = \begin{bmatrix} A_1 & -Z_{CG,LHS} & 0 & \cdots & 0 & 0 & 0 \\ -Z_{CG,LHS} & B & -Z_{CG,LHS} & \cdots & 0 & 0 & 0 \\ \vdots & \ddots & \ddots & \ddots & 0 & 0 & 0 \\ 0 & 0 & -Z_{CG,LHS} & B & -Z_{CG,LHS} & 0 & 0 \\ 0 & 0 & 0 & -Z_{CG,LHS} & C_3 & E_2 & -Z_{CG,RHS} \\ 0 & 0 & 0 & 0 & -1 & 1 & 0 \\ 0 & 0 & 0 & 0 & 0 & -Z_{CG,RHS} & G_1 \end{bmatrix} \tag{54a}$$

$$[\bar{i}] = \begin{bmatrix} i_1 & i_2 & i_3 & \cdots & i_{n-4} & i_{n-3} & i_{n-2} & i_{n-1} & i_n \end{bmatrix}^T \tag{54b}$$

$$[\bar{v}] = \begin{bmatrix} 0 & 0 & \cdots & 0 & 0 & i_s & 0 \end{bmatrix}^T \tag{54c}$$

If the lumped current source is placed at the far-end such that there is no right hand side transmission line region as shown in Fig. 32, the KVL matrix must be modified to (55).

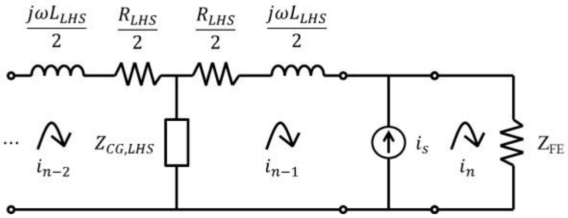

Fig. 32. Lumped current source at the far-end.

$$[KVL\ Z] = \begin{bmatrix} A_1 & -Z_{CG,LHS} & 0 & \cdots & 0 & 0 \\ -Z_{CG,LHS} & B & -Z_{CG,LHS} & \cdots & 0 & 0 \\ \vdots & \ddots & \ddots & \ddots & 0 & 0 \\ 0 & 0 & -Z_{CG,LHS} & B & -Z_{CG,LHS} & 0 \\ 0 & 0 & 0 & -Z_{CG,LHS} & C_3 & Z_{FE} \\ 0 & 0 & 0 & 0 & -1 & 1 \end{bmatrix} \tag{55a}$$

$$[\bar{i}] = \begin{bmatrix} i_1 & i_2 & i_3 & \cdots & i_{n-3} & i_{n-2} & i_{n-1} & i_n \end{bmatrix}^T \tag{55b}$$

$$[\bar{v}] = \begin{bmatrix} 0 & 0 & \cdots & 0 & 0 & i_s \end{bmatrix}^T \tag{55c}$$

It can be noted that for an electrically small coupling region (coupling region length < $\lambda/10$), the noise induced in the victim circuit can be represented by a lumped element voltage and a lumped element current source rather than distributed sources. In the corresponding finite difference simulations the total lumped source voltage and the total lumped source current are found by multiplying the per-unit-length values by the coupling region length. The magnitude of these noise sources are directly influenced by the current and voltage present in the culprit circuit as can be seen in the lumped source formulation. Because of the electrically small coupling region constraint, even if there are standing waves in the culprit circuit, there should be minimal variation in the voltage and current in the coupling region. The finite difference simulation samples the voltage and current values in the middle of the coupling region for the culprit circuit (denoted as $-x_0$) to match the analytical solution.

APPENDIX B

FINITE DIFFERNCE CODES

The finite difference equations presented in Appendix A were implemented in Matlab to validate the analytical expressions for the near-end and far-end coupling in the victim circuit. The weak coupling assumption was explicitly programmed into the finite difference codes, where the voltages and currents in the culprit circuit were calculated using traditional single-ended transmission line theory. The voltages and currents in the culprit coupling region were applied as applicable to voltage and current source terms in the victim circuit.

This appendix contains the Matlab programs used to validate the analytical voltage expressions for the victim circuit. The names of the six programs contained in this appendix are: Lossy_TL_Lumped_V.m, Lossy_TL_Lumped_I.m, Lossy_TL_Uniform_Distributed_V2.m, Lossy_TL_Uniform_Distributed_I1.m, Lossy_TL_Non_Uniform_Distributed_V2.m, Lossy_TL_Non_Uniform_Distributed_I2.m. The first two files validate the lumped voltage and lumped current source analytical formulations, respectively. The third and fourth files validate the uniform distributed voltage sources and current sources analytical formulations, respectively. The fifth and sixth files validate the non-uniform distributed voltage sources and current sources analytical formulations, respectively. The analytical voltage expressions along the victim transmission line were shown to be validated upon the analytical voltage curves matching the finite difference simulation curves.

All six of the Matlab programs contained a similar code layout. An outline of the code structure to simulate the presence of distributed noise sources in the victim is given below.

- Victim Parameters
  - Define per-unit-length parameters
  - Define frequency range of simulation
  - Define common transmission line parameters (γ, α, β, V_p, Z_0)
  - Define geometry parameters (line length, relative noise source position, and length)
  - Define loads and reflection coefficients
- Culprit Parameters

  - Define per-unit-length parameters
  - Define common transmission line parameters (γ, Z_0, V_s)
  - Define geometry parameters (line length, relative noise source position, and length)
  - Define loads and reflection coefficients
- Per-unit-length Section Parameters
  - Define target length for all per-unit-length sections
  - Calculate actual per-unit-length section length for the LHS
  - Calculate RLGC parameters for each per-unit-length section in the LHS
  - Calculate actual per-unit-length section length for the SR
  - Calculate RLGC parameters for each per-unit-length section in the SR
  - Calculate actual per-unit-length section length for the RHS
  - Calculate RLGC parameters for each per-unit-length section in the RHS
- Position Vectors
  - Define position vectors in the victim circuit
  - Define position vectors in the culprit circuit
- Calculate and fill the distributed voltage or distributed current source array
- Fill the KVL or KCL matrix
- Solve the KVL or KCL matrix
- Calculate the unknown node voltages or mesh currents
- Plot the simulation data and compare with the analytical expressions

Matlab File “Lossy_TL_Lumped_V.m”

```
clear all;
close all;
clc;

%This simulation calculates the voltage and current on a transmission line
%where a lumped voltage source is placed anywhere along the line. The
%transmission line can be lossless or lossy.

%Simulation cases for lossy - distortionless line (R/L = G/C)
%Define PUL Parameters - Consider frequency dependence for improvements
C_pul = 100e-12; %F/m
L_pul = 250e-9; %H/m
R_pul = 100;%4; %Ohm/m
G_pul = 2e-8;%2e-10; %S/m
%Define Propagation Parameters
f = (1e6:10e6:1e9)'; %Frequency range simulation (Hz)
w = 2*pi*f;
gamma = sqrt((R_pul+j*w*L_pul).*(G_pul+j*w*C_pul));
alpha = real(gamma); %Loss (Np/m) [interesting when = 1]
B = imag(gamma); %Beta
Vp = w./B; %Phase velocity (m/s)
Z0 = sqrt((R_pul+j*w*L_pul)./(G_pul+j*w*C_pul)); %TL characteristic impedance (Ohm)
lambda_min = min(Vp./f); %Smallest wavelength (m)
j = sqrt(-1);
%Geometry Parameters
L = 1; %Line Length (m)
x0 = 0.4; %Source Location (make this a positive number) (m)
l_length = L-x0; %TL length left of source (m)
r_length = x0; %TL length right of source (m)
%Load Parameters
ZFE = 75+(1./(j*w*(5e-12))).*ones(length(f),1); %Far-end Load Definition (Ohm)
ZNE = 45+j*w*(10e-9).*ones(length(f),1); %Near-end Load Definition (Ohm)
G_NE = (ZNE-Z0)./(ZNE+Z0); %Reflection coefficient at the near-end
G_FE = (ZFE-Z0)./(ZFE+Z0); %Reflection coefficient at the far-end

%Define Source Voltage
Vn = 1; %Noise Source Voltage

%Set up TL KVL Circuit Simulation
%For a good simulation, each PUL section must be no larger than lambda/20
%in length.
pul_length = lambda_min/40; %Target PUL section length
%Must have an integer number of TL sections, so the actual pul_length
%sections for the left and right hand sides of the TL problem may not be at
%the same spacing

%Determine LHS circuit properties
l_pul_secs = ceil(l_length/pul_length); %Number of pul sections LHS represents
if l_length == 0
   l_pul_length = 0;
else %Finite section length
   l_pul_length = l_length/l_pul_secs; %LHS pul section length
end;
C_LHS = C_pul*l_pul_length;
```

```
L_LHS = L_pul*l_pul_length;
R_LHS = R_pul*l_pul_length;
G_LHS = G_pul*l_pul_length;

%Determine RHS circuit properties
r_pul_secs = ceil(r_length/pul_length); %Number of pul sections LHS represents
if r_length == 0
    r_pul_length = 0;
else %Finite section length
    r_pul_length = r_length/r_pul_secs; %RHS pul section length
end;
C_RHS = C_pul*r_pul_length;
L_RHS = L_pul*r_pul_length;
R_RHS = R_pul*r_pul_length;
G_RHS = G_pul*r_pul_length;

%Determine Source Loop
s_loop = l_pul_secs+1; %Source loop number
tot_loops = l_pul_secs+r_pul_secs+1; %Total number of KVL loops to solve
Z_mat = zeros(tot_loops,tot_loops); %Initiailize impedance matrix

%Setup KVL Matrix to solve
%Create voltage matrix
V_mat = zeros(tot_loops,1); %Initialize voltage matrix to zeros
V_mat(s_loop) = Vn; %Insert source voltage
%Create current matrix
I_mat = zeros(length(f),tot_loops); %Initialize current matrix to zeros

for i = 1:length(f)
    %Fill Impedance Matrix for each frequency
    for k = 1:tot_loops
        switch k
            case {1}
                %ZNE loop
                if l_length ~= 0
                    Z_mat(k,k) = ZNE(i)+(R_LHS+j*w(i)*L_LHS)/2+...
                        1/(j*w(i)*C_LHS+G_LHS);
                    Z_mat(k,k+1) = -1/(j*w(i)*C_LHS+G_LHS);
                else %Source at near-end
                    Z_mat(k,k) = ZNE(i)+(R_RHS+j*w(i)*L_RHS)/2+...
                        1/(j*w(i)*C_RHS+G_RHS);
                    Z_mat(k,k+1) = -1/(j*w(i)*C_RHS+G_RHS);
                end;
            case {tot_loops}
                %ZFE loop
                if r_length ~= 0
                    Z_mat(k,k) = ZFE(i)+(R_RHS+j*w(i)*L_RHS)/2+...
                        1/(j*w(i)*C_RHS+G_RHS);
                    Z_mat(k,k-1) = -1/(j*w(i)*C_RHS+G_RHS);
                else %Source at far-end
                    Z_mat(k,k) = ZFE(i)+(R_LHS+j*w(i)*L_LHS)/2+...
                        1/(j*w(i)*C_LHS+G_LHS);
                    Z_mat(k,k-1) = -1/(j*w(i)*C_LHS+G_LHS);
                end;
            case {s_loop}
                %Source loop
```

```
            Z_mat(k,k-1) = -1/(j*w(i)*C_LHS+G_LHS);
            Z_mat(k,k) = 1/(j*w(i)*C_LHS+G_LHS)+(R_LHS+j*w(i)*L_LHS)/2+...
               1/(j*w(i)*C_RHS+G_RHS)+(R_RHS+j*w(i)*L_RHS)/2;
            Z_mat(k,k+1) = -1/(j*w(i)*C_RHS+G_RHS);
         otherwise
            %Internal loops
            if k < s_loop
               Ctemp = C_LHS;
               Ltemp = L_LHS;
               Rtemp = R_LHS;
               Gtemp = G_LHS;
            else %k > s_loop
               Ctemp = C_RHS;
               Ltemp = L_RHS;
               Rtemp = R_RHS;
               Gtemp = G_RHS;
            end;
            Z_mat(k,k-1) = -1/(j*w(i)*Ctemp+Gtemp);
            Z_mat(k,k) = 2/(j*w(i)*Ctemp+Gtemp)+Rtemp+j*w(i)*Ltemp;
            Z_mat(k,k+1) = -1/(j*w(i)*Ctemp+Gtemp);
      end;
   end;
   %Solve for the currents
   I_mat(i,:) =( Z_mat^(-1))*V_mat;
   clear Ctemp Ltemp Rtemp Gtemp;
end;
%Create position vectors
if l_pul_length ~= 0
   x_KVL_LHS = -L+(0:l_pul_length:(l_pul_length*l_pul_secs));
else %Source at near-end
   x_KVL_LHS = -L;
end;
if r_pul_length ~= 0
   x_KVL_RHS = -r_length+(0:r_pul_length:(r_pul_length*r_pul_secs));
else %Source at far-end
   x_KVL_RHS = 0;
end;
if r_pul_length ~= 0
   x_KVL_I = horzcat(x_KVL_LHS,x_KVL_RHS(2:length(x_KVL_RHS)));
else %Source at far-end
   x_KVL_I = x_KVL_LHS;
end;
x_KVL_V = horzcat(x_KVL_LHS,x_KVL_RHS);
% clear x_KVL_LHS x_KVL_RHS;

%Find voltages
V_node_mat = zeros(length(f),tot_loops+1); %Initialize voltage matrix to zeros
%Solve voltages at each node
for k = 1:tot_loops+1
   switch k
      case {1}
         %ZNE node
         V_node_mat(:,k) = -ZNE.*I_mat(:,k);
      case {s_loop+1}
         %Node to the right of the source
         V_node_mat(:,k) = V_node_mat(:,k-1)+Vn;
```

```
    case {tot_loops+1}
      %ZFE node
      V_node_mat(:,k) = ZFE.*I_mat(:,k-1);
    otherwise
      %Internal nodes
      if k <= s_loop+1
        Ctemp = C_LHS;
        Ltemp = L_LHS;
        Rtemp = R_LHS;
        Gtemp = G_LHS;
        V_node_mat(:,k) = (1./(j*w*Ctemp+Gtemp)).*I_mat(:,k-1)-...
          (1./(j*w*Ctemp+Gtemp)+(Rtemp+j*w*Ltemp)/2).*I_mat(:,k);
      else %k > s_loop
        Ctemp = C_RHS;
        Ltemp = L_RHS;
        Rtemp = R_RHS;
        Gtemp = G_RHS;
        %Since there is an extra voltage node in the source loop, there
        %is another factor of -1 running around when calculating the
        %voltages in the RHS of the circuit
        V_node_mat(:,k) = (1./(j*w*Ctemp+Gtemp)).*I_mat(:,k-2)-...
          (1./(j*w*Ctemp+Gtemp)+(Rtemp+j*w*Ltemp)/2).*I_mat(:,k-1);
      end;
  end;
end;
clear Ctemp Ltemp Rtemp Gtemp;

%Define Analytical Expressions
xLHS = x_KVL_LHS; %Position vector for LHS of circuit (m)
xRHS = x_KVL_RHS; %Position vector for RHS of circuit (m)
VLHS = zeros(length(f),length(xLHS)); %Initialize VLHS matrix to zeros
VRHS = zeros(length(f),length(xRHS)); %Initialize VRHS matrix to zeros
%Find the Voltage on the TL for all positions
for i = 1:length(xRHS)
  VRHS(:,i) = (Vn/2)*(1-G_NE.*exp(-2*gamma*(L-x0))).*(1+G_FE.*exp(2*gamma*xRHS(i))).*...
    exp(-gamma*(xRHS(i)+x0))./(1-G_NE.*G_FE.*exp(-2*gamma*L));
end;
for i = 1:length(xLHS)
  VLHS(:,i) = (-Vn/2)*(1-G_FE.*exp(-2*gamma*x0)).*(1+G_NE.*exp(-2*gamma*(xLHS(i)+L))).*...
    exp(gamma*(xLHS(i)+x0))./(1-G_NE.*G_FE.*exp(-2*gamma*L));
end;
VTOT = horzcat(VLHS,VRHS);
xTOT = horzcat(xLHS,xRHS);

%Compare the Analytical Results to the Simulation Results
figure;
plot(xTOT,abs(VTOT(1,:)),x_KVL_V,abs(V_node_mat(1,:)),'r');
xlabel('TL Position (m)');
ylabel('|V|');
title('Low Frequency Response');
legend('Analytical','Simulation','Location','Best');

figure;
plot(xTOT,abs(VTOT(floor(length(f)/2),:)),...
  x_KVL_V,abs(V_node_mat(floor(length(f)/2),:)),'r');
xlabel('TL Position (m)');
```

```
ylabel('|V|');
title('Middle Frequency Response');
legend('Analytical','Simulation','Location','Best');

figure;
plot(xTOT,abs(VTOT(length(f),:)),x_KVL_V,abs(V_node_mat(length(f),:)),'r');
xlabel('TL Position (m)');
ylabel('|V|');
title('High Frequency Response');
legend('Analytical','Simulation','Location','Best');

%Look at phase
% figure;
% plot(xTOT,angle(VTOT(1,:)),x_KVL_V,angle(V_node_mat(1,:)),'r');
% xlabel('TL Position (m)');
% ylabel('angle(V)');
% title('Low Frequency Response');
% legend('Analytical','Simulation','Location','Best');
%
% figure;
% plot(xTOT,angle(VTOT(floor(length(f)/2),:)),...
%     x_KVL_V,angle(V_node_mat(floor(length(f)/2),:)),'r');
% xlabel('TL Position (m)');
% ylabel('angle(V)');
% title('Middle Frequency Response');
% legend('Analytical','Simulation','Location','Best');
%
% figure;
% plot(xTOT,angle(VTOT(length(f),:)),x_KVL_V,angle(V_node_mat(length(f),:)),'r');
% xlabel('TL Position (m)');
% ylabel('angle(V)');
% title('High Frequency Response');
% legend('Analytical','Simulation','Location','Best');

%Plot movie for comparing the Analytical Results to the Simulation Results
figure;
for k = 1:length(f)
    plot(xTOT,abs(VTOT(k,:)),x_KVL_V,abs(V_node_mat(k,:)),'r');
    title(strcat([num2str(f(k)) ' Hz Frequency Response']));
    xlabel('TL Position (m)');
    ylabel('|V|');
    legend('Analytical','Simulation','Location','Best');
    pause(0.01);
end;
```

Matlab File “Lossy_TL_Lumped_I.m”

```
clear all;
close all;
clc;

%This simulation calculates the voltage and current on a transmission line
%where a lumped current source is placed anywhere along the line. The
%transmission line can be lossless or lossy.

%Simulation cases for lossy - distortionless line (R/L = G/C)
%Define PUL Parameters - Consider frequency dependence for improvements
C_pul = 100e-12; %F/m
L_pul = 250e-9; %H/m
R_pul = 100;%4; %Ohm/m
G_pul = 2e-8;%2e-10; %S/m
%Define Propagation Parameters
f = (1e6:10e6:1e9)'; %Frequency range simulation (Hz)
w = 2*pi*f;
gamma = sqrt((R_pul+j*w*L_pul).*(G_pul+j*w*C_pul));
alpha = real(gamma); %Loss (Np/m) [interesting when = 1]
B = imag(gamma); %Beta
Vp = w./B; %Phase velocity (m/s)
Z0 = sqrt((R_pul+j*w*L_pul)./(G_pul+j*w*C_pul)); %TL characteristic impedance (Ohm)
lambda_min = min(Vp./f); %Smallest wavelength (m)
j = sqrt(-1);
%Geometry Parameters
L = 1; %Line Length (m)
x0 = 0.2; %Source Location (make this a positive number) (m)
l_length = L-x0; %TL length left of source (m)
r_length = x0; %TL length right of source (m)
%Load Parameters
ZFE = 75+(1./(j*w*(5e-12))).*ones(length(f),1); %Far-end Load Definition (Ohm)
ZNE = 45+j*w*(10e-9).*ones(length(f),1); %Near-end Load Definition (Ohm)
G_NE = (ZNE-Z0)./(ZNE+Z0); %Reflection coefficient at the near-end
G_FE = (ZFE-Z0)./(ZFE+Z0); %Reflection coefficient at the far-end

%Define Source Voltage
In = 1; %Noise Source Voltage

%Set up TL KVL Circuit Simulation
%For a good simulation, each PUL section must be no larger than lambda/20
%in length.
pul_length = lambda_min/20; %Target PUL section length
%Must have an integer number of TL sections, so the actual pul_length
%sections for the left and right hand sides of the TL problem may not be at
%the same spacing

%Determine LHS circuit properties
l_pul_secs = ceil(l_length/pul_length); %Number of pul sections LHS represents
if l_length == 0
   l_pul_length = 0;
else %Finite section length
   l_pul_length = l_length/l_pul_secs; %LHS pul section length
end;
C_LHS = C_pul*l_pul_length;
```

```
L_LHS = L_pul*l_pul_length;
R_LHS = R_pul*l_pul_length;
G_LHS = G_pul*l_pul_length;

%Determine RHS circuit properties
r_pul_secs = ceil(r_length/pul_length); %Number of pul sections LHS represents
if r_length == 0
   r_pul_length = 0;
else %Finite section length
   r_pul_length = r_length/r_pul_secs; %RHS pul section length
end;
C_RHS = C_pul*r_pul_length;
L_RHS = L_pul*r_pul_length;
R_RHS = R_pul*r_pul_length;
G_RHS = G_pul*r_pul_length;

%Determine Source Loop
s_loop = l_pul_secs+1; %Loop number left of source
tot_loops = l_pul_secs+r_pul_secs+2; %Total number of KVL loops to solve
Z_mat = zeros(tot_loops,tot_loops); %Initiailize impedance matrix

%Setup KVL Matrix to solve
%Create voltage matrix (most equations are voltage equations)
V_mat = zeros(tot_loops,1); %Initialize voltage matrix to zeros
V_mat(s_loop+1) = In; %Insert source current
%Create current matrix
I_mat = zeros(length(f),tot_loops); %Initialize current matrix to zeros

for i = 1:length(f)
   %Fill Impedance Matrix for each frequency
   for k = 1:tot_loops
      switch k
         case {1}
            %ZNE loop
            if l_length ~= 0
               Z_mat(k,k) = ZNE(i)+(R_LHS+j*w(i)*L_LHS)/2+...
                  1/(j*w(i)*C_LHS+G_LHS);
               Z_mat(k,k+1) = -1/(j*w(i)*C_LHS+G_LHS);
            else %Source at near-end
               %Write supermesh equation
               Z_mat(k,k) = ZNE(i);
               Z_mat(k,k+1) = (R_RHS+j*w(i)*L_RHS)/2+1/(j*w(i)*C_RHS+G_RHS);
               Z_mat(k,k+2) = -1/(j*w(i)*C_RHS+G_RHS);
            end;
         case {tot_loops}
            %ZFE loop
            if r_length ~= 0
               Z_mat(k,k) = ZFE(i)+(R_RHS+j*w(i)*L_RHS)/2+...
                  1/(j*w(i)*C_RHS+G_RHS);
               Z_mat(k,k-1) = -1/(j*w(i)*C_RHS+G_RHS);
            else %Source at far-end
               %Write source equation
               Z_mat(k,k-1) = -1;
               Z_mat(k,k) = 1;
            end;
         case {s_loop}
```

```
                %Loop left of source -> Write supermesh equation
                if r_length ~= 0
                    Z_mat(k,k-1) = -1/(j*w(i)*C_LHS+G_LHS);
                    Z_mat(k,k) = 1/(j*w(i)*C_LHS+G_LHS)+(R_LHS+j*w(i)*L_LHS)/2;
                    Z_mat(k,k+1) = 1/(j*w(i)*C_RHS+G_RHS)+(R_RHS+j*w(i)*L_RHS)/2;
                    Z_mat(k,k+2) = -1/(j*w(i)*C_RHS+G_RHS);
                else %Source at far-end -> Different supermesh equation
                    Z_mat(k,k-1) = -1/(j*w(i)*C_LHS+G_LHS);
                    Z_mat(k,k) = (R_LHS+j*w(i)*L_LHS)/2+...
                        1/(j*w(i)*C_LHS+G_LHS);
                    Z_mat(k,k+1) = ZFE(i);
                end;
            case {s_loop+1}
                %Loop right of source -> Write source equation
                Z_mat(k,k-1) = -1;
                Z_mat(k,k) = 1;
            otherwise
                %Internal loops
                if k < s_loop
                    Ctemp = C_LHS;
                    Ltemp = L_LHS;
                    Rtemp = R_LHS;
                    Gtemp = G_LHS;
                else %k > s_loop
                    Ctemp = C_RHS;
                    Ltemp = L_RHS;
                    Rtemp = R_RHS;
                    Gtemp = G_RHS;
                end;
                Z_mat(k,k-1) = -1/(j*w(i)*Ctemp+Gtemp);
                Z_mat(k,k) = 2/(j*w(i)*Ctemp+Gtemp)+Rtemp+j*w(i)*Ltemp;
                Z_mat(k,k+1) = -1/(j*w(i)*Ctemp+Gtemp);
        end;
    end;
    %Solve for the currents
    I_mat(i,:) =( Z_mat^(-1))*V_mat;
    clear Ctemp Ltemp Rtemp Gtemp;
end;
%Create position vectors
if l_pul_length ~= 0
    x_KVL_LHS = -L+(0:l_pul_length:(l_pul_length*l_pul_secs));
else %Source at near-end
    x_KVL_LHS = -L;
end;
if r_pul_length ~= 0
    x_KVL_RHS = -r_length+(0:r_pul_length:(r_pul_length*r_pul_secs));
else %Source at far-end
    x_KVL_RHS = 0;
end;
if r_pul_length ~= 0
    x_KVL_V = horzcat(x_KVL_LHS,x_KVL_RHS(2:length(x_KVL_RHS)));
else %Source at far-end
    x_KVL_V = x_KVL_LHS;
end;
x_KVL_I = horzcat(x_KVL_LHS,x_KVL_RHS);
% clear x_KVL_LHS x_KVL_RHS;
```

```
%The current position vector will have 1 more point than the voltage
%position vector.

%Find voltages
V_node_mat = zeros(length(f),tot_loops-1); %Initialize voltage matrix to zeros
%Solve voltages at each node
for k = 1:tot_loops-1
    switch k
        case {1}
            %ZNE node
            V_node_mat(:,k) = -ZNE.*I_mat(:,k);
        case {tot_loops-1}
            %ZFE node
            V_node_mat(:,k) = ZFE.*I_mat(:,k+1);
        otherwise
            %Internal nodes
            if k <= s_loop
                Ctemp = C_LHS;
                Ltemp = L_LHS;
                Rtemp = R_LHS;
                Gtemp = G_LHS;
                V_node_mat(:,k) = (1./(j*w*Ctemp+Gtemp)).*I_mat(:,k-1)-...
                    (1./(j*w*Ctemp+Gtemp)+(Rtemp+j*w*Ltemp)/2).*I_mat(:,k);
            else %k > s_loop
                Ctemp = C_RHS;
                Ltemp = L_RHS;
                Rtemp = R_RHS;
                Gtemp = G_RHS;
                %Since there is one less voltage node than current, there
                %is a factor of +1 running around when calculating the
                %voltages in the RHS of the circuit
                V_node_mat(:,k) = (1./(j*w*Ctemp+Gtemp)).*I_mat(:,k)-...
                    (1./(j*w*Ctemp+Gtemp)+(Rtemp+j*w*Ltemp)/2).*I_mat(:,k+1);
            end;
    end;
end;
clear Ctemp Ltemp Rtemp Gtemp;

%Define Analytical Expressions
xLHS = x_KVL_LHS; %Position vector for LHS of circuit (m)
xRHS = x_KVL_RHS; %Position vector for RHS of circuit (m)
VLHS = zeros(length(f),length(xLHS)); %Initialize VLHS matrix to zeros
VRHS = zeros(length(f),length(xRHS)); %Initialize VRHS matrix to zeros
%Find the Voltage on the TL for all positions
for i = 1:length(xRHS)
    VRHS(:,i) = (In*Z0/2).*(1+G_NE.*exp(-2*gamma*(L-x0))).*(1+G_FE.*exp(2*gamma*xRHS(i))).*...
        exp(-gamma*(xRHS(i)+x0))./(1-G_NE.*G_FE.*exp(-2*gamma*L));
end;
for i = 1:length(xLHS)
    VLHS(:,i) = (In*Z0/2).*(1+G_FE.*exp(-2*gamma*x0)).*(1+G_NE.*exp(-2*gamma*(xLHS(i)+L))).*...
        exp(gamma*(xLHS(i)+x0))./(1-G_NE.*G_FE.*exp(-2*gamma*L));
end;
VTOT = horzcat(VLHS,VRHS);
xTOT = horzcat(xLHS,xRHS);

%Compare the Analytical Results to the Simulation Results
```

```
figure;
plot(xTOT,abs(VTOT(1,:)),x_KVL_V,abs(V_node_mat(1,:)),'r');
xlabel('TL Position (m)');
ylabel('|V|');
title('Low Frequency Response');
legend('Analytical','Simulation','Location','Best');

figure;
plot(xTOT,abs(VTOT(floor(length(f)/2),:)),...
    x_KVL_V,abs(V_node_mat(floor(length(f)/2),:)),'r');
xlabel('TL Position (m)');
ylabel('|V|');
title('Middle Frequency Response');
legend('Analytical','Simulation','Location','Best');

figure;
plot(xTOT,abs(VTOT(length(f),:)),x_KVL_V,abs(V_node_mat(length(f),:)),'r');
xlabel('TL Position (m)');
ylabel('|V|');
title('High Frequency Response');
legend('Analytical','Simulation','Location','Best');

%Look at phase
% figure;
% plot(xTOT,angle(VTOT(1,:)),x_KVL_V,angle(V_node_mat(1,:)),'r');
% xlabel('TL Position (m)');
% ylabel('angle(V)');
% title('Low Frequency Response');
% legend('Analytical','Simulation','Location','Best');
%
% figure;
% plot(xTOT,angle(VTOT(floor(length(f)/2),:)),...
%     x_KVL_V,angle(V_node_mat(floor(length(f)/2),:)),'r');
% xlabel('TL Position (m)');
% ylabel('angle(V)');
% title('Middle Frequency Response');
% legend('Analytical','Simulation','Location','Best');
%
% figure;
% plot(xTOT,angle(VTOT(length(f),:)),x_KVL_V,angle(V_node_mat(length(f),:)),'r');
% xlabel('TL Position (m)');
% ylabel('angle(V)');
% title('High Frequency Response');
% legend('Analytical','Simulation','Location','Best');

%Plot movie for comparing the Analytical Results to the Simulation Results
figure;
for k = 1:length(f)
    plot(xTOT,abs(VTOT(k,:)),x_KVL_V,abs(V_node_mat(k,:)),'r');
    title(strcat([num2str(f(k)) ' Hz Frequency Response']));
    xlabel('TL Position (m)');
    ylabel('|V|');
    legend('Analytical','Simulation','Location','Best');
    pause(0.01);
end;
```

Matlab File “Lossy_TL_Uniform_Distributed_V2.m”

```
clear all;
close all;
clc;

%This simulation calculates the voltage and current on a victim
%transmission line where a uniform distributed voltage source is placed
%anyhwere along the line. The formulation of the code is taken from the
%case where a non-uniform source is analyzed. This simulation validates the
%non-uniform distributed voltage source simulation code with the simulation
%matching the analytical expressions.

%The transmission line can be lossless or lossy. The distributed voltage
%source is considered to be uniform. Analytical expressions for comparison
%purposes with the simulation are given for the uniform noise source case.

%Assumptions
%1. Weak Coupling
%2. Culprit and Victim propagation parameter gamma must be the same
%3. Characteristic impedance is approximately uniform in the victim

%Simulation cases for lossy - distortionless line (R/L = G/C)
%Define Victim PUL Parameters
C_pul = 100e-12; %F/m
L_pul = 250e-9; %H/m
R_pul = 100;%4; %Ohm/m
G_pul = 2e-8;%2e-10; %S/m
%Define Coupling PUL Parameters
L21 = 100e-9; %H/m
R21 = 1; %Ohm/m
%Define Propagation Parameters
f = (1e6:10e6:1e9)'; %Frequency range simulation (Hz)
w = 2*pi*f;
gamma_v = sqrt((R_pul+j*w*L_pul).*(G_pul+j*w*C_pul));
alpha = real(gamma_v); %Loss (Np/m) [interesting when = 1]
B = imag(gamma_v); %Beta
Vp = w./B; %Phase velocity (m/s)
Z0v = sqrt((R_pul+j*w*L_pul)./(G_pul+j*w*C_pul)); %TL characteristic impedance (Ohm)
lambda_min = min(Vp./f); %Smallest wavelength (m)
j = sqrt(-1);
%Victim Geometry Parameters
Lv = 1; %Line length (m)
x0L = -0.6; %Distributed source left boundary (make this a negative number) (m)
x0R = -0.3; %Distributed source right boundary (make this a negative number) (m)
l_length = x0L+Lv; %TL length left of source (m)
r_length = -x0R; %TL length right of source (m)
s_length = x0R-x0L; %Distributed source length (m)
%Victim Load Parameters
ZFE = 75+(1./(j*w*(5e-12))).*ones(length(f),1); %Far-end Load Definition (Ohm)
ZNE = 45+j*w*(10e-9).*ones(length(f),1); %Near-end Load Definition (Ohm)
G_NE = (ZNE-Z0v)./(ZNE+Z0v); %Reflection coefficient at the near-end
G_FE = (ZFE-Z0v)./(ZFE+Z0v); %Reflection coefficient at the far-end

%Culprit Geometry Parameters
%Define Culprit PUL Parameters
```

```
C_pul_c = C_pul; %F/m
L_pul_c = L_pul; %H/m -(gamma_v.^2)./((w.^2)*C_pul_c)
R_pul_c = R_pul;%4; %Ohm/m
G_pul_c = G_pul;%2e-10; %S/m
gamma_c = sqrt((R_pul_c+j*w.*L_pul_c).*(G_pul_c+j*w*C_pul_c)); %Propagation parameter
Z0c = sqrt((R_pul_c+j*w.*L_pul_c)./(G_pul_c+j*w*C_pul_c)); %TL characteristic impedance (Ohm)

Vs = 100; %Source voltage (V)
a = 1.2; %RHS position variable (usually positive) (m)
b = 1.5; %LHS position variable (usually positive) (m)
Lc = a+b; %Culprit circuit length (m)

ZS_CP = 30+j*w*(100e-9).*ones(length(f),1); %Source Load Defintion (Ohm)
ZL_CP = 75+(1./(j*w*(30e-12))).*ones(length(f),1); %Culprit Load Definition (Ohm)
G_ZS = (ZS_CP-Z0c)./(ZS_CP+Z0c); %Reflection coefficient at the culprit near-end
G_ZL = (ZL_CP-Z0c)./(ZL_CP+Z0c); %Reflection coefficient at the culprit far-end

%Define Coupling Coordinate Extremes on the Culprit Circuit Axis
x_CP_ends = [x0L x0R]; %Same coordinate system as the victim

%Set up TL KVL Circuit Simulation
%For a good simulation, each PUL section must be no larger than lambda/20
%in length.
pul_length = lambda_min/40; %Target PUL section length
%Must have an integer number of TL sections, so the actual pul_length
%sections for the left hand side, distributed source region, and right hand
%sides of the TL problem may not be at the same spacing.

%Determine LHS circuit properties
l_pul_secs = ceil(l_length/pul_length); %Number of pul sections LHS represents
if l_length == 0
   l_pul_length = 0;
else %Finite section length
   l_pul_length = l_length/l_pul_secs; %LHS pul section length
end;
C_LHS = C_pul*l_pul_length;
L_LHS = L_pul*l_pul_length;
R_LHS = R_pul*l_pul_length;
G_LHS = G_pul*l_pul_length;

%Determine source region circuit properties
s_pul_secs = ceil(s_length/pul_length); %Number of pul sections source region represents
if s_length == 0
   s_pul_length = 0;
else %Finite section length
   s_pul_length = s_length/s_pul_secs; %Source region pul section length
end;
C_SR = C_pul*s_pul_length;
L_SR = L_pul*s_pul_length;
R_SR = R_pul*s_pul_length;
G_SR = G_pul*s_pul_length;

%Determine RHS circuit properties
r_pul_secs = ceil(r_length/pul_length); %Number of pul sections LHS represents
if r_length == 0
   r_pul_length = 0;
```

```
else %Finite section length
   r_pul_length = r_length/r_pul_secs; %RHS pul section length
end;
C_RHS = C_pul*r_pul_length;
L_RHS = L_pul*r_pul_length;
R_RHS = R_pul*r_pul_length;
G_RHS = G_pul*r_pul_length;

%Create position vectors
if l_pul_length ~= 0
   x_KVL_LHS = -Lv+(0:l_pul_length:(l_pul_length*l_pul_secs));
else %Source at near-end
   x_KVL_LHS = -Lv;
end;
if s_pul_length ~= 0
   x_KVL_SR = x_KVL_LHS(length(x_KVL_LHS))+...
      (0:s_pul_length:(s_pul_length*s_pul_secs));
else %No source region
end;
if r_pul_length ~= 0
   x_KVL_RHS = -r_length+(0:r_pul_length:(r_pul_length*r_pul_secs));
else %Source at far-end
   x_KVL_RHS = 0;
end;
if s_pul_length ~= 0
   x_KVL = horzcat(x_KVL_LHS,x_KVL_SR(2:length(x_KVL_SR)),...
      x_KVL_RHS(2:length(x_KVL_RHS)));
   % clear x_KVL_LHS x_KVL_SR x_KVL_RHS;
else %No source region
   x_KVL = horzcat(x_KVL_LHS,x_KVL_RHS(2:length(x_KVL_RHS)));
   % clear x_KVL_LHS x_KVL_RHS;
end;

%Create culprit position vector
x_CP_source = x_CP_ends(1):s_pul_length:x_CP_ends(2);
%The above position matrix is offset by a half cell and has one more
%position than desired. A position vector is desired in the middle of the
%cells since this is where the source value will be evaluated. Fixing the
%position matrix:
x_CP_source(length(x_CP_source)) = []; %Delete last value
x_CP_source = x_CP_source+s_pul_length/2; %Positions placed in the middle of the cells
%Create equivlant position matrix in the victim circuit
x_KVL_SR_mid = x_KVL_SR(1:(length(x_KVL_SR)-1))+(s_pul_length/2);
%Formulate the noise voltage source
%Vn = -(R21+j*w*L21)*I(x) <- A function of frequency and space
Vn = zeros(length(f),length(x_CP_source));
%Fill noise voltage matrix in continuous domain (V/m)
for i = 1:length(f)
   Vn(i,:) = -(R21+j*w(i)*L21)*(Vs*exp(-gamma_c(i)*Lc)*...
      (exp(-gamma_c(i)*(x_CP_source(floor(length(x_CP_source)/2))-a))-...
      G_ZL(i)*exp(gamma_c(i)*(x_CP_source(floor(length(x_CP_source)/2))-a)))./...
      ((Z0c(i)+ZS_CP(i)).*(1-G_ZL(i)*G_ZS(i)*exp(-2*gamma_c(i)*Lc))));
end;
%Define Distributed Source Voltage in the Discrete Domain
V_SR = Vn*s_pul_length;
```

```
%Determine Source Region Transition Loops
t_loop1 = l_pul_secs+1; %First transition loop number
t_loop2 = l_pul_secs+s_pul_secs+1; %Second transition loop number
tot_loops = l_pul_secs+s_pul_secs+r_pul_secs+1; %Total number of KVL loops to solve
Z_mat = zeros(tot_loops,tot_loops); %Initiailize impedance matrix

%Create voltage matrix
V_mat = zeros(tot_loops,1); %Initialize voltage matrix to zeros

%Create current matrix
I_mat = zeros(length(f),tot_loops); %Initialize current matrix to zeros

%Setup KVL Matrix to solve
for i = 1:length(f)
    %Insert source voltages
    if t_loop1 ~= t_loop2
        V_mat(t_loop1) = V_SR(i,1)/2; %Transition loop 1
        V_mat(t_loop2) = V_SR(i,s_pul_secs)/2; %Transition loop 2
        V_mat((t_loop1+1):(t_loop2-1)) = V_SR(i,1:(s_pul_secs-1))/2+...
            V_SR(i,2:s_pul_secs)/2; %Source region loops
    else
    end;
    %Fill Impedance Matrix for each frequency
    for k = 1:tot_loops
        switch k
            case {1}
                %ZNE loop
                if l_length ~= 0
                    Z_mat(k,k) = ZNE(i)+(R_LHS+j*w(i)*L_LHS)/2+...
                        1/(j*w(i)*C_LHS+G_LHS);
                    Z_mat(k,k+1) = -1/(j*w(i)*C_LHS+G_LHS);
                else %Source at near-end
                    Z_mat(k,k) = ZNE(i)+(R_SR+j*w(i)*L_SR)/2+...
                        1/(j*w(i)*C_SR+G_SR);
                    Z_mat(k,k+1) = -1/(j*w(i)*C_SR+G_SR);
                end;
            case {tot_loops}
                %ZFE loop
                if r_length ~= 0
                    Z_mat(k,k) = ZFE(i)+(R_RHS+j*w(i)*L_RHS)/2+...
                        1/(j*w(i)*C_RHS+G_RHS);
                    Z_mat(k,k-1) = -1/(j*w(i)*C_RHS+G_RHS);
                else %Source at far-end
                    Z_mat(k,k) = ZFE(i)+(R_SR+j*w(i)*L_SR)/2+...
                        1/(j*w(i)*C_SR+G_SR);
                    Z_mat(k,k-1) = -1/(j*w(i)*C_SR+G_SR);
                end;
            case {t_loop1}
                %LHS transition loop
                Z_mat(k,k-1) = -1/(j*w(i)*C_LHS+G_LHS);
                Z_mat(k,k) = 1/(j*w(i)*C_LHS+G_LHS)+(R_LHS+j*w(i)*L_LHS)/2+...
                    1/(j*w(i)*C_SR+G_SR)+(R_SR+j*w(i)*L_SR)/2;
                Z_mat(k,k+1) = -1/(j*w(i)*C_SR+G_SR);
            case {t_loop2}
                %RHS transition loop
                Z_mat(k,k-1) = -1/(j*w(i)*C_SR+G_SR);
```

```
                Z_mat(k,k) = 1/(j*w(i)*C_RHS+G_RHS)+(R_RHS+j*w(i)*L_RHS)/2+...
                    1/(j*w(i)*C_SR+G_SR)+(R_SR+j*w(i)*L_SR)/2;
                Z_mat(k,k+1) = -1/(j*w(i)*C_RHS+G_RHS);
            otherwise
                %Internal loops
                if k < t_loop1
                    %LHS loops
                    Ctemp = C_LHS;
                    Ltemp = L_LHS;
                    Rtemp = R_LHS;
                    Gtemp = G_LHS;
                elseif k > t_loop2
                    %RHS loops
                    Ctemp = C_RHS;
                    Ltemp = L_RHS;
                    Rtemp = R_RHS;
                    Gtemp = G_RHS;
                else
                    %Source region loops
                    Ctemp = C_SR;
                    Ltemp = L_SR;
                    Rtemp = R_SR;
                    Gtemp = G_SR;
                end;
                Z_mat(k,k-1) = -1/(j*w(i)*Ctemp+Gtemp);
                Z_mat(k,k) = 2/(j*w(i)*Ctemp+Gtemp)+Rtemp+j*w(i)*Ltemp;
                Z_mat(k,k+1) = -1/(j*w(i)*Ctemp+Gtemp);
        end;
    end;
    %Solve for the currents
    I_mat(i,:) =( Z_mat^(-1))*V_mat;
    clear Ctemp Ltemp Rtemp Gtemp;
end;

%Find voltages
V_node_mat = zeros(length(f),tot_loops); %Initialize voltage matrix to zeros
%Solve voltages at each node
for k = 1:tot_loops
    switch k
        case {1}
            %ZNE node
            V_node_mat(:,k) = -ZNE.*I_mat(:,k);
        case {tot_loops}
            %ZFE node
            V_node_mat(:,k) = ZFE.*I_mat(:,k);
        otherwise
            %Internal nodes
            if k <= t_loop1
                Ctemp = C_LHS;
                Ltemp = L_LHS;
                Rtemp = R_LHS;
                Gtemp = G_LHS;
                V_node_mat(:,k) = (1./(j*w*Ctemp+Gtemp)).*I_mat(:,k-1)-...
                    (1./(j*w*Ctemp+Gtemp)+(Rtemp+j*w*Ltemp)/2).*I_mat(:,k);
            elseif k > t_loop2
                Ctemp = C_RHS;
```

```
            Ltemp = L_RHS;
            Rtemp = R_RHS;
            Gtemp = G_RHS;
            V_node_mat(:,k) = (1./(j*w*Ctemp+Gtemp)).*I_mat(:,k-1)-...
               (1./(j*w*Ctemp+Gtemp)+(Rtemp+j*w*Ltemp)/2).*I_mat(:,k);
         else %In source region
            Ctemp = C_SR;
            Ltemp = L_SR;
            Rtemp = R_SR;
            Gtemp = G_SR;
            V_node_mat(:,k) = (1./(j*w*Ctemp+Gtemp)).*I_mat(:,k-1)-...
               (1./(j*w*Ctemp+Gtemp)+(Rtemp+j*w*Ltemp)/2).*I_mat(:,k)+...
               V_SR(:,(k-t_loop1))/2;
         end;
   end;
end;
clear Ctemp Ltemp Rtemp Gtemp;

%Define Analytical Expressions - Distributed Uniform Noise Source
xLHS = x_KVL_LHS; %Position vector for LHS of circuit (m)
xRHS = x_KVL_RHS; %Position vector for RHS of circuit (m)
xSR = x_KVL_SR; %Position vector for the SR of circuit (m)
VLHS = zeros(length(f),length(xLHS)); %Initialize VLHS matrix to zeros
VRHS = zeros(length(f),length(xRHS)); %Initialize VRHS matrix to zeros
VSR = zeros(length(f),length(xSR)); %Initialize VSR matrix to zeros
%Define Equivalent Noise Voltage
%This quantity is defined in case the analytical expression for a uniform
%source is to be compared with a simulation where the sources are not
%uniform. The middle value or the equivalent middle value in the source
%region is used for the equivalent noise voltage.
if size(Vn,2)-(floor(size(Vn,2)/2)*2) == 1
   %Position matrix is odd - take the middle value for all frequencies
   Vn_eq = Vn(:,(floor(size(Vn,2)/2)+1));
else %Position matrix is even - find average equivalent middle value
   Vn_eq = mean([Vn(:,floor(size(Vn,2)/2)) Vn(:,(floor(size(Vn,2)/2)+1))],2);
end;

%Find the Voltage on the TL outside the coupling region
for i = 1:length(xRHS)
   VRHS(:,i) = (Vn_eq./(2*gamma_v)).*(1./(1-G_NE.*G_FE.*exp(-2*gamma_v*Lv))).*...
      ((1+G_NE.*exp(-2*gamma_v*(Lv-abs(x0R)))).*...
      (1+G_FE.*exp(2*gamma_v*xRHS(i))).*exp(-gamma_v*(xRHS(i)+abs(x0R)))-...
      (1+G_NE.*exp(-2*gamma_v*(Lv-abs(x0L)))).*...
      (1+G_FE.*exp(2*gamma_v*xRHS(i))).*exp(-gamma_v*(xRHS(i)+abs(x0L))));
end;
for i = 1:length(xLHS)
   VLHS(:,i) = (Vn_eq./(2*gamma_v)).*(1./(1-G_NE.*G_FE.*exp(-2*gamma_v*Lv))).*...
      ((1+G_NE.*exp(-2*gamma_v*(Lv+xLHS(i)))).*...
      (1+G_FE.*exp(-2*gamma_v*abs(x0R))).*exp(gamma_v*(xLHS(i)+abs(x0R)))-...
      (1+G_NE.*exp(-2*gamma_v*(Lv+xLHS(i)))).*...
      (1+G_FE.*exp(-2*gamma_v*abs(x0L))).*exp(gamma_v*(xLHS(i)+abs(x0L))));
end;
%Find the voltage on the TL inside the coupling region
for i = 1:length(xSR)
   VSR(:,i) = (Vn_eq./(2*gamma_v)).*(1./(1-G_NE.*G_FE.*exp(-2*gamma_v*Lv))).*...
      ((1+G_NE.*exp(-2*gamma_v*(Lv+xSR(i)))).*...
```

```
        (1+G_FE.*exp(-2*gamma_v*abs(x0R))).*exp(gamma_v*(xSR(i)+abs(x0R)))-...
        (1+G_NE.*exp(-2*gamma_v*(Lv-abs(x0L)))).*...
        (1+G_FE.*exp(2*gamma_v*xSR(i))).*exp(-gamma_v*(xSR(i)+abs(x0L))));
end;

xAnal = horzcat(xLHS,xSR(2:(length(xSR)-1)),xRHS);
VTOT = horzcat(VLHS,VSR(:,(2:(length(xSR)-1))),VRHS);

%Compare the Analytical Results to the Simulation Results
%Subplots may be useful here
%    Top Plot - Coupling Voltage Waveform in the coupling region
%    Bottom Plot - Voltage along the victim TL

figure;
subplot(2,1,1);
plot(x_KVL_SR_mid,abs(Vn(1,:)),...
    x_KVL_SR_mid,ones(1,length(x_KVL_SR_mid))*abs(Vn_eq(1)),'-r');
title('Low Frequency Response - Noise Voltage Waveform');
ylabel('|V|');
legend('Actual Noise Source','Approximated Noise Source','Location','Best');
xlim([xLHS(1) xRHS(length(xRHS))]);
subplot(2,1,2);
plot(xAnal,abs(VTOT(1,:)),x_KVL,abs(V_node_mat(1,:)),'r');
title('Low Frequency Response - Victim Voltage Waveform');
xlabel('TL Position (m)');
ylabel('|V|');
legend('Analytical','Simulation','Location','Best');

figure;
subplot(2,1,1);
plot(x_KVL_SR_mid,abs(Vn(floor(length(f)/2),:)),...
    x_KVL_SR_mid,ones(1,length(x_KVL_SR_mid))*abs(Vn_eq(floor(length(f)/2))),'-r');
title('Middle Frequency Response - Noise Voltage Waveform');
ylabel('|V|');
legend('Actual Noise Source','Approximated Noise Source','Location','Best');
xlim([xLHS(1) xRHS(length(xRHS))]);
subplot(2,1,2);
plot(xAnal,abs(VTOT(floor(length(f)/2),:)),...
    x_KVL,abs(V_node_mat(floor(length(f)/2),:)),'r');
title('Middle Frequency Response - Victim Voltage Waveform');
xlabel('TL Position (m)');
ylabel('|V|');
legend('Analytical','Simulation','Location','Best');

figure;
subplot(2,1,1);
plot(x_KVL_SR_mid,abs(Vn(length(f),:)),...
    x_KVL_SR_mid,ones(1,length(x_KVL_SR_mid))*abs(Vn_eq(length(f))),'-r');
title('High Frequency Response - Noise Voltage Waveform');
ylabel('|V|');
legend('Actual Noise Source','Approximated Noise Source','Location','Best');
xlim([xLHS(1) xRHS(length(xRHS))]);
subplot(2,1,2);
plot(xAnal,abs(VTOT(length(f),:)),x_KVL,abs(V_node_mat(length(f),:)),'r');
title('High Frequency Response - Victim Voltage Waveform');
xlabel('TL Position (m)');
```

```
ylabel('|V|');
legend('Analytical','Simulation','Location','Best');

%Look at phase
% figure;
% plot(xAnal,angle(VTOT(1,:)),x_KVL,angle(V_node_mat(1,:)),'r');
% xlabel('TL Position (m)');
% ylabel('angle(V)');
% title('Low Frequency Response');
% legend('Analytical','Simulation','Location','Best');
%
% figure;
% plot(xAnal,angle(VTOT(floor(length(f)/2),:)),...
%     x_KVL,angle(V_node_mat(floor(length(f)/2),:)),'r');
% xlabel('TL Position (m)');
% ylabel('angle(V)');
% title('Middle Frequency Response');
% legend('Analytical','Simulation','Location','Best');
%
% figure;
% plot(xAnal,angle(VTOT(length(f),:)),x_KVL,angle(V_node_mat(length(f),:)),'r');
% xlabel('TL Position (m)');
% ylabel('angle(V)');
% title('High Frequency Response');
% legend('Analytical','Simulation','Location','Best');

%Plot movie for comparing the Analytical Results to the Simulation Results
figure;
for k = 1:length(f)
    subplot(2,1,1);
    plot(x_KVL_SR_mid,abs(Vn(k,:)),...
        x_KVL_SR_mid,ones(1,length(x_KVL_SR_mid))*abs(Vn_eq(k)),'-r');
    title(strcat(['Noise Voltage Waveform @ ' num2str(f(k)) ' Hz']));
    ylabel('|V|');
    legend('Actual Noise Source','Approximated Noise Source','Location','Best');
    xlim([xLHS(1) xRHS(length(xRHS))]);
    subplot(2,1,2);
    plot(xAnal,abs(VTOT(k,:)),x_KVL,abs(V_node_mat(k,:)),'r');
    title(strcat(['Victim Voltage Waveform @ ' num2str(f(k)) ' Hz']));
    xlabel('TL Position (m)');
    ylabel('|V|');
    legend('Analytical','Simulation','Location','Best');
    pause(0.01);
end;
```

Matlab File “Lossy_TL_Uniform_Distributed_I1.m”

```
clear all;
close all;
clc;

%This simulation calculates the voltage and current on a victim
%transmission line where a uniform distributed current source is placed
%anyhwere along the line. The formulation of the code is taken from the
%case where a non-uniform source is analyzed. This simulation validates the
%non-uniform distributed current source simulation code with the simulation
%matching the analytical expressions.

%The transmission line can be lossless or lossy. The distributed
%current source is considered to be uniform. Analytical expressions for
%comparison purposes with the simulation are given for the uniform noise
%source case.

%Assumptions
%1. Weak Coupling
%2. Culprit and Victim propagation parameter gamma must be the same
%3. Characteristic impedance is approximately uniform in the victim

%Simulation cases for lossy - distortionless line (R/L = G/C)
%Define Victim PUL Parameters
C_pul = 100e-12; %F/m
L_pul = 250e-9; %H/m
R_pul = 100;%4; %Ohm/m
G_pul = 2e-8;%2e-10; %S/m
%Define Coupling PUL Parameters
C21 = 20e-9; %F/m 20e-12
G21 = 2e-12; %S/m
%Define Propagation Parameters
f = (1e6:10e6:1e9)'; %Frequency range simulation (Hz)
w = 2*pi*f;
gamma_v = sqrt((R_pul+j*w*L_pul).*(G_pul+j*w*C_pul));
alpha = real(gamma_v); %Loss (Np/m) [interesting when = 1]
B = imag(gamma_v); %Beta
Vp = w./B; %Phase velocity (m/s)
Z0v = sqrt((R_pul+j*w*L_pul)./(G_pul+j*w*C_pul)); %TL characteristic impedance (Ohm)
lambda_min = min(Vp./f); %Smallest wavelength (m)
j = sqrt(-1);
%Victim Geometry Parameters
Lv = 1; %Line length (m)
x0L = -0.6; %Distributed source left boundary (make this a negative number) (m)
x0R = -0.3; %Distributed source right boundary (make this a negative number) (m)
l_length = x0L+Lv; %TL length left of source (m)
r_length = -x0R; %TL length right of source (m)
s_length = x0R-x0L; %Distributed source length (m)
%Victim Load Parameters
ZFE = 75+(1./(j*w*(5e-12))).*ones(length(f),1); %Far-end Load Definition (Ohm)
ZNE = 45+j*w*(10e-9).*ones(length(f),1); %Near-end Load Definition (Ohm)
G_NE = (ZNE-Z0v)./(ZNE+Z0v); %Reflection coefficient at the near-end
G_FE = (ZFE-Z0v)./(ZFE+Z0v); %Reflection coefficient at the far-end

%Culprit Geometry Parameters
```

```
%Define Culprit PUL Parameters
C_pul_c = C_pul; %F/m
L_pul_c = L_pul; %H/m -(gamma_v.^2)./((w.^2)*C_pul_c)
R_pul_c = R_pul;%4; %Ohm/m
G_pul_c = G_pul;%2e-10; %S/m
gamma_c = sqrt((R_pul_c+j*w.*L_pul_c).*(G_pul_c+j*w*C_pul_c)); %Propagation parameter
Z0c = sqrt((R_pul_c+j*w.*L_pul_c)./(G_pul_c+j*w*C_pul_c)); %TL characteristic impedance (Ohm)

Vs = 100; %Source voltage (V)
a = 1.2; %RHS position variable (usually positive) (m)
b = 1.5; %LHS position variable (usually positive) (m)
Lc = a+b; %Culprit circuit length (m)

ZS_CP = 30+j*w*(100e-9).*ones(length(f),1); %Source Load Defintion (Ohm)
ZL_CP = 75+(1./(j*w*(30e-12))).*ones(length(f),1); %Culprit Load Definition (Ohm)
G_ZS = (ZS_CP-Z0c)./(ZS_CP+Z0c); %Reflection coefficient at the culprit near-end
G_ZL = (ZL_CP-Z0c)./(ZL_CP+Z0c); %Reflection coefficient at the culprit far-end

%Define Coupling Coordinate Extremes on the Culprit Circuit Axis
x_CP_ends = [x0L x0R]; %Same coordinate system as the victim

%Set up TL KCL Circuit Simulation
%For a good simulation, each PUL section must be no larger than lambda/20
%in length.
pul_length = lambda_min/40; %Target PUL section length
%Must have an integer number of TL sections, so the actual pul_length
%sections for the left hand side, distributed source region, and right hand
%sides of the TL problem may not be at the same spacing.

%Determine LHS circuit properties
l_pul_secs = ceil(l_length/pul_length); %Number of pul sections LHS represents
if l_length == 0
   l_pul_length = 0;
else %Finite section length
   l_pul_length = l_length/l_pul_secs; %LHS pul section length
end;
C_LHS = C_pul*l_pul_length;
L_LHS = L_pul*l_pul_length;
R_LHS = R_pul*l_pul_length;
G_LHS = G_pul*l_pul_length;

%Determine source region circuit properties
s_pul_secs = ceil(s_length/pul_length); %Number of pul sections source region represents
if s_length == 0
   s_pul_length = 0;
else %Finite section length
   s_pul_length = s_length/s_pul_secs; %Source region pul section length
end;
C_SR = C_pul*s_pul_length;
L_SR = L_pul*s_pul_length;
R_SR = R_pul*s_pul_length;
G_SR = G_pul*s_pul_length;

%Determine RHS circuit properties
r_pul_secs = ceil(r_length/pul_length); %Number of pul sections LHS represents
if r_length == 0
```

```
    r_pul_length = 0;
else %Finite section length
    r_pul_length = r_length/r_pul_secs; %RHS pul section length
end;
C_RHS = C_pul*r_pul_length;
L_RHS = L_pul*r_pul_length;
R_RHS = R_pul*r_pul_length;
G_RHS = G_pul*r_pul_length;

%Create position vectors (same as if KVL equations were used)
if l_pul_length ~= 0
    x_KVL_LHS = -Lv+(0:l_pul_length:(l_pul_length*l_pul_secs));
else %Source at near-end
    x_KVL_LHS = -Lv;
end;
if s_pul_length ~= 0
    x_KVL_SR = x_KVL_LHS(length(x_KVL_LHS))+...
        (0:s_pul_length:(s_pul_length*s_pul_secs));
else %No source region
end;
if r_pul_length ~= 0
    x_KVL_RHS = -r_length+(0:r_pul_length:(r_pul_length*r_pul_secs));
else %Source at far-end
    x_KVL_RHS = 0;
end;
if s_pul_length ~= 0
    x_KVL = horzcat(x_KVL_LHS,x_KVL_SR(2:length(x_KVL_SR)),...
        x_KVL_RHS(2:length(x_KVL_RHS)));
    % clear x_KVL_LHS x_KVL_SR x_KVL_RHS;
else %No source region
    x_KVL = horzcat(x_KVL_LHS,x_KVL_RHS(2:length(x_KVL_RHS)));
    % clear x_KVL_LHS x_KVL_RHS;
end;

%Create culprit position vector
x_CP_source = x_CP_ends(1):s_pul_length:x_CP_ends(2);
%The above position matrix is offset by a half cell and has one more
%position than desired. A position vector is desired in the middle of the
%cells since this is where the source value will be evaluated. Fixing the
%position matrix:
x_CP_source(length(x_CP_source)) = []; %Delete last value
x_CP_source = x_CP_source+s_pul_length/2; %Positions placed in the middle of the cells
%Create equivlant position matrix in the victim circuit
x_KVL_SR_mid = x_KVL_SR(1:(length(x_KVL_SR)-1))+(s_pul_length/2);
%Formulate the noise current source
%In = -(G21+j*w*C21)*V(x) <- A function of frequency and space
In = zeros(length(f),length(x_CP_source));
%Fill noise current matrix in continuous domain (A/m)
for i = 1:length(f)
    In(i,:) = -(G21+j*w(i)*C21)*(Vs*Z0c(i).*exp(-gamma_c(i)*Lc)*...
        (exp(-gamma_c(i)*(x_CP_source(floor(length(x_CP_source)/2))-a))+...
        G_ZL(i)*exp(gamma_c(i)*(x_CP_source(floor(length(x_CP_source)/2))-a)))./...
        ((Z0c(i)+ZS_CP(i)).*(1-G_ZL(i)*G_ZS(i)*exp(-2*gamma_c(i)*Lc))));
end;
%Define Distributed Source Current in the Discrete Domain
I_SR = In*s_pul_length;
```

```
%Determine Source Region Transition Nodes
t_node1 = l_pul_secs+1; %First transition node equation (LHS)
t_node2 = l_pul_secs+s_pul_secs+1; %Second transition node equation (RHS)
tot_nodes = l_pul_secs+s_pul_secs+r_pul_secs+2; %Total number of KCL equations to solve
Y_mat = zeros(tot_nodes,tot_nodes); %Initiailize impedance matrix

%Create current matrix (YV = I)
I_mat = zeros(tot_nodes,1); %Initialize current matrix to zeros

%Create voltage matrix
V_mat = zeros(length(f),tot_nodes); %Initialize voltage matrix to zeros

%Setup KCL Matrix to solve (YV = I)
for i = 1:length(f)
    %Insert source currents
    if t_node1 ~= t_node2
        I_mat((t_node1+1):(t_node2)) = I_SR(i,:); %Source region nodes
    else
    end;
    %Fill Admitance Matrix for each frequency
    for k = 1:tot_nodes
        switch k
            case {1}
                %ZNE node
                if l_length ~= 0
                    Y_mat(k,k) = 1/ZNE(i)+2/(R_LHS+j*w(i)*L_LHS);
                    Y_mat(k,k+1) = -2/(R_LHS+j*w(i)*L_LHS);
                else %Source at near-end
                    Y_mat(k,k) = 1/ZNE(i)+2/(R_SR+j*w(i)*L_SR);
                    Y_mat(k,k+1) = -2/(R_SR+j*w(i)*L_SR);
                end;
            case {2}
                if l_length ~= 0
                    if l_pul_secs == 1
                        Y_mat(k,k-1) = -2/(R_LHS+j*w(i)*L_LHS);
                        Y_mat(k,k) = 2/(R_LHS+j*w(i)*L_LHS)+(j*w(i)*C_LHS+G_LHS)+...
                            2/(R_LHS+j*w(i)*L_LHS+R_SR+j*w(i)*L_SR);
                        Y_mat(k,k+1) = -2/(R_LHS+j*w(i)*L_LHS+R_SR+j*w(i)*L_SR);
                    else %l_pul_secs > 1
                        Y_mat(k,k-1) = -2/(R_LHS+j*w(i)*L_LHS);
                        Y_mat(k,k) = 3/(R_LHS+j*w(i)*L_LHS)+(j*w(i)*C_LHS+G_LHS);
                        Y_mat(k,k+1) = -1/(R_LHS+j*w(i)*L_LHS);
                    end;
                else %Source at near-end
                    Y_mat(k,k-1) = -2/(R_SR+j*w(i)*L_SR);
                    Y_mat(k,k) = 3/(R_SR+j*w(i)*L_SR)+(j*w(i)*C_SR+G_SR);
                    Y_mat(k,k+1) = -1/(R_SR+j*w(i)*L_SR);
                end;
            case {tot_nodes-1}
                if r_length ~= 0
                    if r_pul_secs == 1
                        Y_mat(k,k-1) = -2/(R_RHS+j*w(i)*L_RHS+R_SR+j*w(i)*L_SR);
                        Y_mat(k,k) = 2/(R_RHS+j*w(i)*L_RHS)+(j*w(i)*C_RHS+G_RHS)+...
                            2/(R_RHS+j*w(i)*L_RHS+R_SR+j*w(i)*L_SR);
                        Y_mat(k,k+1) = -2/(R_RHS+j*w(i)*L_RHS);
```

```
        else %r_pul_secs > 1
            Y_mat(k,k-1) = -1/(R_RHS+j*w(i)*L_RHS);
            Y_mat(k,k) = 3/(R_RHS+j*w(i)*L_RHS)+(j*w(i)*C_RHS+G_RHS);
            Y_mat(k,k+1) = -2/(R_RHS+j*w(i)*L_RHS);
        end;
    else %Source at far-end
        Y_mat(k,k-1) = -1/(R_SR+j*w(i)*L_SR);
        Y_mat(k,k) = 3/(R_SR+j*w(i)*L_SR)+(j*w(i)*C_SR+G_SR);
        Y_mat(k,k+1) = -2/(R_SR+j*w(i)*L_SR);
    end;
case {tot_nodes}
    %ZFE node
    if r_length ~= 0
        Y_mat(k,k) = 1/ZFE(i)+2/(R_RHS+j*w(i)*L_RHS);
        Y_mat(k,k-1) = -2/(R_RHS+j*w(i)*L_RHS);
    else %Source at far-end
        Y_mat(k,k) = 1/ZFE(i)+2/(R_SR+j*w(i)*L_SR);
        Y_mat(k,k-1) = -2/(R_SR+j*w(i)*L_SR);
    end;
case {t_node1}
    %LHS transition node 1
    Y_mat(k,k-1) = -1/(R_LHS+j*w(i)*L_LHS);
    Y_mat(k,k) = 1/(R_LHS+j*w(i)*L_LHS)+(j*w(i)*C_LHS+G_LHS)+...
        2/(R_LHS+j*w(i)*L_LHS+R_SR+j*w(i)*L_SR);
    Y_mat(k,k+1) = -2/(R_LHS+j*w(i)*L_LHS+R_SR+j*w(i)*L_SR);
case {t_node1+1}
    %LHS transition node 2
    if s_pul_secs == 1
        Y_mat(k,k-1) = -2/(R_LHS+j*w(i)*L_LHS+R_SR+j*w(i)*L_SR);
        Y_mat(k,k) = 2/(R_LHS+j*w(i)*L_LHS+R_SR+j*w(i)*L_SR)+...
            (j*w(i)*C_SR+G_SR)+...
            2/(R_SR+j*w(i)*L_SR+R_RHS+j*w(i)*L_RHS);
        Y_mat(k,k+1) = -2/(R_SR+j*w(i)*L_SR+R_RHS+j*w(i)*L_RHS);
    else
        Y_mat(k,k-1) = -2/(R_LHS+j*w(i)*L_LHS+R_SR+j*w(i)*L_SR);
        Y_mat(k,k) = 1/(R_SR+j*w(i)*L_SR)+(j*w(i)*C_SR+G_SR)+...
            2/(R_LHS+j*w(i)*L_LHS+R_SR+j*w(i)*L_SR);
        Y_mat(k,k+1) = -1/(R_SR+j*w(i)*L_SR);
    end;
case {t_node2}
    %RHS transition node 2
    Y_mat(k,k-1) = -1/(R_SR+j*w(i)*L_SR);
    Y_mat(k,k) = 1/(R_SR+j*w(i)*L_SR)+(j*w(i)*C_SR+G_SR)+...
        2/(R_RHS+j*w(i)*L_RHS+R_SR+j*w(i)*L_SR);
    Y_mat(k,k+1) = -2/(R_RHS+j*w(i)*L_RHS+R_SR+j*w(i)*L_SR);
case {t_node2+1}
    %RHS transition node 1
    Y_mat(k,k-1) = -2/(R_RHS+j*w(i)*L_RHS+R_SR+j*w(i)*L_SR);
    Y_mat(k,k) = 1/(R_RHS+j*w(i)*L_RHS)+(j*w(i)*C_RHS+G_RHS)+...
        2/(R_RHS+j*w(i)*L_RHS+R_SR+j*w(i)*L_SR);
    Y_mat(k,k+1) = -1/(R_RHS+j*w(i)*L_RHS);
otherwise
    %Internal loops
    if k < t_node1
        %LHS loops
        Ctemp = C_LHS;
```

```
               Ltemp = L_LHS;
               Rtemp = R_LHS;
               Gtemp = G_LHS;
            elseif k > t_node2
               %RHS loops
               Ctemp = C_RHS;
               Ltemp = L_RHS;
               Rtemp = R_RHS;
               Gtemp = G_RHS;
            else
               %Source region loops
               Ctemp = C_SR;
               Ltemp = L_SR;
               Rtemp = R_SR;
               Gtemp = G_SR;
            end;
            Y_mat(k,k-1) = -1/(Rtemp+j*w(i)*Ltemp);
            Y_mat(k,k) = 2/(Rtemp+j*w(i)*Ltemp)+(j*w(i)*Ctemp+Gtemp);
            Y_mat(k,k+1) = -1/(Rtemp+j*w(i)*Ltemp);
      end;
   end;
   %Solve for the voltages
   V_mat(i,:) =(Y_mat^(-1))*I_mat;
   clear Ctemp Ltemp Rtemp Gtemp;
end;

%Most of the voltages are specified internal to the cells rather than end
%points. Need to calculate the cell edge voltages and currents. The number
%of internally solved cell voltages are given by the variables containing
%the number of LHS, SR, and RHS sections.

Z_mat_full = zeros(length(f),(tot_nodes-3));
Z_mat_half = zeros(length(f),(tot_nodes-3));

%Fill impedance matrices showing the impedance between solved internal
%voltage nodes
for k = 1:tot_nodes-3
   if k <= l_pul_secs
      if k ~= l_pul_secs
         %Node internal to a LHS section
         Z_mat_full(:,k) = R_LHS+j*w*L_LHS;
         Z_mat_half(:,k) = (R_LHS+j*w*L_LHS)/2;
      else
         %Node between LHS and SR
         Z_mat_full(:,k) = (R_LHS+j*w*L_LHS)/2+(R_SR+j*w*L_SR)/2;
         Z_mat_half(:,k) = (R_LHS+j*w*L_LHS)/2;
      end;
   elseif k <= l_pul_secs+s_pul_secs
      if k ~= l_pul_secs+s_pul_secs
         %Node internal to a SR section
         Z_mat_full(:,k) = R_SR+j*w*L_SR;
         Z_mat_half(:,k) = (R_SR+j*w*L_SR)/2;
      else
         %Node between SR and RHS
         Z_mat_full(:,k) = (R_SR+j*w*L_SR)/2+(R_RHS+j*w*L_RHS)/2;
         Z_mat_half(:,k) = (R_SR+j*w*L_SR)/2;
```

```
        end;
    else %Node internal to a RHS section
        Z_mat_full(:,k) = R_RHS+j*w*L_RHS;
        Z_mat_half(:,k) = (R_RHS+j*w*L_RHS)/2;
    end;
end;
%Calculate the internal currents and load currents
I_node_mat = zeros(length(f),tot_nodes-1);
I_node_mat(:,2:(tot_nodes-2)) = ...
    (V_mat(:,2:(tot_nodes-2))-V_mat(:,3:(tot_nodes-1)))./Z_mat_full;
I_node_mat(:,1) = -V_mat(:,1)./ZNE;
I_node_mat(:,tot_nodes-1) = V_mat(:,tot_nodes)./ZFE;
%Calculate the internal voltages and fill in load voltages
V_node_mat = zeros(length(f),tot_nodes-1);
V_node_mat(:,2:(tot_nodes-2)) = ...
    V_mat(:,2:(tot_nodes-2))-I_node_mat(:,2:(tot_nodes-2)).*Z_mat_half;
V_node_mat(:,1) = V_mat(:,1);
V_node_mat(:,tot_nodes-1) = V_mat(:,tot_nodes);

%Define Analytical Expressions - Distributed Uniform Noise Source
xLHS = x_KVL_LHS; %Position vector for LHS of circuit (m)
xRHS = x_KVL_RHS; %Position vector for RHS of circuit (m)
xSR = x_KVL_SR; %Position vector for the SR of circuit (m)
VLHS = zeros(length(f),length(xLHS)); %Initialize VLHS matrix to zeros
VRHS = zeros(length(f),length(xRHS)); %Initialize VRHS matrix to zeros
VSR = zeros(length(f),length(xSR)); %Initialize VSR matrix to zeros
%Define Equivalent Noise Current
%This quantity is defined in case the analytical expression for a uniform
%source is to be compared with a simulation where the sources are not
%uniform. The middle value or the equivalent middle value in the source
%region is used for the equivalent noise current.
if size(In,2)-(floor(size(In,2)/2)*2) == 1
    %Position matrix is odd - take the middle value for all frequencies
    In_eq = In(:,(floor(size(In,2)/2)+1));
else %Position matrix is even - find average equivalent middle value
    In_eq = mean([In(:,floor(size(In,2)/2)) In(:,(floor(size(In,2)/2)+1))],2);
end;

%Find the Voltage on the TL outside the coupling region
for i = 1:length(xRHS)
    VRHS(:,i) = (In_eq.*Z0v./(2*gamma_v)).*(1./(1-G_NE.*G_FE.*exp(-2*gamma_v*Lv))).*...
        ((1-G_NE.*exp(-2*gamma_v*(Lv-abs(x0R)))).*...
        (1+G_FE.*exp(2*gamma_v*xRHS(i))).*exp(-gamma_v*(xRHS(i)+abs(x0R)))-...
        (1-G_NE.*exp(-2*gamma_v*(Lv-abs(x0L)))).*...
        (1+G_FE.*exp(2*gamma_v*xRHS(i))).*exp(-gamma_v*(xRHS(i)+abs(x0L))));
end;
for i = 1:length(xLHS)
    VLHS(:,i) = (In_eq.*Z0v./(2*gamma_v)).*(1./(1-G_NE.*G_FE.*exp(-2*gamma_v*Lv))).*...
        ((1+G_NE.*exp(-2*gamma_v*(Lv+xLHS(i)))).*...
        (-1+G_FE.*exp(-2*gamma_v*abs(x0R))).*exp(gamma_v*(xLHS(i)+abs(x0R)))-...
        (1+G_NE.*exp(-2*gamma_v*(Lv+xLHS(i)))).*...
        (-1+G_FE.*exp(-2*gamma_v*abs(x0L))).*exp(gamma_v*(xLHS(i)+abs(x0L))));
end;
%Find the voltage on the TL inside the coupling region
for i = 1:length(xSR)
    VSR(:,i) = (In_eq.*Z0v./(2*gamma_v)).*(1./(1-G_NE.*G_FE.*exp(-2*gamma_v*Lv))).*...
```

```
        ((1+G_NE.*exp(-2*gamma_v*(Lv+xSR(i)))).*...
        (-1+G_FE.*exp(-2*gamma_v*abs(x0R))).*exp(gamma_v*(xSR(i)+abs(x0R)))-...
        (1-G_NE.*exp(-2*gamma_v*(Lv-abs(x0L)))).*...
        (1+G_FE.*exp(2*gamma_v*xSR(i))).*exp(-gamma_v*(xSR(i)+abs(x0L)))+...
        2*(1-G_NE.*G_FE.*exp(-2*gamma_v*Lv)));
end;

xAnal = horzcat(xLHS,xSR(2:(length(xSR)-1)),xRHS);
VTOT = horzcat(VLHS,VSR(:,(2:(length(xSR)-1))),VRHS);

%Compare the Analytical Results to the Simulation Results
%Subplots may be useful here
%    Top Plot - Coupling Voltage Waveform in the coupling region
%    Bottom Plot - Voltage along the victim TL

figure;
subplot(2,1,1);
plot(x_KVL_SR_mid,abs(In(1,:)),...
    x_KVL_SR_mid,ones(1,length(x_KVL_SR_mid))*abs(In_eq(1)),'-r');
title('Low Frequency Response - Noise Current Waveform');
ylabel('|I|');
legend('Actual Noise Source','Approximated Noise Source','Location','Best');
xlim([xLHS(1) xRHS(length(xRHS))]);
subplot(2,1,2);
plot(xAnal,abs(VTOT(1,:)),x_KVL,abs(V_node_mat(1,:)),'r');
title('Low Frequency Response - Victim Voltage Waveform');
xlabel('TL Position (m)');
ylabel('|V|');
legend('Analytical','Simulation','Location','Best');

figure;
subplot(2,1,1);
plot(x_KVL_SR_mid,abs(In(floor(length(f)/2),:)),...
    x_KVL_SR_mid,ones(1,length(x_KVL_SR_mid))*abs(In_eq(floor(length(f)/2))),'-r');
title('Middle Frequency Response - Noise Current Waveform');
ylabel('|I|');
legend('Actual Noise Source','Approximated Noise Source','Location','Best');
xlim([xLHS(1) xRHS(length(xRHS))]);
subplot(2,1,2);
plot(xAnal,abs(VTOT(floor(length(f)/2),:)),...
    x_KVL,abs(V_node_mat(floor(length(f)/2),:)),'r');
title('Middle Frequency Response - Victim Voltage Waveform');
xlabel('TL Position (m)');
ylabel('|V|');
legend('Analytical','Simulation','Location','Best');

figure;
subplot(2,1,1);
plot(x_KVL_SR_mid,abs(In(length(f),:)),...
    x_KVL_SR_mid,ones(1,length(x_KVL_SR_mid))*abs(In_eq(length(f))),'-r');
title('High Frequency Response - Noise Current Waveform');
ylabel('|I|');
legend('Actual Noise Source','Approximated Noise Source','Location','Best');
xlim([xLHS(1) xRHS(length(xRHS))]);
subplot(2,1,2);
plot(xAnal,abs(VTOT(length(f),:)),x_KVL,abs(V_node_mat(length(f),:)),'r');
```

```
title('High Frequency Response - Victim Voltage Waveform');
xlabel('TL Position (m)');
ylabel('|V|');
legend('Analytical','Simulation','Location','Best');

%Look at phase
% figure;
% plot(xAnal,angle(VTOT(1,:)),x_KVL,angle(V_node_mat(1,:)),'r');
% xlabel('TL Position (m)');
% ylabel('angle(V)');
% title('Low Frequency Response');
% legend('Analytical','Simulation','Location','Best');
%
% figure;
% plot(xAnal,angle(VTOT(floor(length(f)/2),:)),...
%     x_KVL,angle(V_node_mat(floor(length(f)/2),:)),'r');
% xlabel('TL Position (m)');
% ylabel('angle(V)');
% title('Middle Frequency Response');
% legend('Analytical','Simulation','Location','Best');
%
% figure;
% plot(xAnal,angle(VTOT(length(f),:)),x_KVL,angle(V_node_mat(length(f),:)),'r');
% xlabel('TL Position (m)');
% ylabel('angle(V)');
% title('High Frequency Response');
% legend('Analytical','Simulation','Location','Best');

%Plot movie for comparing the Analytical Results to the Simulation Results
figure;
for k = 1:length(f)
   subplot(2,1,1);
   plot(x_KVL_SR_mid,abs(In(k,:)),...
      x_KVL_SR_mid,ones(1,length(x_KVL_SR_mid))*abs(In_eq(k)),'-r');
   title(strcat(['Noise Current Waveform @ ' num2str(f(k)) ' Hz']));
   ylabel('|I|');
   legend('Actual Noise Source','Approximated Noise Source','Location','Best');
   xlim([xLHS(1) xRHS(length(xRHS))]);
   subplot(2,1,2);
   plot(xAnal,abs(VTOT(k,:)),x_KVL,abs(V_node_mat(k,:)),'r');
   title(strcat(['Victim Voltage Waveform @ ' num2str(f(k)) ' Hz']));
   xlabel('TL Position (m)');
   ylabel('|V|');
   legend('Analytical','Simulation','Location','Best');
   pause(0.01);
end;
```

Matlab File “Lossy_TL_Non_Uniform_Distributed_V2.m”

```
clear all;
close all;
clc;

%This simulation calculates the voltage and current on a transmission line
%where a non-uniform distributed voltage source is placed anywhere along the
%line. The transmission line can be lossless or lossy. The distributed
%voltage source is considered to be non-uniform. Analytical expressions for
%comparison purposes with the simulation are given for the non-uniform
%noise source case.

%Assumptions
%1. Weak Coupling
%2. Culprit and Victim propagation parameter gamma must be the same
%3. Characteristic impedance is approximately uniform in the victim

%Simulation cases for lossy - distortionless line (R/L = G/C)
%Define Victim PUL Parameters
C_pul = 100e-12; %F/m
L_pul = 250e-9; %H/m
R_pul = 100;%4; %Ohm/m 100
G_pul = 2e-8;%2e-10; %S/m 2e-8
%Define Coupling PUL Parameters
L21 = 100e-9; %H/m
R21 = 1; %Ohm/m
%Define Propagation Parameters
f = (1e6:10e6:1e9)'; %Frequency range simulation (Hz)
w = 2*pi*f;
gamma_v = sqrt((R_pul+j*w*L_pul).*(G_pul+j*w*C_pul)); %Propagation parameter
alpha = real(gamma_v); %Loss (Np/m) [interesting when = 1]
B = imag(gamma_v); %Beta
Vp = w./B; %Phase velocity (m/s)
Z0v = sqrt((R_pul+j*w*L_pul)./(G_pul+j*w*C_pul)); %TL characteristic impedance (Ohm)
lambda_min = min(Vp./f); %Smallest wavelength (m)
j = sqrt(-1);
%Victim Geometry Parameters
Lv = 1; %Line length (m)
x0L = -0.6; %Distributed source left boundary (make this a negative number) (m)
x0R = -0.3; %Distributed source right boundary (make this a negative number) (m)
l_length = x0L+Lv; %TL length left of source (m)
r_length = -x0R; %TL length right of source (m)
s_length = x0R-x0L; %Distributed source length (m)
%Victim Load Parameters
ZFE = 75+(1./(j*w*(5e-12))).*ones(length(f),1); %Far-end Load Definition
ZNE = 45+j*w*(10e-9).*ones(length(f),1); %Near-end Load Definition (Ohm)
G_NE = (ZNE-Z0v)./(ZNE+Z0v); %Reflection coefficient at the near-end
G_FE = (ZFE-Z0v)./(ZFE+Z0v); %Reflection coefficient at the far-end

%Culprit Geometry Parameters
%Define Culprit PUL Parameters
C_pul_c = C_pul; %F/m
L_pul_c = L_pul; %H/m -(gamma_v.^2)./((w.^2)*C_pul_c)
R_pul_c = R_pul;%4; %Ohm/m
G_pul_c = G_pul;%2e-10; %S/m
```

```
gamma_c = sqrt((R_pul_c+j*w.*L_pul_c).*(G_pul_c+j*w*C_pul_c)); %Propagation parameter
Z0c = sqrt((R_pul_c+j*w.*L_pul_c)./(G_pul_c+j*w*C_pul_c)); %TL characteristic impedance (Ohm)

Vs = 100; %Source voltage (V)
a = 1.2; %RHS position variable (usually positive) (m) 1.2
b = 1.5; %LHS position variable (usually positive) (m) 1.5
Lc = a+b; %Culprit circuit length (m)

ZS_CP = 30+j*w*(100e-9).*ones(length(f),1); %Source Load Defintion (Ohm)
ZL_CP = 75+(1./(j*w*(30e-12))).*ones(length(f),1); %Culprit Load Definition (Ohm)
G_ZS = (ZS_CP-Z0c)./(ZS_CP+Z0c); %Reflection coefficient at the culprit near-end
G_ZL = (ZL_CP-Z0c)./(ZL_CP+Z0c); %Reflection coefficient at the culprit far-end

%Define Coupling Coordinate Extremes on the Culprit Circuit Axis
x_CP_ends = [x0L x0R]; %Same coordinate system as the victim

%Set up TL KVL Circuit Simulation
%For a good simulation, each PUL section must be no larger than lambda/20
%in length.
pul_length = lambda_min/40; %Target PUL section length
%Must have an integer number of TL sections, so the actual pul_length
%sections for the left hand side, distributed source region, and right hand
%sides of the TL problem may not be at the same spacing.

%Determine LHS victim circuit properties
l_pul_secs = ceil(l_length/pul_length); %Number of pul sections LHS represents
if l_length == 0
   l_pul_length = 0;
else %Finite section length
   l_pul_length = l_length/l_pul_secs; %LHS pul section length
end;
C_LHS = C_pul*l_pul_length;
L_LHS = L_pul*l_pul_length;
R_LHS = R_pul*l_pul_length;
G_LHS = G_pul*l_pul_length;

%Determine source region victim circuit properties
s_pul_secs = ceil(s_length/pul_length); %Number of pul sections source region represents
if s_length == 0
   s_pul_length = 0;
else %Finite section length
   s_pul_length = s_length/s_pul_secs; %Source region pul section length
end;
C_SR = C_pul*s_pul_length;
L_SR = L_pul*s_pul_length;
R_SR = R_pul*s_pul_length;
G_SR = G_pul*s_pul_length;

%Determine RHS victim circuit properties
r_pul_secs = ceil(r_length/pul_length); %Number of pul sections LHS represents
if r_length == 0
   r_pul_length = 0;
else %Finite section length
   r_pul_length = r_length/r_pul_secs; %RHS pul section length
end;
C_RHS = C_pul*r_pul_length;
```

```
L_RHS = L_pul*r_pul_length;
R_RHS = R_pul*r_pul_length;
G_RHS = G_pul*r_pul_length;

%Create victim position vectors
if l_pul_length ~= 0
    x_KVL_LHS = -Lv+(0:l_pul_length:(l_pul_length*l_pul_secs));
else %Source at near-end
    x_KVL_LHS = -Lv;
end;
if s_pul_length ~= 0
    x_KVL_SR = x_KVL_LHS(length(x_KVL_LHS))+...
        (0:s_pul_length:(s_pul_length*s_pul_secs));
else %No source region
end;
if r_pul_length ~= 0
    x_KVL_RHS = -r_length+(0:r_pul_length:(r_pul_length*r_pul_secs));
else %Source at far-end
    x_KVL_RHS = 0;
end;
if s_pul_length ~= 0
    x_KVL = horzcat(x_KVL_LHS,x_KVL_SR(2:length(x_KVL_SR)),...
        x_KVL_RHS(2:length(x_KVL_RHS)));
    % clear x_KVL_LHS x_KVL_SR x_KVL_RHS;
else %No source region
    x_KVL = horzcat(x_KVL_LHS,x_KVL_RHS(2:length(x_KVL_RHS)));
    % clear x_KVL_LHS x_KVL_RHS;
end;

%Create culprit position vector
x_CP_source = x_CP_ends(1):s_pul_length:x_CP_ends(2);
%The above position matrix is offset by a half cell and has one more
%position than desired. A position vector is desired in the middle of the
%cells since this is where the source value will be evaluated. Fixing the
%position matrix:
x_CP_source(length(x_CP_source)) = []; %Delete last value
x_CP_source = x_CP_source+s_pul_length/2; %Positions placed in the middle of the cells
%Create equivlant position matrix in the victim circuit
x_KVL_SR_mid = x_KVL_SR(1:(length(x_KVL_SR)-1))+(s_pul_length/2);
%Formulate the noise voltage source
%Vn = -(R21+j*w*L21)*I(x) <- A function of frequency and space
Vn = zeros(length(f),length(x_CP_source));
%Fill noise voltage matrix in continuous domain (V/m)
for i = 1:length(f)
    Vn(i,:) = -(R21+j*w(i)*L21)*(Vs*exp(-gamma_c(i)*Lc)*...
        (exp(-gamma_c(i)*(x_CP_source-a))-G_ZL(i)*exp(gamma_c(i)*(x_CP_source-a)))./...
        ((Z0c(i)+ZS_CP(i)).*(1-G_ZL(i)*G_ZS(i)*exp(-2*gamma_c(i)*Lc))));
end;
%Define Distributed Source Voltage in the Discrete Domain
V_SR = Vn*s_pul_length;

%Determine Source Region Transition Loops
t_loop1 = l_pul_secs+1; %First transition loop number
t_loop2 = l_pul_secs+s_pul_secs+1; %Second transition loop number
tot_loops = l_pul_secs+s_pul_secs+r_pul_secs+1; %Total number of KVL loops to solve
Z_mat = zeros(tot_loops,tot_loops); %Initiailize impedance matrix
```

```
%Create voltage matrix
V_mat = zeros(tot_loops,1); %Initialize voltage matrix to zeros

%Create current matrix
I_mat = zeros(length(f),tot_loops); %Initialize current matrix to zeros

%Setup KVL Matrix to solve
for i = 1:length(f)
    %Insert source voltages
    if t_loop1 ~= t_loop2
        V_mat(t_loop1) = V_SR(i,1)/2; %Transition loop 1
        V_mat(t_loop2) = V_SR(i,s_pul_secs)/2; %Transition loop 2
        V_mat((t_loop1+1):(t_loop2-1)) = V_SR(i,1:(s_pul_secs-1))/2+...
            V_SR(i,2:s_pul_secs)/2; %Source region loops
    else
    end;
    %Fill Impedance Matrix for each frequency
    for k = 1:tot_loops
        switch k
            case {1}
                %ZNE loop
                if l_length ~= 0
                    Z_mat(k,k) = ZNE(i)+(R_LHS+j*w(i)*L_LHS)/2+...
                        1/(j*w(i)*C_LHS+G_LHS);
                    Z_mat(k,k+1) = -1/(j*w(i)*C_LHS+G_LHS);
                else %Source at near-end
                    Z_mat(k,k) = ZNE(i)+(R_SR+j*w(i)*L_SR)/2+...
                        1/(j*w(i)*C_SR+G_SR);
                    Z_mat(k,k+1) = -1/(j*w(i)*C_SR+G_SR);
                end;
            case {tot_loops}
                %ZFE loop
                if r_length ~= 0
                    Z_mat(k,k) = ZFE(i)+(R_RHS+j*w(i)*L_RHS)/2+...
                        1/(j*w(i)*C_RHS+G_RHS);
                    Z_mat(k,k-1) = -1/(j*w(i)*C_RHS+G_RHS);
                else %Source at far-end
                    Z_mat(k,k) = ZFE(i)+(R_SR+j*w(i)*L_SR)/2+...
                        1/(j*w(i)*C_SR+G_SR);
                    Z_mat(k,k-1) = -1/(j*w(i)*C_SR+G_SR);
                end;
            case {t_loop1}
                %LHS transition loop
                Z_mat(k,k-1) = -1/(j*w(i)*C_LHS+G_LHS);
                Z_mat(k,k) = 1/(j*w(i)*C_LHS+G_LHS)+(R_LHS+j*w(i)*L_LHS)/2+...
                    1/(j*w(i)*C_SR+G_SR)+(R_SR+j*w(i)*L_SR)/2;
                Z_mat(k,k+1) = -1/(j*w(i)*C_SR+G_SR);
            case {t_loop2}
                %RHS transition loop
                Z_mat(k,k-1) = -1/(j*w(i)*C_SR+G_SR);
                Z_mat(k,k) = 1/(j*w(i)*C_RHS+G_RHS)+(R_RHS+j*w(i)*L_RHS)/2+...
                    1/(j*w(i)*C_SR+G_SR)+(R_SR+j*w(i)*L_SR)/2;
                Z_mat(k,k+1) = -1/(j*w(i)*C_RHS+G_RHS);
            otherwise
                %Internal loops
```

```
            if k < t_loop1
                %LHS loops
                Ctemp = C_LHS;
                Ltemp = L_LHS;
                Rtemp = R_LHS;
                Gtemp = G_LHS;
            elseif k > t_loop2
                %RHS loops
                Ctemp = C_RHS;
                Ltemp = L_RHS;
                Rtemp = R_RHS;
                Gtemp = G_RHS;
            else
                %Source region loops
                Ctemp = C_SR;
                Ltemp = L_SR;
                Rtemp = R_SR;
                Gtemp = G_SR;
            end;
            Z_mat(k,k-1) = -1/(j*w(i)*Ctemp+Gtemp);
            Z_mat(k,k) = 2/(j*w(i)*Ctemp+Gtemp)+Rtemp+j*w(i)*Ltemp;
            Z_mat(k,k+1) = -1/(j*w(i)*Ctemp+Gtemp);
        end;
    end;
    %Solve for the currents
    I_mat(i,:) =( Z_mat^(-1))*V_mat;
    clear Ctemp Ltemp Rtemp Gtemp;
end;

%Find voltages
V_node_mat = zeros(length(f),tot_loops); %Initialize voltage matrix to zeros
%Solve voltages at each node
for k = 1:tot_loops
    switch k
        case {1}
            %ZNE node
            V_node_mat(:,k) = -ZNE.*I_mat(:,k);
        case {tot_loops}
            %ZFE node
            V_node_mat(:,k) = ZFE.*I_mat(:,k);
        otherwise
            %Internal nodes
            if k <= t_loop1
                Ctemp = C_LHS;
                Ltemp = L_LHS;
                Rtemp = R_LHS;
                Gtemp = G_LHS;
                V_node_mat(:,k) = (1./(j*w*Ctemp+Gtemp)).*I_mat(:,k-1)-...
                    (1./(j*w*Ctemp+Gtemp)+(Rtemp+j*w*Ltemp)/2).*I_mat(:,k);
            elseif k > t_loop2
                Ctemp = C_RHS;
                Ltemp = L_RHS;
                Rtemp = R_RHS;
                Gtemp = G_RHS;
                V_node_mat(:,k) = (1./(j*w*Ctemp+Gtemp)).*I_mat(:,k-1)-...
                    (1./(j*w*Ctemp+Gtemp)+(Rtemp+j*w*Ltemp)/2).*I_mat(:,k);
```

```
            else %In source region
                Ctemp = C_SR;
                Ltemp = L_SR;
                Rtemp = R_SR;
                Gtemp = G_SR;
                V_node_mat(:,k) = (1./(j*w*Ctemp+Gtemp)).*I_mat(:,k-1)-...
                    (1./(j*w*Ctemp+Gtemp)+(Rtemp+j*w*Ltemp)/2).*I_mat(:,k)+...
                    V_SR(:,(k-t_loop1))/2;
            end;
    end;
end;
clear Ctemp Ltemp Rtemp Gtemp;

%Define Analytical Expressions - Distributed Non-Uniform Noise Source
xLHS = x_KVL_LHS; %Position vector for LHS of circuit (m)
xRHS = x_KVL_RHS; %Position vector for RHS of circuit (m)
xSR = x_KVL_SR; %Position vector for the SR of circuit (m)
VLHS = zeros(length(f),length(xLHS)); %Initialize VLHS matrix to zeros
VRHS = zeros(length(f),length(xRHS)); %Initialize VRHS matrix to zeros
VSR = zeros(length(f),length(xSR)); %Initialize VSR matrix to zeros
%Define Equivalent Noise Voltage
%This quantity is defined in case the analytical expression for a uniform
%source is to be compared with a simulation where the sources are not
%uniform. The middle value or the equivalent middle value in the source
%region is used for the equivalent noise voltage.
if size(Vn,2)-(floor(size(Vn,2)/2)*2) == 1
    %Position matrix is odd - take the middle value for all frequencies
    Vn_eq = Vn(:,(floor(size(Vn,2)/2)+1));
else %Position matrix is even - find average equivalent middle value
    Vn_eq = mean([Vn(:,floor(size(Vn,2)/2)) Vn(:,(floor(size(Vn,2)/2)+1))],2);
end;

%Find the Voltage on the TL outside the coupling region
%Non-uniform Analytical Equation
for i = 1:length(xRHS)
    VRHS(:,i) = (-(R21+j*w*L21).*(Vs*exp(-gamma_c*Lc)./...
        ((Z0c+ZS_CP).*(1-G_ZL.*G_ZS.*exp(-2*gamma_c*Lc))))*...
        (1/2).*(1./(1-G_NE.*G_FE.*exp(-2*gamma_v*Lv)))).*...
        (((abs(x0L)-abs(x0R))*(1+G_ZL.*G_NE.*exp(-2*gamma_v*(a+Lv)))+...
        (1./(2*gamma_v)).*(G_ZL.*exp(-2*gamma_v*(abs(x0L)+abs(x0R)+a))+...
        G_NE.*exp(-2*gamma_v*Lv)).*(exp(2*gamma_v*abs(x0R))-exp(2*gamma_v*abs(x0L)))).*...
        exp(gamma_c*a).*(exp(-gamma_c*xRHS(i))+G_FE.*exp(gamma_c*xRHS(i))));
end;
%Non-uniform Analytical Equation
for i = 1:length(xLHS)
    VLHS(:,i) = (-(R21+j*w*L21).*(Vs*exp(-gamma_c*Lc)./...
        ((Z0c+ZS_CP).*(1-G_ZL.*G_ZS.*exp(-2*gamma_c*Lc))))*...
        (1/2).*(1./(1-G_NE.*G_FE.*exp(-2*gamma_v*Lv)))).*...
        (((abs(x0L)-abs(x0R))*(G_FE+G_ZL.*exp(-2*gamma_c*a))+...
        (1./(2*gamma_v)).*(1+G_ZL.*G_FE.*exp(-2*gamma_v*(abs(x0L)+abs(x0R)+a))).*...
        (exp(2*gamma_v*abs(x0R))-exp(2*gamma_v*abs(x0L)))).*...
        exp(gamma_c*a).*(G_NE.*exp(-gamma_c*(xLHS(i)+2*Lv))+exp(gamma_c*xLHS(i))));
end;
%Find the voltage on the TL inside the coupling region
%Non-uniform Analytical Equation
for i = 1:length(xSR)
```

```
    VSR(:,i) = (-(R21+j*w*L21).*(Vs*exp(-gamma_c*Lc)./...
        ((Z0c+ZS_CP).*(1-G_ZL.*G_ZS.*exp(-2*gamma_c*Lc))))*...
        (1/2).*(1./(1-G_NE.*G_FE.*exp(-2*gamma_v*Lv)))).*(...
        (((abs(x0L)+xSR(i))*(1+G_ZL.*G_NE.*exp(-2*gamma_v*(Lv+a)))+... %RHS portion
        (1./(2*gamma_v)).*(G_ZL.*exp(2*gamma_v*(xSR(i)-abs(x0L)-a))+...
        G_NE.*exp(-2*gamma_v*Lv)).*(exp(-2*gamma_v*xSR(i))-exp(2*gamma_v*abs(x0L)))).*...
        exp(gamma_c*a).*(exp(-gamma_c*xSR(i))+G_FE.*exp(gamma_c*xSR(i))))+...
        ((-(xSR(i)+abs(x0R))*(G_FE+G_ZL.*exp(-2*gamma_c*a))+... %LHS portion
        (1./(2*gamma_v)).*(1+G_ZL.*G_FE.*exp(2*gamma_v*(xSR(i)-abs(x0R)-a))).*...
        (exp(2*gamma_v*abs(x0R))-exp(-2*gamma_v*xSR(i)))).*...
        exp(gamma_c*a).*(G_NE.*exp(-gamma_c*(xSR(i)+2*Lv))+exp(gamma_c*xSR(i)))));
end;

xAnal = horzcat(xLHS,xSR(2:(length(xSR)-1)),xRHS);
VTOT = horzcat(VLHS,VSR(:,(2:(length(xSR)-1))),VRHS);

%Compare the Analytical Results to the Simulation Results
%Subplots may be useful here
%    Top Plot - Coupling Voltage Waveform in the coupling region
%    Bottom Plot - Voltage along the victim TL

figure;
subplot(2,1,1);
plot(x_KVL_SR_mid,abs(Vn(1,:)),...
    x_KVL_SR_mid,ones(1,length(x_KVL_SR_mid))*abs(Vn_eq(1)),'-r');
title('Low Frequency Response - Noise Voltage Waveform');
ylabel('|V|');
legend('Actual Noise Source','Approximated Noise Source','Location','Best');
xlim([xLHS(1) xRHS(length(xRHS))]);
subplot(2,1,2);
plot(xAnal,abs(VTOT(1,:)),x_KVL,abs(V_node_mat(1,:)),'r');
title('Low Frequency Response - Victim Voltage Waveform');
xlabel('TL Position (m)');
ylabel('|V|');
legend('Analytical','Simulation','Location','Best');

figure;
subplot(2,1,1);
plot(x_KVL_SR_mid,abs(Vn(floor(length(f)/2),:)),...
    x_KVL_SR_mid,ones(1,length(x_KVL_SR_mid))*abs(Vn_eq(floor(length(f)/2))),'-r');
title('Middle Frequency Response - Noise Voltage Waveform');
ylabel('|V|');
legend('Actual Noise Source','Approximated Noise Source','Location','Best');
xlim([xLHS(1) xRHS(length(xRHS))]);
subplot(2,1,2);
plot(xAnal,abs(VTOT(floor(length(f)/2),:)),...
    x_KVL,abs(V_node_mat(floor(length(f)/2),:)),'r');
title('Middle Frequency Response - Victim Voltage Waveform');
xlabel('TL Position (m)');
ylabel('|V|');
legend('Analytical','Simulation','Location','Best');

figure;
subplot(2,1,1);
plot(x_KVL_SR_mid,abs(Vn(length(f),:)),...
    x_KVL_SR_mid,ones(1,length(x_KVL_SR_mid))*abs(Vn_eq(length(f))),'-r');
```

```
title('High Frequency Response - Noise Voltage Waveform');
ylabel('|V|');
legend('Actual Noise Source','Approximated Noise Source','Location','Best');
xlim([xLHS(1) xRHS(length(xRHS))]);
subplot(2,1,2);
plot(xAnal,abs(VTOT(length(f),:)),x_KVL,abs(V_node_mat(length(f),:)),'r');
title('High Frequency Response - Victim Voltage Waveform');
xlabel('TL Position (m)');
ylabel('|V|');
legend('Analytical','Simulation','Location','Best');

%Look at phase
% % % figure;
% % % plot(xAnal,angle(VTOT(1,:)),x_KVL,angle(V_node_mat(1,:)),'r');
% % % xlabel('TL Position (m)');
% % % ylabel('angle(V)');
% % % title('Low Frequency Response');
% % % legend('Analytical','Simulation','Location','Best');
% % %
% % % figure;
% % % plot(xAnal,angle(VTOT(floor(length(f)/2),:)),...
% % %     x_KVL,angle(V_node_mat(floor(length(f)/2),:)),'r');
% % % xlabel('TL Position (m)');
% % % ylabel('angle(V)');
% % % title('Middle Frequency Response');
% % % legend('Analytical','Simulation','Location','Best');
% % %
% % % figure;
% % % plot(xAnal,angle(VTOT(length(f),:)),x_KVL,angle(V_node_mat(length(f),:)),'r');
% % % xlabel('TL Position (m)');
% % % ylabel('angle(V)');
% % % title('High Frequency Response');
% % % legend('Analytical','Simulation','Location','Best');

%Plot movie for comparing the Analytical Results to the Simulation Results
figure;
for k = 1:length(f)
   subplot(2,1,1);
   plot(x_KVL_SR_mid,abs(Vn(k,:)),...
      x_KVL_SR_mid,ones(1,length(x_KVL_SR_mid))*abs(Vn_eq(k)),'-r');
   title(strcat(['Noise Voltage Waveform @ ' num2str(f(k)) ' Hz']));
   ylabel('|V|');
   legend('Actual Noise Source','Approximated Noise Source','Location','Best');
   xlim([xLHS(1) xRHS(length(xRHS))]);
   subplot(2,1,2);
   plot(xAnal,abs(VTOT(k,:)),x_KVL,abs(V_node_mat(k,:)),'r');
   title(strcat(['Victim Voltage Waveform @ ' num2str(f(k)) ' Hz']));
   xlabel('TL Position (m)');
   ylabel('|V|');
   legend('Analytical','Simulation','Location','Best');
   pause(0.01);
end;
```

Matlab File “Lossy_TL_Non_Uniform_Distributed_I2.m”

```
clear all;
close all;
clc;

%This simulation calculates the voltage and current on a transmission line
%where a non-uniform distributed current source is placed anywhere along the
%line. The transmission line can be lossless or lossy. The distributed
%current source is considered to be non-uniform. Analytical expressions for
%comparison purposes with the simulation are given for the non-uniform
%noise source case.

%Assumptions
%1. Weak Coupling
%2. Culprit and Victim propagation parameter gamma must be the same
%3. Characteristic impedance is approximately uniform in the victim

%Simulation cases for lossy - distortionless line (R/L = G/C)
%Define Victim PUL Parameters
C_pul = 100e-12; %F/m
L_pul = 250e-9; %H/m
R_pul = 100;%4; %Ohm/m 100
G_pul = 2e-8;%2e-10; %S/m 2e-8
%Define Coupling PUL Parameters
C21 = 20e-9; %F/m
G21 = 2e-12; %S/m
%Define Propagation Parameters
f = (1e6:10e6:1e9)'; %Frequency range simulation (Hz)
w = 2*pi*f;
gamma_v = sqrt((R_pul+j*w*L_pul).*(G_pul+j*w*C_pul));
alpha = real(gamma_v); %Loss (Np/m) [interesting when = 1]
B = imag(gamma_v); %Beta
Vp = w./B; %Phase velocity (m/s)
Z0v = sqrt((R_pul+j*w*L_pul)./(G_pul+j*w*C_pul)); %TL characteristic impedance (Ohm)
lambda_min = min(Vp./f); %Smallest wavelength (m)
j = sqrt(-1);
%Victim Geometry Parameters
Lv = 1; %Line length (m)
x0L = -0.6; %Distributed source left boundary (make this a negative number) (m)
x0R = -0.3; %Distributed source right boundary (make this a negative number) (m)
l_length = x0L+Lv; %TL length left of source (m)
r_length = -x0R; %TL length right of source (m)
s_length = x0R-x0L; %Distributed source length (m)
%Victim Load Parameters
ZFE = 75+(1./(j*w*(5e-12))).*ones(length(f),1); %Far-end Load Definition (Ohm)
ZNE = 45+j*w*(10e-9).*ones(length(f),1); %Near-end Load Definition (Ohm)
G_NE = (ZNE-Z0v)./(ZNE+Z0v); %Reflection coefficient at the near-end
G_FE = (ZFE-Z0v)./(ZFE+Z0v); %Reflection coefficient at the far-end

%Culprit Geometry Parameters
%Define Culprit PUL Parameters
C_pul_c = C_pul; %F/m
L_pul_c = L_pul; %H/m -(gamma_v.^2)./((w.^2)*C_pul_c)
R_pul_c = R_pul;%4; %Ohm/m
G_pul_c = G_pul;%2e-10; %S/m
```

```
gamma_c = sqrt((R_pul_c+j*w.*L_pul_c).*(G_pul_c+j*w*C_pul_c)); %Propagation parameter
Z0c = sqrt((R_pul_c+j*w.*L_pul_c)./(G_pul_c+j*w*C_pul_c)); %TL characteristic impedance (Ohm)

Vs = 100; %Source voltage (V)
a = 1.2; %RHS position variable (usually positive) (m)
b = 1.5; %LHS position variable (usually positive) (m)
Lc = a+b; %Culprit circuit length (m)

ZS_CP = 30+j*w*(100e-9).*ones(length(f),1); %Source Load Defintion (Ohm)
ZL_CP = 75+(1./(j*w*(30e-12))).*ones(length(f),1); %Culprit Load Definition (Ohm)
G_ZS = (ZS_CP-Z0c)./(ZS_CP+Z0c); %Reflection coefficient at the culprit near-end
G_ZL = (ZL_CP-Z0c)./(ZL_CP+Z0c); %Reflection coefficient at the culprit far-end

%Define Coupling Coordinate Extremes on the Culprit Circuit Axis
x_CP_ends = [x0L x0R]; %Same coordinate system as the victim

%Set up TL KCL Circuit Simulation
%For a good simulation, each PUL section must be no larger than lambda/20
%in length.
pul_length = lambda_min/40; %Target PUL section length
%Must have an integer number of TL sections, so the actual pul_length
%sections for the left hand side, distributed source region, and right hand
%sides of the TL problem may not be at the same spacing.

%Determine LHS circuit properties
l_pul_secs = ceil(l_length/pul_length); %Number of pul sections LHS represents
if l_length == 0
   l_pul_length = 0;
else %Finite section length
   l_pul_length = l_length/l_pul_secs; %LHS pul section length
end;
C_LHS = C_pul*l_pul_length;
L_LHS = L_pul*l_pul_length;
R_LHS = R_pul*l_pul_length;
G_LHS = G_pul*l_pul_length;

%Determine source region circuit properties
s_pul_secs = ceil(s_length/pul_length); %Number of pul sections source region represents
if s_length == 0
   s_pul_length = 0;
else %Finite section length
   s_pul_length = s_length/s_pul_secs; %Source region pul section length
end;
C_SR = C_pul*s_pul_length;
L_SR = L_pul*s_pul_length;
R_SR = R_pul*s_pul_length;
G_SR = G_pul*s_pul_length;

%Determine RHS circuit properties
r_pul_secs = ceil(r_length/pul_length); %Number of pul sections LHS represents
if r_length == 0
   r_pul_length = 0;
else %Finite section length
   r_pul_length = r_length/r_pul_secs; %RHS pul section length
end;
C_RHS = C_pul*r_pul_length;
```

```
L_RHS = L_pul*r_pul_length;
R_RHS = R_pul*r_pul_length;
G_RHS = G_pul*r_pul_length;

%Create position vectors (same as if KVL equations were used)
if l_pul_length ~= 0
   x_KVL_LHS = -Lv+(0:l_pul_length:(l_pul_length*l_pul_secs));
else %Source at near-end
   x_KVL_LHS = -Lv;
end;
if s_pul_length ~= 0
   x_KVL_SR = x_KVL_LHS(length(x_KVL_LHS))+...
      (0:s_pul_length:(s_pul_length*s_pul_secs));
else %No source region
end;
if r_pul_length ~= 0
   x_KVL_RHS = -r_length+(0:r_pul_length:(r_pul_length*r_pul_secs));
else %Source at far-end
   x_KVL_RHS = 0;
end;
if s_pul_length ~= 0
   x_KVL = horzcat(x_KVL_LHS,x_KVL_SR(2:length(x_KVL_SR)),...
      x_KVL_RHS(2:length(x_KVL_RHS)));
   % clear x_KVL_LHS x_KVL_SR x_KVL_RHS;
else %No source region
   x_KVL = horzcat(x_KVL_LHS,x_KVL_RHS(2:length(x_KVL_RHS)));
   % clear x_KVL_LHS x_KVL_RHS;
end;

%Create culprit position vector
x_CP_source = x_CP_ends(1):s_pul_length:x_CP_ends(2);
%The above position matrix is offset by a half cell and has one more
%position than desired. A position vector is desired in the middle of the
%cells since this is where the source value will be evaluated. Fixing the
%position matrix:
x_CP_source(length(x_CP_source)) = []; %Delete last value
x_CP_source = x_CP_source+s_pul_length/2; %Positions placed in the middle of the cells
%Create equivlant position matrix in the victim circuit
x_KVL_SR_mid = x_KVL_SR(1:(length(x_KVL_SR)-1))+(s_pul_length/2);
%Formulate the noise current source
%In = -(G21+j*w*C21)*V(x) <- A function of frequency and space
In = zeros(length(f),length(x_CP_source));
%Fill noise current matrix in continuous domain (A/m)
for i = 1:length(f)
   In(i,:) = -(G21+j*w(i)*C21)*(Vs*Z0c(i).*exp(-gamma_c(i)*Lc)*...
      (exp(-gamma_c(i)*(x_CP_source-a))+G_ZL(i)*exp(gamma_c(i)*(x_CP_source-a)))./...
      ((Z0c(i)+ZS_CP(i)).*(1-G_ZL(i)*G_ZS(i)*exp(-2*gamma_c(i)*Lc))));
end;
%Define Distributed Source Current in the Discrete Domain
I_SR = In*s_pul_length;

%Determine Source Region Transition Nodes
t_node1 = l_pul_secs+1; %First transition node equation (LHS)
t_node2 = l_pul_secs+s_pul_secs+1; %Second transition node equation (RHS)
tot_nodes = l_pul_secs+s_pul_secs+r_pul_secs+2; %Total number of KCL equations to solve
Y_mat = zeros(tot_nodes,tot_nodes); %Initiailize impedance matrix
```

```
%Create current matrix (YV = I)
I_mat = zeros(tot_nodes,1); %Initialize current matrix to zeros

%Create voltage matrix
V_mat = zeros(length(f),tot_nodes); %Initialize voltage matrix to zeros

%Setup KCL Matrix to solve (YV = I)
for i = 1:length(f)
   %Insert source currents
   if t_node1 ~= t_node2
      I_mat((t_node1+1):(t_node2)) = I_SR(i,:); %Source region nodes
   else
   end;
   %Fill Admitance Matrix for each frequency
   for k = 1:tot_nodes
      switch k
         case {1}
            %ZNE node
            if l_length ~= 0
               Y_mat(k,k) = 1/ZNE(i)+2/(R_LHS+j*w(i)*L_LHS);
               Y_mat(k,k+1) = -2/(R_LHS+j*w(i)*L_LHS);
            else %Source at near-end
               Y_mat(k,k) = 1/ZNE(i)+2/(R_SR+j*w(i)*L_SR);
               Y_mat(k,k+1) = -2/(R_SR+j*w(i)*L_SR);
            end;
         case {2}
            if l_length ~= 0
               if l_pul_secs == 1
                  Y_mat(k,k-1) = -2/(R_LHS+j*w(i)*L_LHS);
                  Y_mat(k,k) = 2/(R_LHS+j*w(i)*L_LHS)+(j*w(i)*C_LHS+G_LHS)+...
                     2/(R_LHS+j*w(i)*L_LHS+R_SR+j*w(i)*L_SR);
                  Y_mat(k,k+1) = -2/(R_LHS+j*w(i)*L_LHS+R_SR+j*w(i)*L_SR);
               else %l_pul_secs > 1
                  Y_mat(k,k-1) = -2/(R_LHS+j*w(i)*L_LHS);
                  Y_mat(k,k) = 3/(R_LHS+j*w(i)*L_LHS)+(j*w(i)*C_LHS+G_LHS);
                  Y_mat(k,k+1) = -1/(R_LHS+j*w(i)*L_LHS);
               end;
            else %Source at near-end
               Y_mat(k,k-1) = -2/(R_SR+j*w(i)*L_SR);
               Y_mat(k,k) = 3/(R_SR+j*w(i)*L_SR)+(j*w(i)*C_SR+G_SR);
               Y_mat(k,k+1) = -1/(R_SR+j*w(i)*L_SR);
            end;
         case {tot_nodes-1}
            if r_length ~= 0
               if r_pul_secs == 1
                  Y_mat(k,k-1) = -2/(R_RHS+j*w(i)*L_RHS+R_SR+j*w(i)*L_SR);
                  Y_mat(k,k) = 2/(R_RHS+j*w(i)*L_RHS)+(j*w(i)*C_RHS+G_RHS)+...
                     2/(R_RHS+j*w(i)*L_RHS+R_SR+j*w(i)*L_SR);
                  Y_mat(k,k+1) = -2/(R_RHS+j*w(i)*L_RHS);
               else %r_pul_secs > 1
                  Y_mat(k,k-1) = -1/(R_RHS+j*w(i)*L_RHS);
                  Y_mat(k,k) = 3/(R_RHS+j*w(i)*L_RHS)+(j*w(i)*C_RHS+G_RHS);
                  Y_mat(k,k+1) = -2/(R_RHS+j*w(i)*L_RHS);
               end;
            else %Source at far-end
```

```
        Y_mat(k,k-1) = -1/(R_SR+j*w(i)*L_SR);
        Y_mat(k,k) = 3/(R_SR+j*w(i)*L_SR)+(j*w(i)*C_SR+G_SR);
        Y_mat(k,k+1) = -2/(R_SR+j*w(i)*L_SR);
    end;
case {tot_nodes}
    %ZFE node
    if r_length ~= 0
        Y_mat(k,k) = 1/ZFE(i)+2/(R_RHS+j*w(i)*L_RHS);
        Y_mat(k,k-1) = -2/(R_RHS+j*w(i)*L_RHS);
    else %Source at far-end
        Y_mat(k,k) = 1/ZFE(i)+2/(R_SR+j*w(i)*L_SR);
        Y_mat(k,k-1) = -2/(R_SR+j*w(i)*L_SR);
    end;
case {t_node1}
    %LHS transition node 1
    Y_mat(k,k-1) = -1/(R_LHS+j*w(i)*L_LHS);
    Y_mat(k,k) = 1/(R_LHS+j*w(i)*L_LHS)+(j*w(i)*C_LHS+G_LHS)+...
        2/(R_LHS+j*w(i)*L_LHS+R_SR+j*w(i)*L_SR);
    Y_mat(k,k+1) = -2/(R_LHS+j*w(i)*L_LHS+R_SR+j*w(i)*L_SR);
case {t_node1+1}
    %LHS transition node 2
    if s_pul_secs == 1
        Y_mat(k,k-1) = -2/(R_LHS+j*w(i)*L_LHS+R_SR+j*w(i)*L_SR);
        Y_mat(k,k) = 2/(R_LHS+j*w(i)*L_LHS+R_SR+j*w(i)*L_SR)+...
            (j*w(i)*C_SR+G_SR)+...
            2/(R_SR+j*w(i)*L_SR+R_RHS+j*w(i)*L_RHS);
        Y_mat(k,k+1) = -2/(R_SR+j*w(i)*L_SR+R_RHS+j*w(i)*L_RHS);
    else
        Y_mat(k,k-1) = -2/(R_LHS+j*w(i)*L_LHS+R_SR+j*w(i)*L_SR);
        Y_mat(k,k) = 1/(R_SR+j*w(i)*L_SR)+(j*w(i)*C_SR+G_SR)+...
            2/(R_LHS+j*w(i)*L_LHS+R_SR+j*w(i)*L_SR);
        Y_mat(k,k+1) = -1/(R_SR+j*w(i)*L_SR);
    end;
case {t_node2}
    %RHS transition node 2
    Y_mat(k,k-1) = -1/(R_SR+j*w(i)*L_SR);
    Y_mat(k,k) = 1/(R_SR+j*w(i)*L_SR)+(j*w(i)*C_SR+G_SR)+...
        2/(R_RHS+j*w(i)*L_RHS+R_SR+j*w(i)*L_SR);
    Y_mat(k,k+1) = -2/(R_RHS+j*w(i)*L_RHS+R_SR+j*w(i)*L_SR);
case {t_node2+1}
    %RHS transition node 1
    Y_mat(k,k-1) = -2/(R_RHS+j*w(i)*L_RHS+R_SR+j*w(i)*L_SR);
    Y_mat(k,k) = 1/(R_RHS+j*w(i)*L_RHS)+(j*w(i)*C_RHS+G_RHS)+...
        2/(R_RHS+j*w(i)*L_RHS+R_SR+j*w(i)*L_SR);
    Y_mat(k,k+1) = -1/(R_RHS+j*w(i)*L_RHS);
otherwise
    %Internal loops
    if k < t_node1
        %LHS loops
        Ctemp = C_LHS;
        Ltemp = L_LHS;
        Rtemp = R_LHS;
        Gtemp = G_LHS;
    elseif k > t_node2
        %RHS loops
        Ctemp = C_RHS;
```

```
                Ltemp = L_RHS;
                Rtemp = R_RHS;
                Gtemp = G_RHS;
            else
                %Source region loops
                Ctemp = C_SR;
                Ltemp = L_SR;
                Rtemp = R_SR;
                Gtemp = G_SR;
            end;
            Y_mat(k,k-1) = -1/(Rtemp+j*w(i)*Ltemp);
            Y_mat(k,k) = 2/(Rtemp+j*w(i)*Ltemp)+(j*w(i)*Ctemp+Gtemp);
            Y_mat(k,k+1) = -1/(Rtemp+j*w(i)*Ltemp);
        end;
    end;
    %Solve for the voltages
    V_mat(i,:) =(Y_mat^(-1))*I_mat;
    clear Ctemp Ltemp Rtemp Gtemp;
end;

%Most of the voltages are specified internal to the cells rather than end
%points. Need to calculate the cell edge voltages and currents. The number
%of internally solved cell voltages are given by the variables containing
%the number of LHS, SR, and RHS sections.

Z_mat_full = zeros(length(f),(tot_nodes-3));
Z_mat_half = zeros(length(f),(tot_nodes-3));

%Fill impedance matrices showing the impedance between solved internal
%voltage nodes
for k = 1:tot_nodes-3
    if k <= l_pul_secs
        if k ~= l_pul_secs
            %Node internal to a LHS section
            Z_mat_full(:,k) = R_LHS+j*w*L_LHS;
            Z_mat_half(:,k) = (R_LHS+j*w*L_LHS)/2;
        else
            %Node between LHS and SR
            Z_mat_full(:,k) = (R_LHS+j*w*L_LHS)/2+(R_SR+j*w*L_SR)/2;
            Z_mat_half(:,k) = (R_LHS+j*w*L_LHS)/2;
        end;
    elseif k <= l_pul_secs+s_pul_secs
        if k ~= l_pul_secs+s_pul_secs
            %Node internal to a SR section
            Z_mat_full(:,k) = R_SR+j*w*L_SR;
            Z_mat_half(:,k) = (R_SR+j*w*L_SR)/2;
        else
            %Node between SR and RHS
            Z_mat_full(:,k) = (R_SR+j*w*L_SR)/2+(R_RHS+j*w*L_RHS)/2;
            Z_mat_half(:,k) = (R_SR+j*w*L_SR)/2;
        end;
    else %Node internal to a RHS section
        Z_mat_full(:,k) = R_RHS+j*w*L_RHS;
        Z_mat_half(:,k) = (R_RHS+j*w*L_RHS)/2;
    end;
end;
```

```
%Calculate the internal currents and load currents
I_node_mat = zeros(length(f),tot_nodes-1);
I_node_mat(:,2:(tot_nodes-2)) = ...
   (V_mat(:,2:(tot_nodes-2))-V_mat(:,3:(tot_nodes-1)))./Z_mat_full;
I_node_mat(:,1) = -V_mat(:,1)./ZNE;
I_node_mat(:,tot_nodes-1) = V_mat(:,tot_nodes)./ZFE;
%Calculate the internal voltages and fill in load voltages
V_node_mat = zeros(length(f),tot_nodes-1);
V_node_mat(:,2:(tot_nodes-2)) = ...
   V_mat(:,2:(tot_nodes-2))-I_node_mat(:,2:(tot_nodes-2)).*Z_mat_half;
V_node_mat(:,1) = V_mat(:,1);
V_node_mat(:,tot_nodes-1) = V_mat(:,tot_nodes);

%Define Analytical Expressions - Distributed Noise Source
xLHS = x_KVL_LHS; %Position vector for LHS of circuit (m)
xRHS = x_KVL_RHS; %Position vector for RHS of circuit (m)
xSR = x_KVL_SR; %Position vector for the SR of circuit (m)
VLHS = zeros(length(f),length(xLHS)); %Initialize VLHS matrix to zeros
VRHS = zeros(length(f),length(xRHS)); %Initialize VRHS matrix to zeros
VSR = zeros(length(f),length(xSR)); %Initialize VSR matrix to zeros
%Define Equivalent Noise Current
%This quantity is defined in case the analytical expression for a uniform
%source is to be compared with a simulation where the sources are not
%uniform. The middle value or the equivalent middle value in the source
%region is used for the equivalent noise current.
if size(In,2)-(floor(size(In,2)/2)*2) == 1
   %Position matrix is odd - take the middle value for all frequencies
   In_eq = In(:,(floor(size(In,2)/2)+1));
else %Position matrix is even - find average equivalent middle value
   In_eq = mean([In(:,floor(size(In,2)/2)) In(:,(floor(size(In,2)/2)+1))],2);
end;

%Find the Voltage on the TL outside the coupling region
%Non-uniform Analytical Equation
for i = 1:length(xRHS)
   VRHS(:,i) = (-(G21+j*w*C21).*(Vs*Z0c.*exp(-gamma_c*Lc)./...
      ((Z0c+ZS_CP).*(1-G_ZL.*G_ZS.*exp(-2*gamma_c*Lc)))).*...
      (Z0v/2).*(1./(1-G_NE.*G_FE.*exp(-2*gamma_v*Lv)))).*...
      (((abs(x0L)-abs(x0R))*(1+G_ZL.*G_NE.*exp(-2*gamma_v*(a+Lv)))+...
      (1./(2*gamma_v)).*(G_ZL.*exp(-2*gamma_v*(abs(x0L)+abs(x0R)+a))+...
      G_NE.*exp(-2*gamma_v*Lv)).*(exp(2*gamma_v*abs(x0L))-exp(2*gamma_v*abs(x0R)))).*...
      exp(gamma_c*a).*(exp(-gamma_c*xRHS(i))+G_FE.*exp(gamma_c*xRHS(i))));
end;
%Non-uniform Analytical Equation
for i = 1:length(xLHS)
   VLHS(:,i) = (-(G21+j*w*C21).*(Vs*Z0c.*exp(-gamma_c*Lc)./...
      ((Z0c+ZS_CP).*(1-G_ZL.*G_ZS.*exp(-2*gamma_c*Lc)))).*...
      (Z0v/2).*(1./(1-G_NE.*G_FE.*exp(-2*gamma_v*Lv)))).*...
      (((abs(x0L)-abs(x0R))*(G_FE+G_ZL.*exp(-2*gamma_c*a))+...
      (1./(2*gamma_v)).*(1+G_ZL.*G_FE.*exp(-2*gamma_v*(abs(x0L)+abs(x0R)+a))).*...
      (exp(2*gamma_v*abs(x0L))-exp(2*gamma_v*abs(x0R)))).*...
      exp(gamma_c*a).*(G_NE.*exp(-gamma_c*(xLHS(i)+2*Lv))+exp(gamma_c*xLHS(i))));
end;
%Find the voltage on the TL inside the coupling region
%Non-uniform Analytical Equation
for i = 1:length(xSR)
```

```
    VSR(:,i) = (-(G21+j*w*C21).*(Vs*Z0c.*exp(-gamma_c*Lc)./...
        ((Z0c+ZS_CP).*(1-G_ZL.*G_ZS.*exp(-2*gamma_c*Lc)))).*...
        (Z0v/2).*(1./(1-G_NE.*G_FE.*exp(-2*gamma_v*Lv)))).*(...
        (((abs(x0L)+xSR(i))*(1+G_ZL.*G_NE.*exp(-2*gamma_v*(Lv+a)))+... %RHS portion
        (1./(2*gamma_v)).*(G_ZL.*exp(2*gamma_v*(xSR(i)-abs(x0L)-a))+...
        G_NE.*exp(-2*gamma_v*Lv)).*(exp(2*gamma_v*abs(x0L))-exp(-2*gamma_v*xSR(i)))).*...
        exp(gamma_c*a).*(exp(-gamma_c*xSR(i))+G_FE.*exp(gamma_c*xSR(i))))+...
        ((-(xSR(i)+abs(x0R))*(G_FE+G_ZL.*exp(-2*gamma_c*a))+... %LHS portion
        (1./(2*gamma_v)).*(1+G_ZL.*G_FE.*exp(2*gamma_v*(xSR(i)-abs(x0R)-a))).*...
        (exp(-2*gamma_v*xSR(i))-exp(2*gamma_v*abs(x0R)))).*...
        exp(gamma_c*a).*(G_NE.*exp(-gamma_c*(xSR(i)+2*Lv))+exp(gamma_c*xSR(i)))));
end;

xAnal = horzcat(xLHS,xSR(2:(length(xSR)-1)),xRHS);
VTOT = horzcat(VLHS,VSR(:,(2:(length(xSR)-1))),VRHS);

%Compare the Analytical Results to the Simulation Results
%Subplots may be useful here
%    Top Plot - Coupling Voltage Waveform in the coupling region
%    Bottom Plot - Voltage along the victim TL

figure;
subplot(2,1,1);
plot(x_KVL_SR_mid,abs(In(1,:)),...
    x_KVL_SR_mid,ones(1,length(x_KVL_SR_mid))*abs(In_eq(1)),'-r');
title('Low Frequency Response - Noise Current Waveform');
ylabel('|I|');
legend('Actual Noise Source','Approximated Noise Source','Location','Best');
xlim([xLHS(1) xRHS(length(xRHS))]);
subplot(2,1,2);
plot(xAnal,abs(VTOT(1,:)),x_KVL,abs(V_node_mat(1,:)),'r');
title('Low Frequency Response - Victim Voltage Waveform');
xlabel('TL Position (m)');
ylabel('|V|');
legend('Analytical','Simulation','Location','Best');

figure;
subplot(2,1,1);
plot(x_KVL_SR_mid,abs(In(floor(length(f)/2),:)),...
    x_KVL_SR_mid,ones(1,length(x_KVL_SR_mid))*abs(In_eq(floor(length(f)/2))),'-r');
title('Middle Frequency Response - Noise Current Waveform');
ylabel('|I|');
legend('Actual Noise Source','Approximated Noise Source','Location','Best');
xlim([xLHS(1) xRHS(length(xRHS))]);
subplot(2,1,2);
plot(xAnal,abs(VTOT(floor(length(f)/2),:)),...
    x_KVL,abs(V_node_mat(floor(length(f)/2),:)),'r');
title('Middle Frequency Response - Victim Voltage Waveform');
xlabel('TL Position (m)');
ylabel('|V|');
legend('Analytical','Simulation','Location','Best');

figure;
subplot(2,1,1);
plot(x_KVL_SR_mid,abs(In(length(f),:)),...
    x_KVL_SR_mid,ones(1,length(x_KVL_SR_mid))*abs(In_eq(length(f))),'-r');
```

```
title('High Frequency Response - Noise Current Waveform');
ylabel('|I|');
legend('Actual Noise Source','Approximated Noise Source','Location','Best');
xlim([xLHS(1) xRHS(length(xRHS))]);
subplot(2,1,2);
plot(xAnal,abs(VTOT(length(f),:)),x_KVL,abs(V_node_mat(length(f),:)),'r');
title('High Frequency Response - Victim Voltage Waveform');
xlabel('TL Position (m)');
ylabel('|V|');
legend('Analytical','Simulation','Location','Best');

%Look at phase
% % % figure;
% % % plot(xAnal,angle(VTOT(1,:)),x_KVL,angle(V_node_mat(1,:)),'r');
% % % xlabel('TL Position (m)');
% % % ylabel('angle(V)');
% % % title('Low Frequency Response');
% % % legend('Analytical','Simulation','Location','Best');
% % %
% % % figure;
% % % plot(xAnal,angle(VTOT(floor(length(f)/2),:)),...
% % %     x_KVL,angle(V_node_mat(floor(length(f)/2),:)),'r');
% % % xlabel('TL Position (m)');
% % % ylabel('angle(V)');
% % % title('Middle Frequency Response');
% % % legend('Analytical','Simulation','Location','Best');
% % %
% % % figure;
% % % plot(xAnal,angle(VTOT(length(f),:)),x_KVL,angle(V_node_mat(length(f),:)),'r');
% % % xlabel('TL Position (m)');
% % % ylabel('angle(V)');
% % % title('High Frequency Response');
% % % legend('Analytical','Simulation','Location','Best');

%Plot movie for comparing the Analytical Results to the Simulation Results
figure;
for k = 1:length(f)
    subplot(2,1,1);
    plot(x_KVL_SR_mid,abs(In(k,:)),...
        x_KVL_SR_mid,ones(1,length(x_KVL_SR_mid))*abs(In_eq(k)),'-r');
    title(strcat(['Noise Current Waveform @ ' num2str(f(k)) ' Hz']));
    ylabel('|I|');
    legend('Actual Noise Source','Approximated Noise Source','Location','Best');
    xlim([xLHS(1) xRHS(length(xRHS))]);
    subplot(2,1,2);
    plot(xAnal,abs(VTOT(k,:)),x_KVL,abs(V_node_mat(k,:)),'r');
    title(strcat(['Victim Voltage Waveform @ ' num2str(f(k)) ' Hz']));
    xlabel('TL Position (m)');
    ylabel('|V|');
    legend('Analytical','Simulation','Location','Best');
    pause(0.01);
end;
```

VITA

Matthew Scott Halligan started his undergraduate studies at Missouri University of Science and Technology (Missouri S&T) formerly known as University Missouri-Rolla in August of 2004. In 2007 he joined the Missouri S&T EMC lab as an undergraduate research assistant. He graduated with his Bachelor of Science in Electrical Engineering in May 2008 with summa cum laude honors and a 4.0 GPA. He continued research with the EMC lab for his graduate studies with the Chancellor's Fellowship, a full scholarship for his graduate studies. In May 2010 he was awarded a Master of Science in Electrical Engineering degree from Missouri S&T. In August 2014, he received his Doctor of Philosophy in Electrical Engineering degree from Missouri S&T.

While at Missouri S&T, Matt was active in the university band program and the university Newman Center. As a graduate research assistant he was able to work with a variety companies including: Sandia National Laboratories, General Dynamics OTS, U.S. Navy, U.S. Air Force, IBM, Cobham, Techflow, Rockwell Automation, and Sony. His current research interests include detection and neutralization of explosive devices, immunity of electronic systems, crosstalk in cable bundles, high-speed cable and connector design, and waveguide power divider design.